

THESIS
ON
SEISMIC FRAGILITY ANALYSIS OF IRREGULAR
BUILDINGS UNDER BI-DIRECTIONAL EARTHQUAKE

Submitted By

Sukalyan Sarkar

Master of Civil Engineering

(Structural Engineering)

M.C.E-II (2021-2022)

Class Roll no.- **002010402005**

Examination Roll No.- **M4CIV22005**

University Registration No.- **153961 of 2020-2021**

A Thesis is submitted for the Partial Fulfilment of the Continuous
Assessment of the Course of Master of Civil Engineering (Specialization -
STRUCTURAL ENGINEERING) of Jadavpur University.

Under the guidance of

Dr. Amit Shiuly

Associate Professor

Faculty of Engineering and Technology

Department of Civil Engineering

(Structural Engineering)

Jadavpur University

Kolkata – 700032

June 2022

DECLARATION

This thesis titled “**SEISMIC FRAGILITY ANALYSIS OF IRREGULAR BUILDINGS UNDER BI-DIRECTIONAL EARTHQUAKE**” is prepared and submitted for the partial fulfillment of the continuous assessment of Master of Civil Engineering (with specialization in Structural Engineering) of Jadavpur University.

Date: 28/06/2022
Place: Civil Engineering Department
Jadavpur University, Kolkata



Sukalyan Sarkar
Class: M.C.E2ndyr.
Structural Engg
Class Roll No: 002010402005
Exam Roll No: M4CIV22005
Regn. No.: 153961 of 2020-2021

JADAVPUR UNIVERSITY
DEPARTMENT OF CIVIL ENGINEERING
KOLKATA – 700032

RECOMMENDATION CERTIFICATE

It is here by certified that this thesis titled “SEISMIC FRAGILITY ANALYSIS OF IRREGULAR BUILDINGS UNDER BI-DIRECTIONAL EARTHQUAKE” is prepared and submitted for the partial fulfillment of the continuous assessment of **Master of Civil Engineering in Structural Engineering** course of **Jadavpur University** by **Sukalyan Sarkar**, a student of the said course for the session 2020-2022 under my supervision and guidance. It is also declared that no part of thesis of said work has been presented or published elsewhere.



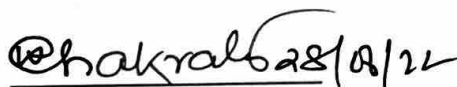
Dr. AMIT SHIULY

(Thesis Supervisor)

Department of Civil Engineering
Jadavpur University

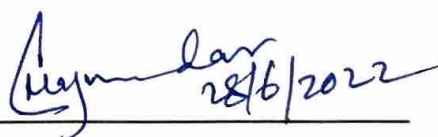
*Associate Professor
Department of Civil Engineering
Jadavpur University
Kolkata-700 032*

Countersigned by:



Head of the Department
Department of Civil
Engineering
Jadavpur University

Head
Department of Civil Engineering
Jadavpur University
Kolkata-700 032



Dean

Faculty of Engineering and Technology
Jadavpur University



DEAN

Faculty of Engineering & Technology
JADAVPUR UNIVERSITY
KOLKATA-700 032

JADAVPUR UNIVERSITY
DEPARTMENT OF CIVIL ENGINEERING
KOLKATA – 700032

CERTIFICATE OF APPROVAL*

This is to certify that this thesis, entitled “**SEISMIC FRAGILITY ANALYSIS OF IRREGULAR BUILDINGS UNDER BIDIRECTIONAL EARTHQUAKE**”, is hereby approved as an original work conducted and presented satisfactory to warrant its acceptance as a prerequisite to the degree for which it has been submitted by **Sukalyan Sarkar** (Class Roll No: **002010402005**). It is implied that by this approval the undersigned do not necessarily endorse or approve any statement made, opinion expressed or conclusion drawn therein, but approve the thesis only for the purpose for which it is submitted.

Final Examination for evaluation of thesis

1).....

2).....

3).....

(Signature of Examiners)

*Only in case the thesis is approved.

ACKNOWLEDGEMENT

I express my deep sense of respect and gratitude to Dr. Amit Shiuly, Associate Professor of the Department of Civil Engineering, Jadavpur University under whose supervision the work has been done and took the strain of giving valuable suggestion to me from time to time. It is his never- ending enthusiasm and constant urge for excellence that has given me hope in times of despair and has helped me to bring this thesis to completion.

I extend my thanks to all the faculty members and the library officials of Department of Civil Engineering, Jadavpur University for providing their moral support, encouragement and the necessary infrastructure for the work. I also acknowledge the co-operation and assistance provided by my friends during this period.


Sukalyan Sarkar

Class: MCE-II

Class Roll No: 002010402005

Examination Roll No.- M4CIV22005

University Registration No.- 153961 of 2020-2021

Date: 28.06.2022

**Place: Civil Engineering Department,
Jadavpur University,
Kolkata.**

"Research is what I'm doing when I don't know what I'm doing."

- Wernher von Braun

CONTENTS

	Page No
Declaration.....	1
Recommendation Certificate.....	2
Certificate of Approval.....	3
Acknowledgement.....	4
List of Notations.....	9
List of Tables.....	15
List of Figures.....	16
Abstract.....	20
Chapter# 1.....	21
Introduction	21
1.1 General.....	21
1.2 Need for Present Study.....	22
1.3 Objective and Scope of Work.....	23
1.4 Organization of the Report	23
Chapter# 2.....	25
Literature Review	25
2.1 General.....	25
2.2 Previous Researches on the Topic.....	25
2.3 Fragility Curve and Probabilistic Seismic Demand Models.....	29
2.4 Reliability Index.....	35
2.5 Response for Bidirectional Earthquake Motion.....	41
2.6 The Effective Duration of Earthquake Strong Motion.....	44
2.7 Critical Appraisal of Literature.....	46
Chapter# 3.....	51
Frame Structures on Uniform Soil	51
3.1 General.....	51

3.2 Problem Formulation.....	51
3.3 Modelling the Problem.....	60
3.4 Input Motions and Their Properties.....	72
3.5 Characteristics of Accelerogram Across Orientations.....	77
3.6 Displacement Time-Histories of Roof and Base Responses.....	81
3.7 Maximum Displacement Profiles.....	90
3.8 Maximum Drift Profiles.....	93
3.9 Fragility Curves.....	95
Chapter# 4.....	101
Frame Structures on Layered Soil	101
4.1 General.....	101
4.2 Problem Formulation.....	101
4.3 Modelling the Problem.....	102
4.4 Input Motions and Their Properties.....	104
4.5 Displacement Time-Histories of Roof and Base Responses.....	105
4.6 Maximum Displacement Profiles.....	108
4.7 Maximum Drift Profiles.....	109
4.8 Fragility Curves.....	111
Chapter# 5.....	114
Reliability Based Analysis	114
5.1 General.....	114
5.2 Seismic Hazard Curve.....	114
5.3 Reliability Curves and Their Formulations.....	115
5.4 Discussion on Reliability Curves.....	123
Chapter# 6.....	124
Frame Structures With Pile Foundation.....	124
6.1 General.....	124

6.2	Pile Foundations Macro-Element - ssilink2.....	124
6.3	Dashpot Damping – dashpt.....	131
6.4	Lumped Mass – lmass.....	133
6.5	Modelling the Problem in Seismostruct.....	133
6.6	Displacement Time-Histories of Roof and Base Responses....	142
6.7	Maximum Displacement Profiles.....	145
6.8	Maximum Drift Profiles.....	146
6.9	Fragility Curves.....	147
6.10	Reliability Curves.....	149
Chapter# 7.....		152
Concluding remarks.....		152
7.1	General.....	152
7.2	Major Findings.....	152
7.3	Limitations of Present Work.....	155
7.4	Future Scopes.....	155
References.....		156

LIST OF NOTATIONS

$F(t)$ = multi-dimensional forcing function
 $F_1(t)$ = relevant multi-dimensional system response process
 τ_1 = timing
 β_{pf} = reliability index
 P_s = safety probability / probability of the maximum response
 Φ_1 = standardized normal distribution
 Y = maximum response
 yc = design criterion
 S_a = spectral Acceleration
 $P(D \geq C | IM)$ = probability of exceedance of ground storey drift for particular limit state capacities
 D = ground storey drift
 C_1 = the drift capacity at chosen limit state
 $\beta_{D|IM}$ = dispersion in the IM / dispersion intensity of ground storey drifts
 β_C = dispersion in the capacities
 β_M = dispersion in the modelling
 S_D = described through PSDMs in terms of IM like ground storey drift at particular PGA levels which can be determined by NLTHA.
 S_C = described in terms of IM at particular limit state capacities (IO, LS, CP)
 IO = immediate occupancy
 LS = life safety
 CP = collapse prevention
 IM = Intensity Measure
 EDP = Engineering Damage Parameter
 a, b = the regression coefficients of the PSDM
 $PSDM$ = probabilistic seismic demand model
 PGA = Peak Ground Acceleration
 PGV = Peak Ground Velocity
 PGD = Peak Ground Displacement
 $NLTHA$ = Non-Linear Time-History Analyses
 β_m = total modelling dispersion
 β_q = defines that, hysteretic models may not accurately capture the behavior of structural components, even if the details of construction are precisely known
 $F_R(z)$ = fragility
 $G_A(z)$ = seismic hazard
 $P[LS]$ = probability of failure at certain performance level
 LSF = Limit State Function
 ζ_H = across variability parameter
 ζ_R = variability parameter which incorporates the variabilities in response modeling, response calculations, material variabilities and design equations
 P_F = unconditional failure probability
 \ddot{a} = median load level
 MF = moment frames
 EBF = eccentrically braced frames
 IDA = Incremental Dynamic Analysis
 FD = forward directivity
 VE = viscoelastic
 PSD = power spectral density
 I_A = Arias intensity
 $a(t)$ = ground acceleration
 g = acceleration due to gravity
 T_d = duration of signal above threshold

PBSD = Performance-Based Seismic Design
MCE = Maximum Considerable Earthquake
DBE = Design Basic Earthquake
PBEE = Performance-Based Earthquake Engineering
s = load
R = resistance
 $f_s(s)$ = probability that s occurs
FORM = first order reliability method
SORM = second order reliability method
IS = importance sampling
 \bar{N} = equivalent hysteretic loop numbers
 d_s = storey drift
 u_{up} = horizontal displacement at the top of the storey
 u_{down} = horizontal displacement at the bottom of the storey
 H_s = height of the storey
 $[M_{soil}]$ = Mass matrix assuming structure and foundation massless
 $\{u_{KI}\}$ = Foundation input motion
 $[K^*]$ = Stiffness matrix
 $\{\ddot{u}_b(t)\}$ = Acceleration at the boundary
 $\{up\}$ = effective excitation acting on the foundation
 $\{uf\}$ = free-field motion
 $\{us\}$ = diffracted wave motion
 τ_2 = ratio of the amplitudes of translational motion of the rigid base and the free-field motion for a certain harmonic component
 $\lambda(\omega)$ = Wavelength,
D = Dimension of the base in y-direction,
 V_a = The apparent wave velocity.
 $[M_{structure}]$ = Mass matrix assuming the soil massless
SSI = Soil structure interaction
BNWF = beam on nonlinear Winkler foundation
M = Mass matrix of the whole system containing entire structure, foundation and soil
C2 = Damping matrix (Material) of the soil and the structure
K1 = Stiffness matrix of the whole system
 M_{st} = Mass matrix consisting of non-zero masses for the structural degree of freedom
I = Influence coefficient vector
 \ddot{u}_g = Free-field ground acceleration
 u = Relative displacement vector with respect to the base
FEM = Finite element method
NDP = Nonlinear Dynamic Procedure
NLTH = Nonlinear Time History
U = Total response
 ϕ = modal matrix
 $\phi^1 \phi^2 \phi^3$ = mode shape vector
P = participation factor
RHA = response history analysis
 $\Delta_{(U)}$ = unidirectional excitation
 $E_{H(U)}$ = hysteretic energy under unidirectional shaking
 $\Delta_{(B)}$ = peak deformation under bidirectional excitation
 $E_{H(B)}$ = hysteretic energy under bidirectional shaking
 E_{Hx} = area of force-displacement history in x axis
 E_{Hy} = area of force-displacement history in y axis
 Ψ = angle of orientation of ground motion component
 $a_x(t), a_y(t)$ = horizontal components of original ground motion record
 $a_{x(\psi)}(t), a_{y(\psi)}(t)$ = components of the ground motion record when rotated anti-clockwise by an angle ψ

θ = incidence angle
 I_{Ax}, I_{Ay} = Arias Intensities of ground motion components x and y
 IM_x, IM_y = Intensity Measures of ground motion components x and y
 L_e = characteristic length which may be interpreted as energetic length scale
 a_g = peak ground acceleration
 T_m = mean period for real records / effective duration of earthquake strong motion
 I_c = characteristics intensity of motion
 NCI = normalized component intensity
 CAV = cumulative absolute velocity
 ψ_{max} = orientation in which NCI assumes a peak
 ψ_{min} = orientation in which NCI may approach to minimum
 r_x, r_y = peak responses under two components of motion uni-directionally and separately applied along two principal axes (x and y) of the structure
 $\Delta_{(CY)}$ = peak deformation estimates from combination rules
 $E_{H(CY)}$ = accumulated hysteretic response estimates from combination rules
 M_w = Magnitude of earthquake / Moment magnitude, defined based on the seismic moment, used for all earthquakes
 D_R = Rupture Duration
 F = Correction factor for effective duration
 L_1, L_2 = longer and shorter distances (measured parallel to the surface break) from the epicenter to the ends of the fault rupture respectively
 D_E = Effective Duration of strong motion
 $\tilde{\epsilon}_t^{pl}, \tilde{\epsilon}_c^{pl}$ = equivalent plastic strains in tension and compression
 $\dot{\tilde{\epsilon}}_t^{pl}, \dot{\tilde{\epsilon}}_c^{pl}$ = Equivalent plastic strain rate under tension and compression
 θ_2 = Temperature
 f_i ($i = 1, 2, \dots$) = Other predefined field variables
 ϵ_{i1}^{pl} = rate of strain
 d_t, d_c = independent uniaxial damage variables in tension and compression
 E_0 = initial or undamaged elastic stiffness of the material
 $\bar{\sigma}_t, \bar{\sigma}_c$ = effective uniaxial stresses in tension and compression
 σ_t, σ_c = uniaxial stresses in tension and compression
 G_1 = plastic potential function
 Ψ_2 = angle of dilatancy
 J_2 = Second invariant of stress deviator
 I_1 = First invariant of stress
 θ_3 = Polar angle through which the third invariant enters the deviatoric plane
 F_2 = Yield function
 α, β, γ = dimensionless material constants
 \bar{p} = effective hydrostatic pressure
 \bar{q} = Mises equivalent effective stress
 \bar{S} = deviatoric part of the effective stress tensor
 $\bar{\sigma}$ = effective stress tensor
 $\hat{\sigma}_{max}$ = algebraically maximum eigenvalue of $\bar{\sigma}$
 σ_{co} = initial equibiaxial yield stress
 σ_{bo} = uniaxial compressive yield stress
 TM = tensile meridian
 CM = compressive meridian
 $\hat{\sigma}_1, \hat{\sigma}_2, \hat{\sigma}_3$ = eigenvalues of the effective stress tensor
 K_c = a constant for any given value of the hydrostatic pressure with $\hat{\sigma}_{max} < 0$
 K_t = a constant for any given value of the hydrostatic pressure with $\hat{\sigma}_{max} > 0$
 G = Shear Modulus
 E = Young's Modulus
 K = Bulk Modulus
 ν = Poisson's Ratio

V_s = Shear Wave Velocity
ρ = Mass Density
d_t = Damage Parameter
CDP = Concrete Damaged Plasticity
α, β = Rayleigh Damping Coefficients
m = Number of significant modes considered
ξ₁ = Damping Ratio of the first mode
ξ_m = Damping Ratio of the m-th mode
ω₁ = Frequency of the first mode
ω_m = Frequency of the m-th mode
[C], [M], [K] = damping, mass and stiffness matrix of the physical system
F₃ = Focus (hypocenter), theoretical point in which the process of rupture and release of seismic energy is initialized
E₂ = Epicenter, point on ground surface that is connected with the Focus with a vertical line
S = Seismic station, where the accelerograms are recorded
h_F = Focal depth
R₂ = Hypocentral distance
d = Epicentral distance
FFT = Fast Fourier Transform
M_L = Local magnitude of earthquake
A = maximum amplitude of the displacement of the terrain
A* = correction of A
M_s = Surface waves magnitude, used for surface earthquakes
M_b = Body waves magnitude, used for intermediate earthquakes
M_d = Duration magnitude, used for weak earthquakes
MM56 = Mercalli modified scale
MSK = Medvedev Sponheuer Karnik scale
EMS-98 = European Macro seismic Scale
MRI = main recurrence intervals
SCDP = simplified concrete damage plasticity
OGS = Open ground storey
VGI = Vertical geometric irregular
BSIM = bidirectional shaking intensity measures
NLS = nonlinear static
IDR = inter-story drift ratio
NLRHA = Non-Linear Response History Analysis
F2MPA = Flexibly-supported 2 DOF Modal Pushover Analysis
LPM = Lumped-Parameter Model
SDOF = single degree of freedom
URM = unreinforced masonry
SPI = soil-pile interaction
PSWS = pile-supported wharf structure
ERB = elastic rubber bearing
SMRF = Special moment-resisting frame
CCDF = complimentary cumulative distribution function
FEA = Finite Element Analysis
HDGM = horizontal differential ground motion
IC = impedance contrast
BTR = basin-transduced Rayleigh
DGM = differential ground motion
PDGM = peak differential ground motion
H_c = horizontal axis length of distorted superellipse configuration of failure surface
M_c = vertical axis length of distorted superellipse configuration of failure surface
DIAM = Pile diameter
K_{VV} = Pile stiffness for vertical direction

K_{HH} = Pile stiffness for horizontal direction
K_{MM}, K_{HM}, K_{TT} = Pile stiffness for rotational directions
QQ_H MAX = Horizontal pile capacity
QQ_M MAX = Vertical pile capacity
Exp_{nH}, Exp_{nM}, GAMMA (γ) = Superellipse BS parameters
ZW = Maximum Gap depth / soil wedge depth corresponding to the failure mechanism
Eplp = Pile Flexural Stiffness
BETA (β) = Gap Evolution Parameter
ETA (η) = Minimum Gap Evolution Parameter
PL_{Ho} (H_o^{pl}) = Reference plastic modulus parameter
PL_{nur} (n_{UR}) = Exponent for plastic modulus evolution
Delta_{LIM} = Lower limit value for delta in unloading/reloading
E_p = Young's modulus of the pile material
E_{SD} = soil modulus of deformation at a depth equal to the pile diameter
I_p or I_{bz} = Moment of inertia of pile
A_b = Area of pile / pile cap
C1, C2, C3, C1, C22, C33, CH2M3, CH3M2 = Damping Coefficients for Dashpot damping element
M_x = Mass in X direction / translational inertia value
M_y = Mass in Y direction / translational inertia value
M_z = Mass in Z direction / translational inertia value
M_{xx} = Rotational inertia value in X direction
M_{yy} = Rotational inertia value in Y direction
M_{zz} = Rotational inertia value in Z direction
F1, F2, F3, M1, M2, M3 = Curve parameters for link element
I_{bx} = Moment of inertia of pile cap in X direction
I_{by} = Moment of inertia of pile cap in Y direction
I_{bz} = Moment of inertia of pile cap in Z direction
E_s = Modulus of elasticity of reinforcement
 μ = Strain hardening parameter
R_o = Transition curve initial shape parameter
a1 & a2 = Transition curve shape calibrating coefficients
a3 & a4 = Isotropic hardening calibrating coefficients
 ϵ_{ult} = Fracture / buckling strain
 γ = Specific weight
f_c = Compressive strength
f_t = Tensile strength
E_c = Modulus of elasticity
 ϵ_c = Strain at peak stress
m_s = SDOF mass
k_s = SDOF stiffness
c_s = SDOF damping coefficient
m_f = foundation mass
H_{eff} = building centroid height
 θ_f = foundation rotation
a(t) = seismic acceleration
f(t) = inertia force history
k_v = stiffness in the vertical direction
c_v = damping in the vertical direction
k_{Hx} = stiffness in the horizontal x-direction
c_{Hx} = damping in the horizontal x-direction
k_{My} = stiffness in the rotational direction around the y-axis
c_{My} = damping in the rotational direction around the y-axis
V_{max} = central vertical load capacity of the footing
t_h = slope related to the footing-soil friction

q_{lim} = ultimate static bearing capacity of the foundation
 s_u = undrained shear strength
 H_{max} = maximum base shear capacity
 M_{max} = maximum base moment capacity
 J_t = polar moment of inertia about z of the actual soil foundation contact surface
 ω = cyclic frequency (in rad/s) of interest / Soil deposit angular frequency
 V_{La} = "Lysmer's analog" wave velocity
 K_x = static stiffness for rectangular foundations on homogenous half-space along Horizontal, x (longitudinal direction)
 K_y = static stiffness for rectangular foundations on homogenous half-space along Horizontal, y (transverse direction)
 K_z = static stiffness for rectangular foundations on homogenous half-space along Vertical, z
 K_{rx} = static stiffness for rectangular foundations on homogenous half-space along Rocking rx, (around x axis)
 K_{ry} = static stiffness for rectangular foundations on homogenous half-space along Rocking ry, (around y axis)
 K_t = static stiffness for rectangular foundations on homogenous half-space along Torsional
 C_x = radiation damping coefficient along Horizontal, x (longitudinal direction)
 C_y = radiation damping coefficient along Horizontal, y (lateral direction)
 C_z = radiation damping coefficient along Vertical, z
 C_{rx} = radiation damping coefficient along Rocking rx, (around x axis)
 C_{ry} = radiation damping coefficient along Rocking ry, (around y axis)
 C_t = Torsional radiation damping coefficient
 α = uplift initiation parameter
 d_{mg} = soil / footing contact degradation
 h_o = reference plastic modulus
 n_{UR} = exponent for loading history in unloading/reloading
 χ_g = plastic potential parameter
 N_{max} = Maximum centred vertical load capacity
 T_{max} = Maximum base torsional moment capacities
 c' = Effective cohesion
 σ_n' = Effective overburden pressure
 ϕ' = Effective friction angle
 L_s = Soil deposit depth
 f_s = Soil deposit fundamental frequency
 $\bar{c}_x, \bar{c}_y, \bar{c}_z, \bar{c}_{rx}, \bar{c}_{ry}, \bar{c}_t$ = Dynamic dashpot coefficients

LIST OF TABLES

	Page No
2.1 Damage Control and Building Performance Levels	32
2.2 Magnitudes of earthquakes used for input motions in software	45
3.1 Properties of the uniform soils	52
3.2 Properties of the constituents of the buildings	52
3.3 Properties and meshing details of the elements used in Abaqus	62
3.4 Input for coupling constraints between various elements in Abaqus models	65
3.5 Rayleigh damping coefficients of materials for different soil-structure combinations of uniform soils	72
3.6 General properties of the earthquakes	73
4.1 Properties of soil 1	102
4.2 Properties of the elements used in Abaqus	103
4.3 Rayleigh damping coefficients of materials for different soil-structure combinations of layered soils	104
6.1 Expressions for pile-head static stiffnesses	128
6.2 Expressions for variation of the damping ratio components with frequency	129
6.3 Bounding surface parameters	129
6.4 Calibration parameters	130
6.5 Lumped mass element - lmass input parameters (in X and Y directions)	133
6.6 Menegotto-Pinto steel model stl_mp input parameters	135
6.7 Mander et al. nonlinear concrete model - con_ma input parameters	137
A.1 Pile foundations macro-element - SSILINK2 input parameters	163
A.2 Dashpot damping element – dashpt input parameters	165

LIST OF FIGURES

	Page No
2.1 Input-output relationship for Fragility Analysis	30
2.2 Schematical of Seismic Fragility Curve	30
2.3 Storey drift [Abaqus]	31
2.4 Schematic representation of storey drift	32
2.5 Damage states of a typical building pushed to failure	33
2.6 Graphical representation of SAC – FEMA 2000 method	34
2.7 SAC – FEMA 2000 method	35
2.8 Fragility-hazard interface	37
2.9 Schematical of Reliability Curve	38
2.10 Schematical of Seismic Hazard Curve	39
2.11 Graphical representation of development of Reliability Index	40
2.12 Correspondence between angle of incidence (θ) and orientation of accelerogram (ψ)	42
3.1 Dimension Details of Pile Cap	53
3.2 Plan of the building with no irregularity	53
3.3 Elevation of the building without irregularity on plane ground as well as elevation of the building with horizontal irregularity on plane ground	54
3.4 Elevation of the building without irregularity on sloping ground as well as elevation of the building with horizontal irregularity on sloping ground	55
3.5 Elevation of the building with vertical irregularity on plane ground	56
3.6 Elevation of the building with vertical irregularity on sloping ground	57
3.7 Ground, 1st, 2nd and 3rd floor plan of the building with vertical irregularity	58
3.8 4th and 5th floor plan of the building with vertical irregularity	58
3.9 6th and 7th floor plan of the building with vertical irregularity as well as typical floor plan of the building with horizontal irregularity	59
3.10 8th and 9th floor plan of the building with vertical irregularity	59
3.11 Stress strain diagram for concrete damaged plasticity model	63
3.12 Stress strain diagram to be given as input in Abaqus for concrete damaged plasticity model	63
3.13 Damage parameter v/s strain diagram to be given as input in Abaqus for concrete damaged plasticity model	64
3.14 Isometric view of the model used for building without	68

	irregularity on sloping ground with shallow foundation	
3.15	Isometric view of the model used for building without irregularity on sloping ground with pile foundation	68
3.16	Isometric view of the model used for building without irregularity on plane ground with shallow foundation	68
3.17	Isometric view of the model used for building without irregularity on plane ground with pile foundation	68
3.18	Isometric view of the model used for building with vertical irregularity on sloping ground with shallow foundation	69
3.19	Isometric view of the model used for building with vertical irregularity on sloping ground with pile foundation	69
3.20	Isometric view of the model used for building with vertical irregularity on plane ground with shallow foundation	69
3.21	Isometric view of the model used for building with vertical irregularity on plane ground with pile foundation	69
3.22	Isometric view of the model used for building with horizontal irregularity on plane ground with shallow foundation	69
3.23	Soil base surrounded by infinite soil	69
3.24	Soil tetrahedron (for isolated footing) embedded in the soil base	70
3.25	Isolated footing embedded in the soil tetrahedron	70
3.26	Soil tetrahedron (for pile footing) embedded in the soil base	70
3.27	Finer meshing of soil layer surrounding holes for piles	70
3.28	Pile footing embedded in the soil tetrahedron	70
3.29	Acceleration time-history of Loma Prieta earthquake for 0°	74
3.30	Velocity time-history of Loma Prieta earthquake for 0°	74
3.31	Displacement time-history of Loma Prieta earthquake for 0°	74
3.32	Acceleration response spectra of Loma Prieta earthquake for 0°	74
3.33	Velocity response spectra of Loma Prieta earthquake for 0°	74
3.34	Displacement response spectra of Loma Prieta earthquake for 0°	74
3.35	FFT of Loma Prieta earthquake for 0°	75
3.36	Acceleration time-history of Loma Prieta earthquake for 90°	75
3.37	Velocity time-history of Loma Prieta earthquake for 90°	75
3.38	Displacement time-history of Loma Prieta earthquake for 90°	75
3.39	Acceleration response spectra of Loma Prieta earthquake for 90°	75
3.40	Velocity response spectra of Loma Prieta earthquake for 90°	75
3.41	Displacement response spectra of Loma Prieta earthquake for 90°	75
3.42	FFT of Loma Prieta earthquake for 90°	75
3.43	Acceleration time-history of Denali earthquake for 0°	76
3.44	Velocity time-history of Denali earthquake for 0°	76
3.45	Displacement time-history of Denali earthquake for 0°	76
3.46	Acceleration response spectra of Denali earthquake for 0°	76
3.47	Acceleration time-history of Denali earthquake for 90°	76
3.48	Velocity time-history of Denali earthquake for 90°	76
3.49	Displacement time-history of Denali earthquake for 90°	76

3.50	Acceleration response spectra of Denali earthquake for 90°	76
3.51	FFT of Denali earthquake for SRSS	77
3.52	Characteristics of spectral acceleration of accelerogram across orientations (Event: Loma Prieta Santa Cruz Mountains earthquake, 1989 (NF), Sa)	77
3.53	Characteristics of Normalized Component Intensity of accelerogram across orientations (Event: Loma Prieta Santa Cruz Mountains earthquake, 1989 (NF), Sa)	78
3.54	Characteristics of Normalized Component Intensity of accelerogram across orientations (Event: Denali Alaska earthquake, 2002 (FF), Sa)	78
3.55	Characteristics of spectral acceleration of accelerogram across orientations (Event: Denali Alaska earthquake, 2002 (FF), Sa)	79
3.56	Characteristics of characteristic length of accelerogram across orientations (Event: Loma Prieta Santa Cruz Mountains earthquake, 1989 (NF), Le)	80
3.57	Characteristics of characteristic length of accelerogram across orientations (Event: Denali Alaska earthquake, 2002 (FF), Le)	80
3.58 – 3.109	Resultant displacement time-history of G+9 buildings with isolated footing on uniform soil	82 – 90
3.110 – 3.119	Resultant maximum displacements of different floors of G+9 buildings with isolated footing on uniform soil	91 – 92
3.120 – 3.129	Resultant maximum drifts of different floors of G+9 buildings with isolated footing on uniform soil	93 – 95
3.130 – 3.154	PSDM & Fragility curves of G+9 buildings with isolated footing on uniform soil	96 – 100
4.1	Shear wave variation along depth of soil 1	102
4.2 – 4.17	Resultant displacement time-history of G+9 buildings with isolated footing on layered soil	105 – 107
4.18 – 4.25	Resultant maximum displacements of different floors of G+9 buildings with isolated footing on layered soil	108 – 109
4.26 – 4.33	Resultant maximum drifts of different floors of G+9 buildings with isolated footing on layered soil	110 – 111
4.34 – 4.42	PSDM & Fragility curves of G+9 buildings with isolated footing on layered soil	112 – 113
5.1	Seismic hazard curve for Conterminous U.S. (USGS, 2014) in semi-logarithmic scale	115
5.2	Probability Density for Limit-state	116
5.3	Flow chart for plotting reliability curves	117
5.4 – 5.35	Reliability Index of G+9 buildings with isolated footing	117 – 122
6.1	Modelling lateral response of the entire soil-pile system	124
6.2	(a) two simplified geotechnical scenarios in terms of undrained shear strength (Su) distribution along the depth of the soil deposit (b) characteristic soil response for a laterally loaded long pile	125
6.3	Distorted superellipse configuration of failure surface	126

6.4	Representation of maximum Gap depth / soil wedge depth corresponding to the failure mechanism. zw	127
6.5	Soil stiffness evolution with depth	127
6.6	Sign convention for pile-head stiffness matrix components	128
6.7	Local Axes and Output Notation	130
6.8	FE model of damping element with link element	132
6.9	Inertia mass with respect to the global reference system	133
6.10	Stress – strain graph of reinforcement in Seismostruct for M-P steel model	136
6.11	Stress – strain graph of concrete in Seismostruct for Mander et al. nonlinear concrete model	137
6.12	Column section in SeismoStruct	138
6.13	Beam section in SeismoStruct	138
6.14	Local Axes and Output Notation	140
6.15	Column section discretization in SeismoStruct	140
6.16	Beam section discretization in SeismoStruct	140
6.17	(a) Isometric view of model in SeismoStruct (b) Link element, lumped mass and restraint at column base at ground level	142
6.18 – 6.33	Resultant displacement time-history of G+9 buildings with pile footing	143 – 145
6.34 – 6.35	Resultant maximum displacements of different floors of G+9 buildings with pile footing	146
6.36 – 6.37	Resultant maximum drifts of different floors of G+9 buildings with pile footing	147
6.38 – 6.46	PSDM & Fragility curves of G+9 buildings with pile footing	148 – 149
6.47 – 6.54	Reliability Index of G+9 buildings with pile footing	150 – 151

ABSTRACT

Seismic demand of structures may be potentially exaggerated due to bi-directional shaking which is strongly influenced by the local site condition. Further, challenging situation may rise if structure rests on sloping ground. It is to be mentioned that, seismic structural fragility constitutes an important step for performance based seismic design.

This paper deals with reliability-based fragility analysis of various types of vertical and plan irregular buildings situated on different types of soil. In addition to that, isolated foundations situated on various uniform and layered soils and sloping ground by using finite element software Abaqus. Uniform soil types include hard, medium and soft soils whereas layered soil type is based on shear wave velocity variation through depth. In this study soil-structure interaction have been considered with near field and far field bidirectional earthquakes (Denali Alaska earthquake and Loma Prieta Santa Cruz Mountains earthquake). It is to be noted that, by studying the characteristics of different properties of the accelerograms across orientations, combination of structural responses has been carried out by 30% and 40% rules as per AASHTO 1998 and ATC 1996; NCHRP 2001. For studying the effect of pile foundation, analysis has been carried out using SeismoStruct.

Results reveal that spectral acceleration and characteristic length of Loma Prieta and Denali earthquake follow desired characteristics over different orientations. Also, building is subjected to an earthquake motion situated on hard soil, it has the least probability of exceeding a limit state. However, it has the largest probability of exceeding a limit state when located on soft soil. In case of most G+9 building configurations, the probability of exceedance of a specific limit state for that soil-structure system is less when it is subjected to a near-field earthquake. Exceptionally, for vertically irregular building, the probability of exceedance value of the soil-structure system will be greater under the influence of near-field earthquake. Further, highest probability of exceedance value of the soil-structure system has been observed in case of building on sloping ground as compared to building on plane ground in case of far field earthquake. On the contrary, for near field earthquake, lowest probability of exceedance value of the soil-structure system has been noted in case of building situated on sloping ground as compared to building situated on plane ground. Furthermore, in case of G+9 building having pile foundation, has the largest probability of exceeding a limit state when located on medium soil for both far and near field earthquake.

CHAPTER 1: INTRODUCTION

1.1 - GENERAL

The numbers of damages during past seismic events around the world have been increasing every year and thus it needs stern thinking for the whole community including scientist, urban planner, engineers to strengthen their efforts to minimize the loss of damages during future seismic events. The society have learnt many lessons, like proper planning, and design of structures and obvious to carry the seismic risk assessment. (Sitharam and Vipin 2010, Anbazhagan and Sheikh 2012, Shiuly 2019)

The earthquakes are the most destructive natural calamity that human kind has experienced like tsunamis, hurricanes, tornados, floods etc. The place and the time of occurrence of earthquake are unpredictable and therefore this makes them disastrous phenomenon. Human has always lived with earthquakes. Some of them are so small that they are not felt, others against, are so strong that they can destroy an entire city and cause major damage in infrastructures (bridges, buildings, etc.) and kill thousands of people. Considerable damage and destruction of property and life occurred due to past seismic events.

In present scenario, it has become a big task for the whole society including scientist, researchers and engineers around the world to minimize the earthquake devastation by adopting proper means of disaster management. In last decades, through further development of computer technology in civil engineering, so many different seismic analyses became possible and accuracy of the analysis is increased. Therefore, there are lots of methodologies for seismic assessment in use. Including the probabilistic approaches into the seismic assessment offer more realistic approaches. Recently, seismic assessments are done with this consideration. Fragility analysis is one of them. The fragility analysis which is a system reliability analysis with correlated demands and capacity is performed with different methodologies to establish the probabilistic characterization of the demands in different aspects.

In recent practice Performance Based Seismic Design (PBSD) are used as a tool to predict seismic risk of buildings. This is because the performance objectives depend on damage of structure and the damage is proportional to displacement and drift of structure. The performance level may be described by FEMA 356 (Immediate Occupancy, Life Safety and Collapse Prevention). FEMA stands for 'Federal Emergency Management Agency'. At Collapse Prevention (CP) level, extensive cracking and hinge formation is occurred in ductile member. Limited cracking failure can be seen in some non-ductile measures like columns and severe damage in short column. There is significant loss of both lateral strength and stiffness with some permanent lateral deformation. At Life Safety (LS) level, there may be significant damages to structural and nonstructural components. However, with low risk of fatalities, the intensive repair may be required, but it may not be economically feasible. At Immediate Occupancy (IO) level, minor hairline crack may take place. Limited yielding may happen at few locations. However, no crushing occurs. Strain is below 0.003. Thus, the building need not be vacated after the earthquake. It is also required to get an idea about the chances of exceed that limit in FEMA 356 for IO, LS, CP both for Maximum Considerable Earthquake (MCE) and Design Basic Earthquake (DBE). However, the structural damage depends on several factors like roof displacement, ground storey drift etc. So, sometime supplemental damping devices may be used to

control the response of structure. Further, probability-based risk assessment should be carried out to minimize the damage of the buildings during future seismic events.

Fragility curve is defined as a curve which signifies the vulnerability of structure. It is the statistical tool by developing a curve of probability of exceeding Engineering Damage Parameter (EDP) against specific demand. The engineering damage parameter may be roof drift, storey drift, energy dissipation etc. Whereas the demand may be Peak Ground Acceleration (PGA), Peak Ground Displacement (PGD) and Spectral Acceleration (Sa) for a specific time period etc. Several researches were conducted on seismic fragility analysis of structure. Singhal and Kiremidjian (1996) studied method for probabilistic evaluation of seismic structural damage.

Reliability can be defined as the risk of a building frame which can be conveyed by the statistical parameter “Reliability Index”. The Reliability Index can be developed by convolving the fragility curve with the derivative of the seismic hazard curve.

Seong-Hoon Jeong & Amr S. Elnashai [3] (2006) presented a methodology for the derivation of fragility curves for structures with plan irregularities. K.A. Korkmaz [9] (2008) performed the fragility analysis, which is a system reliability analysis with correlated demands and capacity, with different methodologies to establish the probabilistic characterization of the demands in different aspects.

Incorporating soil structure interaction and considering near field and far field earthquake in the analysis are the important aspects to be dealt with. In near field earthquake, all types of seismic waves of high and low frequencies are present. While in far field earthquake, only low frequency seismic waves are present. Hence nature of near field earthquake and far field earthquake are different. Their effects on a building are also different. Soil structure interaction is an important consideration and the effect of soft soil, hard soil and layered soil should be considered in the finite element modelling. Bi-directional earthquake should be considered simultaneously and its effect should be studied.

1.2 - NEED FOR PRESENT STUDY

Bidirectional shaking covering all incidence angles for earthquake analysis of buildings attracted the attention of the researchers over a long period after few failures of buildings or part of the buildings during earthquake.

Fragility analysis is needed for the analysis for seismic loss estimation in built environments. They represent the probability of exceeding a damage limit state for a given structure type subjected to a seismic excitation. Seismic fragility analysis is needed as a probabilistic measure for seismic performance assessment of structural components or geometrically irregular systems.

Earthquake has two components in X and Z directions. Earthquake acts in the resultant direction. We measure displacement due to earthquake in X and Z directions but the displacement occurs in the resultant direction. Actually, earthquake has 3 component directions but we generally do not consider Y direction component. We have to consider all these which is primary necessity of our study.

Fragility means ‘probability of failure’. Using Abaqus, we can handle bidirectional

earthquake incorporating soil structure interaction and considering near field and far field earthquake. This type of work is not done yet.

1.3 - OBJECTIVE AND SCOPE OF WORK

Objective of our work is to study the reliability-based fragility analysis of irregular buildings under bidirectional earthquake. The various scopes of our work are:

- To model irregular building with finite element softwares (SeismoStruct and Abaqus).
- To construct a model of irregular shaped building with bidirectional earthquake in X and Z directions.
- To model considering the soil-structure interaction effect.
- To consider near field and far field earthquake in our study.
- To consider separate cases of plane and sloping ground.
- To model both isolated and pile foundation system in our study.
- To take into account both horizontal and vertical irregular buildings.

1.4 - ORGANISATION OF THE REPORT

This thesis is an assembly of seven chapters. The table and figures have been presented sequentially as they appear in the text.

In **Chapter 1**, the SSI concept and its significance have been described in brief. Besides that, an attempt has been made to point out the problems, which emphasize the need for the present research. The objective and scopes of this work are then clarified. At the end of the chapter, the organization of thesis has been discussed briefly.

Chapter 2 furnishes a detailed discussion on various topics relevant to the present thesis work, such as probabilistic seismic demand model, fragility curves with different plotting methods and reliability analysis. Details have been presented on behaviour of ground motion components due to change of angle of incidence. Methods of combining response of bidirectional earthquake are also discussed therein. A general concept of effective duration of earthquake motion is also included in this chapter. A state-of-the-art literature review on relevant topics has also been done to understand the present scenario and research gap is thus evaluated.

Chapter 3 discusses the influence of SSI on frame buildings constructed on uniform soil. Three types of soils (Hard Soil, Medium Soil and Soft Soil) are combined with four types of G+9 buildings (regular, vertically irregular, horizontally irregular and on sloping ground) to develop several analytical models. Each model is subjected to a near-field and a far-field earthquake. Thereafter, Rayleigh Damping Coefficients for all the models were evaluated and used in the models. The characteristics of the accelerograms used were studied for varying orientation of incidence angle. In case of every model, fragility curves are developed for all the floors under the influence of aforesaid two earthquakes.

Chapter 4 deals with the effect of SSI on frame buildings resting on layered soil. Four types of buildings (regular, vertically irregular, horizontally irregular and on sloping ground) are considered for the development of several models used for analysis. Each type of soil has six different layers and each model is subjected to a near-field and a far-field earthquake. For every model, fragility curves are developed for all the floors under the

effect of two earthquakes.

Chapter 5 has been devoted to the reliability-based assessment of different soil-structure combinations. In this chapter, a brief description about seismic hazard curves and reliability curves is provided along with the procedure for developing reliability curves from fragility curves. Finally, the reliability indices for different soil-structure combinations under different seismic excitations have been presented in graphical form.

Chapter 6 deals with framed structures on pile foundation. Only regular building is studied for building with pile foundation. This chapter discusses the influence of SSI on frame buildings with pile foundation constructed on uniform and layered soils. Four types of soils (Hard Soil, Medium Soil, Soft Soil and Layered Soil) are considered to develop several analytical models. Dashpot damping parameters are calculated and used in the models. Each model is subjected to a near-field and a far-field earthquake. In case of every model, fragility curves are developed for all the floors under the influence of aforesaid two earthquakes. Finally, the reliability indices for different soil-structure combinations under different seismic excitations have been presented in graphical form.

Chapter 7 summarizes all the results obtained from the overall thesis work and significant remarks have been drawn out after analyzing the results. The limitations of the present study and future scopes in this regard have also been discussed in this chapter.

The Books, Codes and Standards, Journals, Conference Papers and other articles used for preparing this thesis are listed in the section '**References**' at the end.

CHAPTER 2: LITERATURE REVIEW

2.1 - GENERAL

Bidirectional shaking covering all incidence angles for earthquake analysis of buildings attracted the attention of the researchers over a long period after few failures of buildings or part of the buildings during earthquake. For performing reliability based seismic performance of R.C, buildings understanding of basic knowledge in the relevant field is important. A short discussion on fragility curve, Reliability Index, damage probability matrix, near-field, mid-field and far-field earthquake have been made in the Introduction (Article 1). Some papers were reviewed and the summaries are presented below.

2.2 – PREVIOUS RESEARCHES ON THE TOPIC

Seong-Hoon Jeong & Amr S. Elnashai (2006) [3] presented a methodology for the derivation of fragility curves for structures with plan irregularities. Pramanik et al. (2016) [4] constructed fragility curves under real bi-directional excitation by a simple extension of the conventional Incremental Dynamic Analysis (IDA) under uni-directional shaking. Sengupta et al. (2016) [5] has analyzed a RC bridge pier under a set of bidirectionally applied near-field motions with forward directivity (FD) and fling-step characteristics. Suvonkar Chakroborty & Rana Roy (2016) [7] emphasize on the prevalent controversies and the fundamental fallacies in research studies and traditional design. Roy et al. (2017) [2] have studied implications of incidence angle of ground motions on inelastic demand of bridge piers under bi-directional seismic excitation against the corresponding uni-directional counterparts. Extending conventional Park-Ang damage index, Roy et al. (2017) [6] have evolved a simple yet rational damage measure applicable for bidirectional seismic shaking. Debashis Kar & Rana Roy (2018) [8] examine the implications of bi-directional shaking and local site conditions collectively. Roy et al. (2020) [1] suggested an approach to making an advance estimate of response under both unidirectional and bidirectional shaking for all incidence angles.

Foliente et al. (2000) [15] used a modified version of the BRANZ procedure for lateral capacity rating of bracing walls to determine the sustainable lateral mass of a 910-mm wide '2x4' timber shear wall. Asadour Hadjian (2004) [10] has considered all pairs of ground motion intensities and associated exceedance probabilities and the site hazard curves are substituted by the median curve and an across variability parameter, ζ_H . Iervolino et al. (2004) [18] defined a limit-state function for the seismic risk assessment developed specifically for the territorial case, and completely described probabilistically for quantitative computation. K.A. Korkmaz (2008) [9] performed the fragility analysis, which is a system reliability analysis with correlated demands and capacity, with different methodologies to establish the probabilistic characterization of the demands in different aspects. Alireza Mortezaei & Seyed Mehdi Zahrai (2009) [17] focused on the viscoelastic (VE) dampers to be used as energy-absorbing devices in buildings. Abbas Moustafa & Sankaran Mahadevan (2011) [14] developed a probabilistic methodology for the seismic reliability analysis of structures with random properties. Ming Liu & Boquan Liu (2012) [13] have shown by statistical analysis and significance test of structural seismic response variable that the story maximum ductility ratio μ_{max} and equivalent hysteretic loop numbers N all belong to lognormal distribution. L. Haj Najafi & M. Tehranizadeh (2013) [11] evaluated seismic behavior of moment frames (MF) and eccentrically braced frames (EBF), two common systems in most of the steel codes, due to far-field and near-field

ground motions and to propose practical technique for acquiring demand distributions. Abdelouafi et al. (2015) ^[12] assessed reliability of the expected performance state by using various methodologies based on finite element nonlinear static pushover analysis and specialized reliability software package. Paolo Castaldo & Tatiana Ferrentino (2020) ^[16] employed the seismic reliability-based design approach for inelastic structures isolated by friction pendulum isolators, considering two different highly seismic Italian sites to provide useful design recommendations.

Jonathan Chambers & Trevor Kelly (2004) ^[21] discuss some of the obstacles preventing the widespread adoption of NDP (Nonlinear dynamic analysis), and presents a number of examples where its uncompromised representation is crucial for satisfactorily predicting the seismic response of structures. Devesh P. Soni & Bharat B. Mistry (2006) ^[22] summarize state-of-the-art knowledge in the seismic response of vertically irregular building frames. Moon et al. (2018) ^[20] adopted a different approach that can produce vulnerability curves efficiently, even with a three-dimensional model. Zabihullah et al. (2020) ^[19] deal with the seismic response of RC structures having various individual and combined complicated geometric irregularities. Shah et al. (2020) ^[23] discuss the fragility curves and damage index functions of a 7-storey regular and irregular steel-framed buildings subjected to different earthquake ground motions.

Due to the complexity of the concrete damage plasticity (CDP) theory, Hafezolghorani et al. (2017) ^[24] simplified the procedure and a simplified concrete damage plasticity (SCDP) model was developed in this paper.

Yuman Shakya & Rajan Suwal (2014) ^[25] modeled the slippage between the core and the fill of the rockfill dam using ANSYS 10 with contact elements.

Vijayendra et al. (2010) ^[26] has made attempt to look into the efficiency of procedures for computing fundamental natural period of layered soil deposits in a comparative manner.

Seong-Hoon Jeong & Amr S. Elnashai (2007) ^[38] developed a methodology for the derivation of fragility relationships for three-dimensional (3D) structures with plan irregularities. Davis et al. (2010) ^[32] evaluated the seismic fragility of existing OGS buildings in India and compared them with the corresponding fragility curves for building frames without infill (bare frames) and with full infill in all storeys. Monalisa Priyadarshini (2013) ^[28] focuses on the performance of typical OGS buildings designed considering various magnification factors as well as the stepped type buildings with different geometry configurations using fragility analysis and reliability analysis. Shaikh A. Aijaj & G.S. Deshmukh (2013) ^[35] studied different irregularity response due to plan and vertical irregularity, and analyzed “Geometric irregular”-shaped building while earthquake forces act and calculated the deflection in the columns. Akhavan et al. (2016) ^[27] have investigated the behaviour of special steel moment frame with different configuration of soft storey vertically. Belejo et al. (2017) ^[39] presented results on the effects of ground motion duration on the seismic behaviour of a 3-D plan-asymmetric reinforced concrete building. Stefanidou et al. (2017) ^[41] focus on the effects of Soil-Structure Interaction (SSI) in seismic fragility analysis of reinforced concrete (RC) bridges, considering the vulnerability of multiple critical components of the bridge and different modelling approaches for soil-foundation and bridge-embankment interactions. Cardone et al. (2018) ^[36] derived fragility curves for typical older residential RC buildings, realized in Italy and other southern Europe countries from the 50s to the early 70s,

following a hybrid approach. Latip Kumar Sharma & Kamal Bahadur Thapa (2019) [31] made a humble effort to comprehend the analytic seismic fragility estimate of the existing types of the vertically irregular reinforced concrete buildings in Nepal. Rohan Bhasker & Arun Menon (2020) [33] aimed to examine, the efficiency and sufficiency of a wide spectrum of IMs, in predicting the maximum inter-storey drift demands on plan-irregular RC moment frame buildings subjected to bi-directional ground motion. Pratyush Kumar & Avik Samanta (2020) [34] focused on obtaining the variability functions and fragility curves by considering those uncertainties for low-, mid- and high-rise RC buildings in Patna, India, which is a region of high seismicity. As an alternative to the very time-consuming Non-Linear Response History Analysis (NLRHA) approach, Mohammad S. Birzhandi & Amir M. Halabian (2020) [40] aimed to employ the F2MPA (Flexibly-supported 2 DOF Modal Pushover Analysis) approach in developing fragility curves of flexibly-supported plan-asymmetric structures. Cavalieri et al. (2020) [42] showed the impact of adopting different SSI models on the assessment of seismic fragility functions. To handle the computational challenge in deriving fragility curves, A. Ghanem & D. Moon (2021) [29] utilized a new structural reliability method that incorporates structural analysis and reliability analysis to efficiently and accurately calculate the failure probability with the first-order reliability method (FORM). Patro et al. (2021) [30] carried out a numerical modelling using the finite element software OpenSEES to evaluate the seismic response of a typical eight storey four-bay vertical geometric irregular building considering soil-structure interaction and the results are compared with a reference regular building. Mohamed Mouhine & Elmokhtar Hilali (2021) [37] performed a fragility analysis of RC buildings subjected to seismic loading.

Hoseyni et al. (2014) [47] analyzed the seismic fragility for a typical power plant containment considering the effects of soil structure interaction (SSI). Mitropoulou et al. (2016) [46] have considered 3D reinforced concrete (RC) and steel building structures for studying the effect of soil–structure interaction modelling on the structural fragility assessment of such structures. Ajamy et al. (2018) [44] presented an analytical approach to develop seismic fragility curves of an existing jacket type offshore platform in the Persian Gulf. Su et al. (2019) [43], in order to better understand the SPI (soil-pile interaction) effect, fully investigated the seismic fragility of a large-scale PSWS located at the Port of Los Angeles Berth 100, USA, with and without considering SPI. Su et al. (2019) [45] systematically investigated the seismic fragility of a large-scale pile-supported wharf at both component and system levels. Wang et al. (2019) [48] aimed to rank the sensitivity of fourteen structural and soil parameters for seismic performance assessment of pile-group-supported bridges in liquefiable ground undergoing scour potentials.

Chin-Hsiung Loh & Ming-Jin Ma (1997) [50] conducted statistical analysis of the response spectra due to both horizontal and vertical ground excitations. Holliday et al. (2011) [51] demonstrated the utility of reliability diagrams for earthquake forecast evaluation with an application to a modified version of the Holliday et al. time-dependent earthquake forecasting method.

Chandrakanth Bolisetti (2010) [53] carried out the assessment of the numerical programs, SHAKE and SASSI, using a database of building responses recorded from a centrifuge test performed at the NEES@UCDavis centrifuge facility, as a part of the NEES City Block project. R. Cairo & G. Dente (2014) [52] presented a method for the kinematic interaction analysis of single piles in nonhomogeneous soils. Based on the fixed interface component mode synthesis, Wang et al. (2021) [54] proposed a multiple and multi-level substructure method for the modeling of complex structures.

Julian J. Bommer & Alejandro Martínez-Pereira (1998) [55] reviewed some 30 different definitions of strong motion duration and classified into generic groups. Rohan Bhasker & Arun Menon (2020) [33] aimed to examine, the efficiency and sufficiency of a wide spectrum of IMs, in predicting the maximum inter-storey drift demands on plan-irregular RC moment frame buildings subjected to bi-directional ground motion.

Response of soil-structure system on a soft soil site and seismic soil-structure interaction with substructure method is given by John P. Wolf (1985) [61]. Methods for the analysis of soil-structure interaction is given by Steven L. Kramer (1996) [57]. A derivation of the kinematic interaction effect for a rigid, massless foundation slabs the so-called “Tau effect” is given by Ray W. Clough & Joseph Penzien (2003) [59]. The dynamic soil-structure interaction is given by T. K. Datta (2010) [58]. Seismic soil-structure interaction with substructure method, finite element model of soil-structure system for direct method of analysis and inertial interaction analysis are given in details in NPTEL [60].

Lubliner et al. (1989) [65] presented a constitutive model based on an internal variable-formulation of plasticity theory for the non-linear analysis of concrete. M. N. Fardis & T. B. Panagiotakos (1996) [66] studied the effects of masonry infills on the global seismic response of reinforced concrete structures through numerical analyses. Jeeho Lee & Gregory L. Fenves (1998) [64] developed a new plastic-damage model for concrete subjected to cyclic loading using the concepts of fracture-energy-based damage and stiffness degradation in continuum damage mechanics. Sarkar et al. (2007) [63] adopted the profile of the Koyna dam for the study of the response of a dam subjected to dynamic loading.

Indrajit Chowdhury & Shambhu P. Dasgupta (2003) [67] outlined a procedure, which ensures a rational estimate of α and β even for a system with large degrees of freedom.

The method of plotting the fragility curves considering IO, LS, CP and Indian Codal Limit are given in details in FEMA 356 (2000) [68].

Limitations of probability of exceedance of a particular performance level such as IO, LS, CP are given by IS 1893 (Part 1) – 2002 [73].

Abraham M. Hasofer & Niels C. Lind (1974) [78] presented the second-moment reliability code format for a probabilistic design code, which is based on a fundamental analysis of the meaning of second-moment reliability in multivariate problems, and is entirely derived from one basic assumption concerning the measurement of reliability. To address building performance issues raised by numerous weld fractures in beam-to-column connections in welded special moment-resisting frames due to Northridge earthquake of 1994 and to support improvements in probability-based load resistance factor design for steel building structures, Jianlin Song and Bruce R. Ellingwood (1999) [75] evaluated four welded special moment-resisting frames of different sizes and configurations that suffered connection damage during the earthquake using both deterministic and stochastic approaches. In the second of two companion papers addressing damage to buildings with welded special moment frames, Jianlin Song and Bruce R. Ellingwood (1999) [76] considered the role of inherent randomness and modeling uncertainty on building performance in detail using the nonlinear dynamic analysis procedure from the first paper as an assessment tool. Bruce R. Ellingwood (2001) [77] reviewed some of the special considerations, required for structural design and evaluation of buildings and other facilities with regard to their ability to withstand the effects of

earthquakes, specifically as they pertain to probability-based codified design and reliability-based condition assessment of existing buildings.

Kotronis et al. (1984) [83] presented a new macroelement for single piles in sand (with pile-head on the ground surface) developed within the framework of hypoplasticity. George Gazetas (1992) [85] presented a complete set of algebraic formulas and dimensionless charts for readily computing the dynamic stiffnesses (K) and damping coefficients (C) of foundations harmonically oscillating on/in a homogeneous half-space. L. M. Zhang (2003) [82] aims to investigate the response of laterally loaded large-section barrettes based on the load tests, to simulate the response of the two test barrettes, and to study the influence of loading direction on the lateral response of barrettes. Correia et al. (2010) [56] briefly presented an innovative pile-head macro-element model, recently proposed for the simulation of inertial soil-structure interaction effects in the seismic analysis of structures supported on long piles. Li et al. (2016) [81] presented a novel macroelement for single vertical piles in sand developed within the hypoplasticity theory, where the incremental nonlinear constitutive equations are defined in terms of generalized forces, displacements and rotations. Graine et al. (2018) [84] constructed the failure surface for a single rigid pile in a cohesive-frictional soil, subjected to both horizontal force and bending moment. The material models and analysis types are well explained in Seismostruct Technical Information Sheet (2018) [89]. Francesco Cavalieri & António A. Correia (2019) [86] described a study into the transfer of seismic motion from the soil into the foundation and the structure of buildings, i.e., the soil structure interaction. The macro elements for soil structure interaction of shallow and pile foundations are explained well in SeismoStruct User Manual (2021) [87]. The various link elements in SeismoStruct and their damping parameters are discussed in SeismoStruct Verification Report (2021) [88]. As described in the Verification Report, its accuracy is very well demonstrated by its numerous successes in Blind Test Prediction Exercises. António A. Correia & Alain Pecker (2021) [90] extended the macro-element approach to the analysis of laterally loaded pile-shafts and soil-pile-structure interaction.

Shiuly et al. (2014) [79] presented the ground motion amplification factors at different time period bands and fundamental time period of soft sedimentary deposit in densely populated Kolkata city for seismic micro-zonation. Shiuly et al. (2014) [80] presents the ground motion amplification scenario along with fundamental frequency (F_0) of sedimentary deposit for the seismic microzonation of Kolkata City, situated on the world's largest delta island with very soft soil deposit.

2.3 - FRAGILITY CURVE AND PROBABILISTIC SEISMIC DEMAND MODELS

Fragility analysis is the analysis for seismic loss estimation in built environments. They represent the probability of exceeding a damage limit state for a given structure type subjected to a seismic excitation (Shinozuka et al., 2000, Ellingwood et al., 1980). The damage limit states in fragilities may be defined as global drift ratio (maximum roof drift normalized by the building height), inter story drift ratio (maximum lateral displacement between two consecutive stories normalized by the story height) or story shear force etc. Fragility curves involve uncertainties associated with structural capacity, damage limit state definition and records of ground motion accelerations (Hui, 1991; Hwang and Huo, 1994; Hwang and Jaw, 1989; Corvers, 2000).

Considering a dynamic system subjected to a natural hazard event as an earthquake resulting in a multi-dimensional forcing function $F(t)$, $t \geq 0$, acting on the system.

Denoting by $F^1(t)$, $0 \leq t \leq \tau_1$, a relevant multi-dimensional system response process, where τ_1 is a timing. Figure 2.1 illustrates the relationship between the data $F(t)$ and out $F^1(t)$.

The performance-based engineering approach, as opposed to prescriptive rules of code-based design, is based on simulation of real structural behavior.

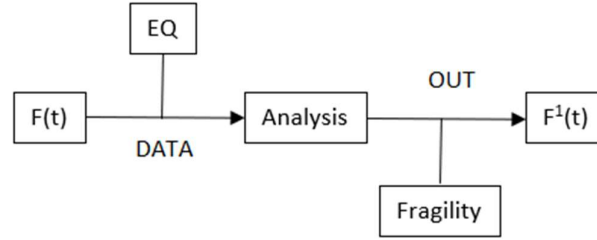


Figure 2.1 - Input-output relationship for Fragility Analysis

Seismic fragility can be defined as the proneness of a structural component or a system to fail to perform satisfactorily under a predefined limit state when subjected to an extensive range of seismic action (Murat Altug Erberik, 2015). In accordance with the above definition, seismic fragility analysis can be regarded as a probabilistic measure for seismic performance assessment of structural components or systems. There are two different end products of seismic fragility analysis: damage probability matrix and fragility curve.

Fragility curve is defined as a curve which signifies the vulnerability of structure. It is the statistical tool by developing a curve of probability of exceeding Engineering Damage Parameter (EDP) against specific demand. The engineering damage parameter may be roof drift, storey drift, energy dissipation etc. Whereas the demand may be Peak Ground Acceleration (PGA), Peak Ground Displacement (PGD) and Spectral Acceleration (S_a) for a specific time period etc. Singhal and Kiremidjian (1996) studied method for probabilistic evaluation of seismic structural damage.

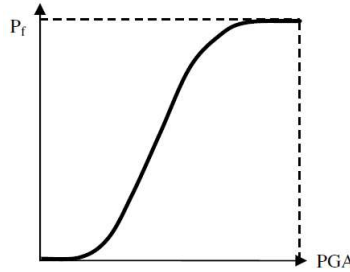


Figure 2.2 - Schematic of Seismic Fragility Curve (P_f = probability of exceedance)

2000 SAC-FEMA Method - The seismic fragility function can be expressed (Celik and Ellingwood, 2010) by

$$P(D \geq C_1 | IM) = 1 - \Phi \left(\frac{\ln \frac{S_C}{S_D}}{\sqrt{\beta_{D|IM}^2 + \beta_C^2 + \beta_M^2}} \right) \quad \dots(1)$$

Where, $P(D \geq C | IM)$ is probability of exceedance of ground storey drift for particular limit state capacities, D is ground storey drift, C_1 is the drift capacity at chosen limit state. Further, $\beta_{D|IM}$, β_C and β_M are dispersions in the Intensity Measure (IM), capacities and modelling respectively. S_D is usually described through PSDMs (probabilistic seismic demand model) in terms of IM like ground storey drift at particular PGA levels which can

be determined by NLTHA (Non-Linear Time-History Analyses). S_C is usually described also in terms of IM at particular limit state capacities (IO, LS, CP). S_D is Engineering Damage Parameter (EDP) which can be represented a generalized form as Equation 2.

[ASCE 41-06 (2007) seismic rehabilitation code defines different damage levels such as: IO = immediate occupancy; LS = life safety; CP = collapse prevention]

EDP = $a(IM)^b$... (2)
where, a and b are the regression coefficients of the PSDM. Equation 1 can be rewritten as

$$P(D \geq C1 | IM) = 1 - \Phi \left(\frac{\ln S_C - \ln(a \cdot IM^b)}{\sqrt{\beta_{D|IM}^2 + \beta_C^2 + \beta_M^2}} \right) \quad \dots (3)$$

$\beta_{D|IM}$ is dispersion intensity of ground storey drifts which can be computed from Equation 4.

$$\beta_{D|IM} = \sqrt{\frac{\sum [\ln(d_i) - \ln(a \cdot IM^b)]^2}{N-2}} \quad \dots (4)$$

where, d_i is the limit of inter storey drift and N is the number of observations.

According to ATC 58 (2012), The total modelling dispersion, β_m can be calculated as Equation 5.

$$\beta_m = \sqrt{\beta_C^2 + \beta_q^2} \quad \dots (5)$$

β_q defines that, hysteretic models may not accurately capture the behavior of structural components, even if the details of construction are precisely known. Generally, a structure subjected to earthquake load needs to fulfill two criteria, namely the strength check and the stability check. For a multi-storey building, the stability check is defined by the assessment of the storey drift. The drift of a storey is a dimensionless parameter and it is given by Equation 6.

$$d_s = \frac{u_{up} - u_{down}}{H_s} \quad \dots (6)$$

where,

d_s = storey drift

u_{up} = horizontal displacement at the top of the storey

u_{down} = horizontal displacement at the bottom of the storey

H_s = height of the storey

The parameters required to calculate the storey drift are depicted in Figure 2.3.

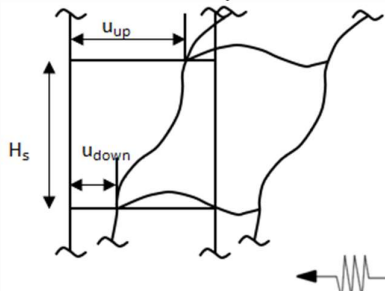


Figure 2.3 - Storey drift [Abaqus]

Storey drift is the lateral displacement of a floor relative to the floor below.

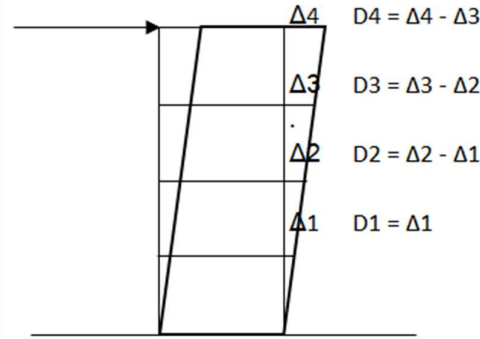


Figure 2.4 - Schematic representation of storey drift

The limiting value of ground storey drift in terms of intensity measure (IM) at particular limit state capacities (IO, LS, CP) is taken from FEMA 356 and IS-1893 (PART 1):2016. According to FEMA 356 (2000), the different performance objectives and their inter storey drift limit for concrete frame structure are presented in Table 2.1. However, according to Indian code (IS-1893 (Part 1):2016), the limit of inter storey drift (d_i) is 0.004 means 0.4%.

Building Type	Member Type	Immediate Occupancy (IO)	Life Safety (LS)	Collapse Prevention (CP)
Concrete Frame	Primary	Minor hairline crack may take place. Limited yielding may occur at few locations. No crushing. Strain is below 0.003.	Extensive damage to beams. Spalling of cover and shear cracking (<1/8" width) for ductile columns. Minor spalling in nonductile columns. Joint cracks <1/8" wide.	Extensive cracking and hinge formation in ductile element. Limited cracking and/or splice failure in some non-ductile columns. Severe damage in short column.
	Secondary	Minor spalling in a few places in ductile columns and beams. Flexural cracking in beams and columns. Shear cracking in joints <1/16" width.	Extensive cracking and hinge formation in ductile elements. Limited cracking and/or splice failure in some nonductile columns. Severe damage in short columns.	Extensive spalling in columns (limited shortening) and beams. Severe joint damage. Some reinforcing buckled.
	Drift	1% transient drift Negligible permanent drift	2% transient; 1% permanent	4% transient drift or permanent drift

Performance levels are the levels to indicate the damage states of the building under seismic loading. Performance levels for a typical building pushed laterally to failure is shown in the Figure 2.5 below. A typical Three performance levels, Immediate Occupancy (IO), Life safety (LS) and collapse Prevention (CP), are considered in the present study.

The inter-storey drift (Δ_c) corresponding to these performance levels has been taken as 1%, 2% and 4% respectively as per FEMA356.

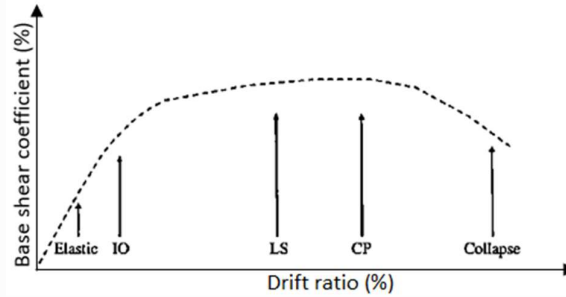


Figure 2.5 - Damage states of a typical building pushed to failure (Courtesy, FEMA356)

Uncertainty values of β_c are dependent on material strength, material properties, construction quality etc. For existing buildings, this will depend on field investigation, built construction and document drawing which is available to verify their accuracy. For new buildings, this will depend on assumptions of accuracy of structural design by matching with construction in field. ATC 58 (2012) stated the value of β_c with representative conditions.

ATC - Applied Technology Council

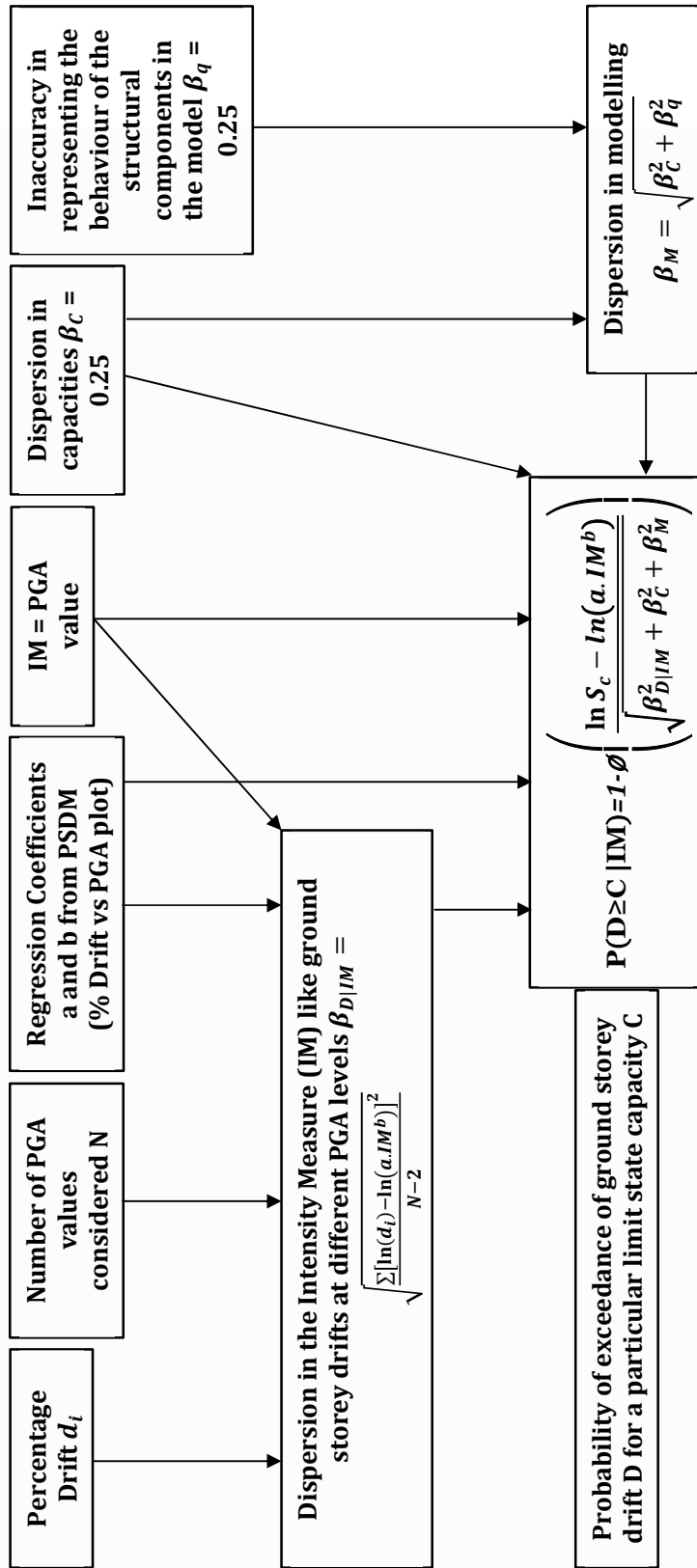


Fig 2.6: Graphical representation of SAC – FEMA 2000 method

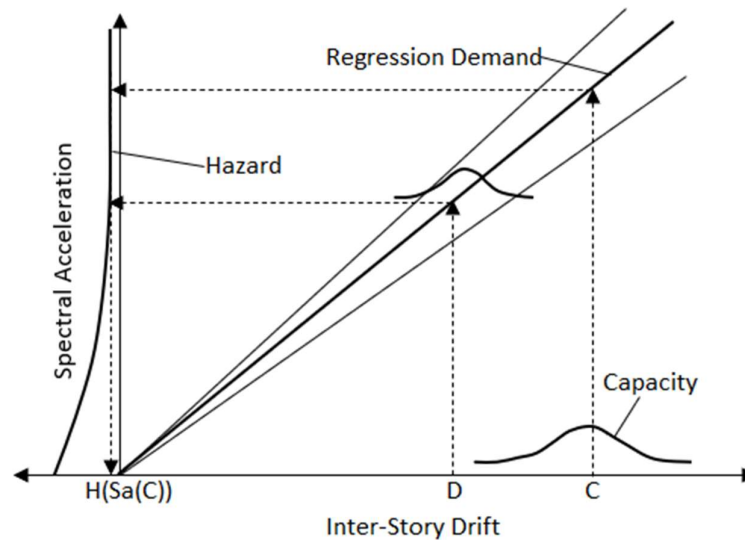


Figure 2.7 - SAC – FEMA 2000 method (Iunio IERVOLINO, Giovanni FABBROCINO and Gaetano MANFREDI, 2004)

LHS-Monte Carlo method - In this method, a selected frame is analyzed under all ground motions to obtain PSDMs and fragility curves. Each ground motion is scaled to several PGA level for NTHA. This procedure is followed for all the selected ground motions. As per this method, the total number for analysis required is equal to 'selected ground motions \times 20'. The maximum ground storey drifts are recorded with respect to PGA. The probability of exceedance of ground storey drift at a certain PGA level for a particular limit state capacity can be calculated using Equation 7 below.

Probability of exceedance at a PGA level =

$$\frac{\text{Number of analysis cases where ground storey drift exceeds the limit}}{\text{Total number of analysis cases at that PGA level}} \dots(7)$$

Damage probability matrix (DPM) is a table that provides discrete values of damage state probabilities for specified levels of ground motion intensities. Each column of DPM stands for a constant level of ground motion intensity whereas each row of DPM denotes the probability of being in a predefined damage state.

DPM is a matrix where each number expresses the probability that a building will experience a particular level of damage when exposed to a given intensity or ground shaking.

2.4 – RELIABILITY INDEX

Reliability of the expected performance state is assessed by using various methodologies based on finite element nonlinear static pushover analysis and specialized reliability software package.

Building design codes achieve a preselected reliability by the use of partial load and capacity reduction factors. Although the determination of these factors, say for dead and

live loads, is rooted in basic reliability concepts, the reliability of structures subjected to earthquake loads is not determined as explicitly. Designing structures to specific scenario events or return periods of earthquake ground motion parameters does not address the earthquake reliability of the resulting structures, except may be heuristically. This is so simply because any structure is potentially exposed to all ground motion occurrences varying from very small to very large return periods. And therefore, to estimate the earthquake “failure” probability, where “failure” is a generic term defining non-performance at any preselected limit state, all ground motion intensities with associated exceedance probabilities must be considered. Thus, the first step in calculating the earthquake reliability of structures is the complete characterization of the site seismic hazard, and not just a single point on the mean hazard curve.

The fragility curves demonstrate the probability of the building will exceed for a particular performance level if it is subjected to an earthquake of a given intensity (in terms of PGA). However, to assess the risk of any structures, these fragility curves should be combined with the hazard curve which signifies the probability of occurrence of earthquakes of a given intensity at a particular location of interest. The primary concern in structural reliability analysis is to estimate probabilities of failure to achieve predefined performance.

In the simplest case of one performance function, the component reliability problem is formulated as

$$P_f = \int_{g(x) \leq 0} f(x) dx \quad \dots(8)$$

where P_f is the probability of failure, x is the vector of random finite element model parameters, $g(x)$ is the performance function and $f(x)$ is the joint PDF of x . Note that the integration is over the set of random variables x , which in finite element reliability analysis can be large.

Reliability can be defined as the risk of a building frame which can be expressed by the statistical parameter “Reliability Index”.

Reliability Index represents the risk of the buildings We can estimate the reliability index β_{pf} by certain procedures.

The reliability index β_{pf} was defined from the safety probability P_s by means of the standardized normal distribution function Φ as follows:

$$\beta_{pf} = \Phi^{-1}(P_s) \quad \dots(9)$$

where P_s is the probability of the maximum response Y not exceeding the design criterion y_c . Details of the calculation of β_{pf} are given in Saito et al. [1998] and Foliente et al. [1999].

The object of structural analysis is to assess the reliability of structures, i.e., to assess quantitatively the structural safety based on probabilistic sense.

The reliability of building is the probability that it will perform its intended function, under the operating conditions considered, in the considered time period.

$$\text{Reliability} = 1 - \text{probability of failure} \quad \dots(10)$$

The structural seismic reliability analysis has to solve the following problems:

1. Probabilistic models of earthquake ground motions.
2. Mechanical models of structures.
3. Mathematical methods to solve nonlinear stochastic vibration problems.
4. Failure criteria of seismic structures and assessment standards of structural seismic reliability.

The Reliability Index can be determined by convolving the fragility curve with the derivative of the seismic hazard curve (Ellingwood 2001). The risk of any frame can be expressed with probability of exceed at different level of performance level like IO, LS, CP and limitation of IS-1893,2002 and probability of occurrence of earthquake of different level of PGA.

The probability of failure at certain performance level can be obtained by convolving the fragility $F_R(z)$ with the derivative of the seismic hazard curve, $G_A(z)$. This conditional probability is sometime assumed to follow lognormal probability distribution (Cornell et. al, 2002; Song and Ellingwood, 1999). Mathematically, it can be represented as Equation 16.

$$P[LS] = \int F_R(z) \frac{dG_A(z)}{dz} dz \quad \dots(11)$$

The Reliability Index (β_{pf}) was defined by Hassofer and Lind (1974) as the shortest distance from the origin to the Limit State Function (LSF), in a standard normal variable space. RI (β_{pf}) corresponding to the probability failure at certain performance limit can be found by the following standard equation as shown below.

$$\beta_{pf} = -\Phi^{-1}(P[LS]) \quad \dots(12)$$

Where, $\Phi^{-1}()$ represents the standard normal distribution.

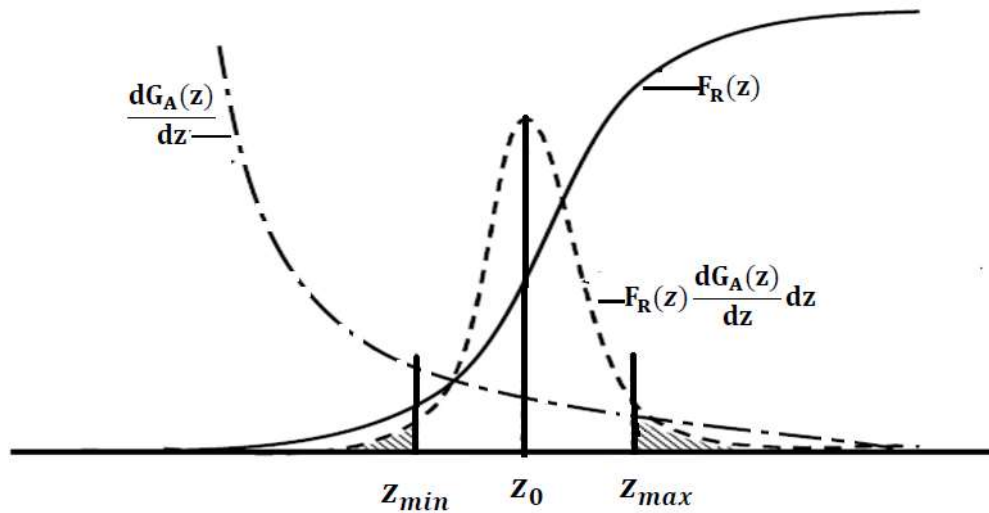


Figure 2.8 - Fragility-hazard interface After Elingwood (2001)

A reliability function β_{pf} is thus defined as the ratio of the expected value of the natural logarithm of the safety margin of the structural system divided by its standard deviation.

Fig 3.95 demonstrates the fragility-hazard interface which was proposed by Elingwood (2001). In this Fig $F_R(z)$ and $\frac{dG_A(z)}{dz}$ are the two parameters from which probability distribution $P[LS]$ can be established.

The seismic reliability of a structural system is an evaluation of the probabilities exceeding the structural performance (SP) within its reference service life (e.g., 50 years). (Paolo Castaldo & Tatiana Ferrentino [16], 2020)

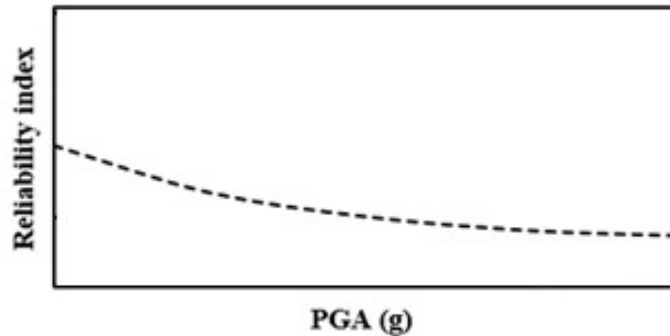


Figure 2.9 - Schematical of Reliability Curve

In accordance with the Pacific Earthquake Engineering Research Center (PEER)-like modular approach and performance-based earthquake engineering (PBEE) approach, the steps to assess seismic reliability are:

1. Definition of an intensity measure (IM), used to separate the seismic intensity uncertainties and the randomness in the characteristics of the record;
2. Carrying out IDAs under a large set of real ground motions scaled to different values of the IM, considering the relevant random variables and monitoring the principal structural parameters;
3. Calculation of fragility curves, which define the probabilities exceeding the structural performance (limit state thresholds) conditional to an IM value;
4. Computation of the average annual rates exceeding the limit state thresholds through the convolution integral between the fragility curves and seismic hazard curves of the sites;
5. Calculation of the probabilities exceeding the structural performance (limit state thresholds) in the time frame of interest (e.g., 50 years) through the Poisson distribution.

Seismic hazard is defined as the probability of occurrence of an earthquake in a given geographic area, within a given window of time, and with ground motion intensity exceeding a given threshold.

Seismic hazard is the hazard associated with potential earthquakes in a particular area. Seismic hazard analysis describes the potential for dangerous, earthquake-related natural phenomena such as ground shaking, fault rupture, or soil liquefaction.

Seismic hazard curve signifies the probability of an earthquake will occur of a given intensity of earthquake.

The seismic hazard at a building site is displayed through a complimentary cumulative distribution function (CCDF), as per. The hazard function is the annual frequency of motion intensity at or above a given level, x , to the intensity. Elementary seismic hazard analysis shows that at moderate to large values of ground acceleration, there is a logarithmic linear relation between annual maximum earthquake ground acceleration or spectral acceleration, and the probability, $G_A(a)$, that specifies values of acceleration are exceeded, reference. This relationship implies that A is described by following equation:

$$G_A(x) = 1 - \exp [-(x/u)^{-k}] \quad \dots(13)$$

u and k are parameters of the distribution. Parameter k defines the slope of the hazard curve which, in turn, is related to the coefficient of variation (COV) in annual maximum peak acceleration.

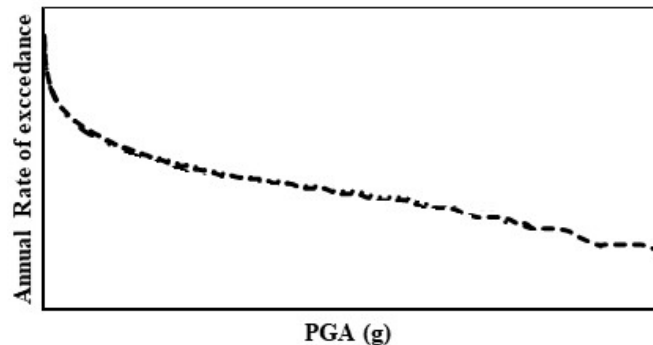


Figure 2.10 - Schematical of Seismic Hazard Curve

Using a hazard curve, one could determine the annual probability of occurrence of each of these ground motions. Then one could decide whether that corresponding probability is acceptable. If one of the probabilities is unacceptably high, the design would have to be revised. A hazard curve is calculated by plotting annual rate of exceedance vs ground motion.

1. Perform the above calculation for 18 other ground motion levels.
2. Plot the results.
3. Make a smooth curve.

Now, for any ground motion we can find the annual rate of exceedance. Likewise, for any annual rate of exceedance we can find the corresponding ground motion.

A flowchart representing graphically the development of reliability index is given in the Figure below.

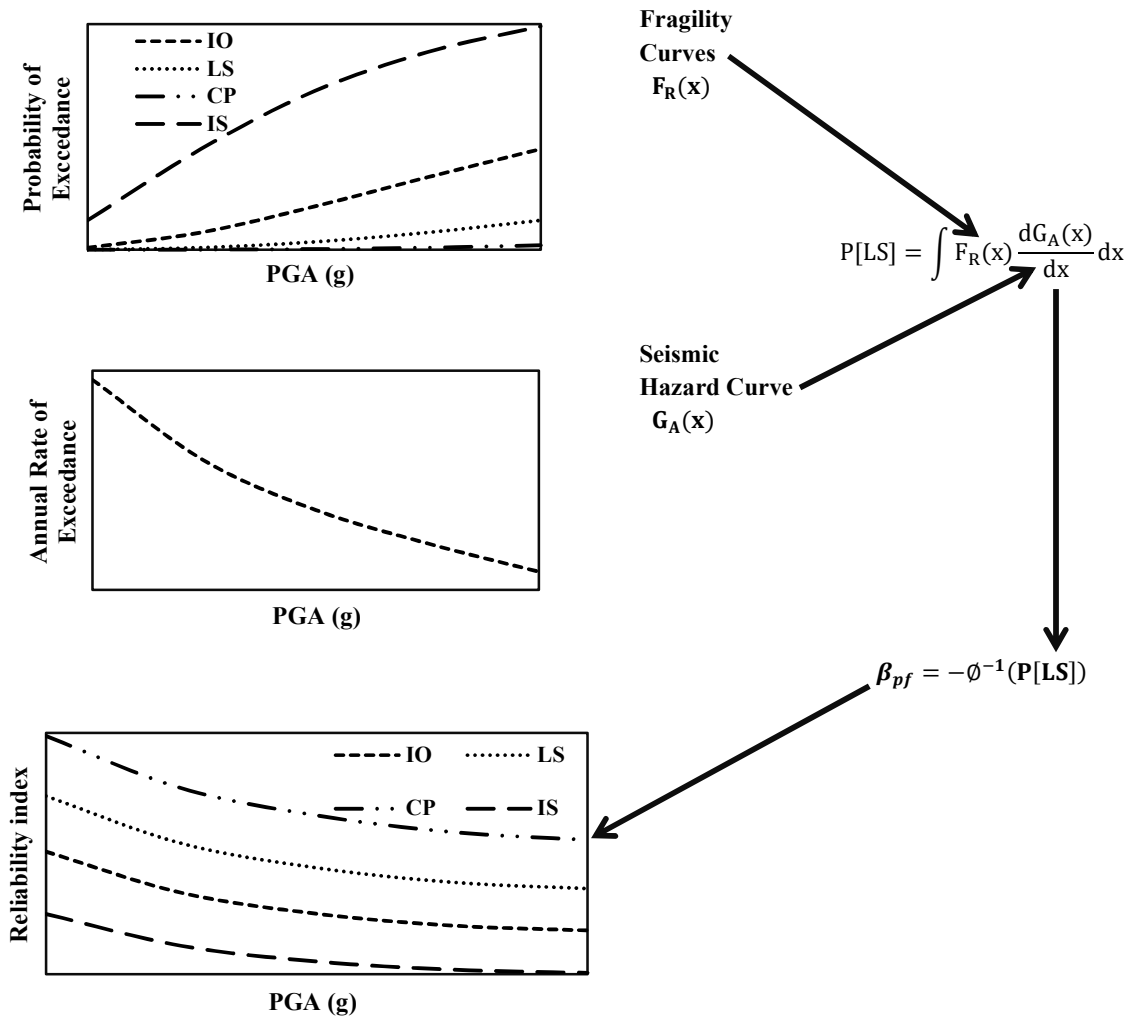


Figure 2.11 - Graphical representation of development of Reliability Index

One outcome of the seismic hazard analysis is a hazard curve that quantifies expected ground motion intensity measures as a function of exceedance probability considered in the PBEE (Performance-Based Earthquake Engineering) analysis of the building. PBEE methodology consists of four successive analyses: hazard analysis, structural analysis, damage analysis, and loss analysis. It focuses on the probabilistic calculation of meaningful system performance measures, by considering the above four analyses in an integrated manner where uncertainties are explicitly considered in all four analyses.

In order to estimate the actual probability of failure and the reliability, which is inversely related to probability of failure, the fragility curves shall be combined with seismic hazard curve at the region selected in the study. The hazard curve should adequately represent the seismicity of the particular area for which the structure has been designed. The probability of failure of the structure is found out by numerical integration. The reliability index is calculated as the inverse of the standard normal distribution. According to Cornell et. al (2002) A point estimate of the limit state probability for state i can be obtained by

convolving the fragility $F_R(x)$ with the derivative of the seismic hazard curve, $G_A(x)$, thus removing the conditioning on acceleration.

2.5 – RESPONSE FOR BIDIRECTIONAL EARTHQUAKE MOTION

Study needs to be done on how to apply the earthquake time history motion data in FEM model in two directions and obtain combined response from it.

In the event of an earthquake, the time-varying magnitude and direction of ground motion inducing damage to structures are conveniently recorded by a pair of orthogonal sensors in the horizontal plane. These recorded ground motion components are generally applied along the principal axes of structures. However, orientations of the preinstalled sensors are often arbitrary with respect to that of the principal axes of structures. Hence, to compute engineering demand parameters (EDPs), a structure should be analyzed under the action of a pair of ground motion components acting simultaneously (bidirectional analysis) for all incidence angles. This necessitates a nonlinear response history analysis (RHA) under a two-component shaking covering all incidence angles.

Methodology: (after Roy et al. [1])

In unidirectional analysis, RHA (Response History Analysis) has been conducted applying each component of motion separately along the principal axis of structure. Peak deformations, corresponding to the pair of components of a selected motion (obtained from two separate RHAs) are compared and the greater of the two is taken as the peak deformation under unidirectional excitation ($\Delta_{(U)}$). Likewise, comparing the areas of force-displacement histories, the greater one of the two is taken as the hysteretic energy under unidirectional shaking ($E_{H(U)}$).

In case of two-component shaking, deformation histories obtained in two principal directions are combined (as square root of sum of squares, i.e., SRSS) over the entire history (not independent peaks as they may not occur together) and the maximum value of deformation is taken as the peak deformation under bidirectional excitation ($\Delta_{(B)}$). Hysteretic energy ($E_{H(B)}$) is then taken as the sum of the areas of force-displacement histories in two principal axes, E_{Hx} and E_{Hy} .

Orientation dependent ground motion characteristics: (after Roy et al. [2])

Ground motion components with reference to a new orientation defined by an angle ψ relative to the recorded component may be calculated by the following transformation:

$$\begin{Bmatrix} a_{x(\psi)}(t) \\ a_{y(\psi)}(t) \end{Bmatrix} = \begin{bmatrix} \cos \psi & \sin \psi \\ -\sin \psi & \cos \psi \end{bmatrix} \begin{Bmatrix} a_x(t) \\ a_y(t) \end{Bmatrix} \quad \dots(14)$$

$a_x(t)$, $a_y(t)$ are horizontal components of original record and $a_{x(\psi)}(t)$, $a_{y(\psi)}(t)$ the components of the record when rotated anti-clockwise by an angle ψ .

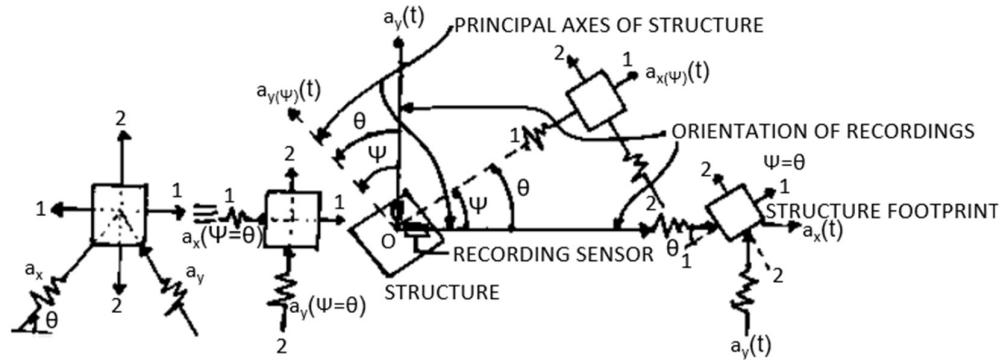


Figure 2.12 - Correspondence between angle of incidence (θ) and orientation of accelerogram (ψ) (after Roy et al. [6])

We use 'orientation' (denoted by ψ) to refer to the issues related to ground motion alone, while 'incidence angle' (denoted by θ) is used when response of structures is evaluated. Clearly, accelerogram at an incidence angle of θ with respect to principal axis of structure is equivalent to the accelerogram acting along the principal axis, but with orientation $\psi = \theta$. It is, albeit evident that the individual components, upon rotation, change themselves from as-recorded forms, implication of this change in ground motion properties is shrouded.

Ground motion parameters: (after Roy et al. [2])

Several ground motion parameters are known to be related with different EDPs (Engineering Demand Parameters). Hence, before evaluating the influence of angle of incidence on structural response, it appears useful to examine the changes of important ground motion characteristics across orientations. We rotate the ground motions over 360° with an interval of 15° in the anti-clockwise sense and the important ground motion properties are evaluated. While component property (e.g., Arias Intensity, I_A of component x and y separately, where x and y refer to any two mutually orthogonal directions) itself is important in uni-directional analysis, properties of two orthogonal components combined by SRSS [i.e., $\sqrt{I_{Ax}^2 + I_{Ay}^2}$] may refer to bi-directional loading scenario.

IDA under two-component shaking: (after Pramanik et al. [4])

In standard IDA under uni-directional shaking, a structure is subjected to a ground motion with increasing intensity. Increasing intensity is achieved by factorizing the component (up and down) to achieve desired response. To extend this traditional IDA to account for bi-directional interaction, we have to follow the proposed method.

The structure is to be analyzed by subjecting it to a pair of horizontal components applied along two principal axes of the structure. Ground motion components are intensified by multiplying each component by a constant factor. IM of the motion pair-wise applied on the structure is to be expressed as the geometric mean of the component IMs ($\sqrt{IM_x \cdot IM_y}$). In each step of analysis, we have to combine the displacement time series (not independent peaks component-wise) in each principal direction by SRSS rule and maximum over the history is taken as the demand under bi-directional excitation.

Ground motion characteristics over orientations:

Newmark has shown that the peak deformation under rectangular acceleration pulse is proportional to characteristic length which may be interpreted as energetic length scale, L_e . The damage estimated by Park-Ang parameter has been shown to be well correlated to I_c . Cumulative Absolute Velocity (CAV) represents the cumulative effects of ground shaking and is also a good indicator of damage. IDA curves under uni-directional and bi-directional shaking as well as the fragility estimates are presented for a set of selected IMs, viz., S_a , PGA, PGV, PGD, I_a , CAV, L_e respectively (after Pramanik et al. [4]).

$$L_e = \text{characteristic length} = a_g T_m^2 \quad \dots(15)$$

a_g = peak ground acceleration

T_m = mean period for real records / effective duration of earthquake strong motion

I_c = characteristics intensity of motion

NCI = normalized component intensity

CAV = cumulative absolute velocity

S_a = spectral acceleration

Cumulative Absolute Velocity (CAV) represents the cumulative effects of ground shaking and is also a good indicator of damage.

The above plots are known as polar plots.

Rotating motion components to multiple orientations, these component properties (L_e and I_c) individually (for unidirectional shaking) and collectively (combined by SRSS for bidirectional shaking) have to be studied. We rotate ground motions by 360 with an interval of 15 in the anti-clockwise sense and properties of each component at each orientation are computed. We define normalized component intensity (NCI) as the ratio of the intensity of stronger to weaker component and hence is always greater than or equal to unity.

Representative results reveal that: (after Roy et al. [6])

- Component characteristics appear to interchange over 90 and repeat over 180 as may also be expected from the transformation matrix.
- Ground motion intensity is sensitive to orientations component-wise and relatively stable pair-wise.
- Orientation corresponding to the peak intensity of one component is closely associated with the minimum of the other. Thus, NCI assumes a peak in this orientation and is denoted as ψ_{\max} (L_e or I_c).
- There exist certain orientations (intersection points) where intensities for two orthogonal components approach to be proximate. Thus, NCI may approach to minimum in this orientation and is denoted as ψ_{\min} (L_e or I_c).

Two components are separately applied and the maximum response is considered in case of unidirectional analysis while, for bi-directional shaking, both the components are together applied. In view of the observations (a) and (b) above, we have to compute response for different incidence angle in the range of $0^\circ - 360^\circ$. Relative component intensity has been shown to regulate the significance of bi-directional analysis over uni-

directional companion. Thus, damage computed from bi-directional analysis relative to uni-directional companion seems to be of special significance in the orientations (c) and (d).

Performance of combination rules: (after Debashis Kar and Rana Roy [81])

In view of the computational rigor involved in bi-directional analysis, code recommends estimating bi-directional response by combining responses of uni-directional analyses. These codified rules include '30%' (AASHTO 1998) or '40%' (ATC 1996; NCHRP 2001) combination rules that may be expressed in a compact form as under:

$$r_{(cy)} = \max. \text{ of } [1.0r_x + \gamma r_y, 1.0r_y + \gamma r_x] \quad \dots(16)$$

where r_x and r_y are peak responses under two components of motion uni-directionally and separately applied along two principal axes (x and y) of the structure and $r_{(cy)}$ is the response from combination rules. γ has been used as 0.3 or 0.4 in '30%' and '40%' rules respectively.

We have to estimate responses per combination rules for each derivative of each motion for both peak deformation ($\Delta_{(cy)}$) and accumulated hysteretic response ($E_{H(cy)}$). Responses under bi-directional analysis (i.e., $\Delta_{(B)}$ and $E_{H(B)}$) are normalized by corresponding estimates from combination rules, i.e., $\Delta_{(cy)}$ and $E_{H(cy)}$ respectively.

2.6 – THE EFFECTIVE DURATION OF EARTHQUAKE STRONG MOTION

The assessment of seismic hazard at a site aims to provide a reliable description of the earthquake motions that can be expected and which, therefore, define the input into the earthquake-resistant design of projects or the evaluation of the seismic safety of existing installations. The earthquake motions are usually characterized by parameters related primarily to the amplitude of the shaking, such as peak ground acceleration and response spectral ordinates. There are a number of situations in which the seismic response depends very strongly not only on the amplitude of the ground motion but also the number of cycles or the duration. On the structural side, it has been shown that the duration of shaking can have a significant effect on the inelastic deformational and energy dissipation demands especially for relatively weak, short-period structures [Mahin, 1980].

Clearly, for any structure with stiffness or strength degrading characteristics, the duration of earthquake shaking will be of critical importance. Therefore, risk assessment for existing structures requires a reliable estimate of the duration of earthquake shaking that can be expected to affect the site. In addition to these situations, it is also necessary to estimate the duration of strong motion whenever acceleration time-histories are required, such as in the calculation of soil response to bedrock motions and in non-linear structural analysis. Whether the accelerograms used in these cases are selected from databanks of real earthquake recordings or generated synthetically, it is important to ensure that the duration of shaking is consistent with the design scenario.

The extent of the influence of the duration in the damage due to earthquake motions depends on many factors. Clearly, if during an earthquake a structure is deformed beyond its elastic limit, then the amount of permanent deformation will partly depend on how long the shaking is then sustained. In this case, however, the duration is of importance

only because the ground motion is sufficiently strong to cause yielding in the structure. Therefore, simply comparing the durations of two accelerograms does not reveal which is more destructive.

At a rock site in the near-field of an earthquake: (After Julian J. Bommer & Alejandro Martínez-Pereira [55] (2008))

$$\log (D_R) = 0.69M_w - 3.62 \quad \dots(17)$$

The best fit to the data is now given by the equation: (After Julian J. Bommer & Alejandro Martínez-Pereira [55] (2008))

$$\log (D_E) = 0.69M_w - 3.70 \quad \dots(18)$$

where,

M_w = Magnitude

D_R = Rupture Duration

Effective durations (mean of horizontal components) as a function of moment magnitude for records from rock sites at distances of less than 10 km were plotted by Julian J. Bommer & Alejandro Martínez-Pereira [55] (2008). The plot thus obtained do not contain any correction factors. Data are corrected by the factors F which are presented in Table 2.2. Julian J. Bommer & Alejandro Martínez-Pereira [55] (2008) had given the equation of F as follows:

$$F = \frac{L_1 + L_2}{L_1} \quad \dots(19)$$

L_1 and L_2 are the longer and shorter distances (measured parallel to the surface break) from the epicenter to the ends of the fault rupture respectively. For many aftershocks it has not been possible to determine the value of F and the same is true for most earthquakes smaller than $M_w = 5$. The best fit to the data is now given by the equation 18 as below:

$$\log (D_E) = 0.69M_w - 3.70$$

where,

D_E = Effective Duration

Table 2.2: Magnitudes of earthquakes used for input motions in software

Year	M	D	Time	Earthquake Name	M_w	h (km)	F
1989	10	18	00:04	Loma Prieta	7.0	17	1.9
2002	11	03	22:12	Denali	7.9	---	---

The predicted values of effective duration are always 20% smaller than the predicted values of rupture duration. A physically meaningful prediction of D_E as a function of magnitude can be made, although the user will need to be aware that the predicted value could be overestimated by a factor of two if the postulated future event involves bilateral

rupture. Somenrille et al. [1997] have developed factors to correct peak ground and response spectra accelerations and strong motion durations for the effects of rupture directivity.

Durations are also adjusted by the directivity factor of Somerville et al. [1997]. The mean values of effective duration are almost identical to the predicted values of rupture duration, although the scatter is actually increased by the application of these factors. It has been suggested that as a result of non-uniform rupture propagation, a simple relationship between magnitude or moment and the duration of ground motion may not exist [Das and Richards, 1979]. For effective duration, it appears that there is a simple correlation between the two parameters, but it is associated with large scatter.

This effective duration, D_E , is shown to consistently constrain the portion of strong earthquake accelerograms that is of greatest engineering significance. The effective duration definition could be refined by varying the values of the thresholds used to constrain the strong shaking phase. It is clear, nonetheless, that it provides a simple and robust way to define a continuous time window on strong accelerograms that contain the motion of real engineering importance.

It would be possible to derive attenuation equations for effective duration on rock sites using a simple function of magnitude and distance. It is clear that a good correlation exists between magnitude and effective duration in the near-field and that this correlation has a sound physical basis. However, it is also important to note from the outset that the durations can vary by up to a factor of two depending on whether the fault rupture is bilateral or unilateral, which cannot easily be predicted for future events.

2.7 - CRITICAL APPRAISAL OF LITERATURE

Seong-Hoon Jeong & Amr S. Elnashai (2006) [3] presented a methodology for the derivation of fragility curves for structures with plan irregularities. Pramanik et al. (2016) [4] constructed fragility curves under real bi-directional excitation by a simple extension of the conventional Incremental Dynamic Analysis (IDA) under uni-directional shaking. Sengupta et al. (2016) [5] has analyzed a RC bridge pier under a set of bidirectionally applied near-field motions with forward directivity (FD) and fling-step characteristics. Suvonkar Chakroborty & Rana Roy (2016) [7] emphasize on the prevalent controversies and the fundamental fallacies in research studies and traditional design. Roy et al. (2017) [2] have studied implications of incidence angle of ground motions on inelastic demand of bridge piers under bi-directional seismic excitation against the corresponding uni-directional counterparts. Extending conventional Park-Ang damage index, Roy et al. (2017) [6] have evolved a simple yet rational damage measure applicable for bidirectional seismic shaking. Debashis Kar & Rana Roy (2018) [8] examine the implications of bi-directional shaking and local site conditions collectively. Roy et al. (2020) [4] suggested an approach to making an advance estimate of response under both unidirectional and bidirectional shaking for all incidence angles. Foliente et al. (2000) [15] used a modified version of the BRANZ procedure for lateral capacity rating of bracing walls to determine the sustainable lateral mass of a 910-mm wide '2x4' timber shear wall. Asadour Hadjian (2004) [10] has considered all pairs of ground motion intensities and associated exceedance probabilities and the site hazard curves are substituted by the median curve and an across variability parameter, ζ_H . Iervolino et al. (2004) [18] defined a limit-state function for the seismic risk assessment developed specifically for the territorial case, and completely described probabilistically for quantitative computation. K.A. Korkmaz (2008) [9] performed the fragility analysis, which is a system reliability analysis with

correlated demands and capacity, with different methodologies to establish the probabilistic characterization of the demands in different aspects. Alireza Mortezaei & Seyed Mehdi Zahrai (2009) ^[17] focused on the viscoelastic (VE) dampers to be used as energy-absorbing devices in buildings. Abbas Moustafa & Sankaran Mahadevan (2011) ^[14] developed a probabilistic methodology for the seismic reliability analysis of structures with random properties. Ming Liu & Boquan Liu (2012) ^[13] have shown by statistical analysis and significance test of structural seismic response variable that the story maximum ductility ratio μ_{\max} and equivalent hysteretic loop numbers N all belong to lognormal distribution. L. Haj Najafi & M. Tehranizadeh (2013) ^[11] evaluated seismic behavior of moment frames (MF) and eccentrically braced frames (EBF), two common systems in most of the steel codes, due to far-field and near-field ground motions and to propose practical technique for acquiring demand distributions. Abdelouafi et al. (2015) ^[12] assessed reliability of the expected performance state by using various methodologies based on finite element nonlinear static pushover analysis and specialized reliability software package. Paolo Castaldo & Tatiana Ferrentino (2020) ^[16] employed the seismic reliability-based design approach for inelastic structures isolated by friction pendulum isolators, considering two different highly seismic Italian sites to provide useful design recommendations. Jonathan Chambers & Trevor Kelly (2004) ^[21] discuss some of the obstacles preventing the widespread adoption of NDP (Nonlinear dynamic analysis), and presents a number of examples where its uncompromised representation is crucial for satisfactorily predicting the seismic response of structures. Devesh P. Soni & Bharat B. Mistry (2006) ^[22] summarize state-of-the-art knowledge in the seismic response of vertically irregular building frames. Moon et al. (2018) ^[20] adopted a different approach that can produce vulnerability curves efficiently, even with a three-dimensional model. Zabihullah et al. (2020) ^[19] deal with the seismic response of RC structures having various individual and combined complicated geometric irregularities. Shah et al. (2020) ^[23] discuss the fragility curves and damage index functions of a 7-storey regular and irregular steel-framed buildings subjected to different earthquake ground motions. Due to the complexity of the concrete damage plasticity (CDP) theory, Hafezolghorani et al. (2017) ^[24] simplified the procedure and a simplified concrete damage plasticity (SCDP) model was developed in this paper. Yuman Shakya & Rajan Suwal (2014) ^[25] modeled the slippage between the core and the fill of the rockfill dam using ANSYS 10 with contact elements. Vijayendra et al. (2010) ^[26] has made attempt to look into the efficiency of procedures for computing fundamental natural period of layered soil deposits in a comparative manner. Seong-Hoon Jeong & Amr S. Elnashai (2007) ^[38] developed a methodology for the derivation of fragility relationships for three-dimensional (3D) structures with plan irregularities. Davis et al. (2010) ^[32] evaluated the seismic fragility of existing OGS buildings in India and compared them with the corresponding fragility curves for building frames without infill (bare frames) and with full infill in all storeys. Monalisa Priyadarshini (2013) ^[28] focuses on the performance of typical OGS buildings designed considering various magnification factors as well as the stepped type buildings with different geometry configurations using fragility analysis and reliability analysis. Shaikh A. Aijaj & G.S. Deshmukh (2013) ^[35] studied different irregularity response due to plan and vertical irregularity, and analyzed “Geometric irregular”-shaped building while earthquake forces act and calculated the deflection in the columns. Akhavan et al. (2016) ^[27] have investigated the behaviour of special steel moment frame with different configuration of soft storey vertically. Belejo et al. (2017) ^[39] presented results on the effects of ground motion duration on the seismic behaviour of a 3-D plan-asymmetric reinforced concrete building. Stefanidou et al. (2017) ^[41] focus on the effects of Soil-Structure Interaction (SSI) in seismic fragility analysis of reinforced concrete (RC) bridges, considering the vulnerability of multiple critical components of the bridge and

different modelling approaches for soil-foundation and bridge-embankment interactions. Cardone et al. (2018) [36] derived fragility curves for typical older residential RC buildings, realized in Italy and other southern Europe countries from the 50s to the early 70s, following a hybrid approach. Latip Kumar Sharma & Kamal Bahadur Thapa (2019) [31] made a humble effort to comprehend the analytic seismic fragility estimate of the existing types of the vertically irregular reinforced concrete buildings in Nepal. Rohan Bhasker & Arun Menon (2020) [33] aimed to examine, the efficiency and sufficiency of a wide spectrum of IMs, in predicting the maximum inter-storey drift demands on plan-irregular RC moment frame buildings subjected to bi-directional ground motion. Pratyush Kumar & Avik Samanta (2020) [34] focused on obtaining the variability functions and fragility curves by considering those uncertainties for low-, mid- and high-rise RC buildings in Patna, India, which is a region of high seismicity. As an alternative to the very time-consuming Non-Linear Response History Analysis (NLRHA) approach, Mohammad S. Birzhandi & Amir M. Halabian (2020) [40] aimed to employ the F2MPA (Flexibly-supported 2 DOF Modal Pushover Analysis) approach in developing fragility curves of flexibly-supported plan-asymmetric structures. Cavalieri et al. (2020) [42] showed the impact of adopting different SSI models on the assessment of seismic fragility functions. To handle the computational challenge in deriving fragility curves, A. Ghanem & D. Moon (2021) [29] utilized a new structural reliability method that incorporates structural analysis and reliability analysis to efficiently and accurately calculate the failure probability with the first-order reliability method (FORM). Patro et al. (2021) [30] carried out a numerical modelling using the finite element software OpenSEES to evaluate the seismic response of a typical eight storey four-bay vertical geometric irregular building considering soil-structure interaction and the results are compared with a reference regular building. Mohamed Mouhine & Elmokhtar Hilali (2021) [37] performed a fragility analysis of RC buildings subjected to seismic loading. Hoseyni et al. (2014) [47] analyzed the seismic fragility for a typical power plant containment considering the effects of soil structure interaction (SSI). Mitropoulou et al. (2016) [46] have considered 3D reinforced concrete (RC) and steel building structures for studying the effect of soil-structure interaction modelling on the structural fragility assessment of such structures. Ajamy et al. (2018) [44] presented an analytical approach to develop seismic fragility curves of an existing jacket type offshore platform in the Persian Gulf. Su et al. (2019) [43], in order to better understand the SPI (soil-pile interaction) effect, fully investigated the seismic fragility of a large-scale PSWS located at the Port of Los Angeles Berth 100, USA, with and without considering SPI. Su et al. (2019) [45] systematically investigated the seismic fragility of a large-scale pile-supported wharf at both component and system levels. Wang et al. (2019) [48] aimed to rank the sensitivity of fourteen structural and soil parameters for seismic performance assessment of pile-group-supported bridges in liquefiable ground undergoing scour potentials. Chin-Hsiung Loh & Ming-Jin Ma (1997) [50] conducted statistical analysis of the response spectra due to both horizontal and vertical ground excitations. Holliday et al. (2011) [51] demonstrated the utility of reliability diagrams for earthquake forecast evaluation with an application to a modified version of the Holliday et al. time-dependent earthquake forecasting method. Chandrakanth Bolisetti (2010) [53] carried out the assessment of the numerical programs, SHAKE and SASSI, using a database of building responses recorded from a centrifuge test performed at the NEES@UCDavis centrifuge facility, as a part of the NEES City Block project. R. Cairo & G. Dente (2014) [52] presented a method for the kinematic interaction analysis of single piles in nonhomogeneous soils. Based on the fixed interface component mode synthesis, Wang et al. (2021) [54] proposed a multiple and multi-level substructure method for the modeling of complex structures. Julian J. Bommer & Alejandro Martínez-Pereira (1998) [55] reviewed some 30 different definitions of strong motion duration and

classified into generic groups. Rohan Bhasker & Arun Menon (2020) [33] aimed to examine, the efficiency and sufficiency of a wide spectrum of IMs, in predicting the maximum inter-storey drift demands on plan-irregular RC moment frame buildings subjected to bi-directional ground motion. Response of soil-structure system on a soft soil site and seismic soil-structure interaction with substructure method is given by John P. Wolf (1985) [61]. Methods for the analysis of soil-structure interaction is given by Steven L. Kramer (1996) [57]. A derivation of the kinematic interaction effect for a rigid, massless foundation slabs the so-called “Tau effect” is given by Ray W. Clough & Joseph Penzien (2003) [59]. The dynamic soil–structure interaction is given by T. K. Datta (2010) [58]. Seismic soil-structure interaction with substructure method, finite element model of soil-structure system for direct method of analysis and inertial interaction analysis are given in details in NPTEL [60]. Lubliner et al. (1989) [65] presented a constitutive model based on an internal variable-formulation of plasticity theory for the non-linear analysis of concrete. M. N. Fardis & T. B. Panagiotakos (1996) [66] studied the effects of masonry infills on the global seismic response of reinforced concrete structures through numerical analyses. Jeeho Lee & Gregory L. Fenves (1998) [64] developed a new plastic-damage model for concrete subjected to cyclic loading using the concepts of fracture-energy-based damage and stiffness degradation in continuum damage mechanics. Sarkar et al. (2007) [63] adopted the profile of the Koyna dam for the study of the response of a dam subjected to dynamic loading. Indrajit Chowdhury & Shambhu P. Dasgupta (2003) [67] outlined a procedure, which ensures a rational estimate of α and β even for a system with large degrees of freedom. The method of plotting the fragility curves considering IO, LS, CP and Indian Codal Limit are given in details in FEMA 356 (2000) [68]. Limitations of probability of exceedance of a particular performance level such as IO, LS, CP are given by IS 1893 (Part 1) – 2002 [73]. Abraham M. Hasofer & Niels C. Lind (1974) [78] presented the second-moment reliability code format for a probabilistic design code, which is based on a fundamental analysis of the meaning of second-moment reliability in multivariate problems, and is entirely derived from one basic assumption concerning the measurement of reliability. To address building performance issues raised by numerous weld fractures in beam-to-column connections in welded special moment-resisting frames due to Northridge earthquake of 1994 and to support improvements in probability-based load resistance factor design for steel building structures, Jianlin Song and Bruce R. Ellingwood (1999) [75] evaluated four welded special moment-resisting frames of different sizes and configurations that suffered connection damage during the earthquake using both deterministic and stochastic approaches. In the second of two companion papers addressing damage to buildings with welded special moment frames, Jianlin Song and Bruce R. Ellingwood (1999) [76] considered the role of inherent randomness and modeling uncertainty on building performance in detail using the nonlinear dynamic analysis procedure from the first paper as an assessment tool. Bruce R. Ellingwood (2001) [77] reviewed some of the special considerations, required for structural design and evaluation of buildings and other facilities with regard to their ability to withstand the effects of earthquakes, specifically as they pertain to probability-based codified design and reliability-based condition assessment of existing buildings. Kotronis et al. (1984) [83] presented a new macroelement for single piles in sand (with pile-head on the ground surface) developed within the framework of hypoplasticity. George Gazetas (1992) [85] presented a complete set of algebraic formulas and dimensionless charts for readily computing the dynamic stiffnesses (K) and damping coefficients (C) of foundations harmonically oscillating on/in a homogeneous half-space. L. M. Zhang (2003) [82] aims to investigate the response of laterally loaded large-section barrettes based on the load tests, to simulate the response of the two test barrettes, and to study the influence of loading direction on the lateral response of barrettes. Correia et al. (2010) [56] briefly

presented an innovative pile-head macro-element model, recently proposed for the simulation of inertial soil-structure interaction effects in the seismic analysis of structures supported on long piles. Li et al. (2016) [81] presented a novel macroelement for single vertical piles in sand developed within the hypo- plasticity theory, where the incremental nonlinear constitutive equations are defined in terms of generalized forces, displacements and rotations. Graine et al. (2018) [84] constructed the failure surface for a single rigid pile in a cohesive-frictional soil, subjected to both horizontal force and bending moment. The material models and analysis types are well explained in Seismostruct Technical Information Sheet (2018) [89]. Francesco Cavalieri & António A. Correia (2019) [86] described a study into the transfer of seismic motion from the soil into the foundation and the structure of buildings, i.e., the soil structure interaction. The macro elements for soil structure interaction of shallow and pile foundations are explained well in SeismoStruct User Manual (2021) [87]. The various link elements in SeismoStruct and their damping parameters are discussed in SeismoStruct Verification Report (2021) [88]. As described in the Verification Report, its accuracy is very well demonstrated by its numerous successes in Blind Test Prediction Exercises. António A. Correia & Alain Pecker (2021) [90] extended the macro-element approach to the analysis of laterally loaded pile-shafts and soil-pile-structure interaction. Shiuly et al. (2014) [79] presented the ground motion amplification factors at different time period bands and fundamental time period of soft sedimentary deposit in densely populated Kolkata city for seismic micro-zonation. Shiuly et al. (2014) [80] presents the ground motion amplification scenario along with fundamental frequency (Fo) of sedimentary deposit for the seismic microzonation of Kolkata City, situated on the world's largest delta island with very soft soil deposit.

Earthquake has two components in X and Z directions. Earthquake acts in the resultant direction. We measure displacement due to earthquake in X and Z directions but the displacement occurs in the resultant direction. Actually, earthquake has 3 component directions but we generally do not consider Y direction component. We have to consider all these which is primarily our study. This study is based on use of the softwares, SeismoStruct and Abaqus incorporating soil structure interaction and considering near field and far field earthquake.

Research Gap: Fragility means ‘probability of failure’. Using Abaqus and SeismoStruct, we can handle bidirectional earthquake incorporating soil structure interaction for both shallow and pile foundations and considering near field and far field earthquake for plane and sloping ground. This type of work using finite element softwares, Abaqus and SeismoStruct, is not done yet. On the basis of above literature study on previous research, the following critical appraisal can be made.

- Performance of R.C. buildings using site specific ground motion has been conducted by nonlinear static analysis. However, the performances of the irregular buildings by nonlinear dynamic analysis incorporating soil structure interaction have not been investigated.
- Performance of irregular buildings with help of PSD (power spectral density) models and fragility curve has not been highlighted earlier. These graphs should reveal the behavior of buildings on their limiting value like IO, LS and CP.
- The determination of Reliability Index (RI) of various types of irregular buildings using finite element softwares, Abaqus and SeismoStruct, for bidirectional earthquake is absent in the literature.

CHAPTER 3: FRAME STRUCTURES ON UNIFORM SOIL

3.1 - GENERAL

The damage pattern during several past earthquakes like Mexico earthquake (1985), San Francisco earthquake (1989), Los Angeles earthquake (1995) have shown that local soil plays significant role in the amplification of ground motion especially in those areas, that are located on unconsolidated young sedimentary deposits [62]. In India during Bhuj earthquake of 2001, Ahmedabad city, situated on younger alluvial deposits, experienced a heavy damage in spite of relatively larger distance from epicentre. Further, during seismic excitations, more attention should be paid to Soil-Structure Interaction (SSI) phenomenon, which is a major problem in the field of Structural Engineering. This chapter presents the behaviour of various parameters under the influence of dynamic soil-structure interaction when frame structures constructed on uniform soil are subjected to near-field and far-field earthquakes. In this chapter, three types of soils (Hard Soil, Medium Soil and Soft Soil) are combined with irregular buildings to develop analytical models. Each model is subjected to both near-field and far-field earthquake. It is to be mentioned that, in case of every model, fragility curves have been developed for all the floors under the influence of aforesaid two earthquakes. Moreover, amplification factors at fundamental frequency for each type of soil under each type of seismic excitation are computed separately and compared. To simulate the non-linear properties of concrete, concrete damaged plasticity model has been used. This model is briefly described in the next section followed by the all the analysis results.

3.2 - PROBLEM FORMULATION

To detect the effect of soil properties on SSI, three types of soils namely - Hard Soil, Medium Soil and Soft Soil have been considered. It is assumed that all the soils are homogenous in nature. The mass density, Young's modulus and shear wave velocity in the soil medium are maximum for the hard soil and minimum for the soft soil. On the other hand, Poisson's ratio is minimum for the hard soil and maximum for the soft one. All the values for the medium soil lie between the hard and soft soil. However, the properties of all the soils used for analysis are mentioned in Table 3.1.

$$G = \frac{1}{2} \frac{E}{1+\nu} \quad \dots(20)$$

$$K = \frac{E}{3(1-2\nu)} \quad \dots(21)$$

$$V_s = \sqrt{G/\rho} \quad \dots(22)$$

where,

G = Shear Modulus in N/m²

E = Young's Modulus in N/m²

K = Bulk Modulus in N/m²

ν = Poisson's Ratio

V_s = Shear Wave Velocity in m/s

ρ = Mass Density in kg/m³

Table 3.1 - Properties of the uniform soils

Type of Soil	Mass Density (ρ) in kg/m ³	Young's Modulus (E) in N/m ²	Poisson's Ratio (ν)	Shear Wave Velocity (V_s) in m/s
Hard Soil	2300	1.99×10^9	0.2	600
Medium Soil	2000	6.5×10^8	0.32	350
Soft Soil	1500	9.7×10^7	0.43	150

It is to be mentioned that, SSI effects also depend on various properties of the structure like stiffness of the structure, height of the structure, type of foundation used etc. To study the contribution to the structures for the SSI effect, G + 9 frame buildings with plan and vertical irregularities have been taken for analysis. All the buildings are irregular in shape having plan dimension 20 m \times 17.5 m. Each building has three bays of equal length in both the directions. The heights of the buildings are taken as 30 m. Floor to floor height of all the buildings is considered as 3 m. Raft footings and pile foundations are used as the foundation of the buildings. Various properties of the constituents of the buildings are shown in Table 3.2.

Table 3.2 - Properties of the constituents of the buildings

1.	Grade of Concrete		M 25
2.	Mass Density (ρ) of Concrete		2500 kg/m ³
3.	Young's Modulus (E) of Concrete		2.5×10^{10} N/m ²
4.	Poisson's Ratio (ν) of Concrete		0.15
6.	Floor to Floor Height of the Building		3 m
7.	Depth of Isolated Footing		2.5 m
8.	Depth of Pile Cap		0.75 m
9.	Size of Pile Cap		4.5 m \times 4.5 m
10.	Diameter of Pile		0.4 m
11.	Length of Pile		23 m
12.	Cross-sectional Area of the Columns	G+9 Building	500 mm \times 500 mm
13.	Cross-sectional Area of the Beams	G+9 Building	300 mm \times 500 mm
14.	Floor to floor height		3.0 m
15.	RCC weight		25 KN/m ³
16.	Building frame type		OMRF

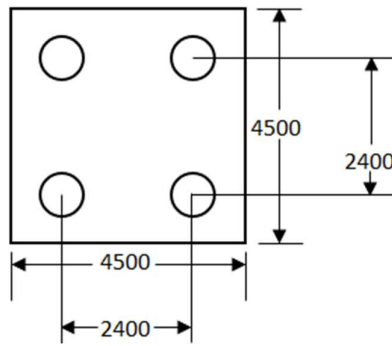


Figure 3.1 - Dimension Details of Pile Cap

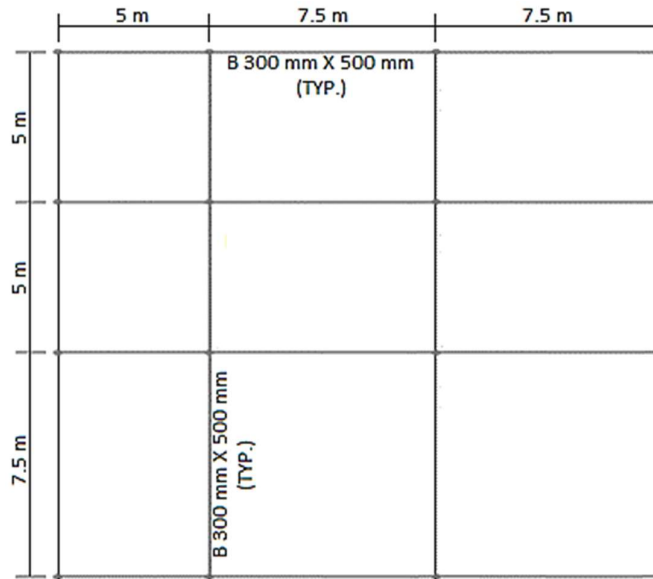


Figure 3.2 - Plan of the building with no irregularity

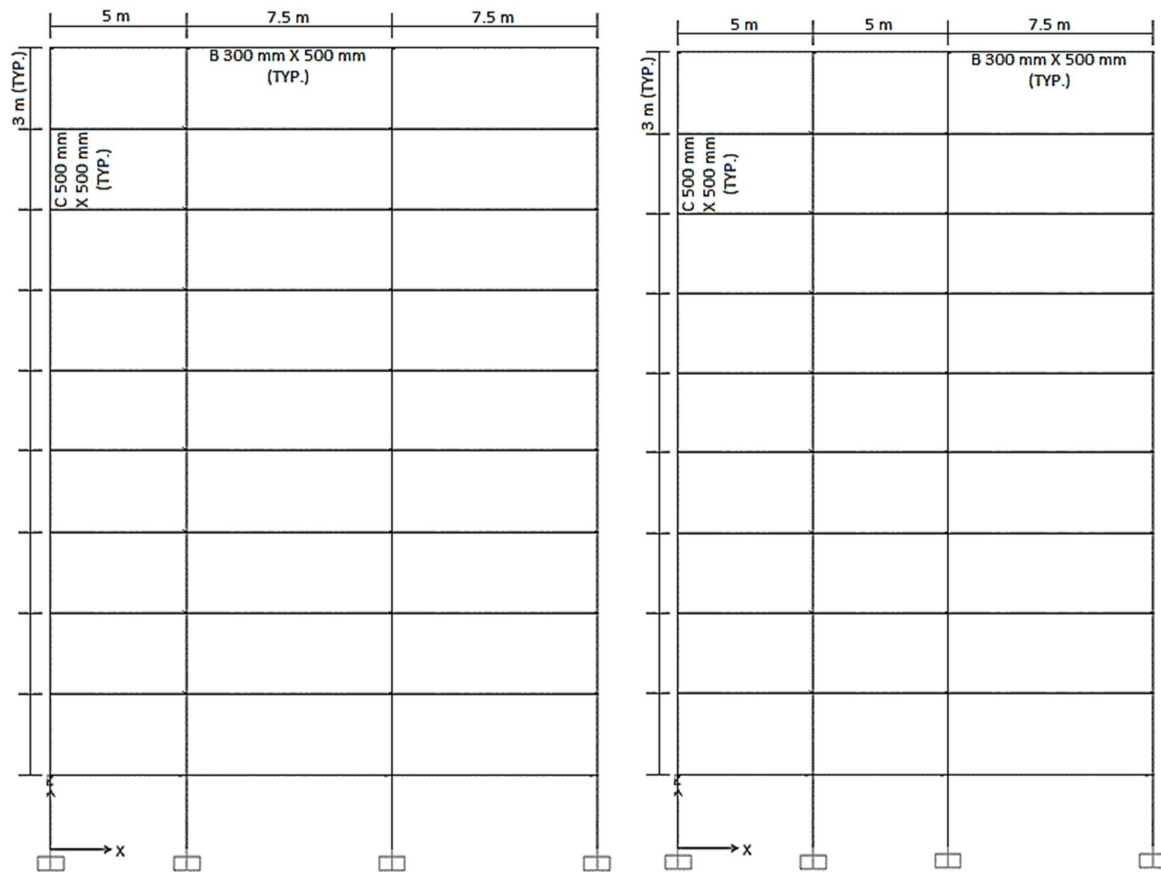


Figure 3.3 - Elevation of the building without irregularity on plane ground as well as elevation of the building with horizontal irregularity on plane ground

Building on sloping ground:

There are two ways to build a house on a sloped lot: using the “cut and fill” method, or making use of stilts. Less than 10% incline is considered slight and is the easiest to build on, while 11-20% is considered moderate. Anything above 20% is deemed steep. Beyond about 15%, costs begin to increase significantly as the risks become greater and the work becomes more difficult. It’s not unheard of to have houses built on grades of as much as 50%; however, the cost of the complex foundation systems required for such houses is often more than the cost of an entire house on flat ground.

Buildings on sloping ground are more detrimental to bidirectional earthquake motion. In our study we have considered the same model as in Figure 3.3, but with an exception that the lengths of base level columns vary for different bays. Three different heights of base columns used are 3 m, 8 m and 13 m. We have studied the aforesaid structure for both shallow foundation and pile foundation.

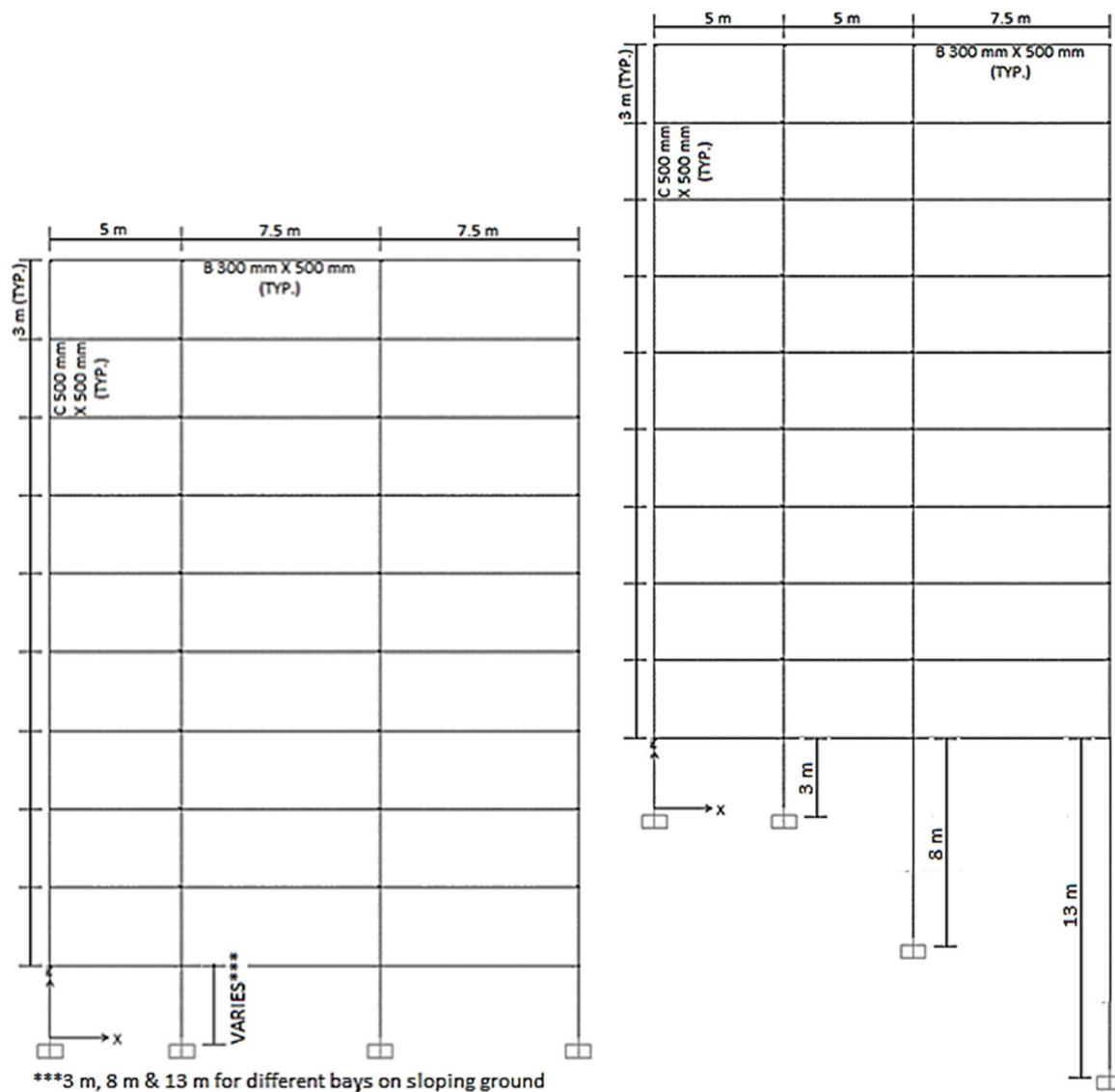


Figure 3.4 - Elevation of the building without irregularity on sloping ground as well as elevation of the building with horizontal irregularity on sloping ground

Vertically irregular building on plane ground:

When building structures with irregular distributions in their mass, stiffness and strength along the height of building are located in a high seismic zone, the structural engineer's role becomes more challenging. Therefore, the structural engineer needs to have a thorough understanding of the seismic response of irregular structures. In recent past, several studies have been carried out to evaluate the response of irregular buildings work that has been already done pertaining to the seismic response of vertically irregular building frames. Buildings with plan irregularities (e.g., those with re-entrant corners such as L-shape plans on corner plots) and those with elevation irregularities (e.g., large vertical setbacks in elevation such as a plaza-type configuration in commercial structures) are common in the affected area. Major failures occurred due to irregularities like soft

storey Failure, Mass Irregularity Failure, Plan Irregularity Failure, Shear Failure.

We have studied the aforesaid structure for both shallow foundation and pile foundation. For detail understanding of the irregularity, refer the floor plans.

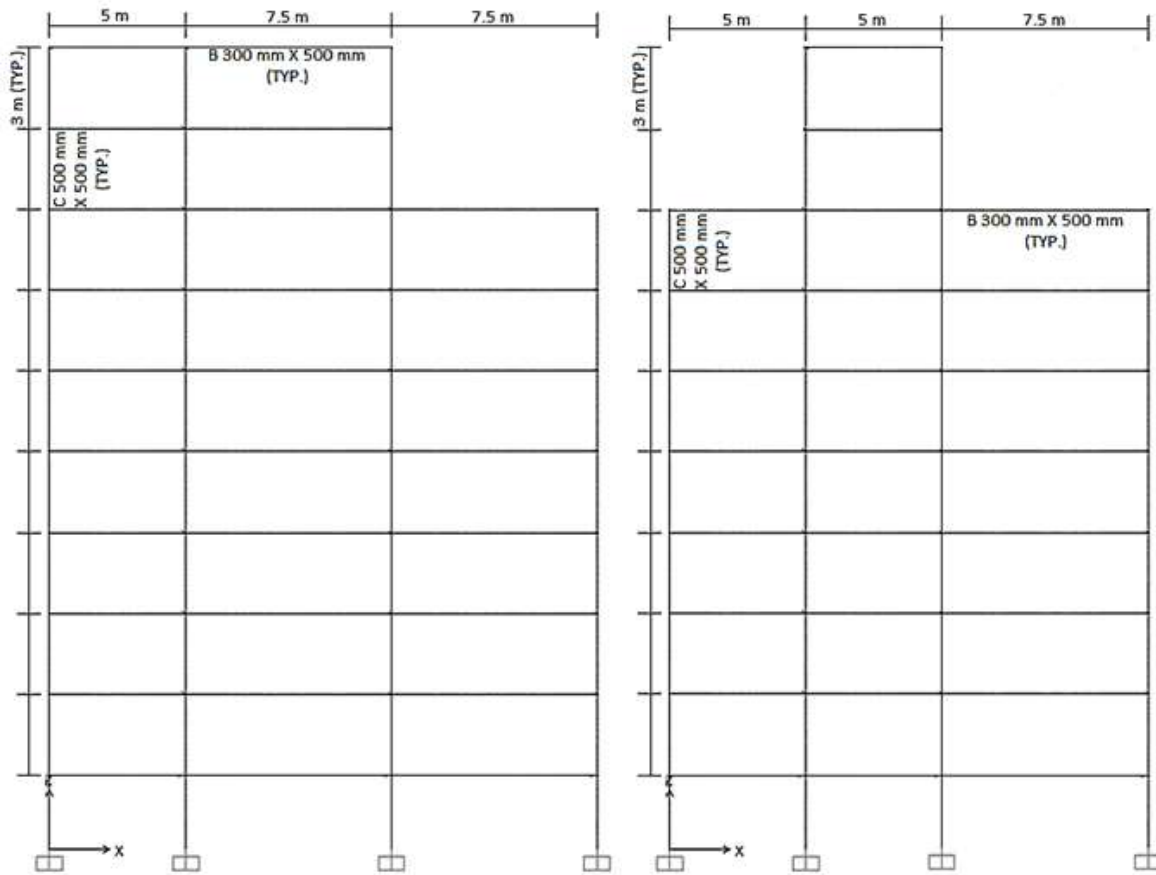


Figure 3.5 - Elevation of the building with vertical irregularity on plane ground

Vertically irregular building on sloping ground:

The challenge increases when the irregular building is situated on sloping ground. We have studied the same irregular building on sloping ground as studied on the plane ground.

For detail understanding of the irregularity, refer the floor plans.

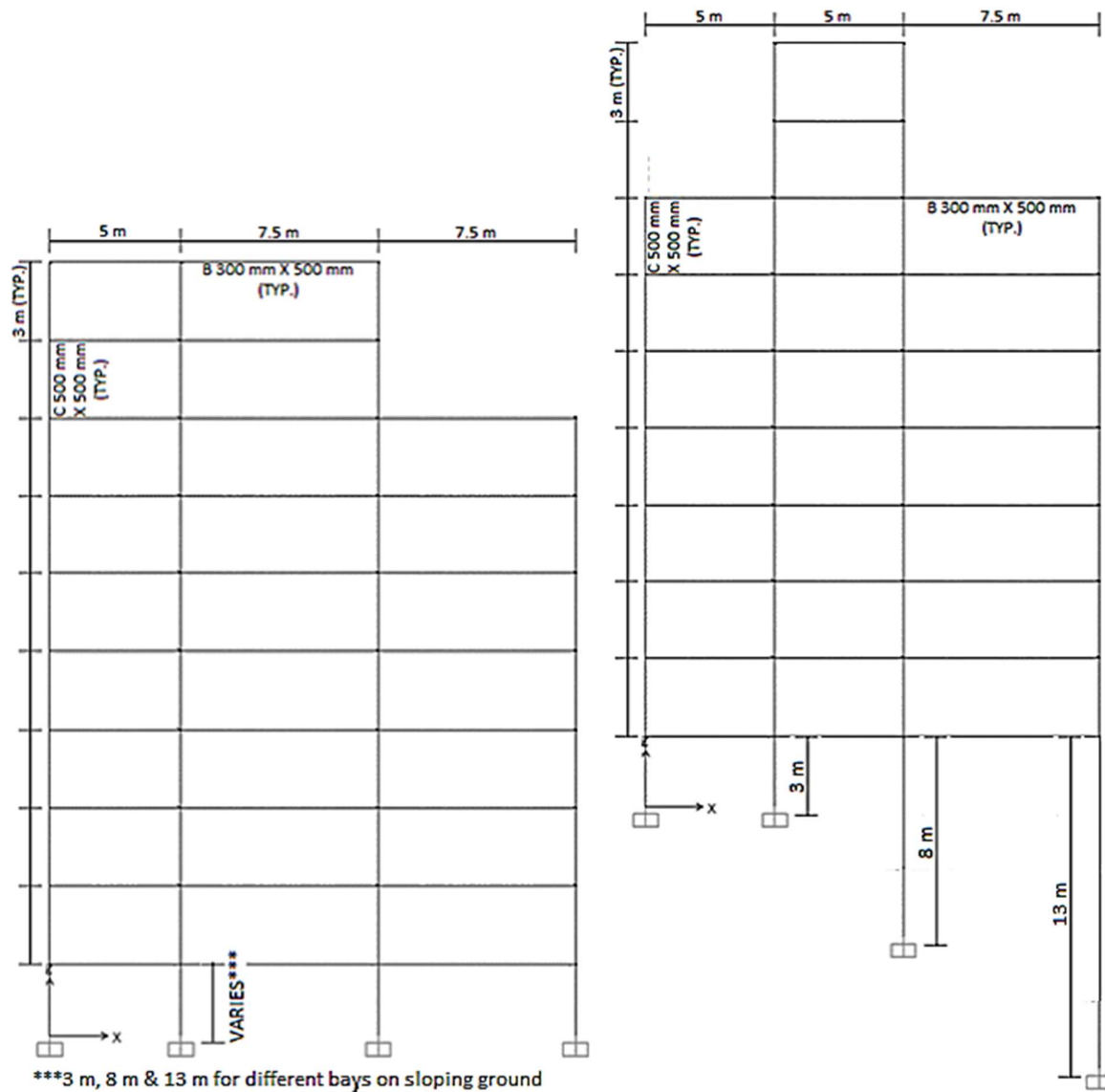


Figure 3.6 - Elevation of the building with vertical irregularity on sloping ground

The irregularity of the building frame considered for analysis has been inspired by the pattern of vertical irregularity of Sears Tower, Chicago. Floors ground, 1st, 2nd and 3rd have the same floor plan which is identical to that of the building with only plan irregularity considered for analysis. Floors 4th and 5th have identical floor plan which is different from that of the rest. In the similar manner, floors 6th and 7th have identical floor plan which is different from that of the rest. And likewise, floors 8th and 9th also have identical floor plan which is different from that of the rest.

The different floor plans of different floor levels are presented in the figures 4.14 to 4.17.

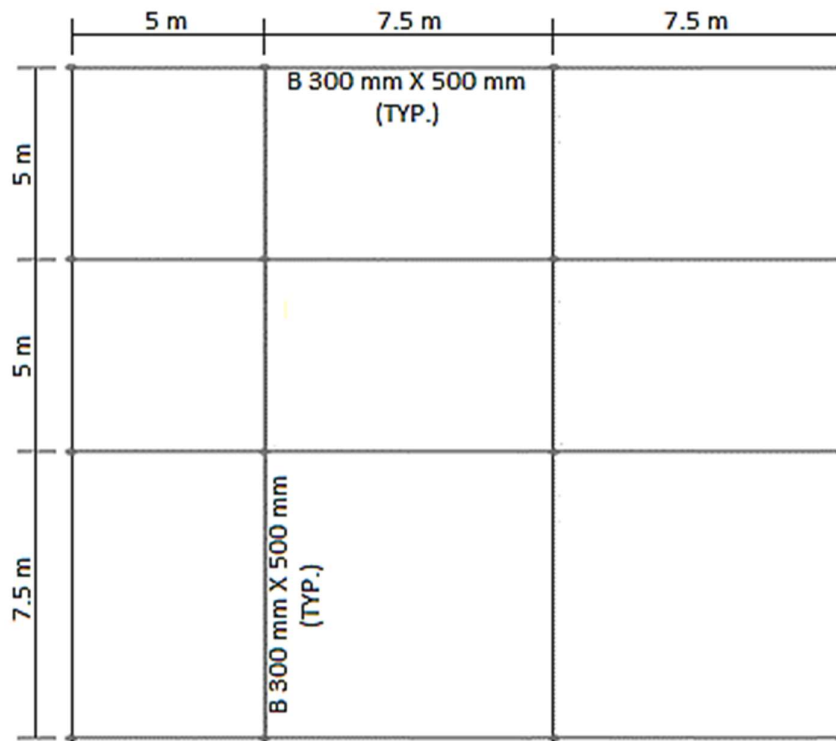


Figure 3.7 - Ground, 1st, 2nd and 3rd floor plan of the building with vertical irregularity

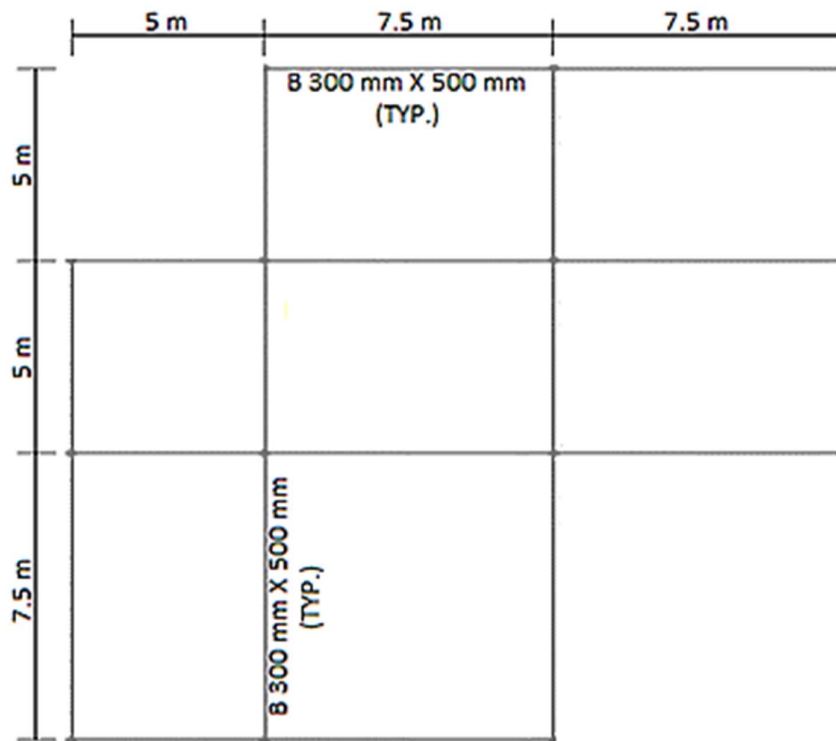


Figure 3.8 - 4th and 5th floor plan of the building with vertical irregularity

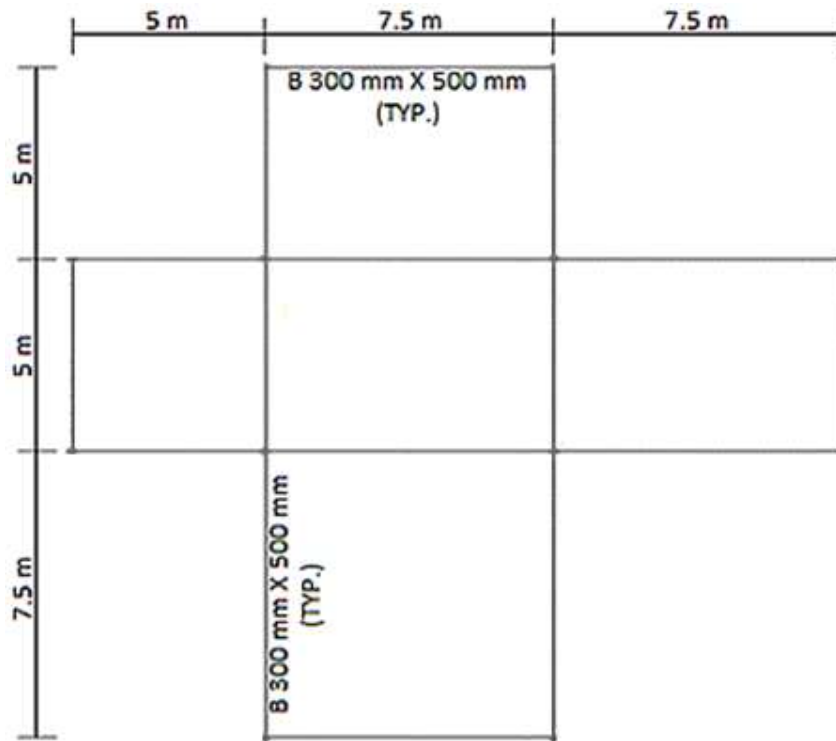


Figure 3.9 - 6th and 7th floor plan of the building with vertical irregularity as well as typical floor plan of the building with horizontal irregularity

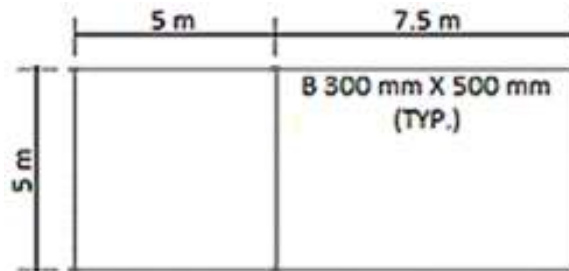


Figure 3.10 - 8th and 9th floor plan of the building with vertical irregularity

Horizontally irregular building on plane ground:

During an earthquake, failure of structure starts at points of weakness. This weakness arises due to discontinuity in mass, stiffness and geometry of structure. The structures having this discontinuity are termed as Irregular structures. Irregular structures contribute a large portion of urban infrastructure. To understand seismic damage to building structures, we also have to compare the seismic behavior of regular building with horizontally irregular buildings.

The typical plan of horizontally irregular building considered in our study is exactly the same as one shown in Figure 3.9. Whereas, the elevation drawing matches with Figure 3.3

Horizontally irregular building on sloping ground:

The behaviour and stability of a building in a sloped region depend on structural configuration. With the rapid growth of urbanization occurring across the entire world, irregular buildings are quite frequently built in almost every country, including India. Due to this, population density in the hilly region has increased enormously. Therefore, there is a popular and most pressing demand for the construction of multi-storey buildings on a slope and around the cities.

In the last few years, many seismic studies have been carried out on sloping ground frames. Many problems occur on the sloping ground when considering irregularity in the different configurations of structures. Therefore, it is also necessary to compare the seismic behavior of regular building on sloping ground with horizontally irregular buildings on sloping ground.

The elevation of the structure considered matches with Figure 3.4.

We will only consider various cases of G+9 buildings for our study.

3.3 - MODELLING THE PROBLEM

There are numerous methods to model and analyze the dynamic SSI phenomenon. Among them, finite element method (FEM) is one of the easiest numerical techniques which can accurately simulate SSI effect and most commonly used. Nowadays, many software packages are available in the market to solve different problems using FEM. In the present work, a software named Abaqus (v.14.5) has been used for modelling and solving the above stated problem.

To solve an SSI problem using Abaqus software, generally, the steps mentioned below are sequentially followed:

1. Forming the geometries of different parts of the soil-structure model in the PART module.
2. Creating the materials and sections with desired properties and assigning them to the parts created before in the PROPERTIES module.
3. Generating the whole soil-structure model combining all the parts suitably in the ASSEMBLY module.
4. Mentioning the type of analysis required in the STEP module.
5. Choosing the sizes and properties of the elements of individual parts as per requirement in the MESH module.
6. Defining appropriate boundary conditions of the model in the LOAD module.
7. Indicating the type of interaction (or, constraints) between the different components of the model in the INTERACTION module.
8. Creating the job and submitting it for analysis in the JOB module.
9. Viewing the outputs and obtaining the desired results in the VISUALIZATION module.

In this study, six parts, such as Infinite Soil, Soil Base, Soil Tetrahedron, Footing or Pile Cap and Pile, Column and Beam, have been used to model the above stated soil-structure interaction problem. The plan dimensions of the soil base part (37.5 m × 35 m) is kept almost double compared to the plan dimensions of the structure (20 m × 17.5 m) so that

its boundaries cannot disturb the response of the structure. Its depth (30 m) is also kept higher than the depth of footing (2.5 m) or pile cap (1 m) due to the same reason. Pile termination level is 24 m below ground level. A 27.5 m × 25 m × 5 m rectangular groove is created at the centre of the soil base in order to fit the soil tetrahedron into it. The soil tetrahedron part actually works as a bridge between the footing and the soil base. This part also has a square shaped groove where the dimensions of the groove are same as that of the footing or pile cap. The depth of the footing is 2.5 m or that of pile cap is 1 m. The footing or pile cap is positioned in its respective groove. The beams of length 5 m & 7.5 m are positioned on top of each two adjacent columns.

Homogeneous materials are created as per the predefined properties. The required sections for all the parts are generated and have been assigned accordingly. Proper orientations are also provided to the beams and the columns.

After forming all the parts and assigning all the material properties and section properties to them, they are assembled in the correct pattern to get the complete soil-structure model.

Two steps are created for two different types of analysis. The first step named Frequency is generated to carry out modal analysis of the whole model. The other step has been named as Seismic, which performs the seismic analysis. From this step, all the stress and displacement components under the action of the input seismic motion can be easily obtained.

Meshing is the most vital part of the finite element method. The size of mesh plays an important role in the calculation process. If the mesh size is reduced gradually, the solution becomes more accurate. But the problem is that with the reduction in mesh size, the number of nodes and elements increases which leads to more computer memory consumption and more computation time requirement. Therefore, an optimum mesh size has to be selected so that neither problem in accuracy of solution nor problem in computer memory and computation time arises. Keeping this in mind, the soil base and the infinite soil are meshed using eight-noded linear brick elements of size 2.5 m × 2.5 m × 2.5 m, while the footing is meshed using eight-noded linear brick elements of size 0.625 m × 0.625 m × 0.625 m. The soil tetrahedron is suitably meshed using four-noded linear tetrahedron elements so that it can be connected to the soil base as well as to the footing. The beams and the columns are meshed using two-noded linear elements of 1 m and 0.6 m length respectively. The properties and meshing details of all the elements used for analysis are summarized below in Table 3.3.

In case of pile foundation friction interaction property between the pile and soil is considered. Friction coefficient of 0.5 is used. Pile is modelled using shell element of diameter 0.8 m. The shell thickness is provided as 0.2 m.

Earthquake amplitudes are applied in X direction and Y direction in different models. The resultant responses are studied in order to take the effect of bidirectional earthquake. For modal analysis, the whole model is considered fixed at the base. To incorporate this property, all the displacement and rotation components of the nodes present at the bottom of the model are restricted to zero. On the other hand, to perform seismic analysis, only the displacement component of the bottom nodes along the direction of earthquake force is released.

At last, all the duplicate nodes are merged to fix all the parts with one another and to get

the complete model.

Isometric views of the prepared models for the G+9 buildings are shown in Figure 3.14 to Figure 3.21.

Table 3.3 - Properties and meshing details of the elements used in Abaqus

Name of the Part		Cross-sectional Area	Depth or Length of the Part	Element Size for Meshing	No. of Nodes in Each Element	Type of Element
Infinite Soil		2.5 m × 2.5 m	N/A	2.5 m × 2.5 m × Infinite Length	8	Linear Hexahedron (Type CIN3D8)
Soil Base (Surrounded by the Infinite Soil)		37.5 m × 35 m	30 m	2.5 m × 2.5 m × 2.5 m	8	Linear Hexahedron (Type C3D8)
Soil Tetrahedron (Embedded in the Soil Base)		27.5 m × 25 m	5 m	N/A	4	Linear Tetrahedron (Type C3D4)
Isolated Footing (Embedded in the Soil Tetrahedron)		22.5 m × 20 m	2.5 m	0.625 m × 0.625 m × 0.625 m	8	Linear Hexahedron (Type C3D8)
Pile Cap (Embedded in the Soil Tetrahedron)		4.5 m × 4.5 m	1 m	0.625 m × 0.625 m × 0.625 m	8	Linear Hexahedron (Type C3D8)
Pile (Embedded in the Soil Base)		0.8 m diameter	24 m	1.25 m × 0.314 m	4	Liner Shell (Type S4R)
Column (Each column is placed on a Footing)	For G+9 Building	500 mm × 500 mm	3 m, 8 m & 13 m	0.6 m	2	Linear Line (Type B31)
Beam (Each beam is placed on two Columns)	For G+9 Building	300 mm × 500 mm	5 m & 7.5 m	1 m	2	Linear Line (Type B31)

Concrete Damaged Plasticity model input sample:

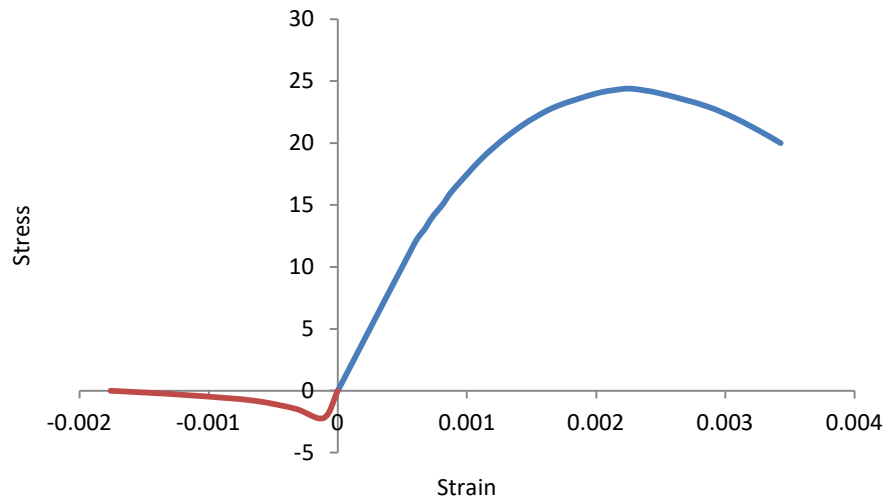


Figure 3.11 - Stress strain diagram for concrete damaged plasticity model

Stress and strain values in Table 4.7 above needs to be used in Abaqus for compressive behaviour. Stress and strain values in Table 4.6 above needs to be used in Abaqus for tensile behaviour but with positive sign instead of negative sign provided in the table. Negative sign is used in the table just to create the graph. We cannot input zero stress strain value (first row of Table 4.6 and Table 4.7) in Abaqus.

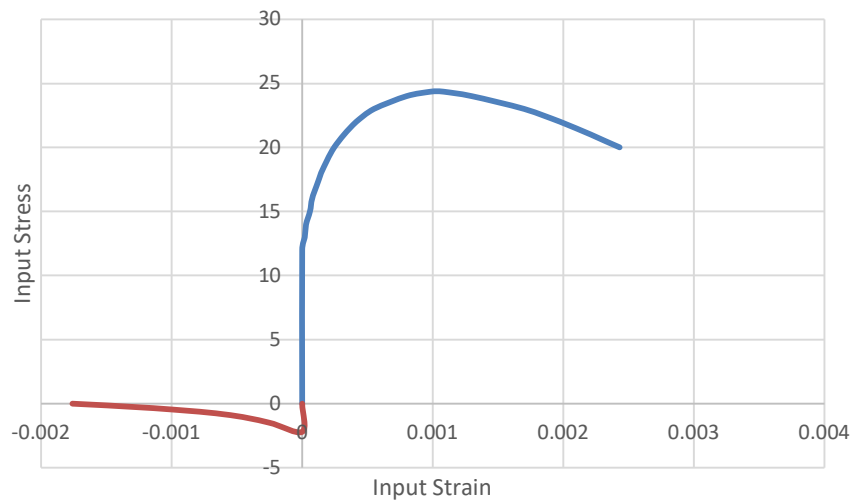


Figure 3.12 - Stress strain diagram to be given as input in Abaqus for concrete damaged plasticity model

$$\text{Strain} = \text{input strain} + \text{stress} / 20000 \quad \dots(23)$$

Compression and Tension Plasticity:

Plasticity flow parameters to be considered in the model are as follows: (after Lubliner et al. (1989) [65] and Lee and Fenves (1998) [64])

Dilation Angle = $30 \sim 40$

Eccentricity = 0.1

f_{bo} / f_{co} (i.e., $\sigma_{bo} / \sigma_{co}$) = 1.16

$K = 2/3$

Viscosity parameter = 0.0

Damage Parameters to be given as input in the model:

We have to input d_c v/s inelastic strain data for Concrete Compression Damage and d_t v/s cracking strain data for Concrete Tension Damage in Abaqus while defining Concrete Damaged Plasticity. It is strongly recommended to specify the tabular definition of tensile and compressive damage variables for the same values of cracking and inelastic strains / displacements as those used in the tabular definitions of tension stiffening and compressive behaviour, respectively.

d_c and d_t represent the damage parameters for compressive and tensile behaviour of concrete respectively.

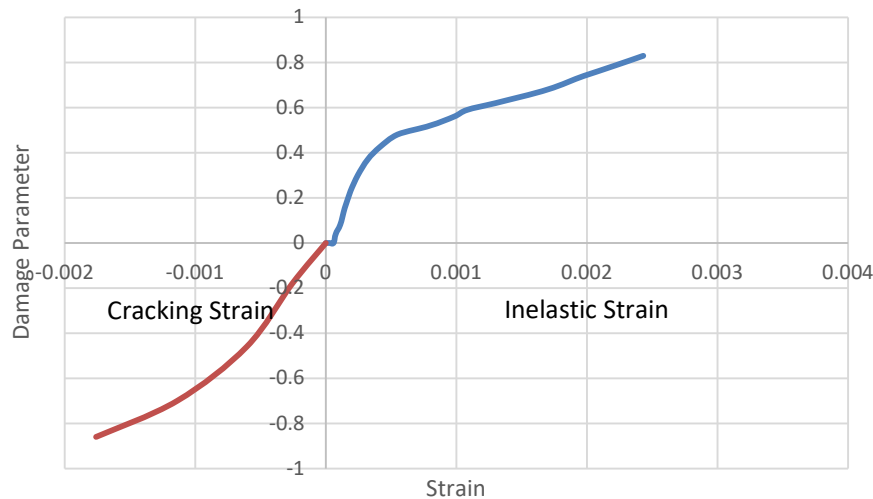


Figure 3.13 - Damage parameter v/s strain diagram to be given as input in Abaqus for concrete damaged plasticity model

Failure and element deletion:

To trigger element deletion in ABAQUS, we need to specify a criterion for the complete failure of concrete. This cannot be done currently in the material definition interface. Instead, we need to insert a new Keyword to ABAQUS input file after the damage definitions. The Keyword is as below:

*Concrete Failure, TYPE=Strain

$\epsilon_{ck, fail}$, $\epsilon_{in, fail}$, d_t , d_c

$\epsilon_{ck, fail}$ = cracking tensile failure strain = 0.00176

$\epsilon_{in, fail}$ = inelastic compressive failure strain = 0.00243

d_t = damage parameter at failure point for cracking strain = 0.86

d_c = damage parameter at failure point for inelastic strain = 0.83

For isolated foundation or pile cap, we are interested in visual representation of damage. So, we have activated the “Element deletion” option with the mesh element type definition dialogue. By default, ABAQUS considers complete failure of the constitutive material model when the degradation is equal to 1.0. We have associated the mesh element with a “Max degradation” value other than 1.0, such as 0.8. Element deletion and Max Degradation are only available for 3D Stress elements. These are not available for line elements (beams and columns) or shell elements (piles).

In the same time, in the “Field History Output”, we have made sure to include the damage parameters field variables DAMAGEC, DAMAGET and DAMAGESHR as well as the STATUS.

Constraints:

Providing constraints between various elements is one of the most critical and important part of modelling in Abaqus.

While creating constraints, we have to make sure that the mesh density of the slave surface in the tie pair is finer than the master surface. The analysis may run slower, may yield inaccurate results, and may require more memory if this is not the case. If significant clearance/overclosure exists between surface pair and the master surface does not have rotational degrees of freedom, adjustment is recommended for correct enforcement of the tie constraint.

Table 3.4 - Input for coupling constraints between various elements in Abaqus models

Constraint Type	Coupling Type	Constrained Degrees of Freedom	Influence Radius	‘Adjust control points to lie on surface’	Coordinate System (CSYS)
Kinematic Coupling between Pile Cap and Superstructure Frame (Coupling)	Kinematic	U1, U2, U3, UR1, UR2, UR3	To outermost point on the region	Disabled	(Global)

Kinematic coupling constrained is only required in models with pile foundation.

Interactions:

This input is required only in case of the Abaqus models with pile foundations. This typically caters the frictional resistance between piles and soil. The details of the contact property are given below:

Name – Friction

Mechanical Property – Tangential Behaviour

Friction Formulation – Penalty

Friction properties:

Directionality – Isotropic

Number of field variables – 0

Friction Coeff. – 0.5

Shear Stress properties:

Shear stress limit – No limit

Elastic Slip properties:

Maximum elastic slip (Standard only) in Fraction of characteristic surface dimension – 0.005

Elastic slip stiffness (Explicit only) – Infinite (no slip)

Interaction details are given below:

Name – Pile to Soil Friction

Type – Surface-to-surface contact (Standard)

Step – Initial

Sliding formulation – Finite sliding

Discretization Method – Surface to surface

Contact tracking – Two configurations (path)

Slave Adjustment – No adjustment

Surface Smoothing – Do not smooth

Bonding – ‘Limit bonding to slave nodes in subset’ is disabled.

Contact interaction property – Friction

Contact controls – (Default)

Steps:

Three steps of analysis are used in our models namely, Initial, Frequency and Seismic. Frequency step will evaluate the outputs of modal analysis of the structure whereas Seismic step will evaluate the various response time histories of the structure. Details of each step are provided below:

Name – Frequency

Type – Frequency

Nlgeom – Off

Eigensolver – Lanczos

Number of eigenvalues requested – 15

Maximum frequency of interest (cycles / time) – 50

Project acoustic-structural coupling where applicable – Disabled

Block size – Default

Maximum number of block Lanczos steps – Default

Use SIM – based linear dynamics procedures – Enabled

Project damping operators – Enabled

Include residual modes – Disabled
Equation Solver Matrix storage – Symmetric
Normalize eigen vectors by – Mass
Evaluate dependent properties at frequency – Disabled

Name – Seismic
Type – Dynamic, Implicit
Time period – 85 for Denali Earthquake / 40 for Loma Prieta Earthquake
Nlgeom – Off
Application – Analysis product default
Include adiabatic heating effects – Disabled
Incrementation type – Fixed
Maximum number of increments – 1000000000
Increment size – 0.1
Half-increment Residual – Suppress calculation is disabled.
Equation Solver Matrix storage – Use solver default
Solution technique – Full Newton
Convert severe discontinuity iterations – Propagate from previous step
Default load variation with time – Instantaneous
Extrapolation of previous state at start of each increment – Analysis product default
Time Integrator Parameter, Alpha – Analysis product default
Initial acceleration calculation at beginning of step – Analysis product default
Accept solution after reaching maximum number of iterations – Disabled

Nlgeom is a setting which controls the inclusion of nonlinear effects of large displacements and affects subsequent steps. Decreasing increment size will increase run time substantially.

Boundary Conditions:

We have used three types of boundary conditions, one for frequency step and other two for seismic step for bidirectional earthquake. The details of the steps used are discussed below:

Name – Fixed
Type – Symmetry / Antisymmetry / Encastre
Step – Frequency (Frequency)
Region – Bottom of base soil of bottommost layer
CSYS – (Global)
ENCASTRE ($U_1 = U_2 = U_3 = UR_1 = UR_2 = UR_3 = 0$) – Enabled

Name – Fixed Except X
Type – Displacement / Rotation
Step – Seismic (Dynamic, Implicit)
Region – Bottom of base soil of bottommost layer
CSYS – (Global)
Distribution – Uniform
 $U_1 = 1, U_2 = 0, U_3 = 0, UR_1 = 0, UR_2 = 0, UR_3 = 0$
Amplitude – Denali_Earthquake_0 / Loma Prieta_Earthquake_0

Name – Fixed Except Y
Type – Displacement / Rotation

Step – Seismic (Dynamic, Implicit)

Region – Bottom of base soil of bottommost layer

CSYS – (Global)

Distribution – Uniform

$U_1 = 0$, $U_2 = 1$, $U_3 = 0$, $UR_1 = 0$, $UR_2 = 0$, $UR_3 = 0$

Amplitude – Denali_Earthquake_90 / Loma Prieta_Earthquake_90

We cannot use two boundary conditions (Fixed Except X & Fixed Except Y) for the same Step i.e., Seismic (Dynamic, Implicit), in one model. So, it is advisable to create two different models for two different boundary conditions in the same Step. Alternatively, we can make a copy of the Seismic step as a new step and assign two boundary conditions (Fixed Except X & Fixed Except Y) to the two identical Seismic steps.

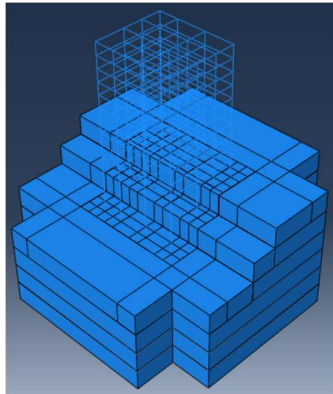


Figure 3.14 - Isometric view of the model used for building without irregularity on sloping ground with shallow foundation

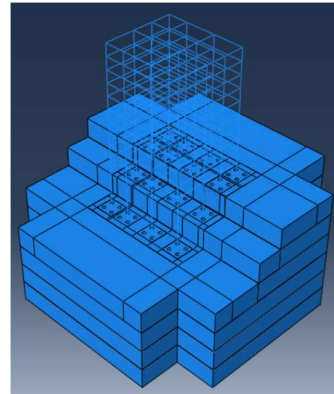


Figure 3.15 - Isometric view of the model used for building without irregularity on sloping ground with pile foundation

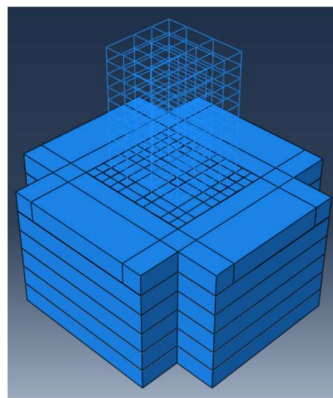


Figure 3.16 - Isometric view of the model used for building without irregularity on plane ground with shallow foundation

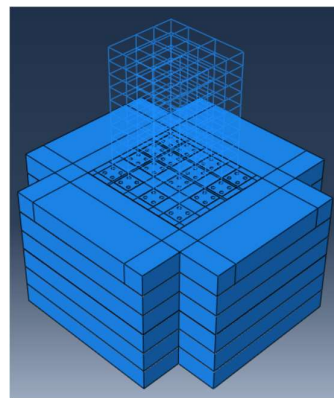


Figure 3.17 - Isometric view of the model used for building without irregularity on plane ground with pile foundation

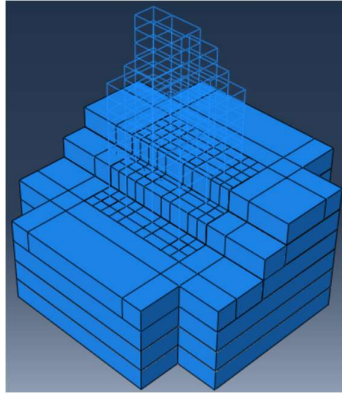


Figure 3.18 - Isometric view of the model used for building with vertical irregularity on sloping ground with shallow foundation

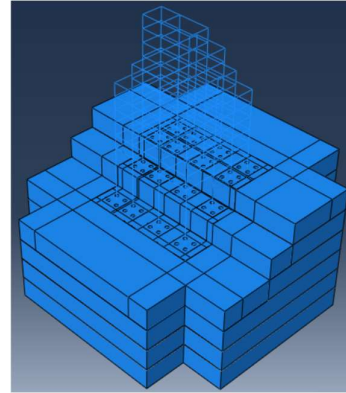


Figure 3.19 - Isometric view of the model used for building with vertical irregularity on sloping ground with pile foundation

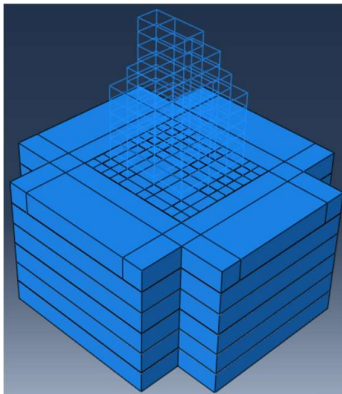


Figure 3.20 - Isometric view of the model used for building with vertical irregularity on plane ground with shallow foundation

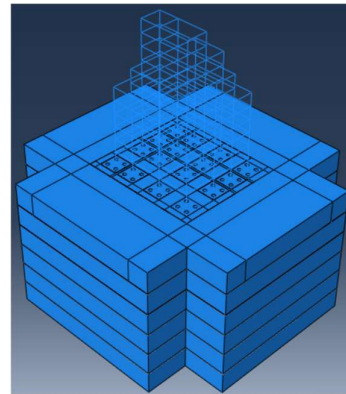


Figure 3.21 - Isometric view of the model used for building with vertical irregularity on plane ground with pile foundation

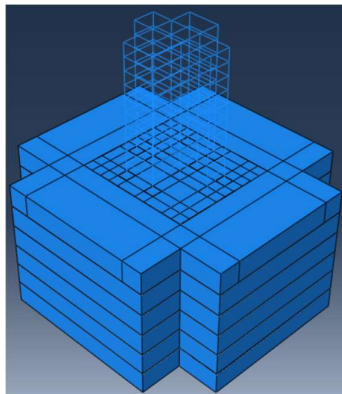


Figure 3.22 - Isometric view of the model used for building with horizontal irregularity on plane ground with shallow foundation

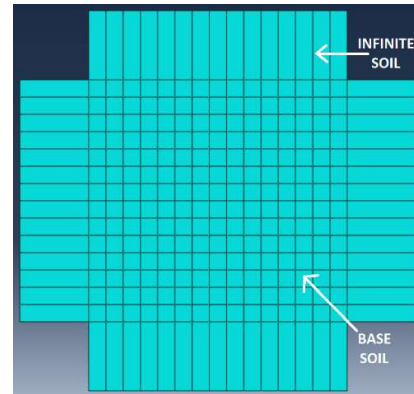


Figure 3.23 - Soil base surrounded by infinite soil

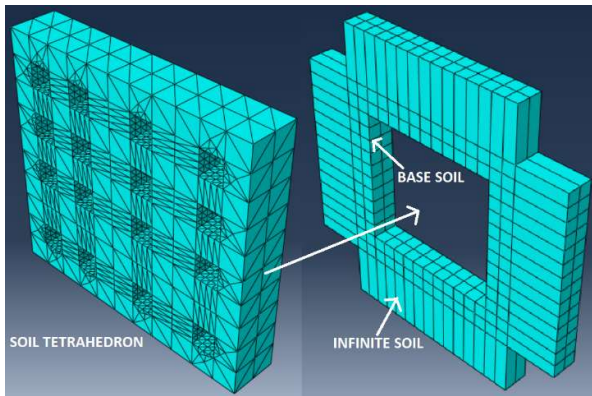


Figure 3.24 - Soil tetrahedron (for isolated footing) embedded in the soil base

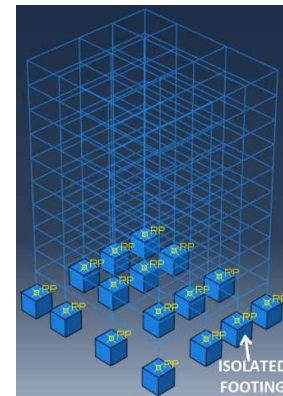


Figure 3.25 - Isolated footing embedded in the soil tetrahedron

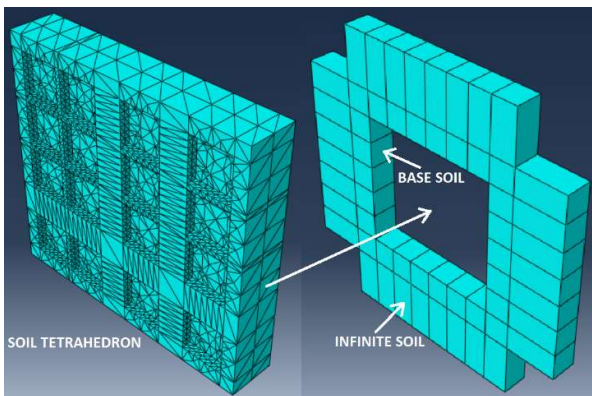


Figure 3.26 - Soil tetrahedron (for pile footing) embedded in the soil base

Models for pile foundation involve finer meshing of the soil layers due to presence of holes in them for the piles. There is no way of coarsening mesh of the soil layers around those holes. Due to this the run time will be extremely high.

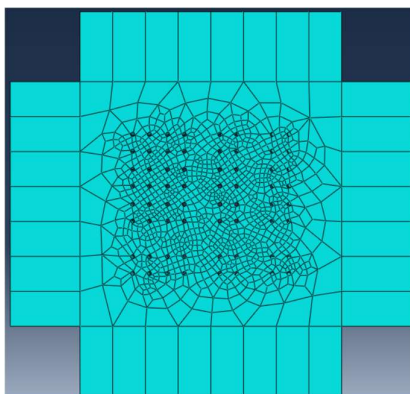


Figure 3.27 - Finer meshing of soil layer surrounding holes for piles

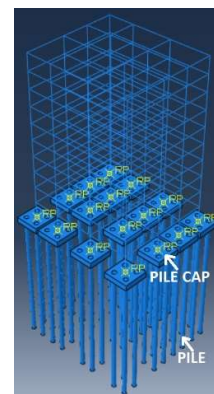


Figure 3.28 - Pile footing embedded in the soil tetrahedron

After preparing all the models, jobs are created. The first step of each job is submitted for analysis to obtain the first mode and fifth mode frequencies. Considering a damping ratio of 0.05, Rayleigh Damping Coefficients α and β are determined for every model using the equations 24 and 25. [67].

$$\beta = \frac{2\xi_1\omega_1 - 2\xi_m\omega_m}{\omega_1^2 - \omega_m^2} \quad \dots(24)$$

$$2\xi\omega_1 = \alpha + \beta\omega_1^2 \quad \dots(25)$$

where,

m = Number of significant modes considered (Here, $m=5$),

ξ_1 = Damping Ratio of the first mode,

ξ_m = Damping Ratio of the m -th mode,

(In this problem, $\xi_1 = \xi_m = \xi$)

ω_1 = Frequency of the first mode,

ω_m = Frequency of the m -th mode.

The modal damping ratio ξ for the soil system would typically be much higher than other civil engineering structures, say 15 to 20%.

In dynamic analysis of structures and foundations, damping plays an important role. However, due to the limitation in our knowledge about damping, the most effective way to treat damping within modal analysis framework is to treat the damping value of a MDOF system as an equivalent Rayleigh Damping in the form:

$$[C] = \alpha[M] + \beta[K] \quad \dots(26)$$

in which $[C]$, $[M]$ and $[K]$ are the damping, mass and stiffness matrix of the physical system respectively; α and β are the predefined constants called Rayleigh damping coefficients. As such, in most of the practical engineering analysis, the analyst makes the simplifying assumptions in selecting damping ratios (constant for all significant modes). It is a fact that modal mass participation decreases with increase in modes. Based on above, one can infer that, as mass participation decreases with higher modes, the frequency increases and it is indeed an observed phenomenon. With reduction in modal mass for successive modes, critical damping will decrease with increase in mode. Overall damping of a system being a constant (since total mass and stiffness are constant for a system), the damping ratio will increase with increasing modes. To incorporate this reality, one option may be to compute the Rayleigh coefficients using the basic formulation incorporating range values for the first significant modes.

Some general values and their effect are listed below:

Table 3.5 shows the first mode frequency, fifth mode frequency and Rayleigh damping coefficients for each possible soil-structure combination.

Table 3.5 - Rayleigh damping coefficients of materials for different soil-structure combinations of uniform soils

SOIL TYPE	STRUCTURE TYPE	FREQUENCY OF 1ST MODE (cps)	FREQUENCY OF 5TH MODE (cps)	DAMPING RATIO (ξ)	RAYLEIGH DAMPING COEFFICIENTS	
					α	β
HARD	MODEL 1	0.74447	2.2912	0.05	0.35305	0.00524
	MODEL 5	0.60505	2.2911	0.05	0.30074	0.00550
	MODEL 6	0.49046	1.1857	0.05	0.21799	0.00950
	MODEL 7	0.88764	2.8106	0.05	0.42386	0.00430
	MODEL 9	0.56275	2.1219	0.05	0.27947	0.00593
MED-IUM	MODEL 1	0.74231	2.1948	0.05	0.34853	0.00542
	MODEL 5	0.60347	2.1686	0.05	0.29663	0.00574
	MODEL 6	0.48881	1.2823	0.05	0.22236	0.00899
	MODEL 7	0.88511	2.2404	0.05	0.39864	0.00509
	MODEL 9	0.56167	2.1348	0.05	0.27940	0.00590
SOFT	MODEL 1	0.71649	1.0983	0.05	0.27245	0.00877
	MODEL 5	0.58807	1.0007	0.05	0.23273	0.01002
	MODEL 6	0.47571	1.1064	0.05	0.20902	0.01006
	MODEL 7	0.84266	1.1192	0.05	0.30205	0.00811
	MODEL 9	0.55176	0.99005	0.05	0.22262	0.01032

***Notes for Table 3.5:

MODEL 1: Vertically irregular with isolated footing on plane ground
 MODEL 2: Vertically irregular with isolated footing on sloping ground
 MODEL 3: Vertically irregular with pile footing on plane ground
 MODEL 4: Vertically irregular with pile footing on sloping ground
 MODEL 5: Regular with isolated footing on plane ground
 MODEL 6: Regular with isolated footing on sloping ground
 MODEL 7: Regular with pile footing on plane ground
 MODEL 8: Regular with pile footing on sloping ground
 MODEL 9: Horizontally irregular with isolated footing on plane ground

These Rayleigh damping coefficient values are added to all the materials except infinite soil (acoustic material) of the respective models in order to get the correct models.

3.4 - INPUT MOTIONS AND THEIR PROPERTIES

Earthquakes are geological phenomena produced by the sudden release of energy in seismic sources, located at different depths (tens of kilometers or hundreds of kilometers), and generate seismic waves. At the ground surface, earthquakes manifest by means of seismic motion, with a duration that can be expressed in terms of seconds (tens of seconds or hundreds of seconds).

F₃ = Focus (hypocenter), theoretical point in which the process of rupture and release of seismic energy is initialized

E₂ = Epicenter, point on ground surface that is connected with the Focus with a vertical line

S = Seismic station, where the accelerograms are recorded

h_F = Focal depth
 R_2 = Hypocentral distance
 d = Epicentral distance

The seismic energy is released in the seismic source and it is transmitted throughout the propagation media by means of propagation waves. The seismic source can be:

- punctual
- linear (linear fault)
- surface like (fault plane)

An accelerogram is a graph that shows the variation of a ground acceleration in time during an earthquake. Accelerograms are recorded in seismic stations, by means of accelerometers, on three different directions:

- north-south (NS)
- east-west (EW)
- up-down (UD)

In order to observe the effect of epicentre distance on dynamic SSI phenomenon, all the models are subjected to a near-field and a far-field earthquake. Loma prieta earthquake, which occurred in 1989, has been taken as a sample from the near-field earthquakes. On the other hand, Denali earthquake (2002) is considered a representative of the far-field earthquakes. We have considered earthquake motion data in two orthogonal directions to study the effect of bidirectional earthquake. Some general properties of Loma prieta and Denali earthquakes are tabulated in Table 3.6.

Table 3.6 - General properties of the earthquakes

Earthquake Name	Loma Prieta	Denali
Year	1989	2002
Station Name	Corralitos, CA	Valdez - Valdez Dock Company
Earthquake Type	Near-Field	Far-Field
Epicenter Distance (Rrup)	2.8 km	239.52 km
Mechanism	Reverse Oblique	Strike Slip
Magnitude	6.93	7.9
Vs30	713.59 m/s	708.02 m/s
Spectral Ordinate	0° & 90°	90° & 360° / 0°
Scale Factor	1	1
Peak Ground Acceleration	0.63 g (0°) & 0.479 g (90°)	0.00974 g (0°) & 0.00872 g (90°)
Peak Ground Velocity	55.196 cm/s (0°) & 47.49 cm/s (90°)	2.228 cm/s (0°) & 2.571 cm/s (90°)
Peak Ground Displacement	9.541 cm (0°) & 11.527 cm (90°)	3.968 cm (0°) & 7.187 cm (90°)

The acceleration time-histories of the above two earthquakes are displayed in the Figures below. respectively. Further, for better understanding of the properties of Loma prieta and Denali earthquakes, velocity time-histories, displacement time-histories, acceleration response spectra, velocity response spectra, displacement response spectra and Fast Fourier Transform (FFT) have been developed for both the earthquakes, which are shown in Figure 3.29 to Figure 3.51.

We have obtained motion data from PEER Ground Motion Database & Strong-Motion Virtual Data Center (VDC).
 PEER Ground Motion Database URL: <https://ngawest2.berkeley.edu/>
 Strong-Motion Virtual Data Center (VDC) URL: <https://www.strongmotioncenter.org/vdc/scripts/default.plx>
 The ground motions were obtained for two horizontal orthogonal directions, 0° and 90°.

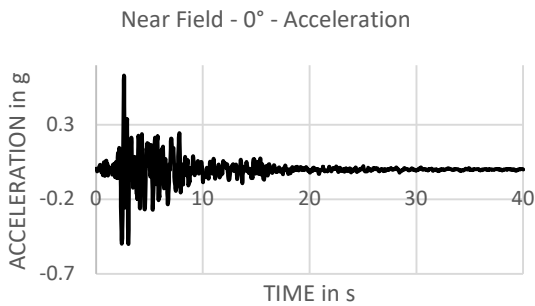


Figure 3.29 - Acceleration time-history of Loma Prieta earthquake for 0°

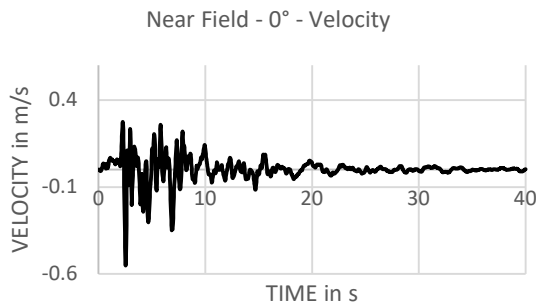


Figure 3.30 - Velocity time-history of Loma Prieta earthquake for 0°

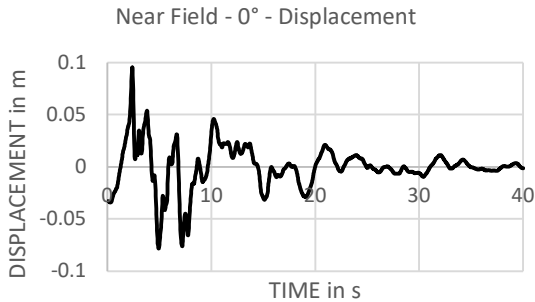


Figure 3.31 - Displacement time-history of Loma Prieta earthquake for 0°

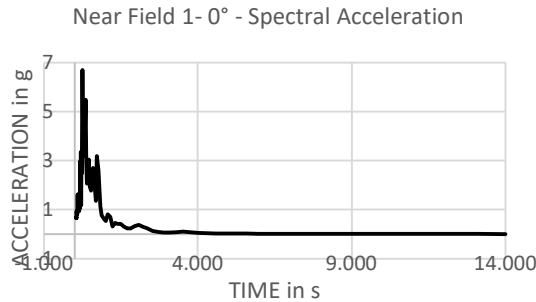


Figure 3.32 - Acceleration response spectra of Loma Prieta earthquake for 0°

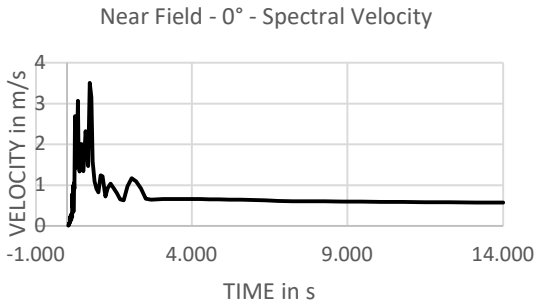


Figure 3.33 - Velocity response spectra of Loma Prieta earthquake for 0°

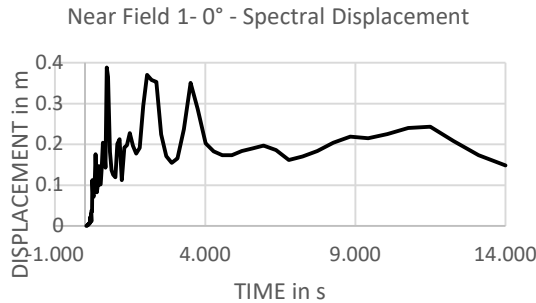


Figure 3.34 - Displacement response spectra of Loma Prieta earthquake for 0°

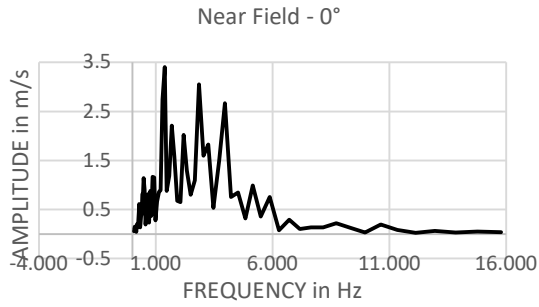


Figure 3.35 - FFT of Loma Prieta earthquake for 0°

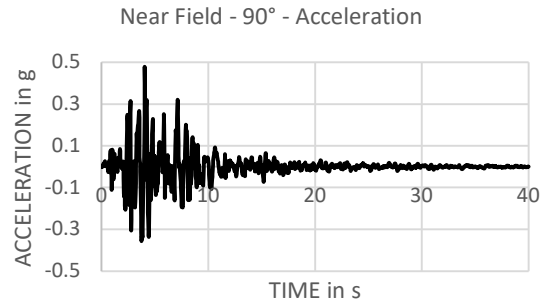


Figure 3.36 - Acceleration time-history of Loma Prieta earthquake for 90°

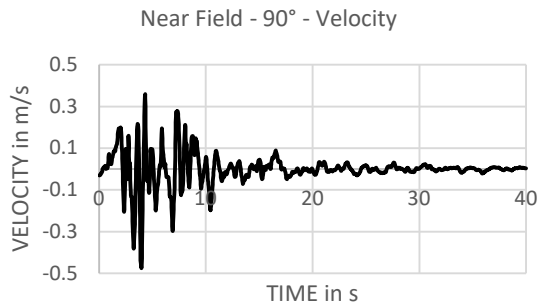


Figure 3.37 - Velocity time-history of Loma Prieta earthquake for 90°

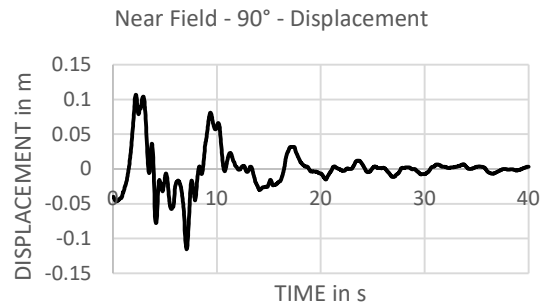


Figure 3.38 - Displacement time-history of Loma Prieta earthquake for 90°

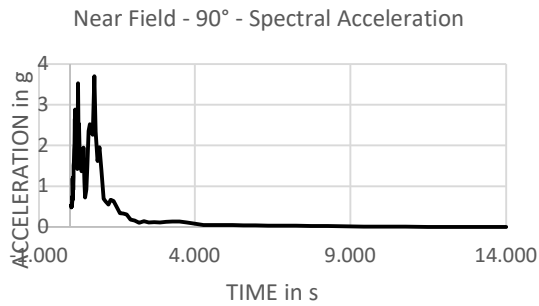


Figure 3.39 - Acceleration response spectra of Loma Prieta earthquake for 90°

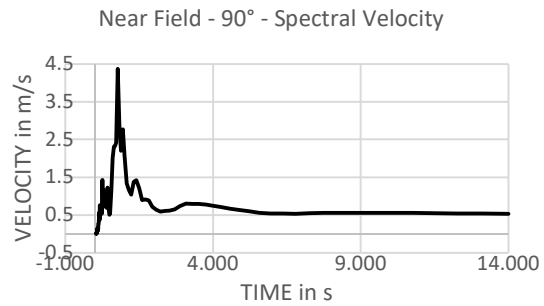


Figure 3.40 - Velocity response spectra of Loma Prieta earthquake for 90°

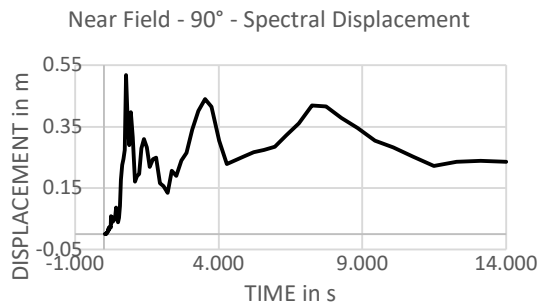


Figure 3.41 - Displacement response spectra of Loma Prieta earthquake for 90°

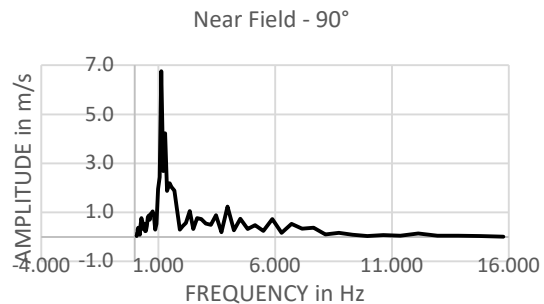


Figure 3.42 - FFT of Loma Prieta earthquake for 90°

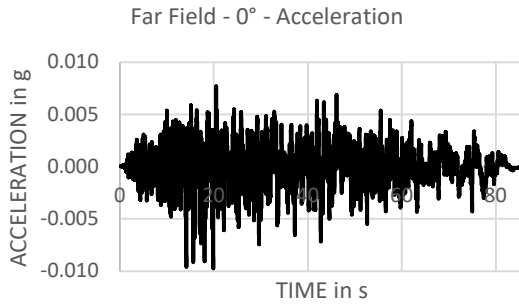


Figure 3.43 - Acceleration time-history of Denali earthquake for 0°

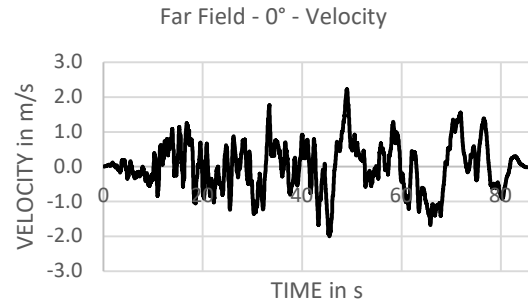


Figure 3.44 - Velocity time-history of Denali earthquake for 0°

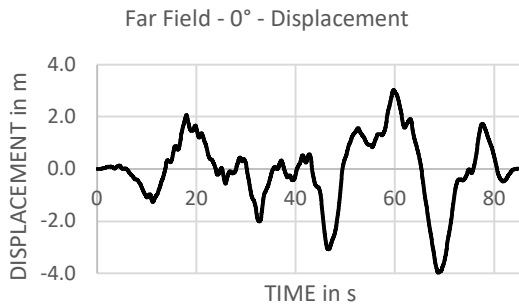


Figure 3.45 - Displacement time-history of Denali earthquake for 0°

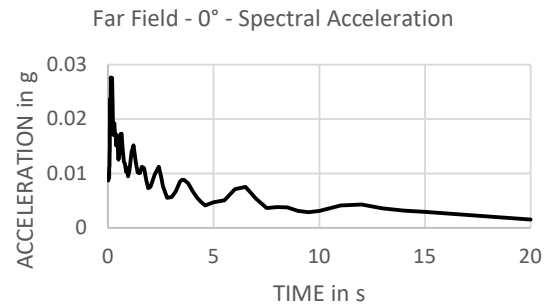


Figure 3.46 - Acceleration response spectra of Denali earthquake for 0°

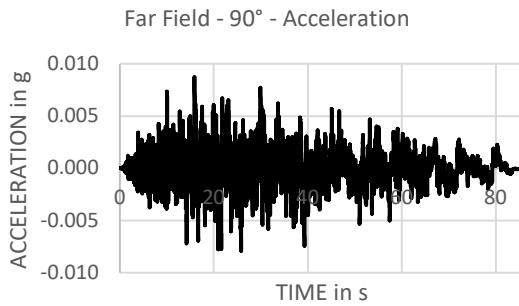


Figure 3.47 - Acceleration time-history of Denali earthquake for 90°

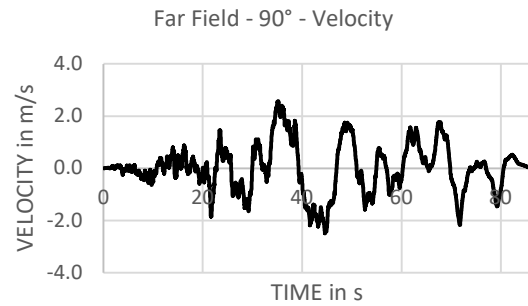


Figure 3.48 - Velocity time-history of Denali earthquake for 90°

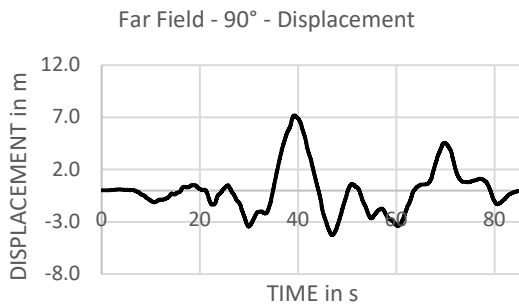


Figure 3.49 - Displacement time-history of Denali earthquake for 90°

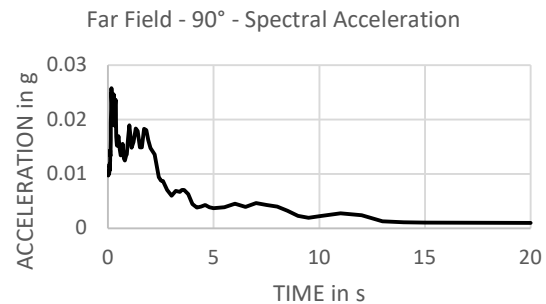


Figure 3.50 - Acceleration response spectra of Denali earthquake for 90°

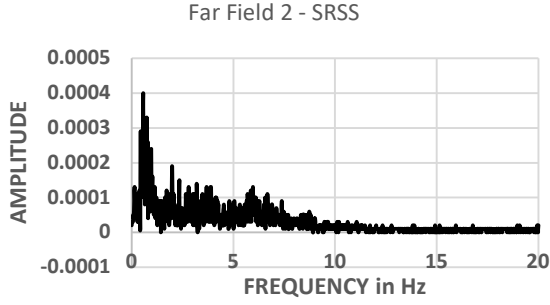


Figure 3.51 - FFT of Denali earthquake for SRSS

3.5 - CHARACTERISTICS OF ACCELEROGRAM ACROSS ORIENTATIONS

This topic has been elaborately discussed in Article 2.5. From Equation 14,

$$\begin{Bmatrix} a_{x(\psi)}(t) \\ a_{y(\psi)}(t) \end{Bmatrix} = \begin{bmatrix} \cos \psi & \sin \psi \\ -\sin \psi & \cos \psi \end{bmatrix} \begin{Bmatrix} a_x(t) \\ a_y(t) \end{Bmatrix}$$

$$a_{x(\psi)}(t) = \cos \psi \cdot a_x(t) + \sin \psi \cdot a_y(t) \quad \dots(27)$$

$$a_{y(\psi)}(t) = -\sin \psi \cdot a_x(t) + \cos \psi \cdot a_y(t) \quad \dots(28)$$

$a_x(t)$, $a_y(t)$ are horizontal components of original record and $a_{x(\psi)}(t)$, $a_{y(\psi)}(t)$ the components of the record when rotated anti-clockwise by an angle ψ . For Loma Prieta near field earthquake:

$$a_x(t) = 0.6300489g$$

$$a_y(t) = 0.47877168g$$

$$a_{SRSS}(t) = \sqrt{a_{x(\psi)}(t)^2 + a_{y(\psi)}(t)^2} \quad \dots(29)$$

$$\begin{aligned} NCI &= a_{x(\psi)}(t) / a_{y(\psi)}(t) \text{ if } a_{x(\psi)}(t) > a_{y(\psi)}(t) \\ &= a_{y(\psi)}(t) / a_{x(\psi)}(t) \text{ if } a_{x(\psi)}(t) < a_{y(\psi)}(t) \end{aligned} \quad \dots(30)$$

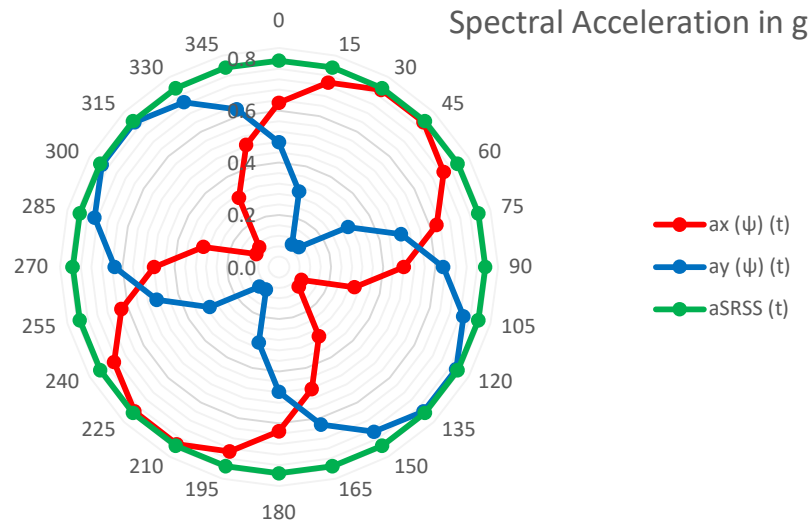


Figure 3.52 - Characteristics of spectral acceleration of accelerogram across orientations
(Event: Loma Prieta Santa Cruz Mountains earthquake, 1989 (NF), Sa)

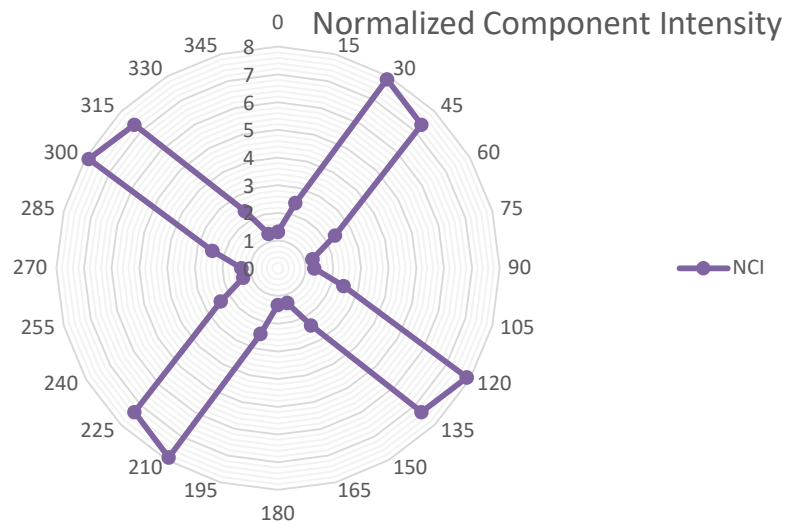


Figure 3.53 - Characteristics of Normalized Component Intensity of accelerogram across orientations (Event: Loma Prieta Santa Cruz Mountains earthquake, 1989 (NF), Sa)

For Denali far field earthquake:

$$a_x(t) = 0.00769811g$$

$$a_y(t) = 0.00871602g$$

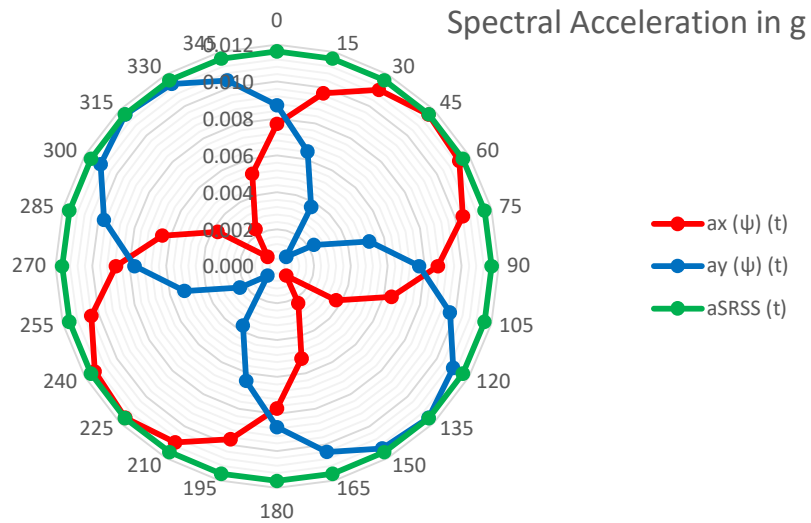


Figure 3.54 - Characteristics of Normalized Component Intensity of accelerogram across orientations (Event: Denali Alaska earthquake, 2002 (FF), Sa)

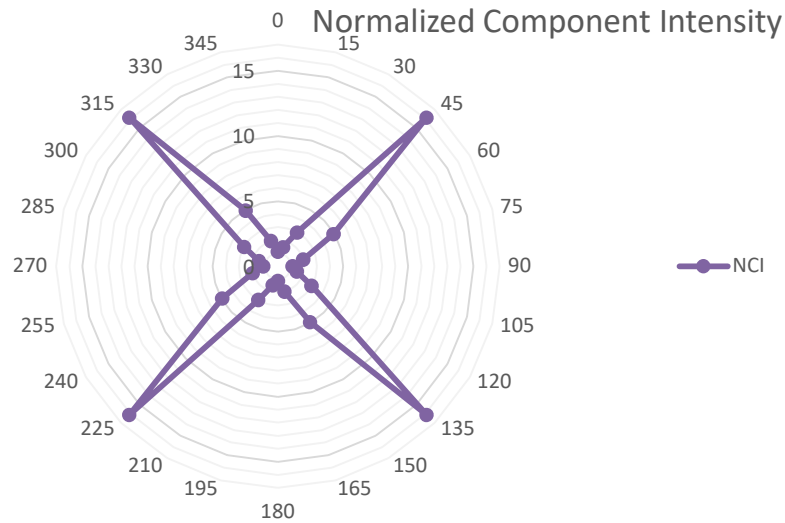


Figure 3.55 - Characteristics of spectral acceleration of accelerogram across orientations
(Event: Denali Alaska earthquake, 2002 (FF), S_a)

Likewise, the variation of characteristic length, L_e with orientations is also studied.

From Equation 18,

$$\log(D_E) = 0.69M_w - 3.70$$

where,

D_E = Effective duration

M_w = Magnitude of earthquake

For Loma Prieta near field earthquake:

$$M_w = 7.0$$

$$\log(D_E) = (0.69 * 7) - 3.7 = 1.13$$

$$D_E = 10^{1.13} = 13.490 \text{ sec}$$

From Equation 15,

$$L_e = \text{characteristic length} = a_g T_m^2$$

where,

a_g = peak ground acceleration

T_m = mean period for real records / effective duration of earthquake strong motion

$$L_{ex} = a_{gx} T_m^2 = a_{x(\psi)} T_m^2 \quad \dots(31)$$

$$L_{ey} = a_{gy} T_m^2 = a_{y(\psi)} T_m^2 \quad \dots(32)$$

$$L_{eSRSS} = a_{gSRSS} T_m^2 = a_{SRSS} T_m^2 \quad \dots(33)$$

$$T_m = D_E = 13.490 \text{ sec}$$

Since characteristic length is linearly dependent on peak ground acceleration, variation of

spectral acceleration and characteristic length will show similar pattern. Equation 30 clearly indicates that. Now we have used Microsoft Excel 2019 to create a polar plot for the above three parameters. In the plot below, characteristic length is expressed in km. The polar coordinate is taken from 0° to 360° at an interval of 15°.

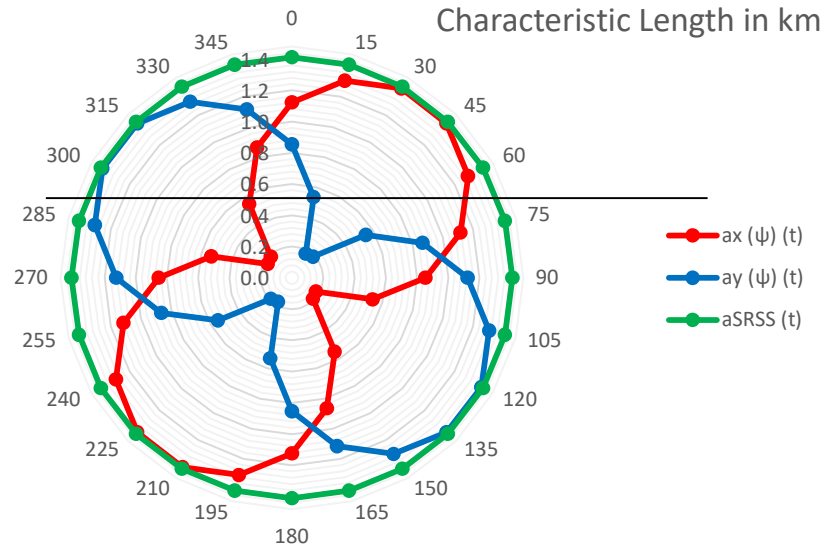


Figure 3.56 - Characteristics of characteristic length of accelerogram across orientations
(Event: Loma Prieta Santa Cruz Mountains earthquake, 1989 (NF), L_e)

For Denali far field earthquake, $M_w = 7.9$. From Equation 18,

$$\log(D_E) = (0.69 * 7.9) - 3.7 = 1.751$$

$$D_E = 10^{1.13} = 56.364 \text{ sec}$$

$$T_m = D_E = 56.364 \text{ sec}$$

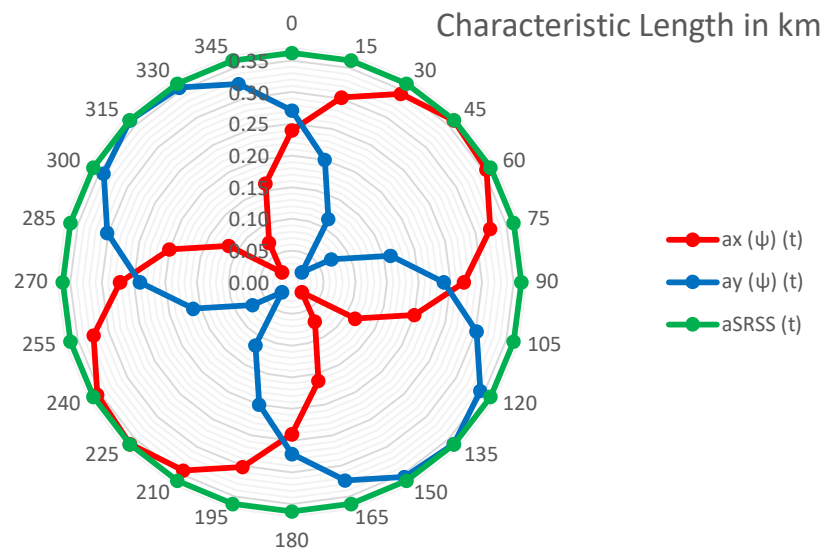


Figure 3.57 - Characteristics of characteristic length of accelerogram across orientations
(Event: Denali Alaska earthquake, 2002 (FF), L_e)

Representative results of spectral acceleration and characteristic length of Loma Prieta and Denali earthquake match with the following characteristics as proposed by Roy et al. [2]:

- Component characteristics appear to interchange over 90 and repeat over 180 as may also be expected from the transformation matrix.
- Ground motion intensity is sensitive to orientations component-wise and relatively stable pair-wise.
- Orientation corresponding to the peak intensity of one component is closely associated with the minimum of the other. Thus, NCI assumes a peak in this orientation.
- There exist certain orientations (intersection points) where intensities for two orthogonal components approach to be proximate. Thus, NCI may approach to minimum in this orientation.

Similarly, other input motion properties such as characteristics intensity and cumulative absolute velocity can be studied which are kept for future scope of study.

3.6 - DISPLACEMENT TIME-HISTORIES OF ROOF AND BASE RESPONSES

The procedure to obtain displacement time history data for different floors from Abaqus is as follows:

1. Run the Job for the Seismic step. Save the .odb file for future.
2. In the Visualization module, open the .odb file created under Output Databases.
3. Click on 'Create XY Data'. Select Source as 'ODB field output' and click on Continue...
4. Click on 'Active Steps/Frames' and deselect the Frequency step. Click on OK.
5. Under Output Variables, choose Position as 'Unique Nodal'.
6. In the checkbox list below, select the 'U1' for getting displacement in X direction, whereas select the 'U2' for getting displacement in Y direction.
7. Under Elements/Nodes Selection, select Method as 'Pick from viewport'. Click on 'Edit Selection' and select the desired nodes from the viewport and click on Done.
8. Click on Save to save the displacement time history data.
9. Go to Report → XY. 'Report XY Data' dialogue box opens.
10. Select all the XY data. Under 'Setup', give a file name and deselect 'Append to file'.
11. The 'Output Format' is given as follows:
 - i. Layout: Single table for all XY data
 - ii. Page width (characters): No limit
 - iii. Number of significant digits: 6
 - iv. Number format: Scientific
12. For 'Data' select Write as XY Data and click on OK. The data will be saved as .rpt file in Output folder of Abaqus.
13. Transfer the data to Microsoft Excel and plot the corresponding graphs.

After performing the entire analysis in Abaqus, displacement time-histories of the roof and the base have been plotted in case of every model. These plots are presented in Figure 3.58 to 3.109. At first the output response data for X direction (as per model) is plotted. Similarly, response data for Y direction (as per model) is plotted for all the cases. Now we applied the 0.4 rule for combining the responses in the two directions for each case. This rule is explained in details in Equation 16. In that equation, we have considered γ as 0.4 or 40%. A typical example of the plots in X and Y directions and subsequent formation of the combined plot from those two is presented for a sample model of regular building

(G+9) with isolated footing on plane ground on hard soil for Denali Earthquake in Figures 3.58 – 3.63. For the rest of the models considered in our study, we have presented only the combined response for bidirectional earthquake, keeping excess information flow in mind. It is important to note that all the responses presented below are corresponding to acceleration time history input normalized to PGA of 1.0g for both the near field and far field earthquakes.

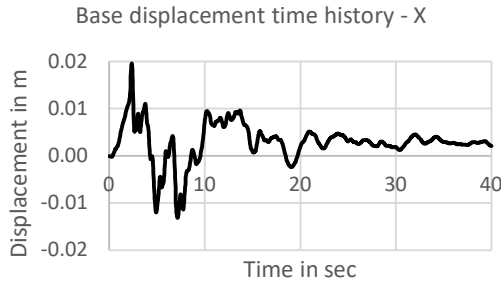


Figure 3.58 - Displacement time-history for base in X direction of a G+9 regular building with isolated footing on hard soil on plane ground under Loma Prieta earthquake

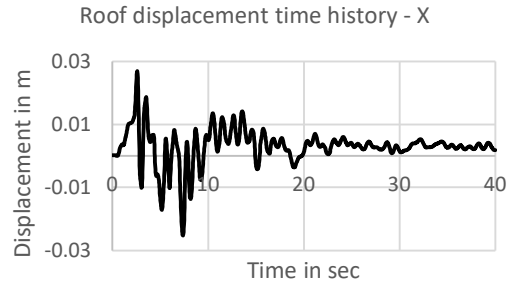


Figure 3.59 - Displacement time-history for roof in X direction of a G+9 regular building with isolated footing on hard soil on plane ground under Loma Prieta earthquake

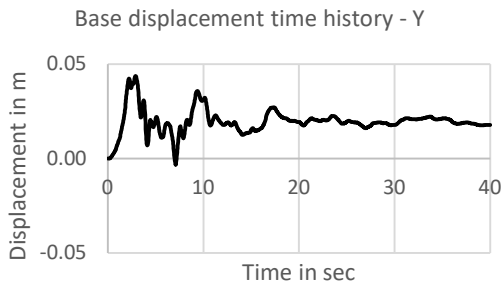


Figure 3.60 - Displacement time-history for base in Y direction of a G+9 regular building with isolated footing on hard soil on plane ground under Loma Prieta earthquake

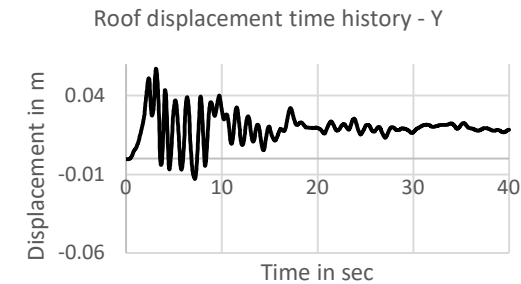


Figure 3.61 - Displacement time-history for roof in Y direction of a G+9 regular building with isolated footing on hard soil on plane ground under Loma Prieta earthquake

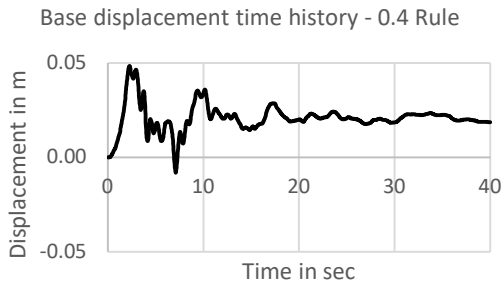


Figure 3.62 – Resultant displacement time-history for base of a G+9 regular building with isolated footing on hard soil on plane ground under Loma Prieta earthquake

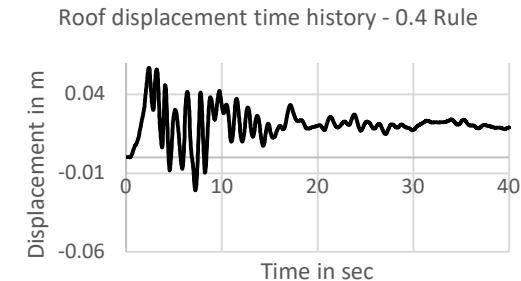


Figure 3.63 – Resultant displacement time-history for roof of a G+9 regular building with isolated footing on hard soil on plane ground under Loma Prieta earthquake

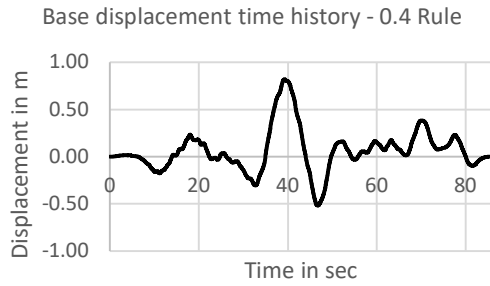


Figure 3.64 – Resultant displacement time-history for base of a G+9 regular building with isolated footing on hard soil on plane ground under Denali earthquake

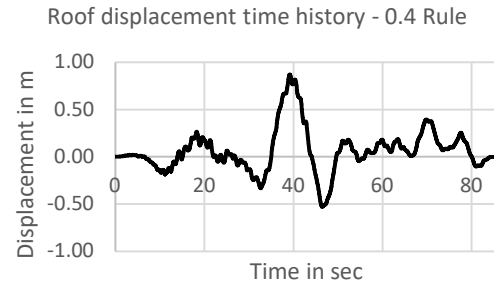


Figure 3.65 – Resultant displacement time-history for roof of a G+9 regular building with isolated footing on hard soil on plane ground under Denali earthquake



Figure 3.66 – Resultant displacement time-history for base of a G+9 vertically irregular building with isolated footing on hard soil on plane ground under Loma Prieta earthquake

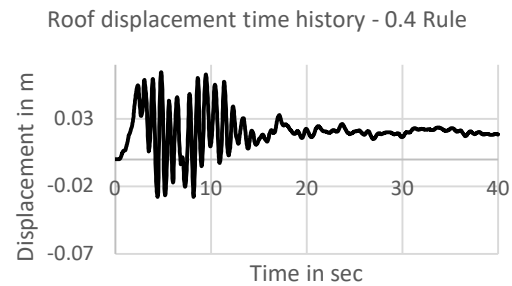


Figure 3.67 – Resultant displacement time-history for roof of a G+9 vertically irregular building with isolated footing on hard soil on plane ground under Loma Prieta earthquake

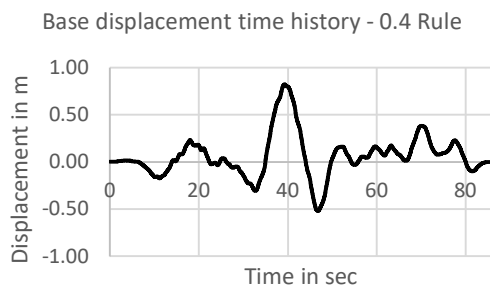


Figure 3.68 – Resultant displacement time-history for base of a G+9 vertically irregular building with isolated footing on hard soil on plane ground under Denali earthquake

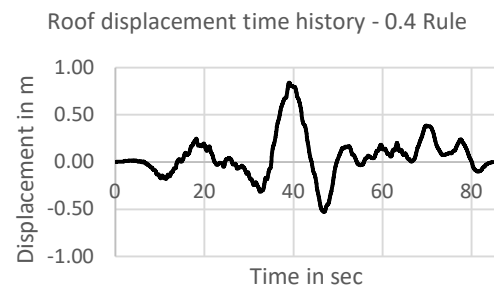


Figure 3.69 – Resultant displacement time-history for roof of a G+9 vertically irregular building with isolated footing on hard soil on plane ground under Denali earthquake

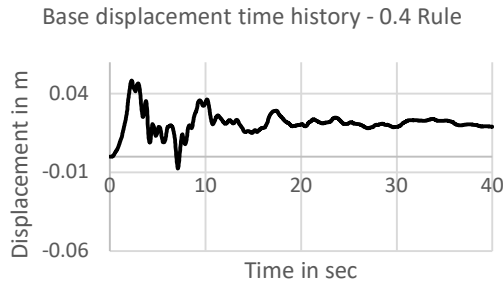


Figure 3.70 – Resultant displacement time-history for base of a G+9 horizontally irregular building with isolated footing on hard soil on plane ground under Loma Prieta earthquake

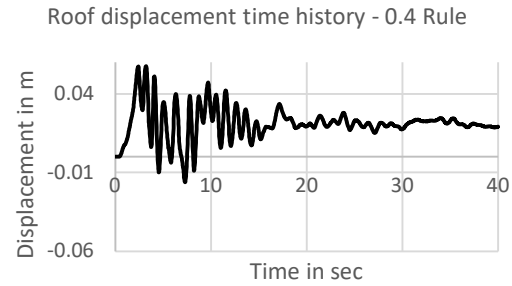


Figure 3.71 – Resultant displacement time-history for roof of a G+9 horizontally irregular building with isolated footing on hard soil on plane ground under Loma Prieta earthquake

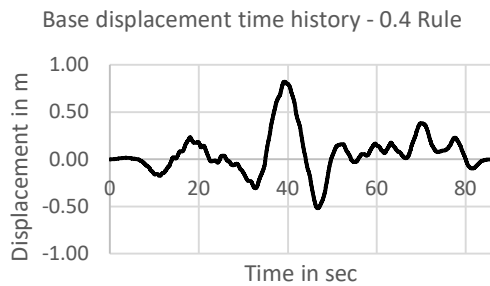


Figure 3.72 – Resultant displacement time-history for base of a G+9 horizontally irregular building with isolated footing on hard soil on plane ground under Denali earthquake

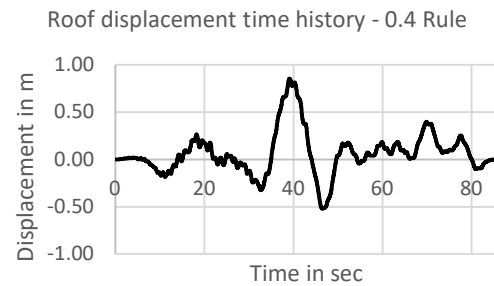


Figure 3.73 – Resultant displacement time-history for roof of a G+9 horizontally irregular building with isolated footing on hard soil on plane ground under Denali earthquake



Figure 3.74 – Resultant displacement time-history for base of a G+9 regular building with isolated footing on hard soil on sloping ground under Loma Prieta earthquake

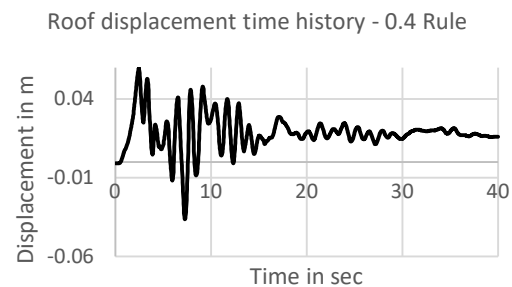


Figure 3.75 – Resultant displacement time-history for roof of a G+9 regular building with isolated footing on hard soil on sloping ground under Loma Prieta earthquake

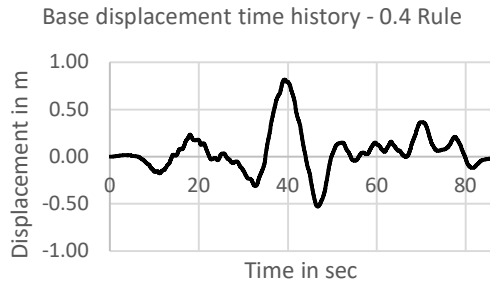


Figure 3.76 – Resultant displacement time-history for base of a G+9 regular building with isolated footing on hard soil on sloping ground under Denali earthquake

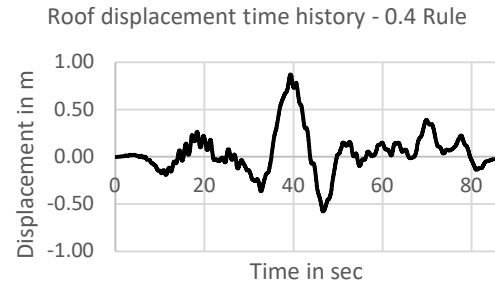


Figure 3.77 – Resultant displacement time-history for roof of a G+9 regular building with isolated footing on hard soil on sloping ground under Denali earthquake



Figure 3.78 – Resultant displacement time-history for base of a G+9 regular building with isolated footing on medium soil on plane ground under Loma Prieta earthquake

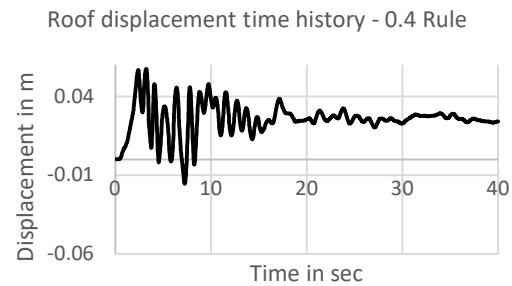


Figure 3.79 – Resultant displacement time-history for roof of a G+9 regular building with isolated footing on medium soil on plane ground under Loma Prieta earthquake

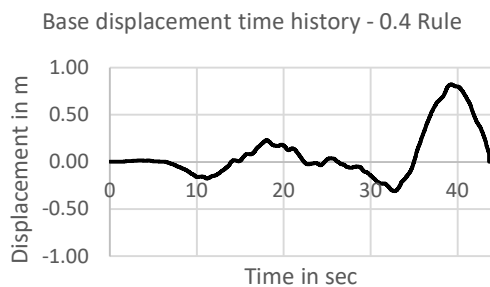


Figure 3.80 – Resultant displacement time-history for base of a G+9 regular building with isolated footing on medium soil on plane ground under Denali earthquake

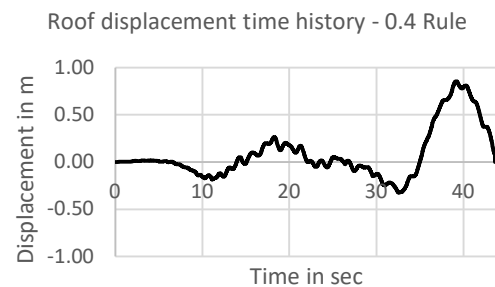


Figure 3.81 – Resultant displacement time-history for roof of a G+9 regular building with isolated footing on medium soil on plane ground under Denali earthquake



Figure 3.82 – Resultant displacement time-history for base of a G+9 vertically irregular building with isolated footing on medium soil on plane ground under Loma Prieta earthquake

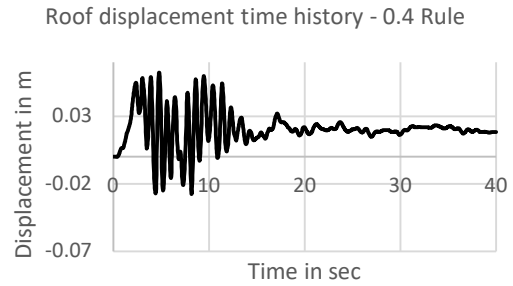


Figure 3.83 – Resultant displacement time-history for roof of a G+9 vertically irregular building with isolated footing on medium soil on plane ground under Loma Prieta earthquake

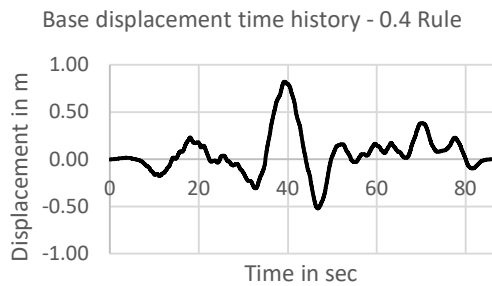


Figure 3.84 – Resultant displacement time-history for base of a G+9 vertically irregular building with isolated footing on medium soil on plane ground under Denali earthquake

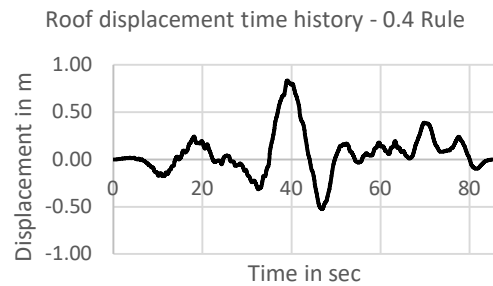


Figure 3.85 – Resultant displacement time-history for roof of a G+9 vertically irregular building with isolated footing on medium soil on plane ground under Denali earthquake

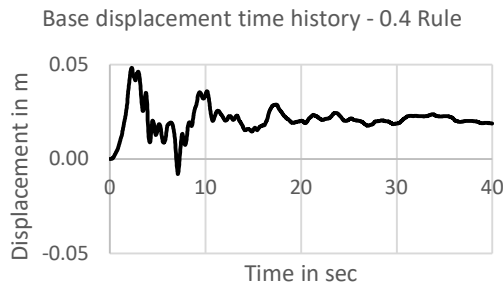


Figure 3.86 – Resultant displacement time-history for base of a G+9 horizontally irregular building with isolated footing on medium soil on plane ground under Loma Prieta earthquake

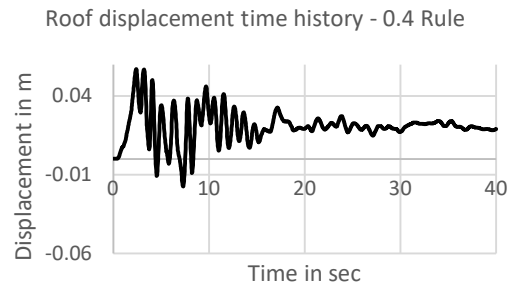


Figure 3.87 – Resultant displacement time-history for roof of a G+9 horizontally irregular building with isolated footing on medium soil on plane ground under Loma Prieta earthquake

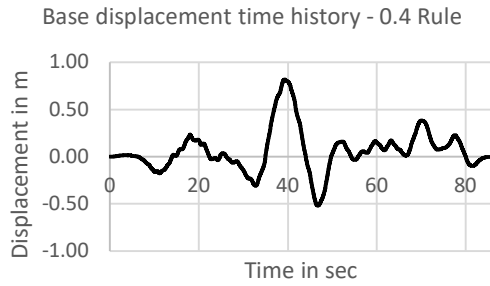


Figure 3.88 – Resultant displacement time-history for base of a G+9 horizontally irregular building with isolated footing on medium soil on plane ground under Denali earthquake

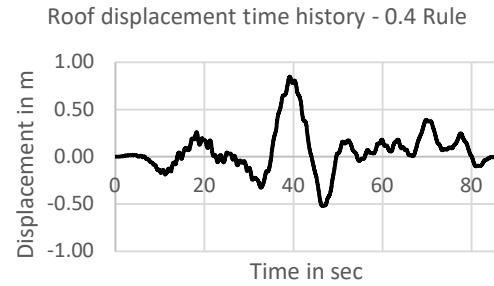


Figure 3.89 – Resultant displacement time-history for roof of a G+9 horizontally irregular building with isolated footing on medium soil on plane ground under Denali earthquake



Figure 3.90 – Resultant displacement time-history for base of a G+9 regular building with isolated footing on medium soil on sloping ground under Loma Prieta earthquake



Figure 3.91 – Resultant displacement time-history for roof of a G+9 regular building with isolated footing on medium soil on sloping ground under Loma Prieta earthquake

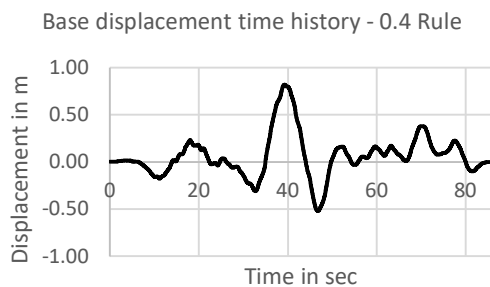


Figure 3.92 – Resultant displacement time-history for base of a G+9 regular building with isolated footing on medium soil on sloping ground under Denali earthquake

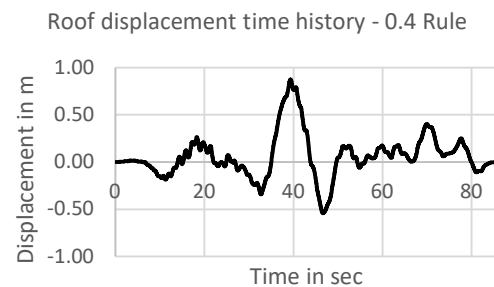


Figure 3.93 – Resultant displacement time-history for roof of a G+9 regular building with isolated footing on medium soil on sloping ground under Denali earthquake

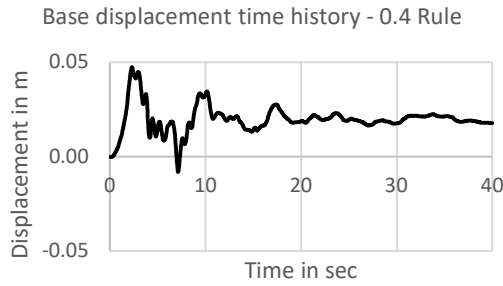


Figure 3.94 – Resultant displacement time-history for base of a G+9 regular building with isolated footing on soft soil on plane ground under Loma Prieta earthquake

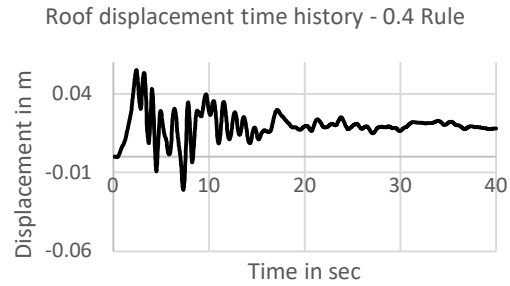


Figure 3.95 – Resultant displacement time-history for roof of a G+9 regular building with isolated footing on soft soil on plane ground under Loma Prieta earthquake

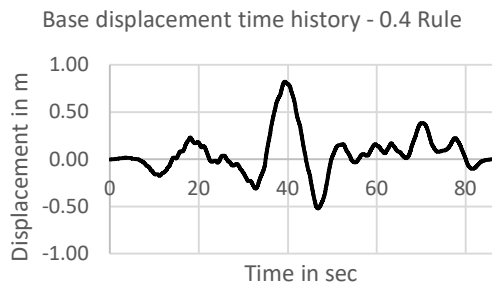


Figure 3.96 – Resultant displacement time-history for base of a G+9 regular building with isolated footing on soft soil on plane ground under Denali earthquake

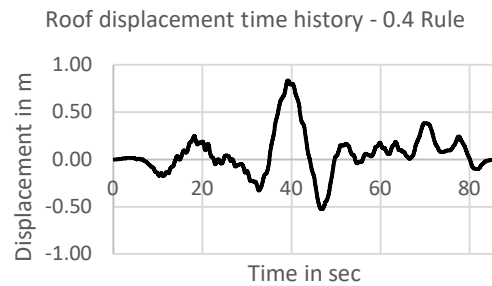


Figure 3.97 – Resultant displacement time-history for roof of a G+9 regular building with isolated footing on soft soil on plane ground under Denali earthquake

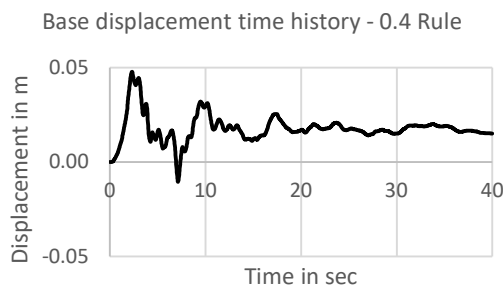


Figure 3.98 – Resultant displacement time-history for base of a G+9 vertically irregular building with isolated footing on soft soil on plane ground under Loma Prieta earthquake

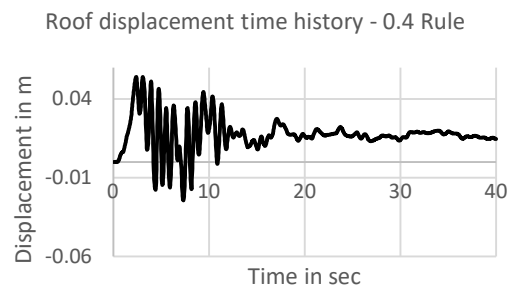


Figure 3.99 – Resultant displacement time-history for roof of a G+9 vertically irregular building with isolated footing on soft soil on plane ground under Loma Prieta earthquake

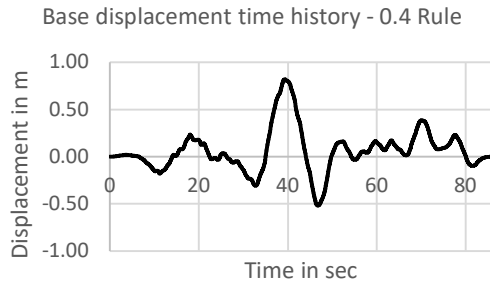


Figure 3.100 – Resultant displacement time-history for base of a G+9 vertically irregular building with isolated footing on soft soil on plane ground under Denali earthquake

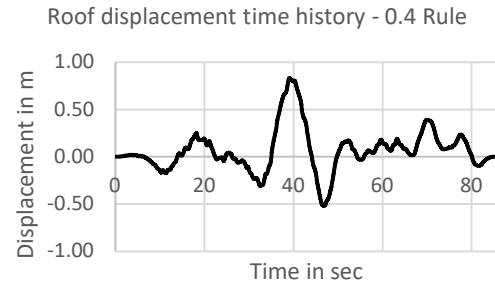


Figure 3.101 – Resultant displacement time-history for roof of a G+9 vertically irregular building with isolated footing on soft soil on plane ground under Denali earthquake

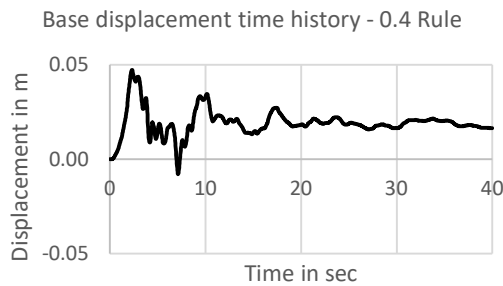


Figure 3.102 – Resultant displacement time-history for base of a G+9 horizontally irregular building with isolated footing on soft soil on plane ground under Loma Prieta earthquake

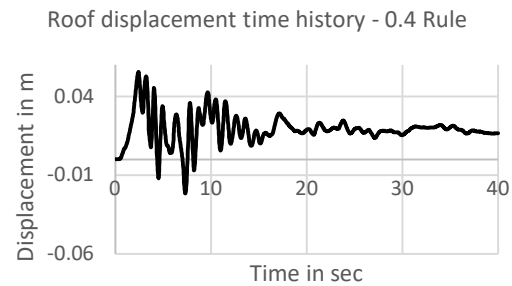


Figure 3.103 – Resultant displacement time-history for roof of a G+9 horizontally irregular building with isolated footing on soft soil on plane ground under Loma Prieta earthquake

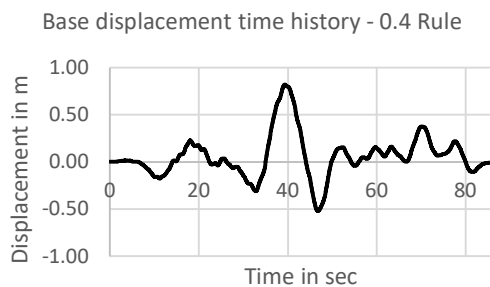


Figure 3.104 – Resultant displacement time-history for base of a G+9 horizontally irregular building with isolated footing on soft soil on plane ground under Denali earthquake

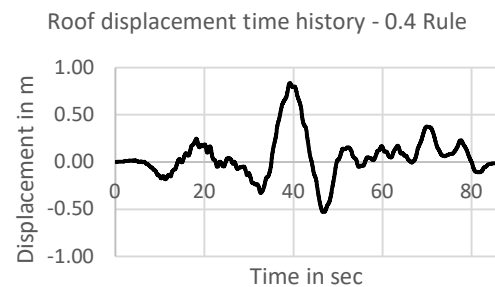


Figure 3.105 – Resultant displacement time-history for roof of a G+9 horizontally irregular building with isolated footing on soft soil on plane ground under Denali earthquake

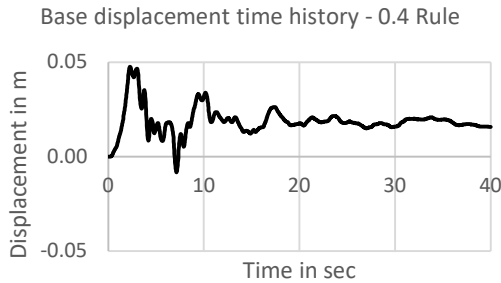


Figure 3.106 – Resultant displacement time-history for base of a G+9 regular building with isolated footing on soft soil on sloping ground under Loma Prieta earthquake



Figure 3.107 – Resultant displacement time-history for roof of a G+9 regular building with isolated footing on soft soil on sloping ground under Loma Prieta earthquake

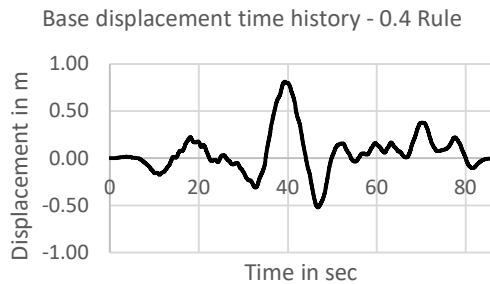


Figure 3.108 – Resultant displacement time-history for base of a G+9 regular building with isolated footing on soft soil on sloping ground under Denali earthquake

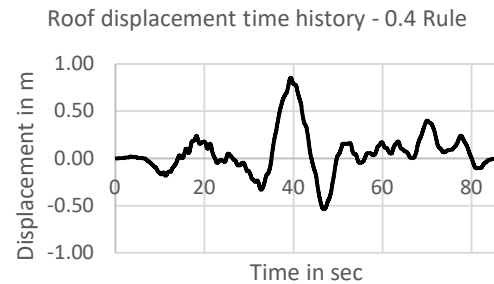


Figure 3.109 – Resultant displacement time-history for roof of a G+9 regular building with isolated footing on soft soil on sloping ground under Denali earthquake

The base response under the action of a particular earthquake differs mainly due to the variation in soil properties. It is to be mentioned that for most cases, when a particular building is subjected to a certain earthquake, roof drift is the highest when the building is located on hard soil. On the contrary, when the building rests on soft soil, roof displacement is the least. This may be due to higher flexibility effect of soft soil. Further, the response of roof due to a far-field earthquake is more than the response of roof due to a near-field earthquake. This may be due to presence of low frequency wave in the far field ground motion. The displacement time history pattern varies considerably for near field and far field earthquake because of wide variation in the acceleration time history of the two earthquakes.

3.7 - MAXIMUM DISPLACEMENT PROFILES

The maximum displacements of all the floors of each model are determined from the displacement time-history data of the respective floor. These values are plotted accordingly to obtain the maximum displacement profile of every building. These plots are shown in Figure 3.110 to 3.119. At first the maximum response data for X direction (as

per model) is plotted. Similarly, maximum response data for Y direction (as per model) is plotted for all the cases. Now we applied the 0.4 rule for combining the time history responses in the two directions for each case and plot the corresponding maximum response data from the combined time history data thus obtained. In Equation 16, we have considered γ as 0.4 or 40%.

A typical example of the maximum displacement plots in X and Y directions and subsequent formation of the combined plot from those two is presented for a sample model of regular building (G+9) with isolated footing on plane ground on hard soil for Denali Earthquake in Figures 3.110 – 3.112. For the rest of the models considered in our study, we have presented only the combined maximum response for bidirectional earthquake, keeping excess information flow in mind. It is important to note that all the responses presented below are corresponding to acceleration time history input normalized to PGA of 1.0g for both the near field and far field earthquakes.

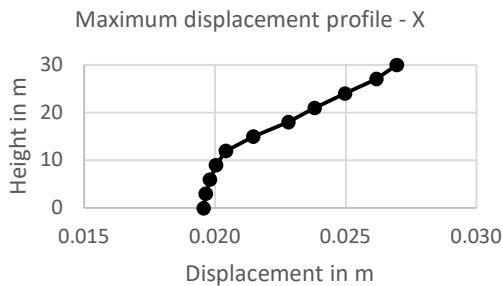


Figure 3.110 - Maximum displacements of different floors in X direction of a G+9 regular building with isolated footing on hard soil on plane ground under Loma Prieta earthquake

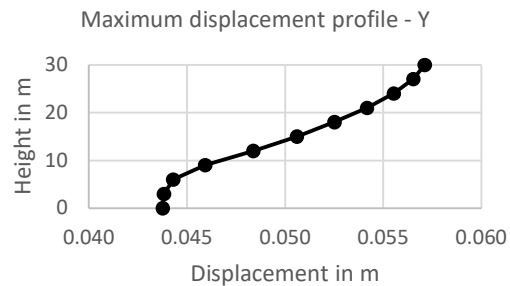


Figure 3.111 - Maximum displacements of different floors in Y direction of a G+9 regular building with isolated footing on hard soil on plane ground under Loma Prieta earthquake

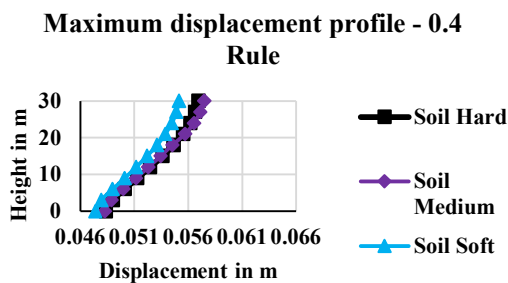


Figure 3.112 – Resultant maximum displacements of different floors of a G+9 regular building with isolated footing on plane ground under Loma Prieta earthquake

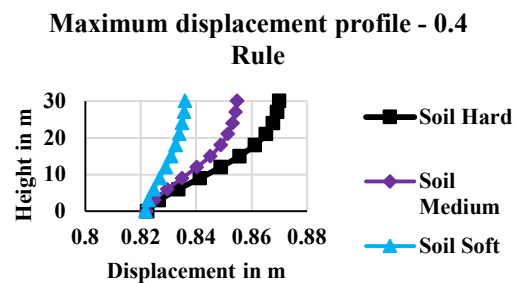


Figure 3.113 – Resultant maximum displacements of different floors of a G+9 regular building with isolated footing on plane ground under Denali earthquake

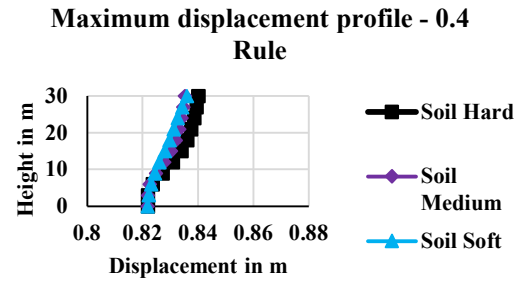
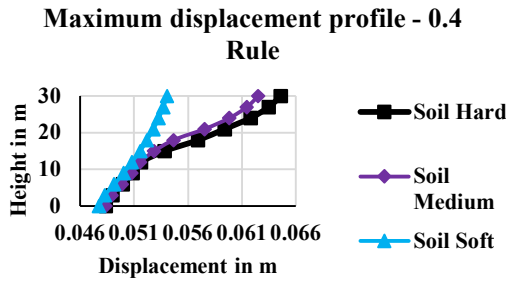


Figure 3.114 – Resultant maximum displacements of different floors of a G+9 vertically irregular building with isolated footing on plane ground under Loma Prieta earthquake

Figure 3.115 – Resultant maximum displacements of different floors of a G+9 vertically irregular building with isolated footing on plane ground under Denali earthquake

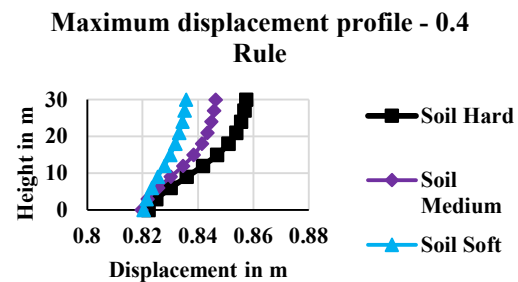
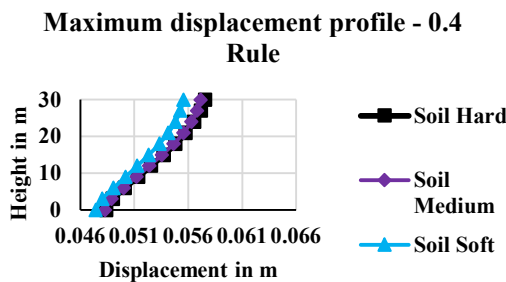


Figure 3.116 – Resultant maximum displacements of different floors of a G+9 horizontally irregular building with isolated footing on plane ground under Loma Prieta earthquake

Figure 3.117 – Resultant maximum displacements of different floors of a G+9 horizontally irregular building with isolated footing on plane ground under Denali earthquake

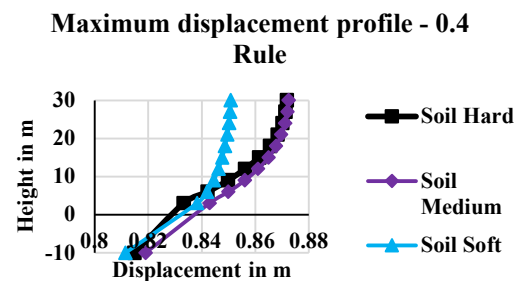
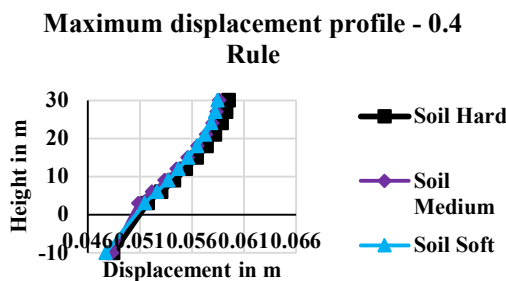


Figure 3.118 – Resultant maximum displacements of different floors of a G+9 regular building with isolated footing on sloping ground under Loma Prieta earthquake

Figure 3.119 – Resultant maximum displacements of different floors of a G+9 regular building with isolated footing on sloping ground under Denali earthquake

The figures clearly depict that, when a G+9 building is subjected to a far-field or near-field earthquake, its maximum displacement profile is concave upward. The shape of the maximum displacement profile strictly depends on the type of structure and soil. Vertical irregular building tends to deflect more compared to other building types for near field earthquake. On the contrary, for far field earthquake, vertical irregular building tends to

deflect least compared to other building types. For both far field and near field earthquake, deflection decreases from hard soil to soft soil. Finally, it is seen that the response of roof due to a far-field earthquake is more than the response of roof due to a near-field earthquake.

3.8 - MAXIMUM DRIFT PROFILES

Drift is a very important parameter in assessing the damage extent of a structure under earthquake. Definition and importance of drift are illustrated in Article 2.3.

At first the maximum response data for X direction (as per model) is plotted. Similarly, maximum response data for Y direction (as per model) is plotted for all the cases. Now we applied the 0.4 rule for combining the time history responses in the two directions for each case and thus obtained maximum drifts for all the floors in percentage.

A typical example of the maximum drift percentage plots in X and Y directions and subsequent formation of the combined plot from those two is presented for a sample model of regular building (G+9) with isolated footing on plane ground on hard soil for Denali Earthquake in Figures 3.120 – 3.122. For the rest of the models considered in our study, we have presented only the combined maximum drift percentage for bidirectional earthquake, keeping excess information flow in mind.

It is important to note that all the responses presented below are corresponding to acceleration time history input normalized to PGA of 1.0g for both the near field and far field earthquakes.

From equation 6, we get,

Drift in percentage of i^{th} floor w.r.t. $(i-1)^{\text{th}}$ floor = $(\text{displacement of } i^{\text{th}} \text{ floor} - \text{displacement of } (i-1)^{\text{th}} \text{ floor} / \text{height between } i^{\text{th}} \text{ floor and } (i-1)^{\text{th}} \text{ floor}) * 100$

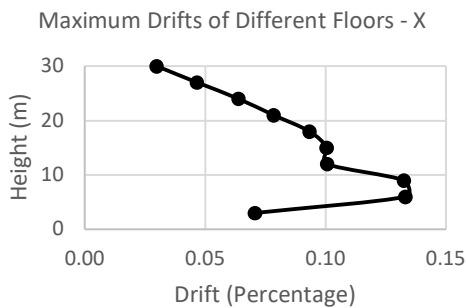


Figure 3.120 - Maximum drifts of different floors in X direction of a G+9 regular building with isolated footing on hard soil on plane ground under Loma Prieta earthquake

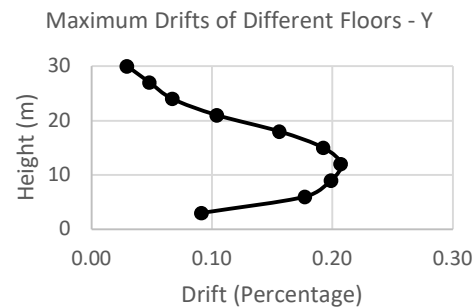


Figure 3.121 - Maximum drifts of different floors in Y direction of a G+9 regular building with isolated footing on hard soil on plane ground under Loma Prieta earthquake

**Maximum Drifts of Different Floors
- 0.4 Rule**

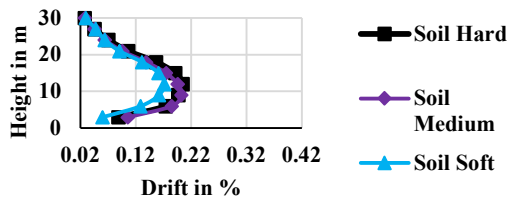


Figure 3.122 – Resultant maximum drifts of different floors of a G+9 regular building with isolated footing on plane ground under Loma Prieta earthquake

**Maximum Drifts of Different Floors -
0.4 Rule**

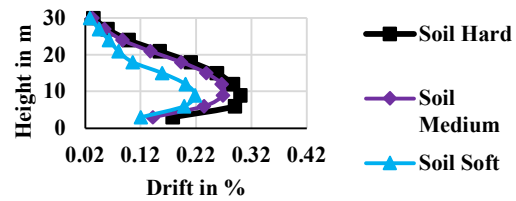


Figure 3.123 – Resultant maximum drifts of different floors of a G+9 regular building with isolated footing on plane ground under Denali earthquake

**Maximum Drifts of Different Floors
- 0.4 Rule**

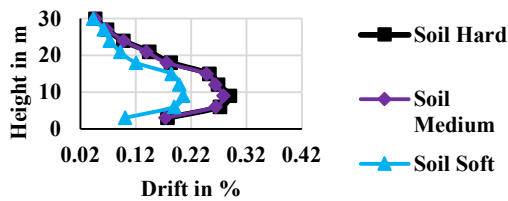


Figure 3.124 – Resultant maximum drifts of different floors of a G+9 vertically irregular building with isolated footing on plane ground under Loma Prieta earthquake

**Maximum Drifts of Different Floors -
0.4 Rule**

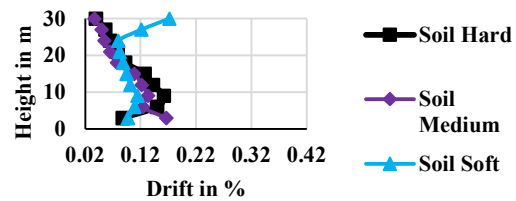


Figure 3.125 – Resultant maximum drifts of different floors of a G+9 vertically irregular building with isolated footing on plane ground under Denali earthquake

**Maximum Drifts of Different Floors
- 0.4 Rule**

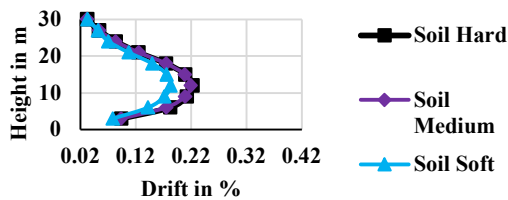


Figure 3.126 – Resultant maximum drifts of different floors of a G+9 horizontally irregular building with isolated footing on plane ground under Loma Prieta earthquake

**Maximum Drifts of Different Floors -
0.4 Rule**

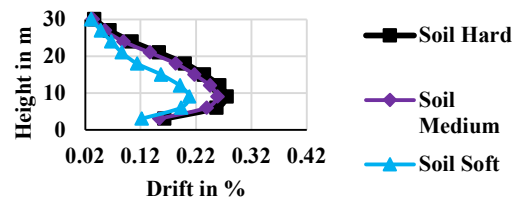


Figure 3.127 – Resultant maximum drifts of different floors of a G+9 horizontally irregular building with isolated footing on plane ground under Denali earthquake

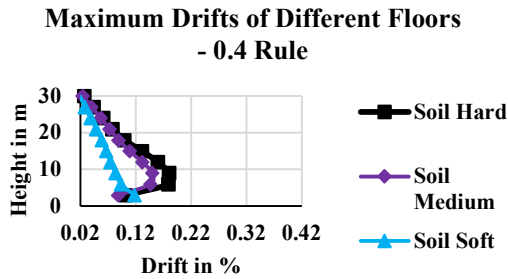


Figure 3.128 – Resultant maximum drifts of different floors of a G+9 regular building with isolated footing on sloping ground under Loma Prieta earthquake

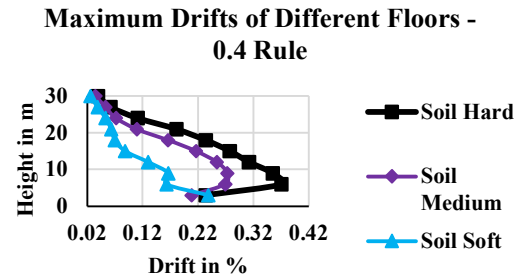


Figure 3.129 – Resultant maximum drifts of different floors of a G+9 regular building with isolated footing on sloping ground under Denali earthquake

After studying the maximum drift curves, the following points can be concluded. Generally maximum drift is obtained in 2nd, 3rd and 4th floors in most of the cases of a G+9 building. As an exception maximum drift is obtained in 1st floor in cases of vertically irregular building on medium soil under far field earthquake, regular building on soft soil on sloping ground under near field earthquake and far field earthquake. Another huge exception is observed in case of vertically irregular building on soft soil under far field earthquake where maximum drift is obtained at roof. In most cases drift due to far field earthquake is more than due to near field earthquake. The variation in the pattern of the acceleration time histories quite well explains the phenomenon. However, in cases of vertically irregular buildings, drift due to far field earthquake is less than due to near field earthquake. Maximum drifts are observed in vertical irregular building as compared to other types of G+9 building structures in case of near field earthquake. In case of far field earthquake, generally, maximum drifts are observed in regular building as compared to other types of G+9 building structures.

3.9 - FRAGILITY CURVES

A detailed overview about the fragility curves along with different methods of plotting them has already been presented in Chapter 2 of this thesis. In this chapter at first PSDMs, for all the models, are developed from the percentage roof drifts. Thereafter, 2000 SAC/FEMA method [68] has been used for plotting the fragility curves considering IO, LS, CP and Indian Codal Limit. The PSDMs and fragility curves for all the models are shown in Figure 3.130 to 3.154.

After analyzing the PSDMs and fragility curves of frame buildings resting on uniform soil, several important remarks have been made. All the PSDMs are straight line in nature, which passes through the origin. The steep slope of the PSDM curve indicates the probability of exceeding the prescribed limit state (IO, LS, CP or Indian Codal Limit) under a specific earthquake intensity (in terms of PGA). Further, it is obvious that under a particular earthquake, the probability of exceeding Indian Codal Limit is the maximum and that of Collapse Prevention is the minimum. It has the largest probability of exceeding a limit state when located on soft soil. However, it should also be noted that in case of most G+9 building configurations, the probability of exceedance of a specific limit state for that soil-structure system is less when it is subjected to a near-field earthquake. Exceptionally, for vertically irregular building, the probability of exceedance value of the

soil-structure system will be greater under the influence of near-field earthquake. Highest probability of exceedance value of the soil-structure system is seen in case of building on sloping ground as compared to building on plane ground. Almost in all cases, the graph for CP is extremely flat almost touching the baseline.

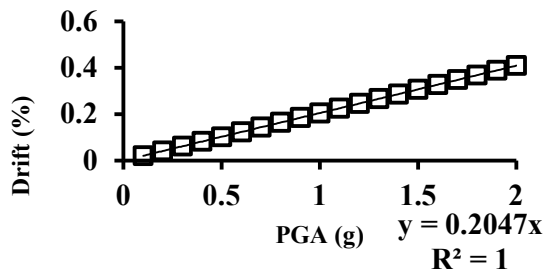


Figure 3.130 – PSDM for a G+9 regular building with isolated footing on hard soil on plane ground under Loma Prieta earthquake

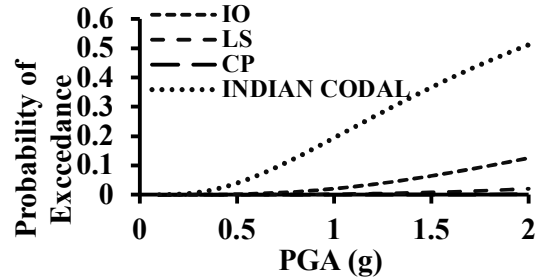


Figure 3.131 – Fragility curves for roof of a G+9 regular building with isolated footing on hard soil on plane ground under Loma Prieta earthquake

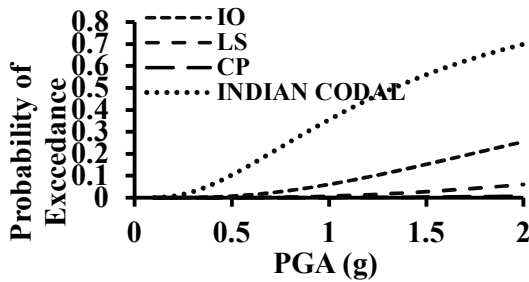


Figure 3.132 – Fragility curves for roof of a G+9 regular building with isolated footing on hard soil on plane ground under Denali earthquake

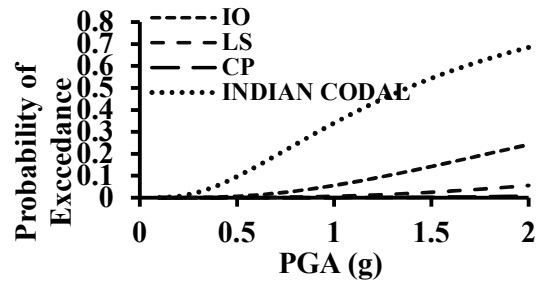


Figure 3.133 – Fragility curves for roof of a G+9 vertically irregular building with isolated footing on hard soil on plane ground under Loma Prieta earthquake

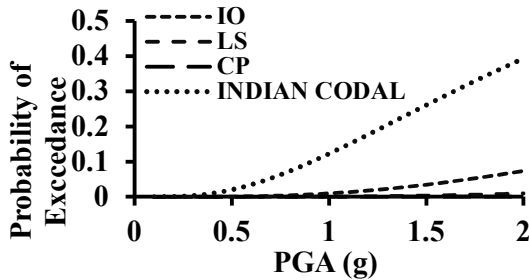


Figure 3.134 – Fragility curves for roof of a G+9 vertically irregular building with isolated footing on hard soil on plane ground under Denali earthquake

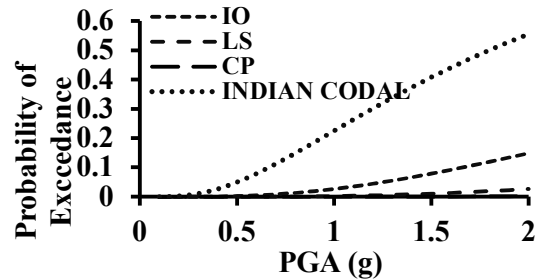


Figure 3.135 – Fragility curves for roof of a G+9 horizontally irregular building with isolated footing on hard soil on plane ground under Loma Prieta earthquake

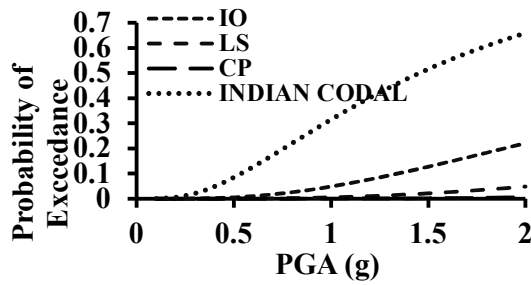


Figure 3.136 – Fragility curves for roof of a G+9 horizontally irregular building with isolated footing on hard soil on plane ground under Denali earthquake

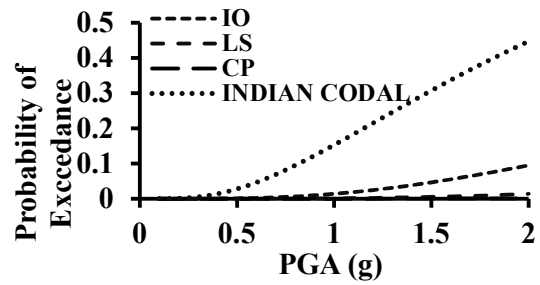


Figure 3.137 – Fragility curves for roof of a G+9 regular building with isolated footing on hard soil on sloping ground under Loma Prieta earthquake

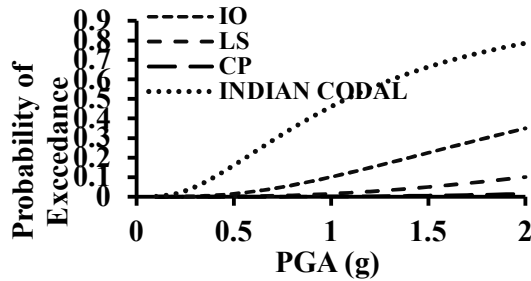


Figure 3.138 – Fragility curves for roof of a G+9 regular building with isolated footing on hard soil on sloping ground under Denali earthquake

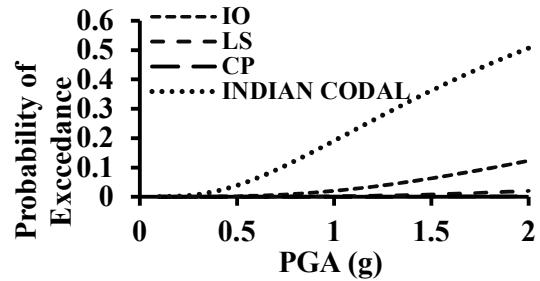


Figure 3.139 – Fragility curves for roof of a G+9 regular building with isolated footing on medium soil on plane ground under Loma Prieta earthquake

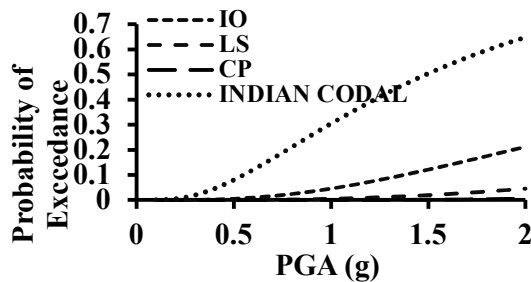


Figure 3.140 – Fragility curves for roof of a G+9 regular building with isolated footing on medium soil on plane ground under Denali earthquake

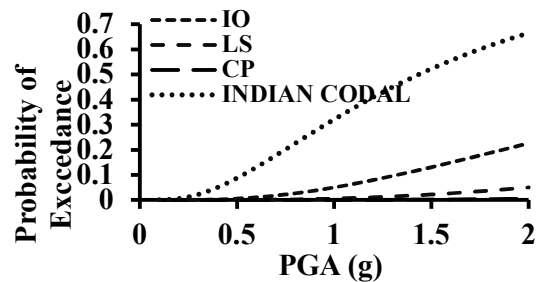


Figure 3.141 – Fragility curves for roof of a G+9 vertically irregular building with isolated footing on medium soil on plane ground under Loma Prieta earthquake

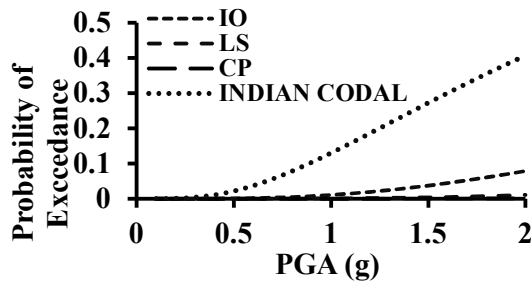


Figure 3.142 – Fragility curves for roof of a G+9 vertically irregular building with isolated footing on medium soil on plane ground under Denali earthquake

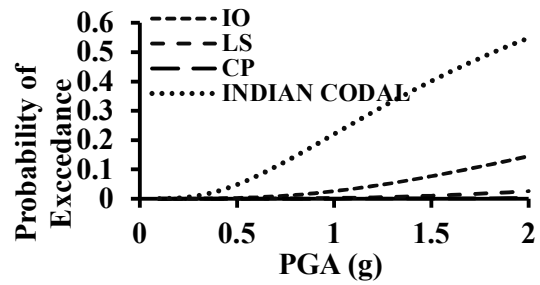


Figure 3.143 – Fragility curves for roof of a G+9 horizontally irregular building with isolated footing on medium soil on plane ground under Loma Prieta earthquake

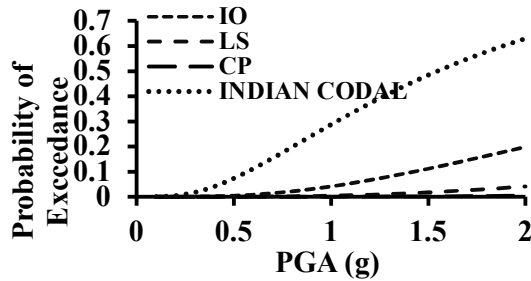


Figure 3.144 – Fragility curves for roof of a G+9 horizontally irregular building with isolated footing on medium soil on plane ground under Denali earthquake

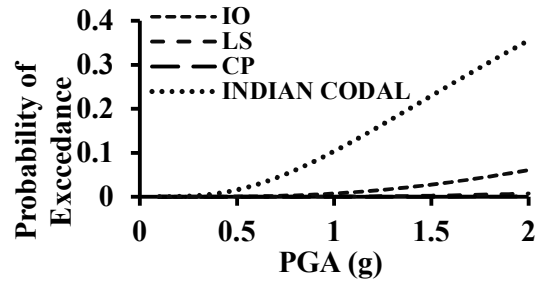


Figure 3.145 – Fragility curves for roof of a G+9 regular building with isolated footing on medium soil on sloping ground under Loma Prieta earthquake

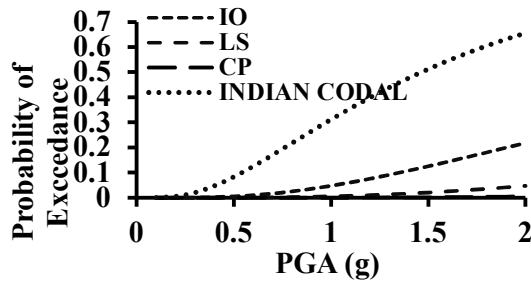


Figure 3.146 – Fragility curves for roof of a G+9 regular building with isolated footing on medium soil on sloping ground under Denali earthquake

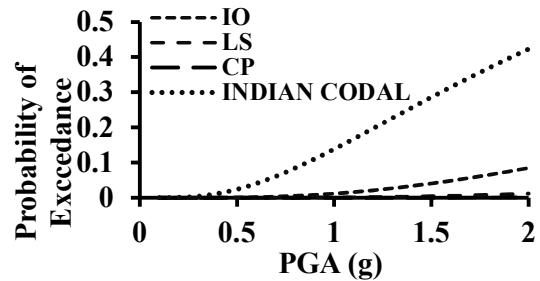


Figure 3.147 – Fragility curves for roof of a G+9 regular building with isolated footing on soft soil on plane ground under Loma Prieta earthquake

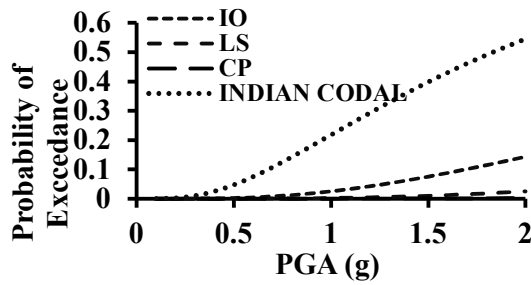


Figure 3.148 – Fragility curves for roof of a G+9 regular building with isolated footing on soft soil on plane ground under Denali earthquake

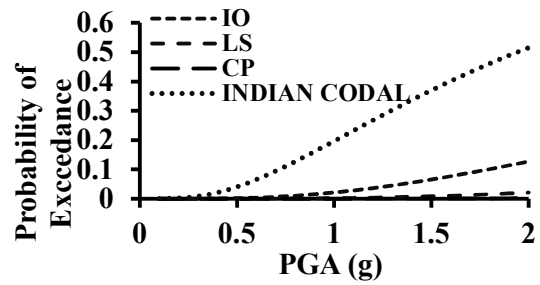


Figure 3.149 – Fragility curves for roof of a G+9 vertically irregular building with isolated footing on soft soil on plane ground under Loma Prieta earthquake

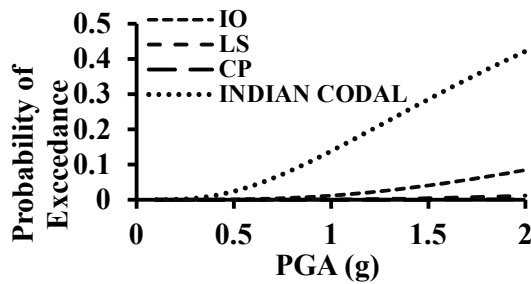


Figure 3.150 – Fragility curves for roof of a G+9 vertically irregular building with isolated footing on soft soil on plane ground under Denali earthquake

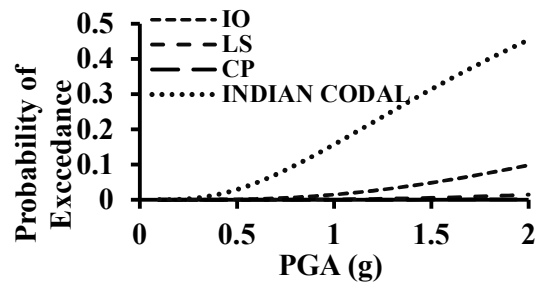


Figure 3.151 – Fragility curves for roof of a G+9 horizontally irregular building with isolated footing on soft soil on plane ground under Loma Prieta earthquake

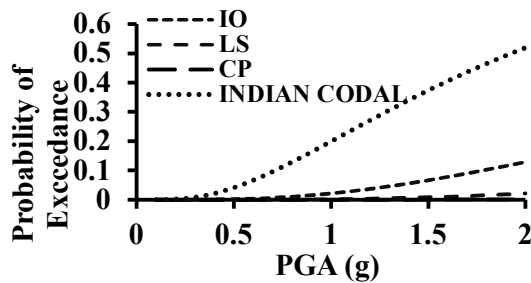


Figure 3.152 – Fragility curves for roof of a G+9 horizontally irregular building with isolated footing on soft soil on plane ground under Denali earthquake

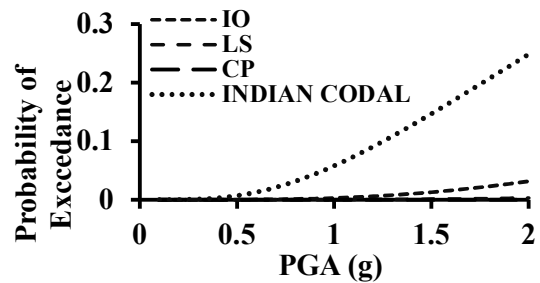


Figure 3.153 – Fragility curves for roof of a G+9 regular building with isolated footing on soft soil on sloping ground under Loma Prieta earthquake

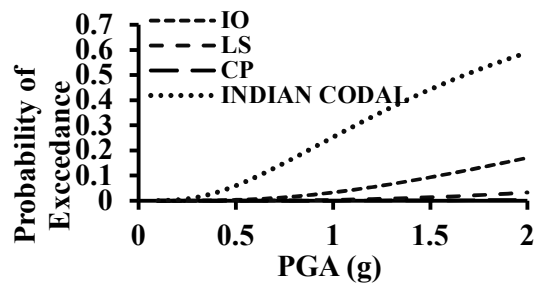


Figure 3.154 – Fragility curves for roof of a G+9 regular building with isolated footing on soft soil on sloping ground under Denali earthquake

CHAPTER 4: FRAME STRUCTURES ON LAYERED SOIL

4.1 - GENERAL

Local soil largely affects the ground motion characteristics and plays an important role in damage distribution during an earthquake [69]–[72]. Significant differences in structural damage in basin on soft soil as compared with the surrounding exposed rocks or even in the basin itself from place to place have been reported during the past earthquakes. When there are sharp changes in soil properties like impedance contrasts many things can happen. By the principle of conservation of energy, amplitude increases in low velocity soil deposits. There may be trapping of seismic waves due to large impedance contrast between soft sediment and underline bedrock and this lead resonance pattern. When the peak acceleration is small, acceleration at soil surface is slightly greater than rock surface. This is what happened in Mexico City and San Francisco Bay area. But at moderate or high acceleration level acceleration level at rock surface is greater than soil surface. At higher acceleration levels, due to low stiffness and non-linearity prevent to develop peak acceleration.

In this chapter, response of buildings due to variation of different soil layers under the action of near-field and far-field earthquakes ground motion has been observed for sloping ground and plane ground. In the present study, the layered soil has six different layers, have been combined with different types of G+9 frame buildings on isolated foundation. Each model is analyzed using the same procedure as mentioned in Chapter 3.

4.2 - PROBLEM FORMULATION

In the present study an investigation has been made to find the effect of dynamic SSI due to variation of thickness of soft soil layer in different depth. The layered soil is an assembly of six different layers. All the soil layers are considered homogeneous in nature. The properties of the layered soil used for developing the models have been presented in Table 4.1. Further, to determine the effects of various structural properties on dynamic SSI phenomenon, different types of G+9 frame buildings on isolated foundation have been considered. The shapes and properties of the buildings along with their components are identical to that of the buildings used in Chapter 3.

From Equations 20, 21 and 22,

$$G = \frac{1}{2} \frac{E}{1+\nu}$$
$$K = \frac{E}{3(1-2\nu)}$$
$$V_s = \sqrt{G/\rho}$$

where,

G = Shear Modulus in N/m²

E = Young's Modulus in N/m^2
 K = Bulk Modulus in N/m^2
 ν = Poisson's Ratio
 V_s = Shear Wave Velocity in m/s
 ρ = Mass Density in kg/m^3

Table 4.1 - Properties of soil 1

Depth from Ground Level (m)		Mass Density (ρ) in kg/m^3	Young's Modulus (E) in N/m^2	Shear Modulus (G) in N/m^2	Poisson's Ratio (ν)	Shear Wave Velocity (V_s) in m/s	Bulk Modulus (K) in N/m^2
From	To						
0	5	1500	$9.7\text{E}+07$	$3.4\text{E}+07$	0.43	150.369	230952381
5	10	1950	$3.3\text{E}+08$	$1.2\text{E}+08$	0.35	250.356	366666667
10	15	1980	$4.8\text{E}+08$	$1.8\text{E}+08$	0.34	300.760	500000000
15	20	2000	$6.5\text{E}+08$	$2.5\text{E}+08$	0.32	350.865	601851852
20	25	2100	$1.1\text{E}+09$	$4.3\text{E}+08$	0.30	450.884	925000000
25	30	2300	$2.0\text{E}+09$	$8.3\text{E}+08$	0.20	600.423	1105555556

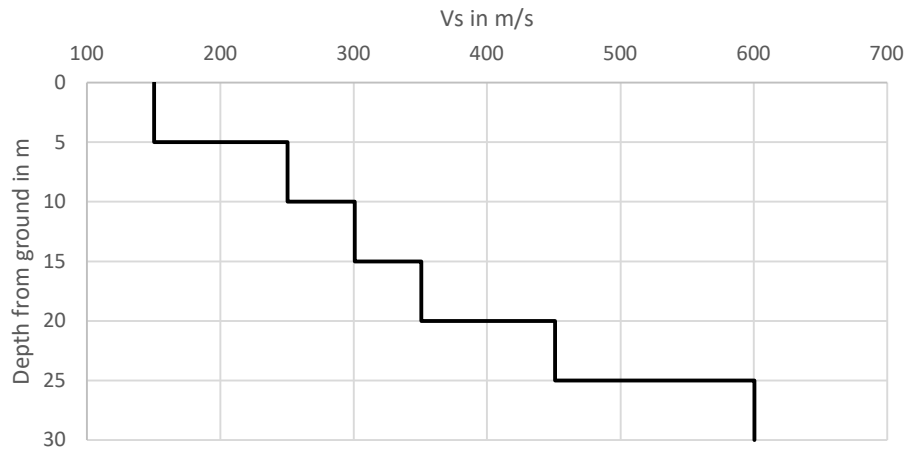


Figure 4.1 - Shear wave variation along depth of soil 1

4.3 - MODELLING THE PROBLEM

Generally, the soils are of different strata in earth, they are not homogeneous in nature, different layers of subsoil's are occurred, they all have different soil properties. At many places there exists multi layered soil with different depths. Sometimes the hard strata overlay by the soft soil and vice versa. The procedure for modelling a general SSI problem using Abaqus software has been discussed briefly in Chapter 3. However, to model the problem stated in this chapter, several parts (Infinite Soil, Soil Layer 1, Soil Layer 2, Soil Layer 3, Soil Layer 4, Soil Layer 5, Soil Layer 6, Soil Tetrahedron, Footing or Pile Cap & Pile, Column and Beam) are used. The nodes present on the interface of two adjacent soil layers have been merged to develop the entire layered soil base. Rest of the model is kept similar to the model used for analyzing frame structures resting on uniform soil in Chapter

3. The analysis procedure followed in this chapter is also same as in the previous chapter. However, the meshing details of the elements used along with their properties have been tabulated in Table 4.2. In order to incorporate the effect of damping in the soil-structure models, Rayleigh damping coefficients are computed and assigned to every model following the procedure demonstrated in Chapter 3. For calculating Rayleigh damping coefficients, first and fifth mode frequencies are taken into account. In all cases, damping ratio value is taken as 0.05. Rayleigh damping coefficients for all the models along with their first and fifth mode frequencies are presented in Table 4.3.

Table 4.2 - Properties of the elements used in Abaqus

Name of the Part		Cross-sectional Area	Depth or Length of the Part	Element Size for Meshing	No. of Nodes in Each Element	Type of Element
Infinite Soil		2.5 m × 2.5 m	N/A	2.5 m × 2.5 m × Infinite Length	8	Linear Hexahedron (Type CIN3D8)
Soil Layers (Surrounded by the Infinite Soil)		37.5 m × 35 m	5 m	2.5 m × 2.5 m × 2.5 m	8	Linear Hexahedron (Type C3D8)
Soil Tetrahedron (Embedded in the Soil Layer 1)		27.5 m × 25 m	5 m	N/A	4	Linear Tetrahedron (Type C3D4)
Isolated Footing (Embedded in the Soil Tetrahedron)		22.5 m × 20 m	2.5 m	0.625 m × 0.625 m × 0.625 m	8	Linear Hexahedron (Type C3D8)
Pile Cap (Embedded in the Soil Tetrahedron)		4.5 m × 4.5 m	1 m	0.625 m × 0.625 m × 0.625 m	8	Linear Hexahedron (Type C3D8)
Pile (Embedded in the Soil Base)		0.8 m diameter	24 m	1.25 m × 0.314 m	4	Liner Shell (Type S4R)
Column (Each column is placed on a Footing)	For G+9 Building	500 mm × 500 mm	3 m, 8 m & 13 m	0.6 m	2	Linear Line (Type B31)
Beam (Each beam is placed on two Columns)	For G+9 Building	300 mm × 500 mm	5 m & 7.5 m	1 m	2	Linear Line (Type B31)

In order to incorporate the effect of damping in the soil-structure models, Rayleigh damping coefficients are computed and assigned to every model following the procedure

demonstrated in Chapter 3. For calculating Rayleigh damping coefficients, first and fifth mode frequencies are taken into account. In all cases, damping ratio value is taken as 0.05. Rayleigh damping coefficients for all the models along with their first and fifth mode frequencies are presented in Table 4.3.

Table 4.3 - Rayleigh damping coefficients of materials for different soil-structure combinations of layered soils

SOIL TYPE	STRUCTURE TYPE	FREQUENCY OF 1ST MODE (cps)	FREQUENCY OF 5TH MODE (cps)	DAMPING RATIO (ξ)	RAYLEIGH DAMPING COEFFICIENTS	
					α	β
SOIL 1	MODEL 1	0.73862	2.3278	0.05	0.35230	0.00519
	MODEL 5	0.60039	2.2713	0.05	0.29837	0.00554
	MODEL 6	0.48403	1.2821	0.05	0.22078	0.00901
	MODEL 7	0.88529	2.6488	0.05	0.41690	0.00450
	MODEL 9	0.5585	2.2089	0.05	0.28010	0.00575
SOIL 2	MODEL 7	0.88468	2.3865	0.05	0.40553	0.00487
SOIL 3	MODEL 7	0.88427	2.0684	0.05	0.38921	0.00539
SOIL 4	MODEL 7	0.88366	1.8179	0.05	0.37361	0.00589
SOIL 5	MODEL 7	0.88127	1.5989	0.05	0.35697	0.00642
SOIL 6	MODEL 7	0.87921	1.4115	0.05	0.34040	0.00695
SOIL 7	MODEL 7	0.88513	2.3943	0.05	0.40604	0.00485

***Notes for Table 4.3:

MODEL 1: Vertically irregular with isolated footing on plane ground
 MODEL 2: Vertically irregular with isolated footing on sloping ground
 MODEL 3: Vertically irregular with pile footing on plane ground
 MODEL 4: Vertically irregular with pile footing on sloping ground
 MODEL 5: Regular with isolated footing on plane ground
 MODEL 6: Regular with isolated footing on sloping ground
 MODEL 7: Regular with pile footing on plane ground
 MODEL 8: Regular with pile footing on sloping ground
 MODEL 9: Horizontally irregular with isolated footing on plane ground

4.4 - INPUT MOTIONS AND THEIR PROPERTIES

The input motions used for analyzing the models are identical to the motions used in Chapter 3. Various properties of those seismic excitations, such as acceleration time-history, acceleration response spectra and FFT, have already been presented in that chapter. It should be kept in mind that the two input motions (bidirectional) should be applied in two orthogonal principal directions of the structure simultaneously in a model in order to cater the proper effect of bidirectional earthquake.

4.5 - DISPLACEMENT TIME-HISTORIES OF ROOF AND BASE RESPONSES

The procedure to obtain displacement time history data from Abaqus is discussed in details in Article 3.6. Also, a typical example for application of the 0.4 rule for combining the responses in the two directions is shown for a uniform soil model in the same aforesaid article in Figures 3.58 – 3.63.

We were unable to perform time history analysis in Abaqus for the models with pile foundation due to unrealistic huge run time. Those models were taking extremely small time steps to converge to a solution in each time step. The possible reasons for such issue may be involvement of finer meshing of the soil layers due to presence of holes in them for the piles, use of shell element for 64 number of piles, use of friction interaction between all the piles and the boreholes etc.

Hence FEM models for pile foundation should be done with some other software such as SeismoStruct. Hence models with isolated foundation are analyzed for time history output for Soil 1. The various responses are given in Figure 4.2 to 4.17. It is important to note that all the responses presented below are corresponding to acceleration time history input normalized to PGA of 1.0g for both the near field and far field earthquakes.

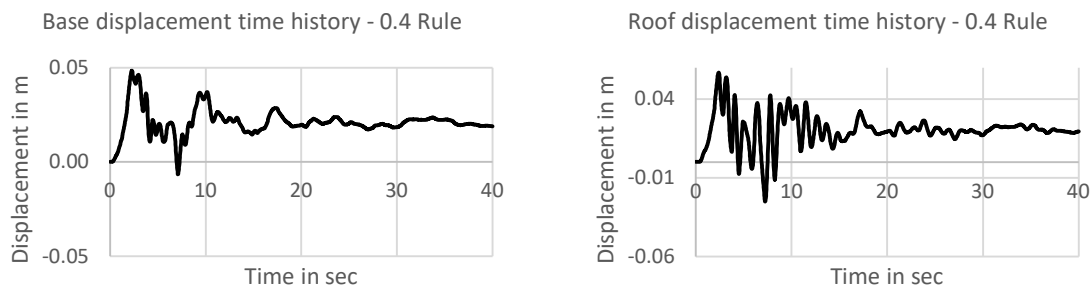


Figure 4.2 – Resultant displacement time-history for base of a G+9 regular building with isolated footing on soil 1 on plane ground under Loma Prieta earthquake

Figure 4.3 – Resultant displacement time-history for roof of a G+9 regular building with isolated footing on soil 1 on plane ground under Loma Prieta earthquake

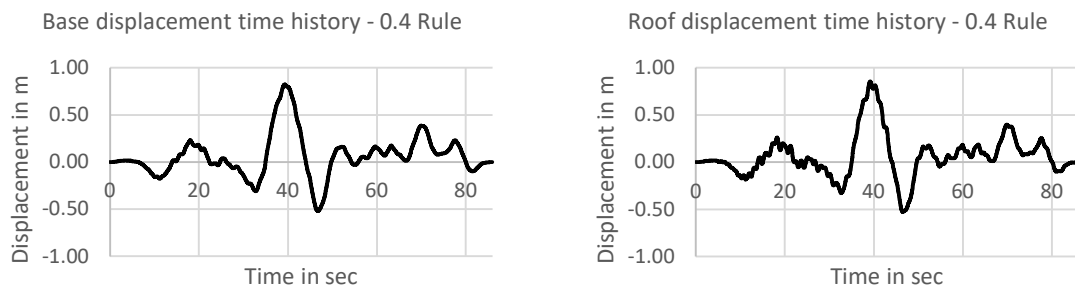


Figure 4.4 – Resultant displacement time-history for base of a G+9 regular building with isolated footing on soil 1 on plane ground under Denali earthquake

Figure 4.5 – Resultant displacement time-history for roof of a G+9 regular building with isolated footing on soil 1 on plane ground under Denali earthquake



Figure 4.6 – Resultant displacement time-history for base of a G+9 vertically irregular building with isolated footing on soil 1 on plane ground under Loma Prieta earthquake

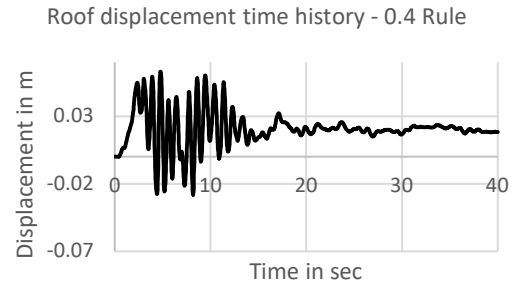


Figure 4.7 – Resultant displacement time-history for roof of a G+9 vertically irregular building with isolated footing on soil 1 on plane ground under Loma Prieta earthquake

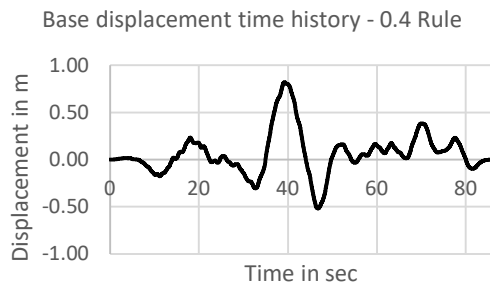


Figure 4.8 – Resultant displacement time-history for base of a G+9 vertically irregular building with isolated footing on soil 1 on plane ground under Denali earthquake

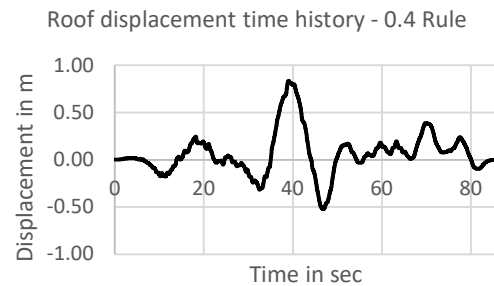


Figure 4.9 – Resultant displacement time-history for roof of a G+9 vertically irregular building with isolated footing on soil 1 on plane ground under Denali earthquake

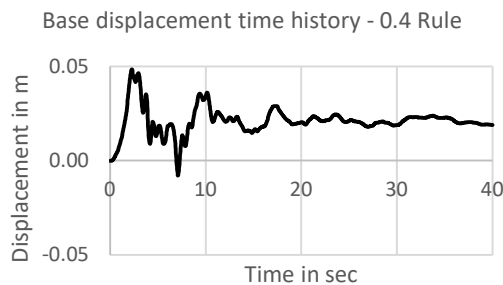


Figure 4.10 – Resultant displacement time-history for base of a G+9 horizontally irregular building with isolated footing on soil 1 on plane ground under Loma Prieta earthquake

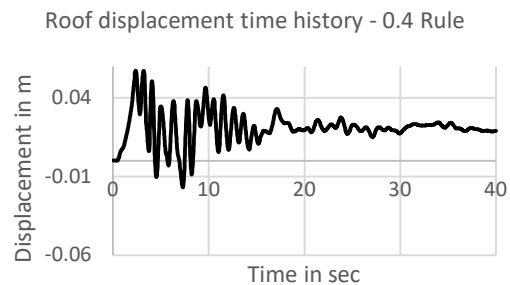


Figure 4.11 – Resultant displacement time-history for roof of a G+9 horizontally irregular building with isolated footing on soil 1 on plane ground under Loma Prieta earthquake

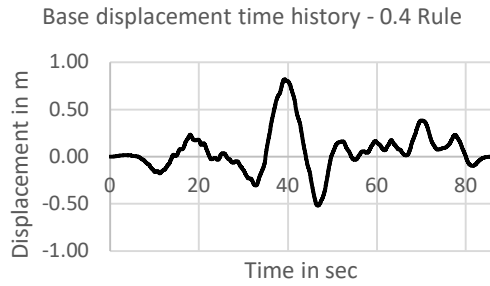


Figure 4.12 – Resultant displacement time-history for base of a G+9 horizontally irregular building with isolated footing on soil 1 on plane ground under Denali earthquake

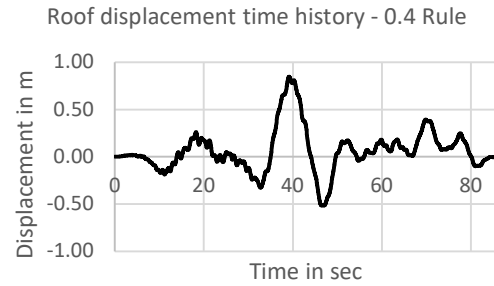


Figure 4.13 – Resultant displacement time-history for roof of a G+9 horizontally irregular building with isolated footing on soil 1 on plane ground under Denali earthquake



Figure 4.14 – Resultant displacement time-history for base of a G+9 regular building with isolated footing on soil 1 on sloping ground under Loma Prieta earthquake



Figure 4.15 – Resultant displacement time-history for roof of a G+9 regular building with isolated footing on soil 1 on sloping ground under Loma Prieta earthquake

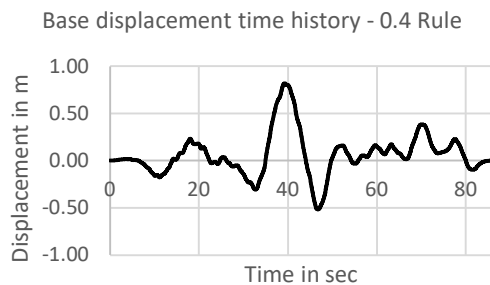


Figure 4.16 – Resultant displacement time-history for base of a G+9 regular building with isolated footing on soil 1 on sloping ground under Denali earthquake

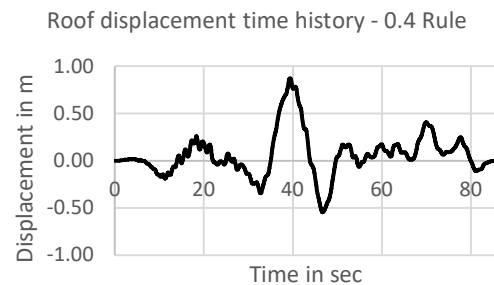


Figure 4.17 – Resultant displacement time-history for roof of a G+9 regular building with isolated footing on soil 1 on sloping ground under Denali earthquake

After analyzing all the developed models using Abaqus software, the displacement time-histories of both roof and base responses are plotted for every case which are presented in Figure 4.2 to Figure 4.17. The displacement time-history graphs in Chapter 3 & 4 clearly reveal that the base responses change only due to the variation in soil properties. In other

words, change in building type does not alter the base response, if all other parameters are kept unchanged. It is also to be mentioned that the roof and base responses under the action of a near-field earthquake are smaller than the far-field one. This may be due to the presence of low frequency seismic wave in far-field earthquake. The displacement time history pattern varies considerably for near field and far field earthquake because of wide variation in the acceleration time history of the two earthquakes.

4.6 - MAXIMUM DISPLACEMENT PROFILES

The maximum displacement profiles for all the buildings, plotted as described in Chapter 3, Article 3.7, have been presented in Figure 4.18 to Figure 4.25. A typical example for application of the 0.4 rule for combining the time history responses in the two directions and thus obtaining maximum displacements of different floors from the combined response is shown for a uniform soil model in the same aforesaid article in Figures 3.110 – 3.112.

It is important to note that all the responses presented below are corresponding to acceleration time history input normalized to PGA of 1.0g for both the near field and far field earthquakes.

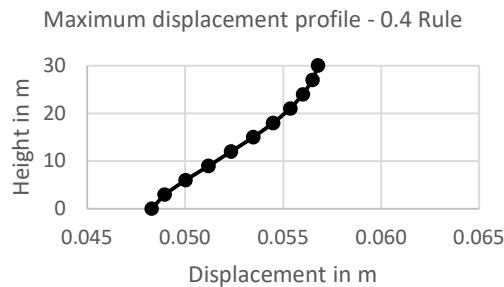


Figure 4.18 – Resultant maximum displacements of different floors of a G+9 regular building with isolated footing on soil 1 on plane ground under Loma Prieta earthquake

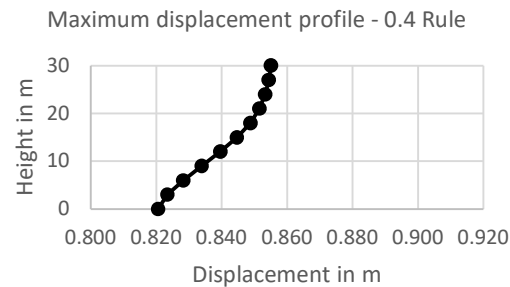


Figure 4.19 – Resultant maximum displacements of different floors of a G+9 regular building with isolated footing on soil 1 on plane ground under Denali earthquake

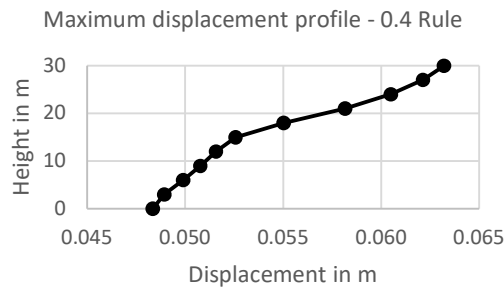


Figure 4.20 – Resultant maximum displacements of different floors of a G+9 vertically irregular building with isolated footing on soil 1 on plane ground under Loma Prieta earthquake

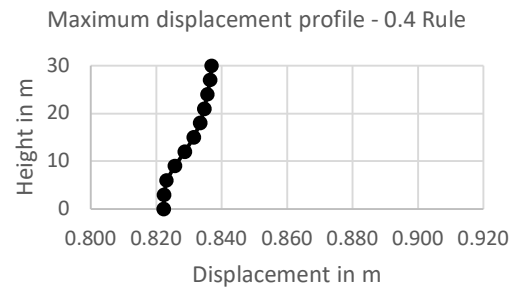


Figure 4.21 – Resultant maximum displacements of different floors of a G+9 vertically irregular building with isolated footing on soil 1 on plane ground under Denali earthquake

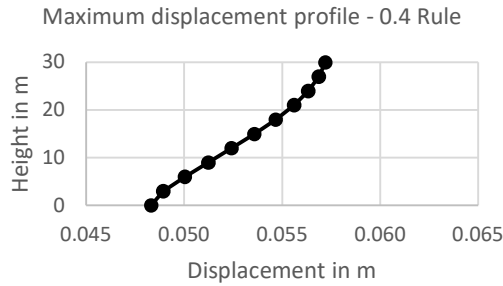


Figure 4.22 – Resultant maximum displacements of different floors of a G+9 horizontally irregular building with isolated footing on soil 1 on plane ground under Loma Prieta earthquake

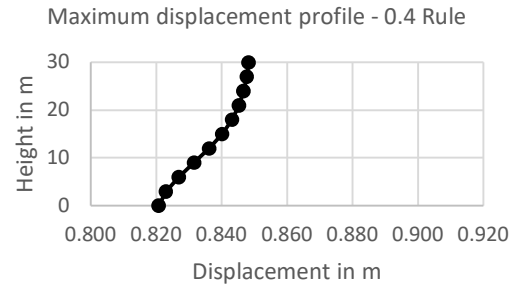


Figure 4.23 – Resultant maximum displacements of different floors of a G+9 horizontally irregular building with isolated footing on soil 1 on plane ground under Denali earthquake

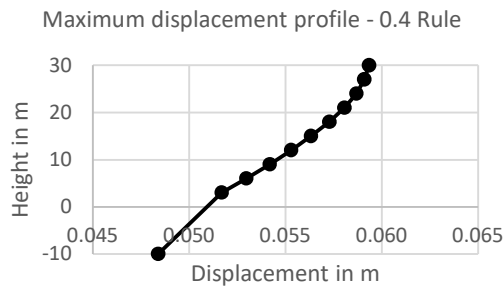


Figure 4.24 – Resultant maximum displacements of different floors of a G+9 regular building with isolated footing on soil 1 on sloping ground under Loma Prieta earthquake

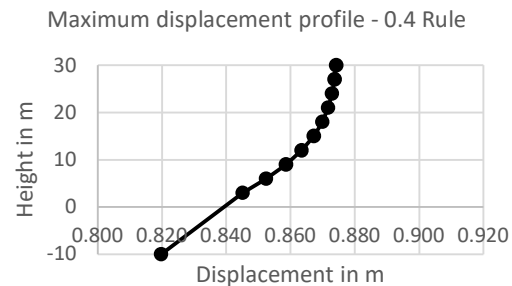


Figure 4.25 – Resultant maximum displacements of different floors of a G+9 regular building with isolated footing on soil 1 on sloping ground under Denali earthquake

The figures clearly reveal that irrespective of the type of soil and structure, when any soil-structure system is subjected to a near or far-field earthquake, the shape of the maximum displacement profile is concave upward. Further, maximum displacements of the floors always increase monotonically with their heights. This may be due to presence of only low frequency seismic wave. However, the shape of the maximum displacement profile of a building purely depends upon the type of soil and structure. Vertical irregular building tends to deflect more compared to other building types for near field earthquake. On the contrary, for far field earthquake, vertical irregular building tends to deflect least compared to other building types. Finally, it is seen that the response of roof due to a far-field earthquake is more than the response of roof due to a near-field earthquake.

4.7 - MAXIMUM DRIFT PROFILES

The maximum drift profiles for all the buildings, plotted as described in Chapter 3, Article 3.8, have been presented in Figure 4.26 to Figure 4.33. A typical example for application of the 0.4 rule for combining the time history responses in the two directions and thus obtaining maximum drifts of different floors from the combined response is shown for a uniform soil model in the same aforesaid article in Figures 3.120 – 3.122.

It is important to note that all the responses presented below are corresponding to acceleration time history input normalized to PGA of 1.0g for both the near field and far field earthquakes.

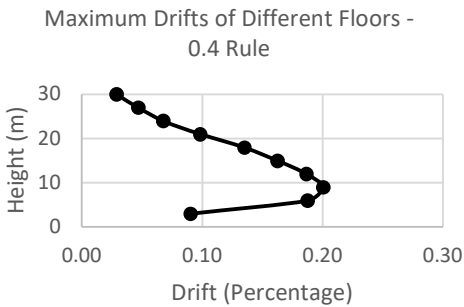


Figure 4.26 – Resultant maximum drifts of different floors of a G+9 regular building with isolated footing on soil 1 on plane ground under Loma Prieta earthquake

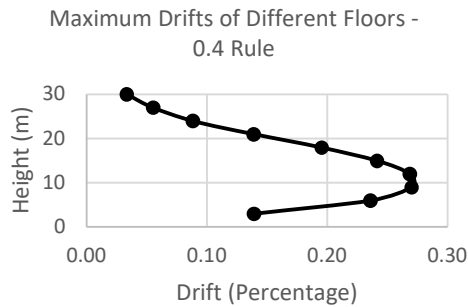


Figure 4.27 – Resultant maximum drifts of different floors of a G+9 regular building with isolated footing on soil 1 on plane ground under Denali earthquake

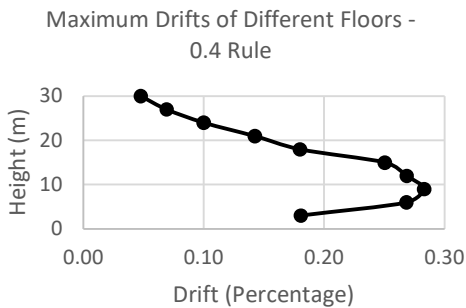


Figure 4.28 – Resultant maximum drifts of different floors of a G+9 vertically irregular building with isolated footing on soil 1 on plane ground under Loma Prieta earthquake

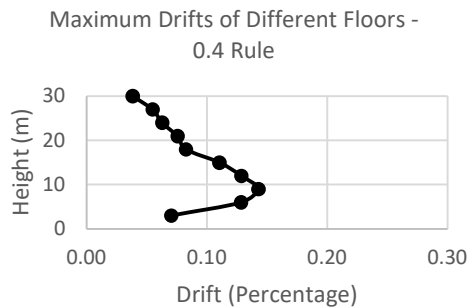


Figure 4.29 – Resultant maximum drifts of different floors of a G+9 vertically irregular building with isolated footing on soil 1 on plane ground under Denali earthquake

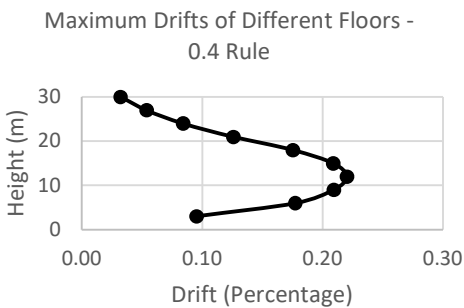


Figure 4.30 – Resultant maximum drifts of different floors of a G+9 horizontally irregular building with isolated footing on soil 1 on plane ground under Loma Prieta earthquake

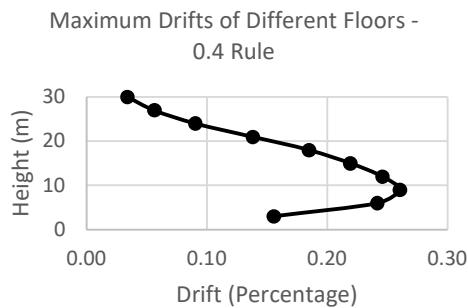


Figure 4.31 – Resultant maximum drifts of different floors of a G+9 horizontally irregular building with isolated footing on soil 1 on plane ground under Denali earthquake

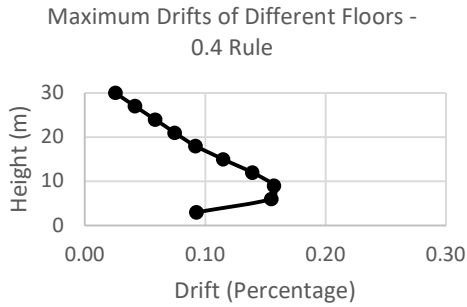


Figure 4.32 – Resultant maximum drifts of different floors of a G+9 regular building with isolated footing on soil 1 on sloping ground under Loma Prieta earthquake

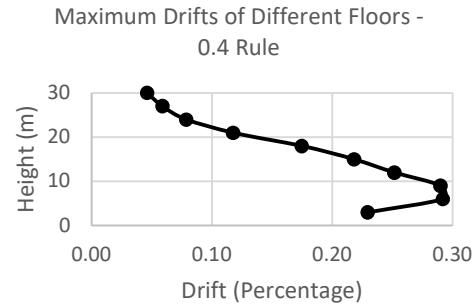


Figure 4.33 – Resultant maximum drifts of different floors of a G+9 regular building with isolated footing on soil 1 on sloping ground under Denali earthquake

After studying the maximum drift curves, the following points can be concluded. Maximum drift is obtained in 2nd, 3rd and 4th floors in most of the cases of a G+9 building. In most cases drift due to far field earthquake is more than due to near field earthquake. The variation in the pattern of the acceleration time histories quite well explains the phenomenon. However, in cases of vertically irregular buildings, drift due to far field earthquake is less than due to near field earthquake. Maximum drifts are observed in vertical irregular building as compared to other types of G+9 building structures in case of near field earthquake. In case of far field earthquake, maximum drifts are observed in regular building on sloping ground as compared to other types of G+9 building structures.

4.8 - FRAGILITY CURVES

In the present study PSDMs and fragility curves have been plotted following the 2000 SAC/FEMA method [68] as discussed in Chapter 2. The developed PSDMs along with the fragility curves are presented in Figure 4.34 to Figure 4.42. Several conclusions can be drawn after observing the PSDMs and fragility curves of the frame buildings located on layered soil. For all the models, the generated PSDMs are actually straight lines passing through the origin. It is to be noted that under the action of a particular earthquake, the probability of exceedance of CP is the minimum and that of Indian Codal Limit is the maximum.

Generally, under the action of a near-field earthquake, the limit state exceedance probability is less compared to the far-field earthquake in case of most G+9 building configurations. Exceptionally, in case of vertically irregular building, the probability of exceedance value of the soil-structure system will be greater under the influence of near-field earthquake. Highest probability of exceedance value of the soil-structure system is seen in case of building on sloping ground as compared to building on plane ground in case of far field earthquake. On the contrary for near field earthquake, lowest probability of exceedance value of the soil-structure system is seen in case of building on sloping ground as compared to building on plane ground. Almost in all cases, the graph for CP is extremely flat almost touching the baseline.

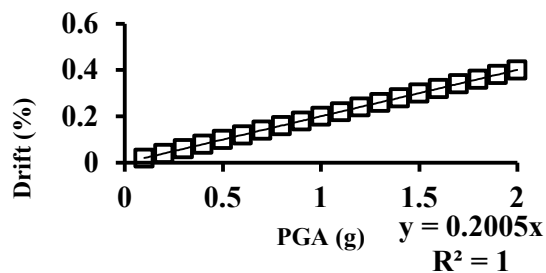


Figure 4.34 – PSDM for a G+9 regular building with isolated footing on soil 1 on plane ground under Loma Prieta earthquake

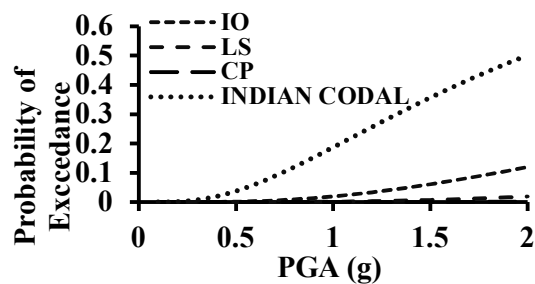


Figure 4.35 – Fragility curves for roof of a G+9 regular building with isolated footing on soil 1 on plane ground under Loma Prieta earthquake

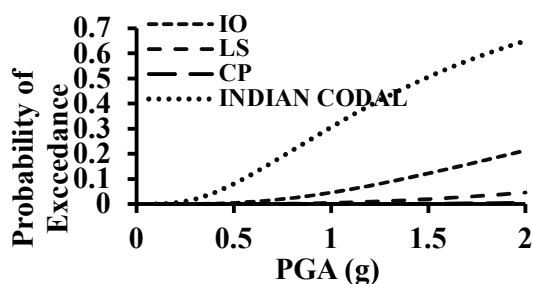


Figure 4.36 – Fragility curves for roof of a G+9 regular building with isolated footing on soil 1 on plane ground under Denali earthquake

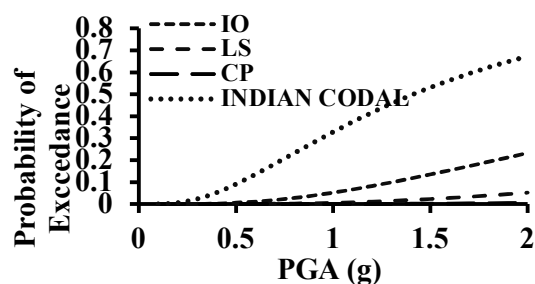


Figure 4.37 – Fragility curves for roof of a G+9 vertically irregular building with isolated footing on soil 1 on plane ground under Loma Prieta earthquake

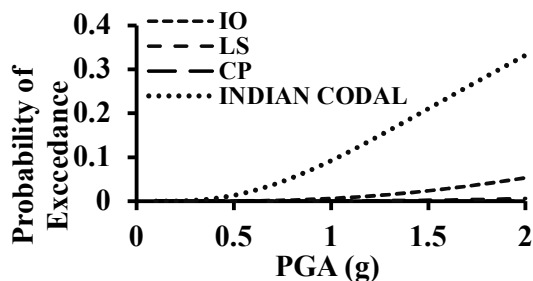


Figure 4.38 – Fragility curves for roof of a G+9 vertically irregular building with isolated footing on soil 1 on plane ground under Denali earthquake

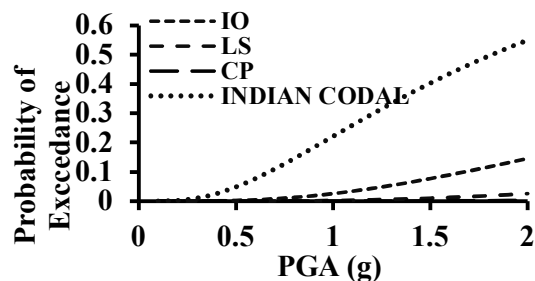


Figure 4.39 – Fragility curves for roof of a G+9 horizontally irregular building with isolated footing on soil 1 on plane ground under Loma Prieta earthquake

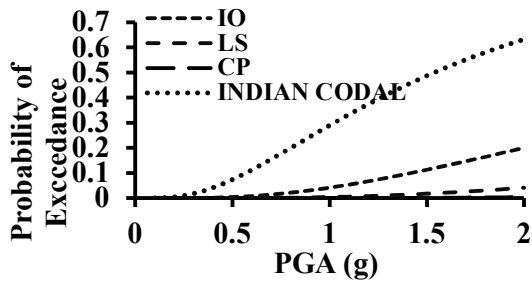


Figure 4.40 – Fragility curves for roof of a G+9 horizontally irregular building with isolated footing on soil 1 on plane ground under Denali earthquake

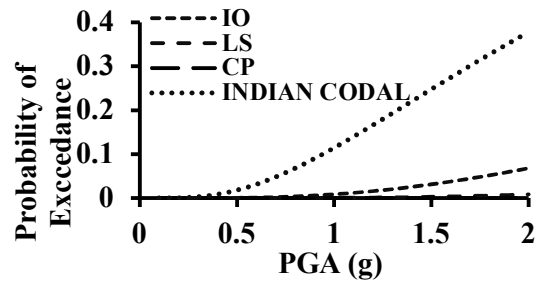


Figure 4.41 – Fragility curves for roof of a G+9 regular building with isolated footing on soil 1 on sloping ground under Loma Prieta earthquake

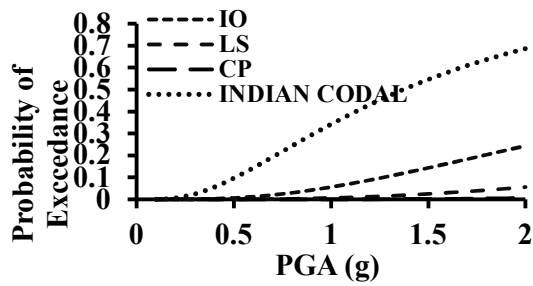


Figure 4.42 – Fragility curves for roof of a G+9 regular building with isolated footing on soil 1 on sloping ground under Denali earthquake

CHAPTER 5: RELIABILITY BASED ANALYSIS

5.1 - GENERAL

The fragility curves indicate the probability of exceedance of a particular performance level for a soil-structure system if the system is subjected to a seismic excitation of predefined intensity (in terms of PGA). However, to assess the risk of any soil-structure system, these fragility curves should be combined with the seismic hazard curve, which corroborates the probability of occurrence of an earthquake having more than certain intensity at a particular location of interest.

Reliability is a measure of safety of a building frame, which can be expressed by a statistical parameter named 'Reliability Index'. This Reliability Index can be obtained by subtracting the probability of failure of a structure from unity. Risk of any frame can be expressed using the probability of exceedance of a particular performance level such as IO, LS, CP and limitation given by IS 1893 (Part I):2002 [73] along with the probability of occurrence of an earthquake having more than a specified intensity. In this chapter, reliability indices for all the aforementioned models have been presented graphically using the seismic hazard curve for Conterminous U.S. under the action of Loma prieta and Denali earthquakes.

5.2 - SEISMIC HAZARD CURVE

Seismic hazard is defined as the probability of occurrence of an earthquake in a particular geographic area, within a specified window of time, and with ground motion intensity exceeding a given threshold. A hazard curve depicts the variation of probability of exceedance of an earthquake with respect to maximum seismic intensities (mainly in terms of PGA). In the present study, seismic hazard curve for Conterminous U.S. proposed by USGS (2014) has been used to obtain the reliability curves for various G+9 frame buildings (with and without vertical irregularity) constructed on uniform as well as layered soils on plane and sloping ground and subjected to near-field and far-field earthquakes. The seismic hazard curve for the Conterminous U.S., given by USGS (2014), used for analysis is shown below in Figure 5.1.

$$\text{Return period} = 1 - \text{annual rate of exceedance} \quad \dots(34)$$

$$\text{Factor} = \frac{\text{PGA for return period of 475 years}}{\text{PGA for the location of the seismic hazard graph}} \quad \dots(35)$$

$$\text{PGA of seismic hazard curve} = \text{PGA at bed rock} * \text{Factor} \quad \dots(36)$$

Our objective is to consider a seismic hazard curve which has data upto PGA of 1.0g or higher. After lots of search work, we finally considered the seismic hazard curve of Conterminous U.S. for the formation of reliability curves since it has records upto PGA of 4.92g. The data of seismic hazard curves of Alaska and Conterminous U.S. are obtained from USGS website: <https://earthquake.usgs.gov/hazards/interactive/>

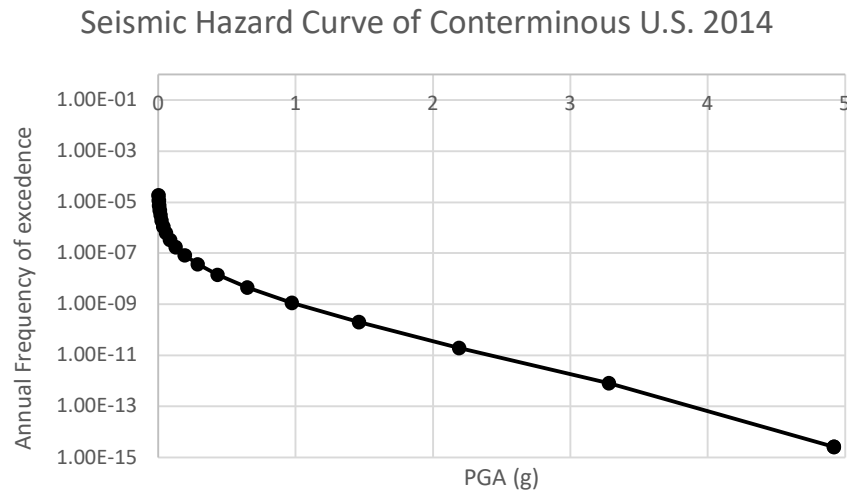


Figure 5.1 - Seismic hazard curve for Conterminous U.S. (USGS, 2014) in semi-logarithmic scale

This seismic hazard curve of Conterminous U.S. is finally considered for further study and formation of reliability curves.

The reliability diagram is a very straightforward way of assessing how well forecasts of binary events agree with the actual rates of occurrence.

5.3 - RELIABILITY CURVES AND THEIR FORMULATIONS FOR BUILDINGS WITH SHALLOW FOUNDATION

Although we have explained in details about reliability in Chapter 2, we will revise some of the salient points and definitions regarding the same before finding out the different reliability curves of our models of study.

The reliability is the probability that a structure will perform its intended function during a specified time period under the considered operating conditions. Mathematically, it can be expressed using equation 10 as:

$$\text{Reliability} = 1 - \text{Probability of Failure}$$

The probability of failure at a specific performance level can be obtained by convolving the fragility curve $F_R(x)$ with the derivative of the seismic hazard curve $G_A(x)$. This conditional probability is sometimes assumed to follow a lognormal probability distribution [75] & [76]. Mathematically, it can be expressed using equation 11 as:

$$P[LS] = \int F_R(x) \frac{dG_A(x)}{dx} dx$$

The fragility-hazard interface, as illustrated by Ellingwood (2001) [77], has been presented

in Figure 2.8.

In this figure, $F_R(x)$ and $\frac{dG_A(x)}{dx}$ are the two parameters from which probability distribution $P[LS]$ is established. In order to determine the performance of every soil-structure system, reliability index (RI) has been computed which is a direct measure of the safety margin. Hassofer and Lind (1974) [78] defined RI (β_{pf}) as the shortest distance between the origin and the Limit State Function (LSF) in a standard normal variable space. RI (β_{pf}) corresponding to a specific probability of failure at a certain performance limit can be found from equation 12 as:

$$\beta_{pf} = -\Phi^{-1}(P[LS])$$

where, $\Phi()$ represents the standard normal distribution.

In Figure 5.2, the shaded area indicates the probability of failure. This figure clearly reveals that the Reliability Index (β_{pf}) is the shortest distance from the origin to the limit state function (LSF) in a standard normal variable space.

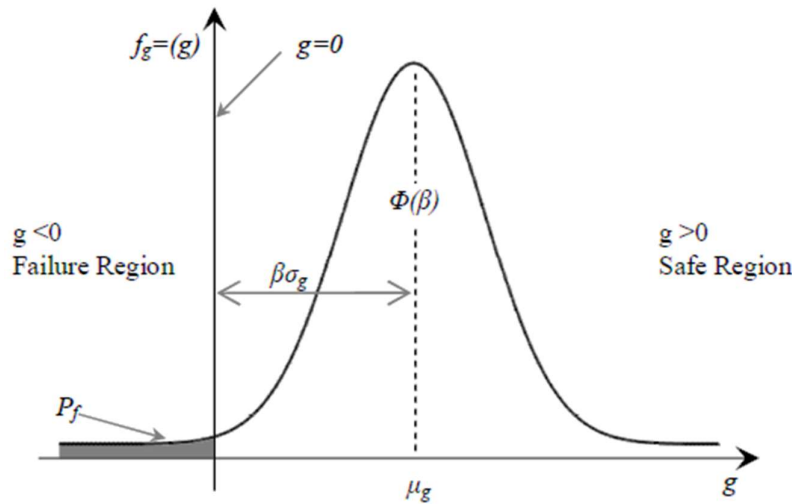


Figure 5.2 - Probability Density for Limit-state (Ellingwood, 2001) [77]

Reliability problem involves two main sources of uncertainties, namely in the structural properties and the ground motion. The structural uncertainty arises due to natural variability, data limitations, and modelling assumptions with respect to the geometry, boundary conditions, and constitutive behaviour of the material. The uncertainty associated with the earthquake load can be grouped into two categories, namely, those associated with the long-term features (e.g., frequency, magnitude, time, location of occurrence, fault mechanism and soil amplification) and those associated with the details of the ground motion (e.g. duration, amplitude, frequency content and non-stationary trend). The steps to be followed for plotting the reliability curves have been illustrated graphically in Figure 5.3.

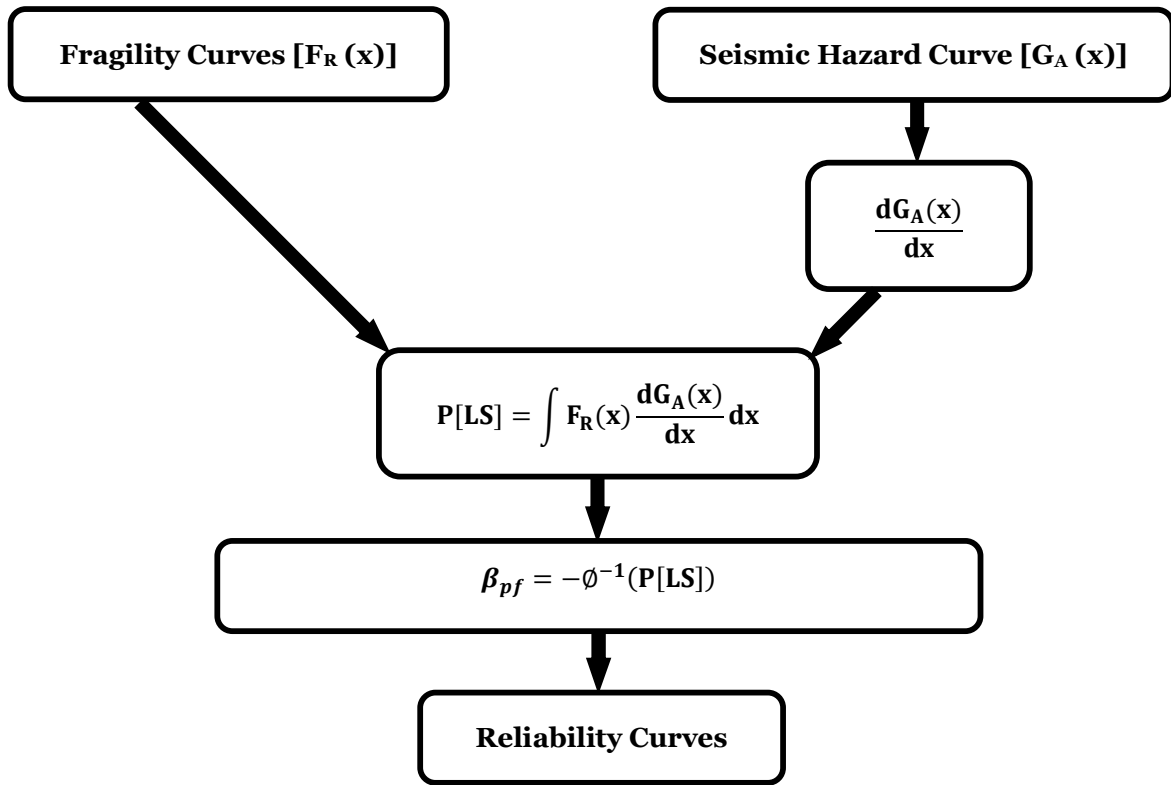


Figure 5.3 - Flow chart for plotting reliability curves

In this study, total 32 reliability curves have been generated for vertically regular and vertically irregular G+9 frame buildings located on three types of uniform soils (Hard, Medium and Soft) and one type of layered soils (Soil 1) in the Conterminous U.S. on plane ground and sloping ground with isolated footing and pile foundation which are subjected to a near-field (Loma Prieta) and a far-field (Denali) seismic excitation.

These curves are displayed in Figure 5.4 to Figure 6.41.

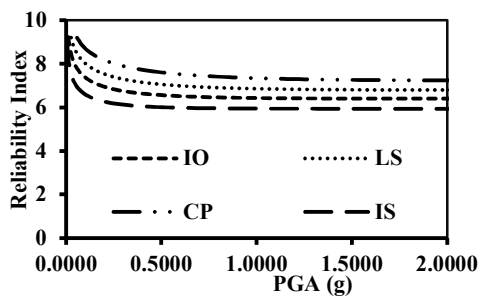


Figure 5.4 – Reliability Index for a G+9 regular building with isolated footing on hard soil on plane ground under Loma Prieta earthquake at Conterminous U.S.

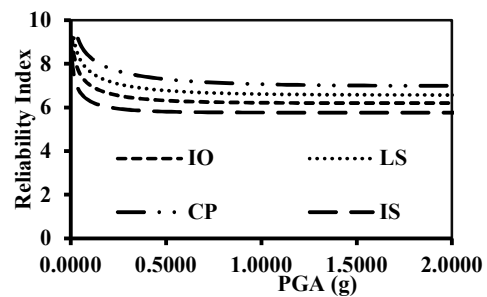


Figure 5.5 – Reliability Index for a G+9 regular building with isolated footing on hard soil on plane ground under Denali earthquake at Conterminous U.S.

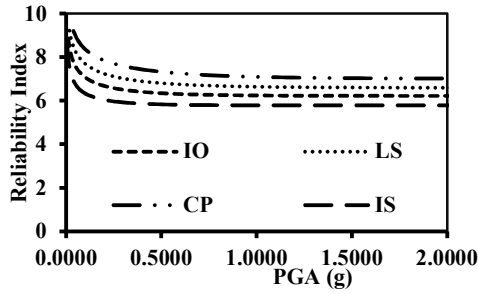


Figure 5.6 – Reliability Index for a G+9 vertically irregular building with isolated footing on hard soil on plane ground under Loma Prieta earthquake at Conterminous U.S.

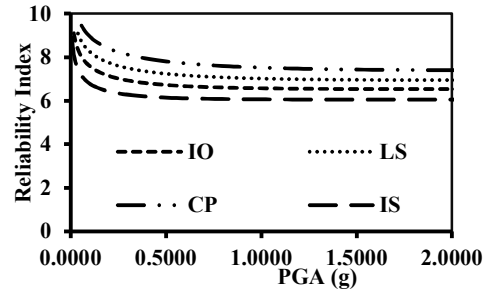


Figure 5.7 – Reliability Index for a G+9 vertically irregular building with isolated footing on hard soil on plane ground under Denali earthquake at Conterminous U.S.

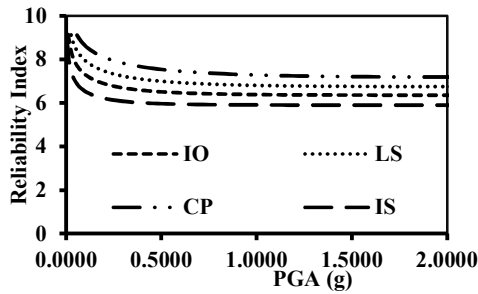


Figure 5.8 – Reliability Index for a G+9 horizontally irregular building with isolated footing on hard soil on plane ground under Loma Prieta earthquake at Conterminous U.S.

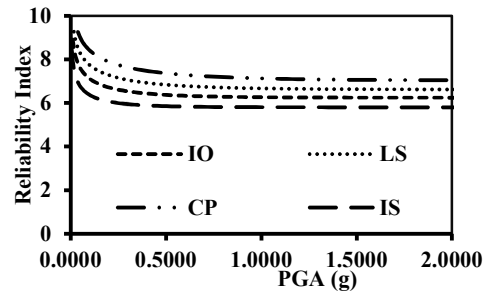


Figure 5.9 – Reliability Index for a G+9 horizontally irregular building with isolated footing on hard soil on plane ground under Denali earthquake at Conterminous U.S.

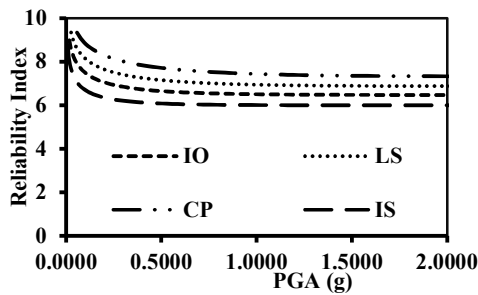


Figure 5.10 – Reliability Index for a G+9 regular building with isolated footing on hard soil on sloping ground under Loma Prieta earthquake at Conterminous U.S.

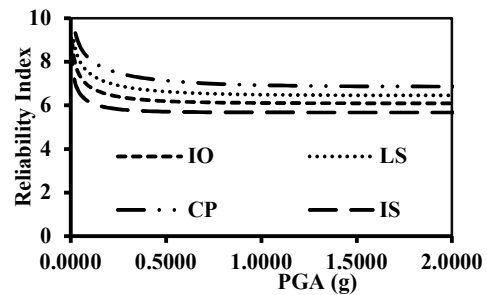


Figure 5.11 – Reliability Index for a G+9 regular building with isolated footing on hard soil on sloping ground under Denali earthquake at Conterminous U.S.

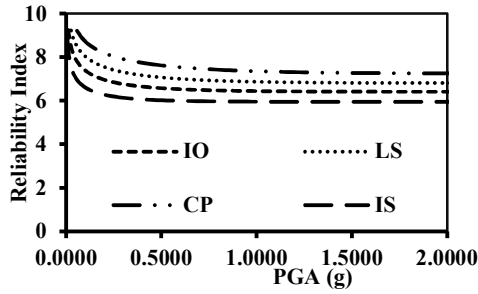


Figure 5.12 – Reliability Index for a G+9 regular building with isolated footing on medium soil on plane ground under Loma Prieta earthquake at Conterminous U.S.

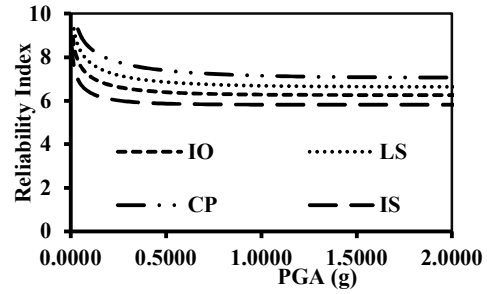


Figure 5.13 – Reliability Index for a G+9 regular building with isolated footing on medium soil on plane ground under Denali earthquake at Conterminous U.S.

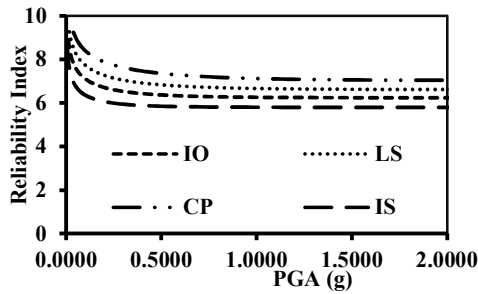


Figure 5.14 – Reliability Index for a G+9 vertically irregular building with isolated footing on medium soil on plane ground under Loma Prieta earthquake at Conterminous U.S.

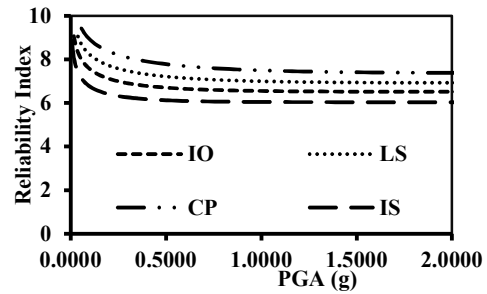


Figure 5.15 – Reliability Index for a G+9 vertically irregular building with isolated footing on medium soil on plane ground under Denali earthquake at Conterminous U.S.

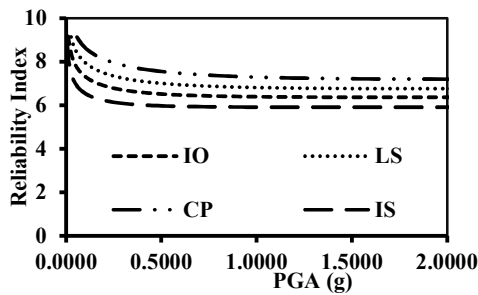


Figure 5.16 – Reliability Index for a G+9 horizontally irregular building with isolated footing on medium soil on plane ground under Loma Prieta earthquake at Conterminous U.S.

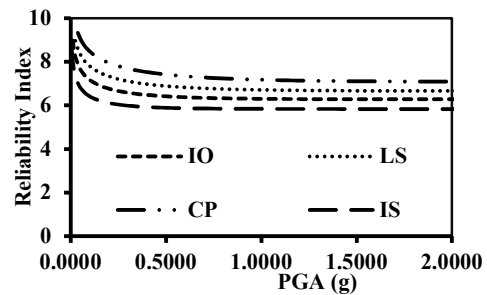


Figure 5.17 – Reliability Index for a G+9 horizontally irregular building with isolated footing on medium soil on plane ground under Denali earthquake at Conterminous U.S.

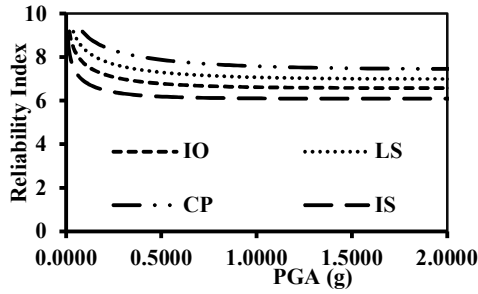


Figure 5.18 – Reliability Index for a G+9 regular building with isolated footing on medium soil on sloping ground under Loma Prieta earthquake at Conterminous U.S.

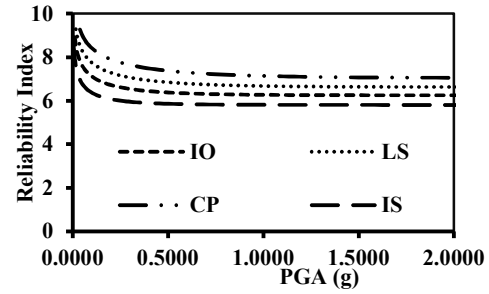


Figure 5.19 – Reliability Index for a G+9 regular building with isolated footing on medium soil on sloping ground under Denali earthquake at Conterminous U.S.

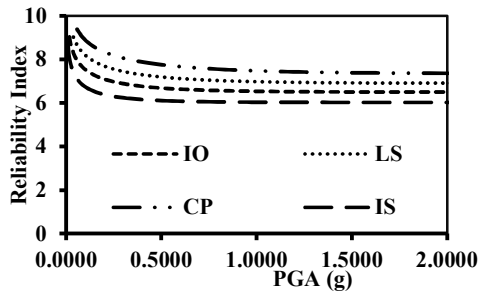


Figure 5.20 – Reliability Index for a G+9 regular building with isolated footing on soft soil on plane ground under Loma Prieta earthquake at Conterminous U.S.

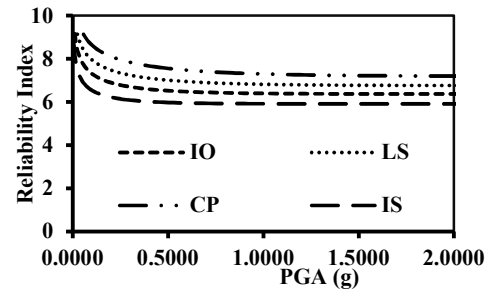


Figure 5.21 – Reliability Index for a G+9 regular building with isolated footing on soft soil on plane ground under Denali earthquake at Conterminous U.S.

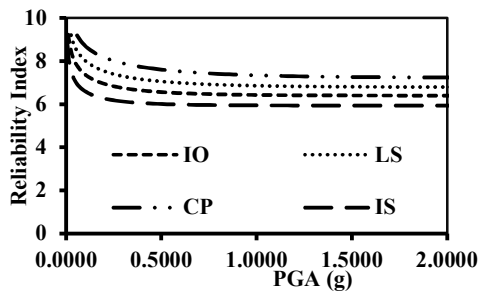


Figure 5.22 – Reliability Index for a G+9 vertically irregular building with isolated footing on soft soil on plane ground under Loma Prieta earthquake at Conterminous U.S.

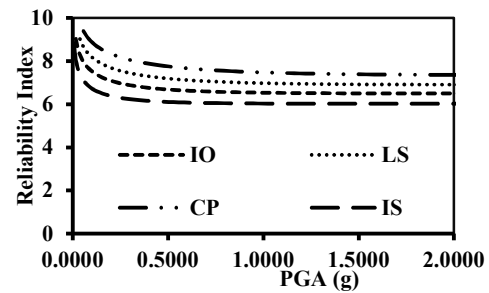


Figure 5.23 – Reliability Index for a G+9 vertically irregular building with isolated footing on soft soil on plane ground under Denali earthquake at Conterminous U.S.

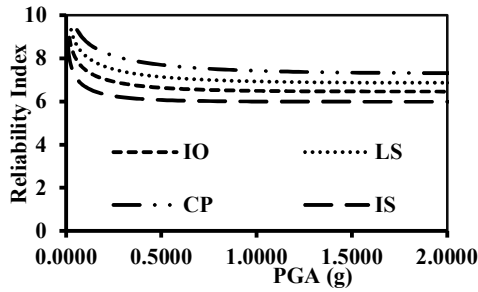


Figure 5.24 – Reliability Index for a G+9 horizontally irregular building with isolated footing on soft soil on plane ground under Loma Prieta earthquake at Conterminous U.S.

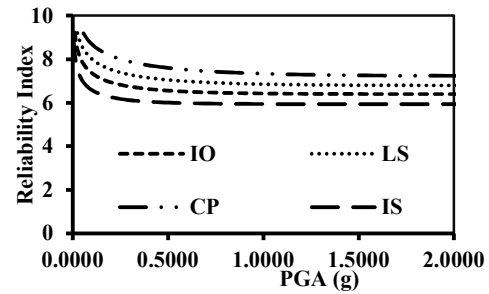


Figure 5.25 – Reliability Index for a G+9 horizontally irregular building with isolated footing on soft soil on plane ground under Denali earthquake at Conterminous U.S.

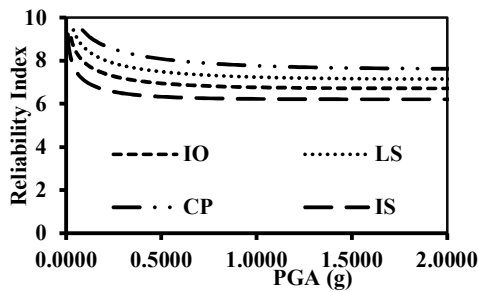


Figure 5.26 – Reliability Index for a G+9 regular building with isolated footing on soft soil on sloping ground under Loma Prieta earthquake at Conterminous U.S.

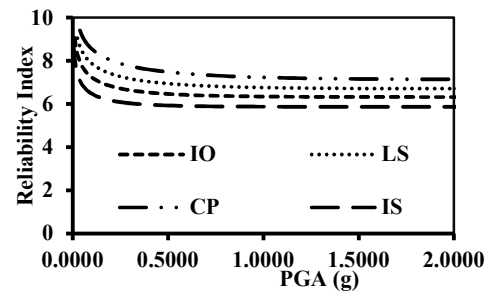


Figure 5.27 – Reliability Index for a G+9 regular building with isolated footing on soft soil on sloping ground under Denali earthquake at Conterminous U.S.

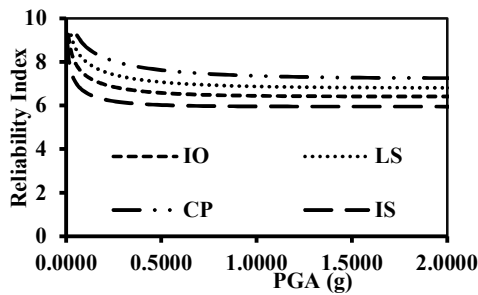


Figure 5.28 – Reliability Index for a G+9 regular building with isolated footing on soil 1 on plane ground under Loma Prieta earthquake at Conterminous U.S.

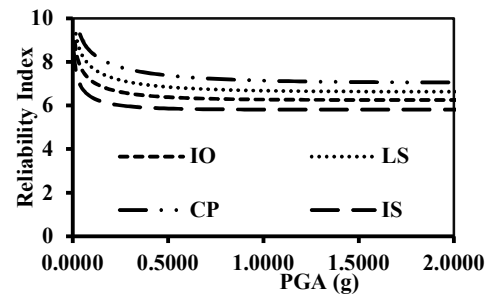


Figure 5.29 – Reliability Index for a G+9 regular building with isolated footing on soil 1 on plane ground under Denali earthquake at Conterminous U.S.

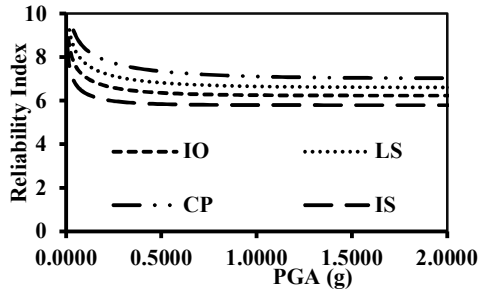


Figure 5.30 – Reliability Index for a G+9 vertically irregular building with isolated footing on soil 1 on plane ground under Loma Prieta earthquake at Conterminous U.S.

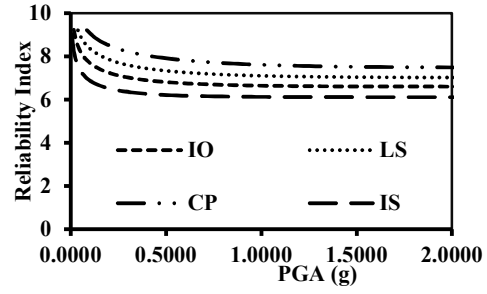


Figure 5.31 – Reliability Index for a G+9 vertically irregular building with isolated footing on soil 1 on plane ground under Denali earthquake at Conterminous U.S.

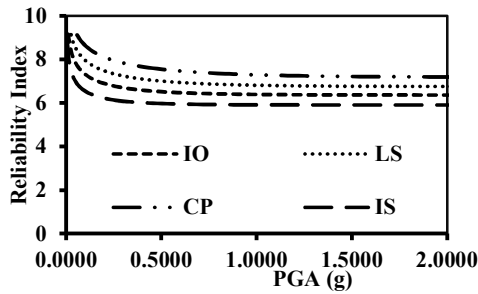


Figure 5.32 – Reliability Index for a G+9 horizontally irregular building with isolated footing on soil 1 on plane ground under Loma Prieta earthquake at Conterminous U.S.

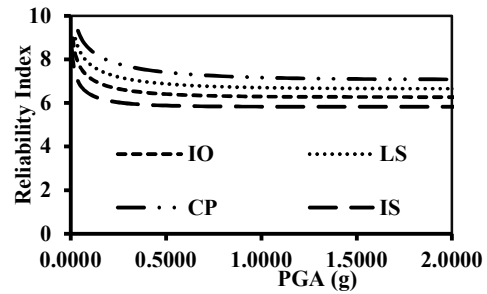


Figure 5.33 – Reliability Index for a G+9 horizontally irregular building with isolated footing on soil 1 on plane ground under Denali earthquake at Conterminous U.S.

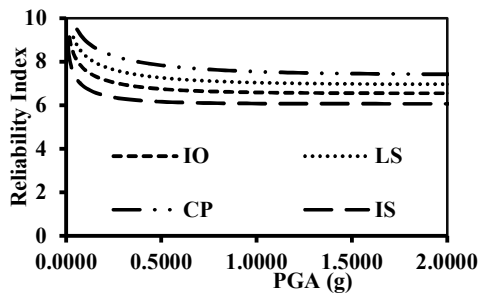


Figure 5.34 – Reliability Index for a G+9 regular building with isolated footing on soil 1 on sloping ground under Loma Prieta earthquake at Conterminous U.S.

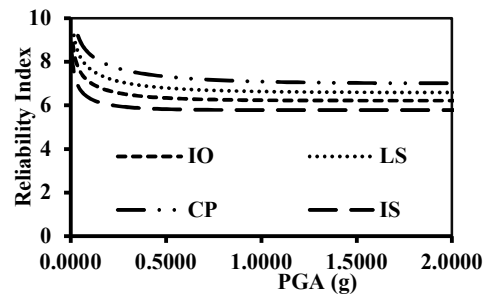


Figure 5.35 – Reliability Index for a G+9 regular building with isolated footing on soil 1 on sloping ground under Denali earthquake at Conterminous U.S.

5.4. DISCUSSION ON RELIABILITY CURVES

After analyzing reliability curves of frame buildings situated on uniform soil some important observations have been made. When a G+9 building is subjected to a particular earthquake, it has the most RI value when it is situated on soft soil. On the other hand, it has the least RI value when it is located on hard soil.

It is also to be noted that in most cases of a G+9 building, RI of the soil-structure system is more when it is subjected to a near-field earthquake like Loma Prieta earthquake. Exceptionally, in case of vertically irregular buildings, RI of the soil-structure system is more when it is subjected to a far-field earthquake like Denali earthquake. Minimum RIs are observed in vertical irregular building as compared to other types of G+9 building structures in case of near field earthquake. In case of far field earthquake, generally, minimum RIs are observed in regular building as compared to other types of G+9 building structures.

Now from the reliability curves of the frame buildings resting on layered soil, the following conclusions may be drawn. Generally, under the influence of a far-field earthquake RI of a soil-structure system is less than the RI of that system under the action of a near-field earthquake. However, in cases of vertically irregular buildings, RI due to far field earthquake is more than due to near field earthquake. Minimum RIs are observed in vertical irregular building as compared to other types of G+9 building structures in case of near field earthquake. In case of far field earthquake, minimum RIs are observed in regular building on sloping ground as compared to other types of G+9 building structures.

CHAPTER 6: FRAME STRUCTURES WITH PILE FOUNDATION

FOUNDATION

6.1 - GENERAL

We have chosen SeismoStruct software to perform nonlinear time history analysis of a G+9 regular building on pile foundation considering soil structure interaction. The element thus used for modelling such foundation is called 'Pile Foundations macro-element - ssilink2'.

6.2 - PILE FOUNDATIONS MACRO-ELEMENT - SSILINK2

This element extends the nonlinear macro-element approach to the analysis of laterally loaded flexible piles and soil-pile-structure interaction. It is based on the work of Correia and Pecker [2019b]. The lateral response of the entire soil-pile system to seismic actions is thus condensed at the pile-head, being represented by a zero-length element located at the base of the columns and subjected to the foundation input motion, as shown in the Figure below:

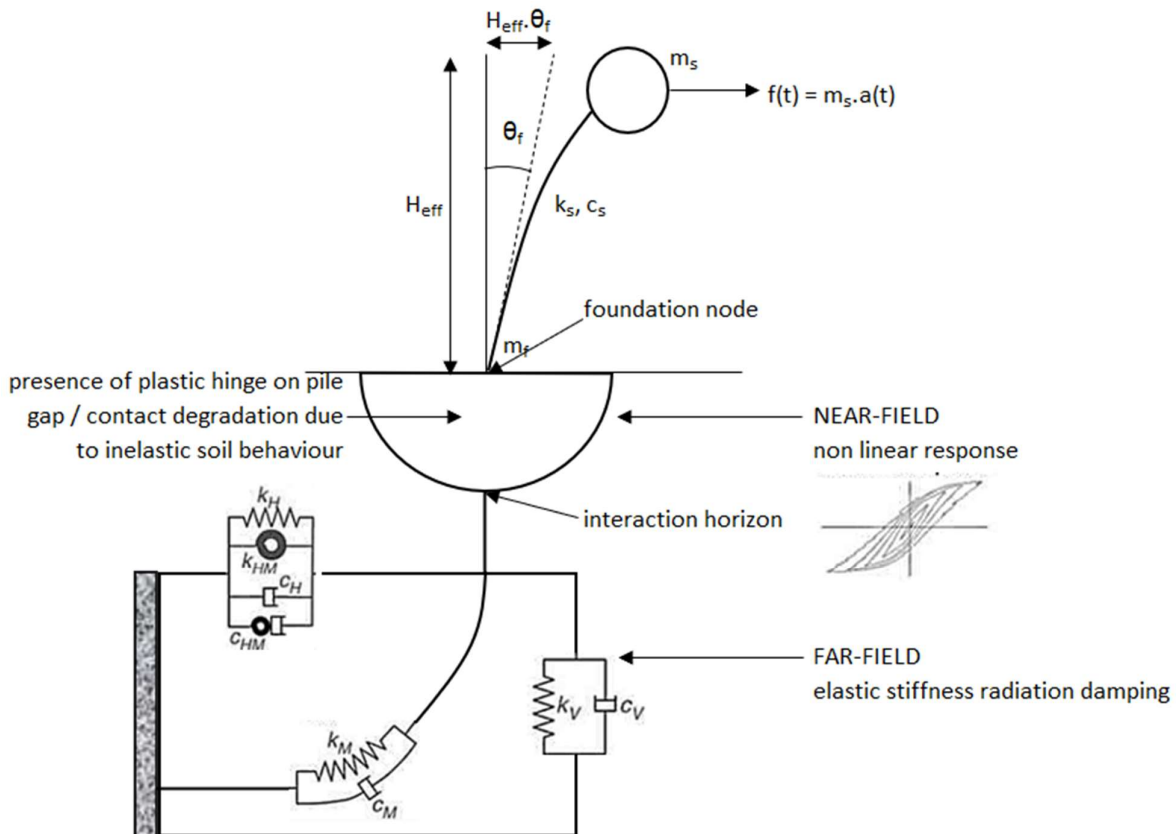


Figure 6.1 – Modelling lateral response of the entire soil-pile system [49]

The pile-head macro-element model represents the lateral behaviour of single vertical piles, subjected to a horizontal load and a moment, from the initial stages of loading up

until reaching failure. The effects of vertical loading are not directly considered in this model except for its influence on the plastic moment of the pile cross-section. Otherwise, it is considered that the upper zone of the soil profile, until the depth at which the plastic hinge will form, only contributes to the lateral load resistance. The vertical load is assumed to be transferred to the surrounding soil below that depth, where there is no influence of gap opening.

A saturated soil deposit is considered and, upon seismic motion, it is assumed to be impervious. The soil is thus considered to have undrained behaviour since the aim of the macro-element is to simulate the pile response under seismic actions, or short-term cyclic loads, and the Tresca failure criterion is assumed to be valid. In the Figure below, figure a represents the two simplified geotechnical scenarios considered, in terms of undrained shear strength (S_u) distribution along the depth of the soil deposit: constant or linear. Figure b illustrates the characteristic soil response for a laterally loaded long pile, namely: a soil passive wedge failure at shallow depths and flow-around failure at larger depths, with a possible gap formation at the back of the pile.

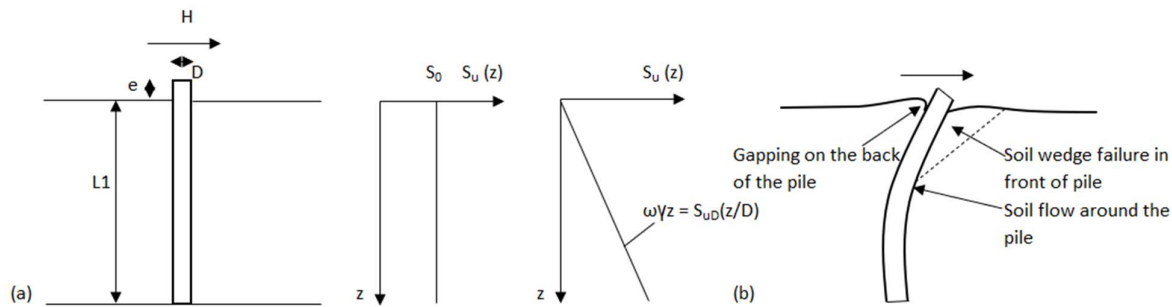


Figure 6.2 – (a) two simplified geotechnical scenarios in terms of undrained shear strength (S_u) distribution along the depth of the soil deposit (b) characteristic soil response for a laterally loaded long pile [49]

The proposed macro-element is based on the three major features of the behaviour of laterally loaded piles, namely:

1. Initial elastic response,
2. Gap opening and closure,
3. Failure loading conditions.

The bounding surface plasticity model is used to represent a continuous transition between the initial elastic response and the plastic flow at failure, for monotonic as well as cyclic pile-head loading conditions. The gapping behaviour is represented by a nonlinear elastic model which, however, takes into account and is influenced by the plastic deformation state in the surrounding soil.

The bounding surface in the macro-element model corresponds to the failure surface for laterally loaded piles. Since there is no evidence showing that non-associative behaviour should be considered, associative plasticity is used and the bounding surface acts simultaneously as the plastic potential surface. No axial load effects are considered in this macro-element formulation and, consequently, the failure surface is defined in the loading space of the pile-head horizontal force and moment only. Furthermore, a planar loading is

assumed.

A “rounded” approximate failure surface was proposed in Correia and Pecker [2019a], which is based on the so-called superellipse. Supposing a superellipse centred at the point (H_c, M_c) , with a horizontal axis length H_c and a vertical axis length M_c , which is also superimposed to a distortion of its shape, $g < 0$, this approximate failure surface can be expressed as [49]:

$$\frac{\bar{H}-H_c}{H_{n,e=0}} - \gamma \left| \frac{\bar{M}-M_c}{M_y} \right|^{n_H} + \left| \frac{\bar{M}-M_c}{M_y} \right|^{n_M} = 1 \quad \dots(37)$$

The positive exponents n_H and n_M control the curvature of the sides of the superellipse. The Figure below represents such distorted superellipse configuration, centred at the origin ($H_c = M_c = 0$), with its parameters calibrated in order to fit the failure surface for the linear S_u soil profile.

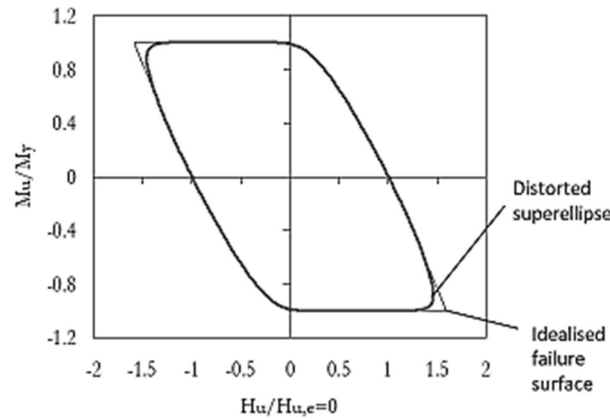


Figure 6.3 – Distorted superellipse configuration of failure surface [49]

Twenty-three parameters are required for the definition of the macro-element model:

- The Pile Diameter (DIAM)
- The Pile Stiffnesses for vertical, horizontal and rotational directions (K_{VV} , K_{HH} , K_{MM} , K_{HM} , K_{TT})
- The Pile Capacity (QQ_H_{MAX} , QQ_M_{MAX})
- The Superellipse BS parameters (Exp_{nH} , Exp_{nM} , $GAMMA$)
- The Maximum Gap depth (ZW)
- The Pile Flexural Stiffness (E_{plp})
- The Gap Evolution Parameter (BETA)
- The Minimum Gap Evolution Parameter (ETA)
- The Reference plastic modulus parameter (PL_{Ho})
- The exponent for plastic modulus evolution (PL_{nur})
- The Lower limit value for delta in unloading/reloading (Δ_{LIM})

The pile flexural stiffness, E_{plp} can be easily computed, while the pile yield moment, M_y , can be computed using any cross-section analysis tool (and considering the static vertical load on the pile).

On the other hand, formulas for $H_{u, e=0}$ and z_w , are derived in Correia and Pecker [2019a].

We have considered z_w as 3.73.

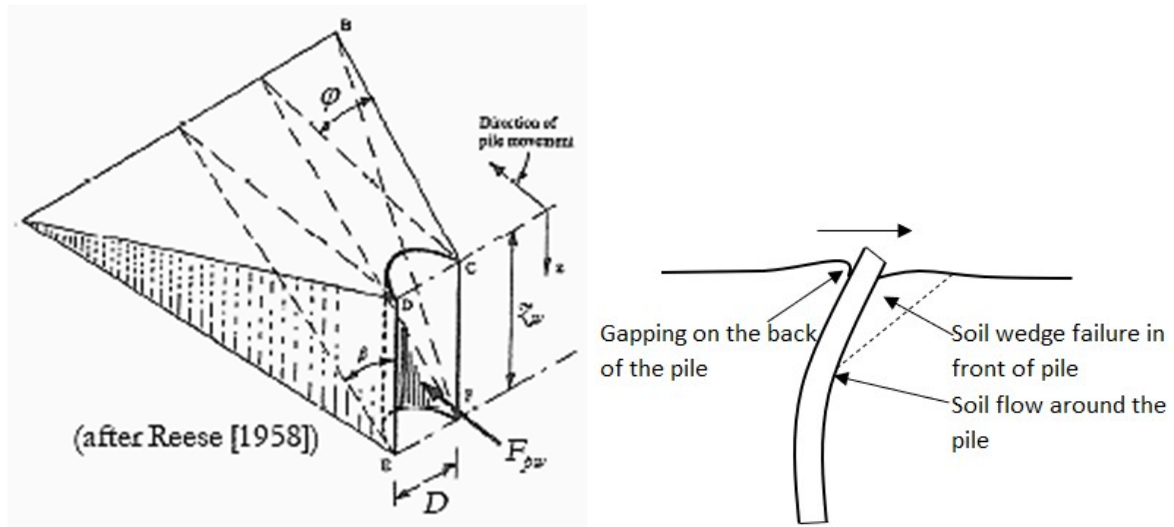


Figure 6.4 – Representation of maximum Gap depth / soil wedge depth corresponding to the failure mechanism. z_w [56]

Gazetas [1991] provides formulas for a direct computation of pile-head lateral and axial stiffness and damping coefficients. These are valid for soil profiles with constant, linear or parabolic increase of soil stiffness with depth, which are representative of OC clay, NC clay and sand, respectively. The Figure below represents the soil stiffness evolution with depth in such idealized soil profiles.

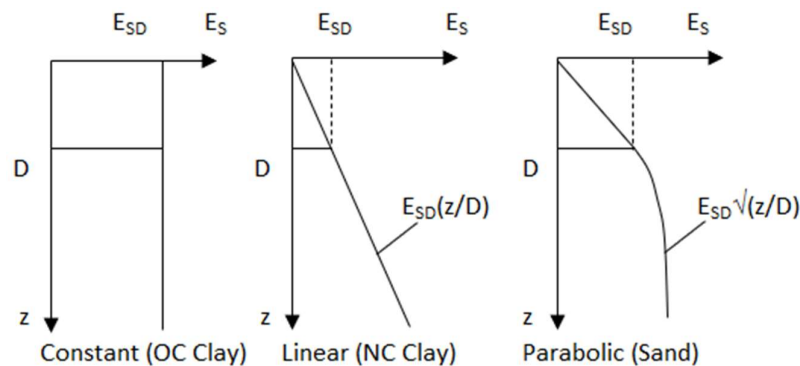


Figure 6.5 – Soil stiffness evolution with depth [49]

The constant graph will represent medium soil, linear graph will represent soft soil and parabolic graph will represent hard soil and soil 1.

His expressions for pile-head static stiffnesses have been adopted, with slight modifications, in the current version of EC 8 – Part 5 [2003]. These are valid for flexible or long piles and are summarized in the Table below.

Table 6.1 - Expressions for pile-head static stiffnesses [49]

Soil stiffness profile	$\frac{K_{HH}}{E_{SD}D}$	$\frac{K_{MM}}{E_{SD}D^3}$	$\frac{K_{HM}}{E_{SD}D^2}$
Constant $E_S = E_{SD}$	$1.08 \left(\frac{E_p}{E_{SD}} \right)^{0.21}$	$0.16 \left(\frac{E_p}{E_{SD}} \right)^{0.75}$	$-0.22 \left(\frac{E_p}{E_{SD}} \right)^{0.50}$
Linear $E_S = E_{SD}z / D$	$0.60 \left(\frac{E_p}{E_{SD}} \right)^{0.35}$	$0.14 \left(\frac{E_p}{E_{SD}} \right)^{0.80}$	$-0.17 \left(\frac{E_p}{E_{SD}} \right)^{0.60}$
Parabolic $E_S = E_{SD}\sqrt{(z / D)}$	$0.79 \left(\frac{E_p}{E_{SD}} \right)^{0.28}$	$0.15 \left(\frac{E_p}{E_{SD}} \right)^{0.77}$	$-0.24 \left(\frac{E_p}{E_{SD}} \right)^{0.53}$

In those expressions, D is the pile diameter, E_{SD} is the soil modulus of deformation at a depth equal to the pile diameter and E_p is the Young's modulus of the pile material. The pile-head stiffness matrix components follow the sign convention expressed in the Figure below.

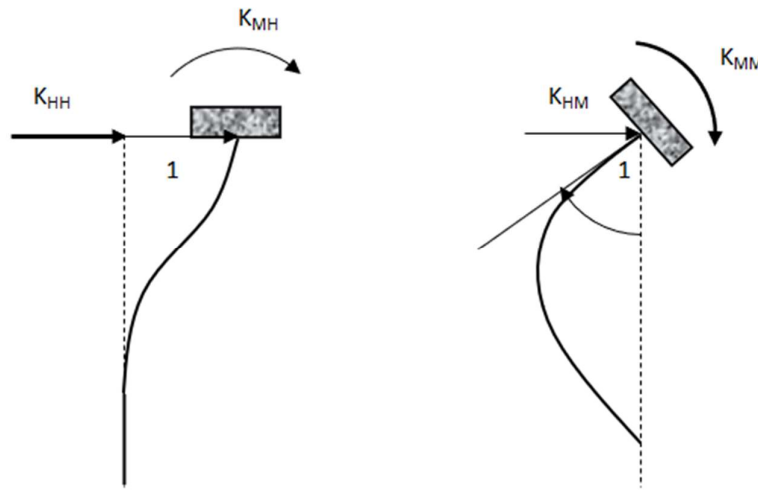


Figure 6.6 – Sign convention for pile-head stiffness matrix components [49]

Gazetas [1991] also presents the corresponding pile-head damping coefficients, which are computed for each frequency f according to the expressions in the table below.

The dynamic components of the pile-head stiffnesses have been shown by Gazetas [1984] to be roughly equal to one, for the usual frequency range of interest for structural response. Hence, pile-head static stiffnesses may be approximately used as dynamic ones, for single flexible piles. Variation of the damping ratio components with frequency is linear, as predicted by the expressions in the Table below. This means that radiation damping behaviour may be approximated by physical dashpots with constant damping coefficient C .

Table 6.2 – Expressions for variation of the damping ratio components with frequency

[49]

Soil stiffness profile	$\frac{\xi_{HH} V_{SD}}{fD}$	$\frac{\xi_{MM} V_{SD}}{fD}$	$\frac{\xi_{HM} V_{SD}}{fD}$	$\frac{f_s L_s}{V_{SL}}$
Constant $E_S = E_{SD}$	$1.10 \left(\frac{E_p}{E_{SD}} \right)^{0.17}$	$0.35 \left(\frac{E_p}{E_{SD}} \right)^{0.20}$	$0.85 \left(\frac{E_p}{E_{SD}} \right)^{0.18}$	0.25
Linear $E_S = E_{SDZ} / D$	1.80	0.40	1.00	0.19
Parabolic $E_S = E_{SD} \sqrt{(z / D)}$	$1.20 \left(\frac{E_p}{E_{SD}} \right)^{0.08}$	$0.35 \left(\frac{E_p}{E_{SD}} \right)^{0.10}$	$0.70 \left(\frac{E_p}{E_{SD}} \right)^{0.05}$	0.223

Gazetas (1991) has also presented the corresponding pile-head damping coefficients, which are computed for each frequency (f) according to the expressions in Table 6.2. These correspond only to the radiation damping component. Moreover, they are only valid for frequencies above the fundamental frequency of vibration of the soil deposit, since, if the bedrock is assumed to be rigid, no radiation damping exists below that frequency. The soil deposit fundamental frequencies (f_s) associated to each idealized soil profile are also given in Table 6.2, with L_s being the soil deposit depth and V_{SD} and V_{SL} being the shear wave velocity at a depth of one pile diameter and at the bottom of the soil profile, respectively. These damping ratio components will be used to formulate dashpot damping coefficients in Article 6.3.

The bounding surface parameters are fixed for each of the soil strength profiles and are shown in the Table below. The limit value d_{Lim} is a parameter related to the numerical convergence and varies between 0.01 and 0.2, with a default value of 0.1.

Table 6.3 – Bounding surface parameters [49]

S_u profile	n_H	n_M	γ
Constant S_u	8.435	2.000	-0.597
Linear S_u	7.040	2.000	-0.667

Finally, the remaining 4 calibration parameters, 2 of them are related to monotonic response –b and, and the 2 others are related to cyclic behaviour –h and n_{ur} . Alternatively, 2 of the parameters are related to the gapping behaviour –b and h, and 2 others are related to the plasticity model – and n_{ur} . The parameters b, and n_{ur} are always positive, while h can also be equal to zero if no residual gap opening is considered. Their default values and ranges of variation are presented in the table below.

Table 6.4 – Calibration parameters [49]

β	η	H_0^{pl}	n_{UR}
1	1	0.4	1
0.1-10	0-100	0.1-10	0.5-2

Note: Care should be taken on the ground motion input when a dynamic time history analysis with the SSI macro-element is made. In fact, given that the two nodes of the macro-element should have the same motion while no inertial interaction is present, the soundest way of performing the analysis is not by imposing the ground motion acceleration history at the base node but by imposing the corresponding inertia forces on the structural masses above.

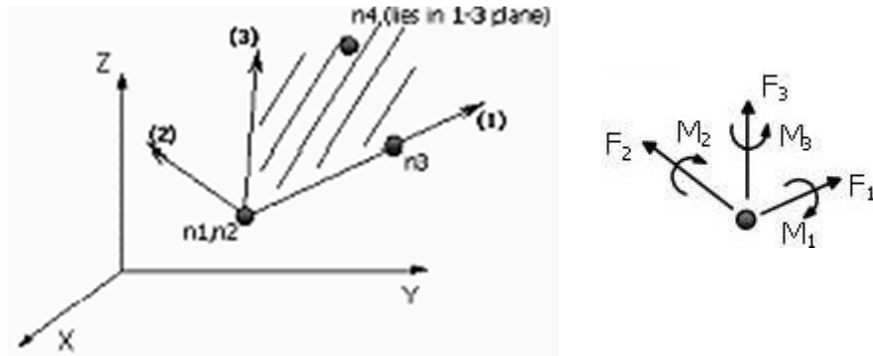


Figure 6.7 – Local Axes and Output Notation [49]

The value of Pile stiffness for vertical direction (K_{VV}) should be calculated by the following formula after George Gazetas [85].

$$K_z = [2GL/(1 - \nu)](0.73 + 1.54\chi^{0.75}) \text{ with } \chi = A_b/4L^2 \quad \dots(38)$$

Similarly, the value of Pile stiffness for rotational direction (K_{TT}) should also be calculated by the following formula after George Gazetas [85].

$$K_t = 3.5GI_{bz}^{0.75}(B/L)^{0.4}(I_{bz}/B^4)^{0.2} \quad \dots(39)$$

• A_b = area; and I_{bx} , I_{by} , and I_{bz} = area moments of inertia about the x-, y-, and z-axes of the actual soil-foundation contact surface. If loss of contact under part of the foundation (e.g., along the edges of a rocking foundation) is likely, the engineer may use his judgment to discount the contribution of this part of the basemat.

• B and L = half-width and half-length of the circumscribed rectangle.

• G and ν , the shear modulus and Poisson's ratio; or V_s and V_{La} , the shear wave velocity and Lysmer's analog wave velocity; the latter is the apparent propagation velocity of

compression-extension waves under a foundation, related to V_s and v according to (Gazetas et al. 1985; Dobry and Gazetas 1986)

- E_p = Young's modulus of the pile material
- E_{SD} = soil modulus of deformation at a depth equal to the pile diameter

Among the parameters for inputs of pile capacity, QQ_H_MAX represents horizontal capacity (maximum horizontal pile head force with no eccentricity) whereas QQ_M_MAX represents pile head yield moment.

The basic units for input parameters in SeismoStruct are as follows:

1. Length – m
2. Force – kN
3. Mass – tonne
4. Stress – kPa
5. Acceleration – m/sec^2

The values of pile foundations macro-element - SSILINK2 input parameters used in our model are provided in the table A.1 in Appendix. The values correspond to effect of four piles.

6.3 - DASHPOT DAMPING – DASHPT

This is a two-node damping element, which may be employed to represent a linear dashpot between any two given nodes, e.g., it can be used to represent a damper installed on a steel brace. Damping coefficients may be defined on all six global degrees-of-freedom, though, commonly, dampers will work only in one or two directions. The dashpot accounts for the relative motion between two element nodes, in order to calculate the dashpot forces.

In SeismoStruct, dampers are normally modelled by means of link elements with adequate response curves that may be able to characterise the non-velocity-dependent (at least within the typical range of earthquake velocities) force-displacement relationship of a given damper. However, in those cases where velocity dependence is important, this dashpt element may be employed instead, noting that currently only a linear force-velocity relationship is featured.

This dashpt element may also be employed whenever the need arises for the introduction of a Maxwell model (i.e. series coupling of damping and stiffness), by placing in series a link and a dashpt element. For a Kelvin-Voigt model (i.e., parallel coupling of damping and stiffness), one may again make use of a link element, this time placed in parallel with a dashpt, though in these cases it may result easier to simply assign directly to the link element a given viscous damping value.

Dashpot elements

1. can couple a force with a relative velocity;
2. can couple a moment with a relative angular velocity;
3. can be linear or nonlinear;
4. if linear, can be dependent on frequency in direct-solution steady-state dynamic analysis;

5. can be dependent on temperature and field variables; and
6. can be used in any stress analysis procedure.

The terms “force” and “velocity” are used throughout the description of dashpot elements. When the dashpot is associated with displacement degrees of freedom, these variables are the force and relative velocity in the dashpot. If the dashpots are associated with rotational degrees of freedom, they are torsional dashpots; these variables will then be the moment transmitted by the dashpot and the relative angular velocity across the dashpot.

In dynamic analysis the velocities are obtained as part of the integration operator; in quasi-static analysis the velocities are obtained by dividing the displacement increments by the time increment.

Dashpots are used to model relative velocity-dependent force or torsional resistance. They can also provide viscous energy dissipation mechanisms.

Dashpots are often useful in unstable, nonlinear, static analyses where the modified Riks algorithm is not appropriate (see Unstable collapse and post buckling analysis for a discussion of the modified Riks algorithm) and where the automatic time stepping algorithm is used because sudden shifts in configuration can be controlled by the forces that arise in the dashpots.

In such cases the magnitude of the damping must be chosen in conjunction with the time period so that enough damping is available to control such difficulties but the damping forces are negligible when a stable static response is obtained.

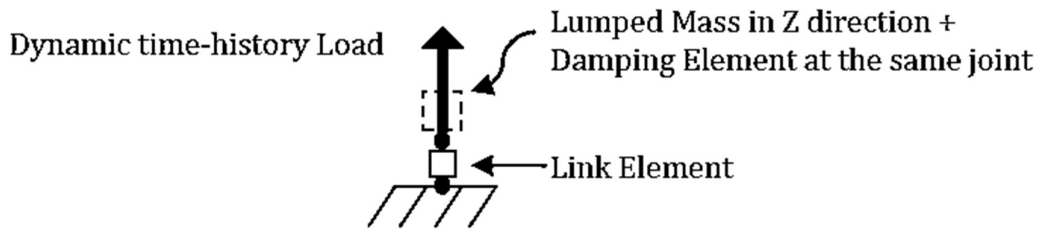


Figure 6.8 – FE model of damping element with link element (as per SeismoStruct manual)

The radiation damping equivalent dashpot coefficients in Table 6.2 are non-dimensional; the corresponding dimensional form can be retrieved using the following expressions:

$$\begin{aligned}
 C_{HH} &= \frac{2K_{HH} \cdot \xi_{HH}}{\omega} \\
 C_{MM} &= \frac{2K_{MM} \cdot \xi_{MM}}{\omega} \\
 C_{HM} &= \frac{2K_{HM} \cdot \xi_{HM}}{\omega}
 \end{aligned}
 \quad \dots(40)$$

ξ are the damping coefficients as per Table 6.2. The values of damping element input parameters used in our model are provided in the table A.2 in Appendix.

6.4 - LUMPED MASS - LMASS

We have to assign Lumped (concentrated) mass element for pile in SeismoStruct. This is a single-node lumped mass element, characterized by three translational and three rotational inertia values. The latter are defined by means of the mass moment of inertia (not to be confused with the second moment of area, commonly named also as moment of inertia), and may be computed using formulae available in the literature [e.g., Pilkey, 1994; Gere and Timoshenko, 1997].

The inertia mass values are to be defined with respect to the global reference system (X, Y and Z), and lead to a diagonal 6x6 element mass matrix.

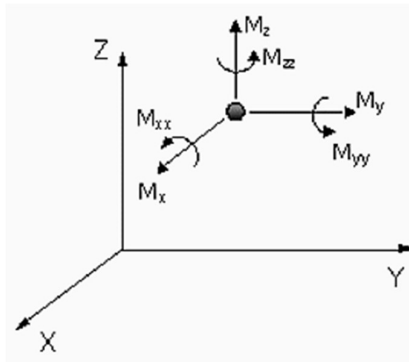


Figure 6.9 – Inertia mass with respect to the global reference system

In our case the lumped mass in X / Z and Y directions will consist of 4 piles and 1 pile cap. The values of lumped mass element input parameters used in our model are provided in the table below.

Table 6.5 – Lumped mass element - lmass input parameters (in X and Y directions)

Parameter	Symbol	Value	Unit
Mass in X direction / translational inertia value	Mx	66.871	t
Mass in Y direction / translational inertia value	My	66.871	t
Mass in Z direction / translational inertia value	Mz	0.000	t
Rotational inertia value in X direction	Mxx	0.000	t-m ²
Rotational inertia value in Y direction	Myy	0.000	t-m ²
Rotational inertia value in Z direction	Mzz	0.000	t-m ²

6.5 - MODELLING THE PROBLEM IN SEISMOSTRUCT

STEP 1: Units selected for our models are SI units and are as follows:

Length = m

Force = kN

Mass = tonne

Stress = kPa

Acceleration = m/sec²

Specific weight = kN/m³

STEP 2: Rebar topology is selected as European sizes. Analysis type is given as Dynamic Time History Analysis.

STEP 3: The material type for reinforcement considered in the analysis is Menegotto-Pinto steel model - `stl_mp`.

Menegotto-Pinto steel model - `stl_mp`: [as per SeismoStruct Manual]

This is a uniaxial steel model initially programmed by Yassin [1994] based on a simple, yet efficient, stress-strain relationship proposed by Menegotto and Pinto [1973], coupled with the isotropic hardening rules proposed by Filippou et al. [1983]. The current implementation follows that carried out by Monti et al. [1996]. An additional memory rule proposed by Fragiadakis et al. [2008] is also introduced, for higher numerical stability/accuracy under transient seismic loading. Its employment should be confined to the modelling of reinforced concrete structures, particularly those subjected to complex loading histories, where significant load reversals might occur.

As discussed by Prota et al. [2009], with the correct calibration, this model, initially developed with ribbed reinforcement bars in mind, can also be employed for the modelling of smooth rebars, often found in existing structures. Ten model calibrating parameters must be defined in order to fully describe the mechanical characteristics of the material:

Modulus of elasticity - E_s

This is the initial elastic stiffness of the material. Its value usually oscillates between 200 and 210 GPa. The default value is 200 GPa.

Yield strength - f_y

This is the stress at yield. Its value typically varies from 230 MPa up to 650 MPa. The default value is 500 MPa.

Strain hardening parameter - μ

This is the ratio between the post-yield stiffness (E_{sp}) and the initial elastic stiffness (E_s) of the material. The former is defined as $E_{sp} = (f_{ult} - f_y) / (\epsilon_{ult} - f_y / E_s)$, where f_{ult} and ϵ_{ult} represent the ultimate or maximum stress and strain capacity of the material, respectively. Its value commonly ranges from 0.005 to 0.015. The default value is 0.005.

Transition curve initial shape parameter - R_0

This is the initial (first loading cycle) value of the parameter R , that controls the shape of the transition curve between initial and post-yield stiffness, necessary to accurately represent Baushinger effects and pinching of the hysteretic loops. The default value is 20.

Transition curve shape calibrating coefficients - a_1 & a_2

These are the two coefficients used to calibrate the changes that must be applied to parameter R_0 in order to obtain the updated transition curve shape parameter R_n . Whilst a_1 is usually adopted with an invariable value of 18.5, a_2 might range between 0.05 and 0.15. The default values are 18.5 and 0.15 for coefficients a_1 and a_2 , respectively.

Isotropic hardening calibrating coefficients - a_3 & a_4

These are the two coefficients used to define the degree to which isotropic hardening is introduced in the stress-strain cyclic response characteristics of the material. In the case of a_3 , a variation between 0.01 and 0.025 can usually be found in practice, whilst for coefficient a_4 oscillations between 2 and 7 are commonly observed.

It is noted, however, that since the contribution of isotropic hardening is usually considerably smaller than its kinematic counterpart, variation of these parameters does not affect noticeably the cyclic response characteristics of the material. However, when large cyclic straining takes place, isotropic hardening may lead to unrealistically large member capacities (especially if no fracture/buckling strain has been set). For this reason, by default, isotropic hardening is disabled, and hence the default values are 0 and 1 for coefficients a_3 and a_4 , respectively.

It is possible to assign a negative value to parameter a_3 in order to artificially introduce softening in the response of a structural element featuring this material model. In such cases, however, users should check the results carefully, since this material model was not initially devised with such feature in mind.

Fracture/buckling strain - ϵ_{ult}

This is the strain at which fracture or buckling occurs. The default value is 0.1 (this may be a reasonable value for steel rebars in reinforced concrete sections, but rather inappropriate for steel profiles - users should thus set it with care (even using an infinitely large value when no fracture/buckling modelling is desired)).

Specific weight - γ

This is the specific weight of the material. The default value is 78 kN/m³.

The values of Menegotto-Pinto steel model input parameters used in our model are provided in the table below.

Table 6.6 – Menegotto-Pinto steel model stl_mp input parameters

Parameter	Symbol	Value	Unit
Modulus of elasticity	E_s	2.00E+08	kPa
Yield strength	f_y	500000	kPa
Strain hardening parameter	μ	0.005	
Transition curve initial shape parameter	R_0	20	
Transition curve shape calibrating coefficient	a_1	18.5	
Transition curve shape calibrating coefficient	a_2	0.15	
Isotropic hardening calibrating coefficient	a_3	0	
Isotropic hardening calibrating coefficient	a_4	1	
Fracture/buckling strain	ϵ_{ult}	0.1	
Specific weight	γ	78	kN/m ³
Mean strength		500000	kPa
Lower-bound strength		434782.609	kPa

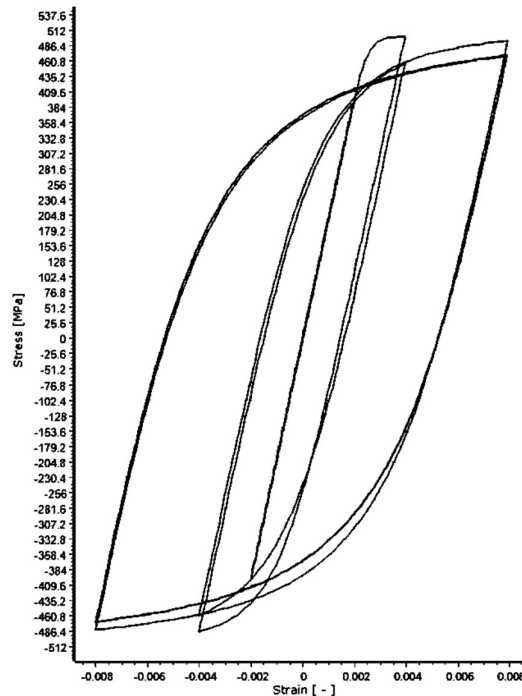


Figure 6.10 – Stress – strain graph of reinforcement in Seismostruct for M-P steel model

STEP 4: The material type for concrete considered in the analysis is Mander et al. nonlinear concrete model - con_ma.

Mander et al. nonlinear concrete model - con_ma: [as per SeismoStruct Manual]

This is a uniaxial nonlinear constant confinement model, initially programmed by Madas [1993], that follows the constitutive relationship proposed by Mander et al. [1988] and the cyclic rules proposed by Martinez-Rueda and Elnashai [1997].

The confinement effects provided by the lateral transverse reinforcement are incorporated through the rules proposed by Mander et al. [1988] whereby constant confining pressure is assumed throughout the entire stress-strain range. Five model calibrating parameters must be defined in order to fully describe the mechanical characteristics of the material:

Compressive strength - f_c

This is the cylinder (100x200 mm) compressive stress capacity of the material. Its value typically varies from 15 MPa up to 45 MPa. The default value is 28 MPa.

Tensile strength - f_t

This is the tensile stress capacity of the material. It can usually be estimated as $f_t = k_t \sqrt{f_c}$, where f_t varies from 2 MPa (concrete in direct tension) to 3 MPa (concrete in flexural tension), as suggested by Priestley et al. [1996]. When this value is reached, the concrete is assumed to abruptly lose its tensile resistance, without any sort of tension softening. The default value is 2.2 MPa (see note below).

Modulus of elasticity - E_c

This is the initial elastic stiffness of the material. Its value usually oscillates between 18000 and 30000 MPa. The default value is 24870 MPa.

Strain at peak stress - ϵ_c

This is the strain corresponding to the point of unconfined peak compressive stress (f_c). For normal strength plain concrete, this value is usually considered to lie within the range of 0.002 to 0.0022. The default value is 0.002 mm/mm.

Specific weight - γ

This is the specific weight of the material. The default value is 24 kN/m³. Here we have considered concrete grade as M25. The values of Mander et al. nonlinear concrete model input parameters used in our model are provided in the table below.

Table 6.7 – Mander et al. nonlinear concrete model - con_ma input parameters

Parameter	Symbol	Value	Unit
Compressive strength	f_c	25000	kPa
Tensile strength	f_t	3500	kPa
Modulus of elasticity	E_c	23500000	kPa
Strain at peak stress	ϵ_c	0.002	m/m
Specific weight	γ	24	kN/m ³
Mean strength		25000	kPa
Lower-bound strength		16666.667	kPa
Confinement factor		1.0	

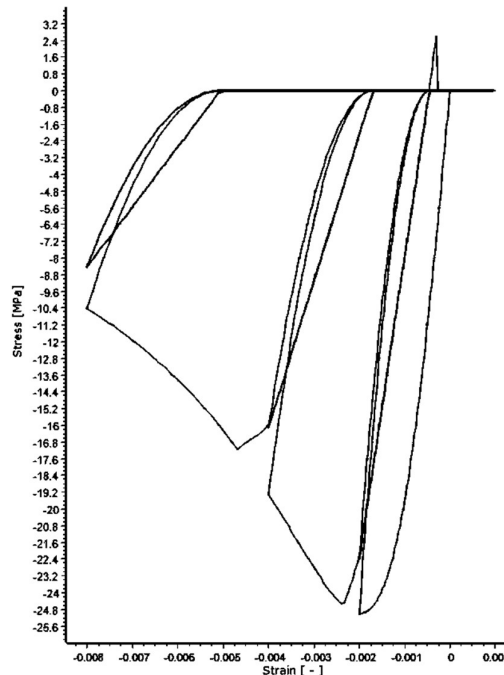


Figure 6.11 – Stress – strain graph of concrete in Seismostruct for Mander et al. nonlinear concrete model

STEP 5: The column section type is taken as reinforced concrete rectangular section – rcrs. A 0.5 m x 0.5 m column section is taken with cover of 25 mm. Longitudinal and transverse reinforcement are provided. 4 corner bars of 20 mm diameter, 4 nos. top and bottom bars of 16 mm diameter & 4 nos. left and right bars of 16 mm diameter are provided. Transverse reinforcement of 10 mm diameter bars having 4 legs with 100 mm spacing are considered in column. Accordingly, confinement factor calculated is 1.4732.

The confinement effect is usually quantified by the confinement factor λ , expressed by $\lambda = (f_s A_s) / (f_c A_c)$ in which A_s and A_c are the cross-sectional area of steel tube and concrete; and f_s and f_c are the strength of steel and concrete, respectively.

Confinement in concrete is achieved by the suitable placement of transverse reinforcement. This results in a significant increase in the strength and ductility of concrete. Correct interpretation and use of this improved performance of confined concrete, should be based on an appropriate analytic stress -strain model that captures the real behaviour.

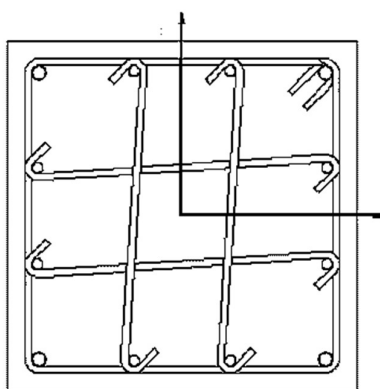


Figure 6.12 – Column section in SeismoStruct

STEP 6: Similarly, the beam section type is also taken as reinforced concrete rectangular section – rcrs. A 0.5 m x 0.3 m beam section is taken with cover of 25 mm. Longitudinal and transverse reinforcement are provided. 4 corner bars of 20 mm diameter, 4 nos. top and bottom bars of 16 mm diameter & 4 nos. left and right bars of 16 mm diameter are provided. Transverse reinforcement of 10 mm diameter bars having 4 legs with 100 mm spacing are considered in column. Accordingly, confinement factor calculated is 1.5215.

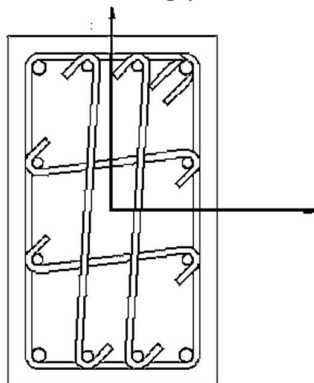


Figure 6.13 – Beam section in SeismoStruct

STEP 7: Column element class is selected as Inelastic force-based plastic hinge frame element type – *infrmFBPH*. Plastic hinge range is 16.67%. Rayleigh Damping is defined in column element class. For mode 1, period of 0.7 sec and damping ratio of 5% is considered. For mode 2, period of 0.3 sec and damping ratio of 5% is considered.

Inelastic force-based plastic hinge frame element type- *infrmFBPH*: [as per SeismoStruct Manual]

This is the plastic-hinge counterpart to the *infrmFB* element, featuring a similar distributed inelasticity forced-based formulation, but concentrating such inelasticity within a fixed length of the element, as proposed by Scott and Fenves [2006].

The advantages of such formulation are not only a reduced analysis time (since fibre integration is carried out for the two-member end sections only), but also a full control/calibration of the plastic hinge length (or spread of inelasticity), which allows the overcoming of localization issues, as discussed e.g., in Calabrese et al. [2010].

The number of section fibres used in equilibrium computations carried out at the element's end sections needs to be defined. The ideal number of section fibres, sufficient to guarantee an adequate reproduction of the stress-strain distribution across the element's cross-section, varies with the shape and material characteristics of the latter, depending also on the degree of inelasticity to which the element will be forced to. As a crude rule of thumb, users may consider that single-material sections will usually be adequately represented by 100 fibres, whilst more complicated sections, subjected to high levels of inelasticity, will normally call for the employment of 200 fibres or more. However, and clearly, only a sensitivity study carried out by the user on a case-by-case basis can unequivocally establish the optimum number of section fibres.

In addition, the plastic hinge length needs also to be defined, with the user being referred to the literature [e.g., Scott and Fenves 2006, Papadrakakis 2008, Calabrese et al. 2010] for guidance.

In this element's dialog box, it is also possible to define an element-specific damping, as opposed to the global damping described in here. To do so, users need simply to press the Damping button and then select the type of damping that better suits the element in question (users should refer to the Damping menu for a discussion on the different types of damping available and hints on which might be the better options). Users are reminded also that damping defined at element level takes precedence over global damping, that is, the "globally-computed" damping matrix coefficients that are associated to the degrees-of-freedom of a given element will be replaced by coefficients that will have been calculated through the multiplication of the mass matrix of the element by a mass-proportional parameter, or through the multiplication of the element stiffness matrix by a stiffness-proportional parameter, or through the calculation of an element damping Rayleigh matrix.

Similarly, to *infrmFB*, changes in reinforcement details can be achieved with the use of a single *infrmFBPH* element per member, when multiple sections have been defined. It is noted that these sections may differ only in the reinforcement (i.e., section type, dimensions and materials have to be the same).

If Rayleigh damping is defined at element level, using varied coefficients from one element to the other, or with respect to those employed in the global damping settings, then non-

classical Rayleigh damping is being modelled, classing Rayleigh damping requires uniform damping definition.

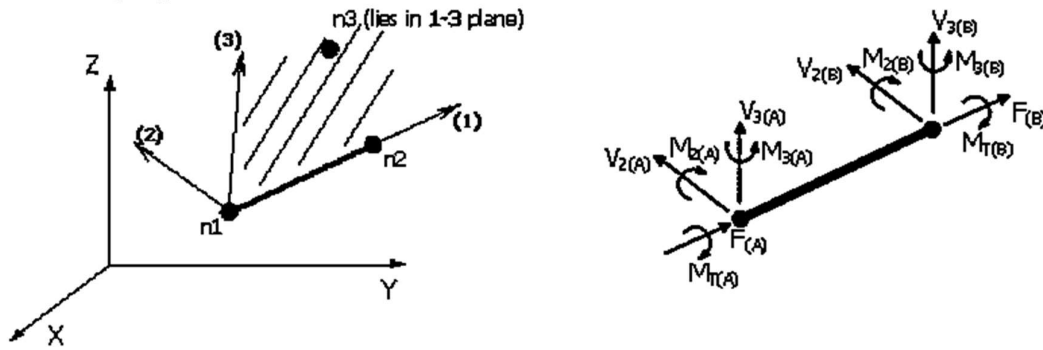


Figure 6.14 – Local Axes and Output Notation

The column section discretization is done as shown below.

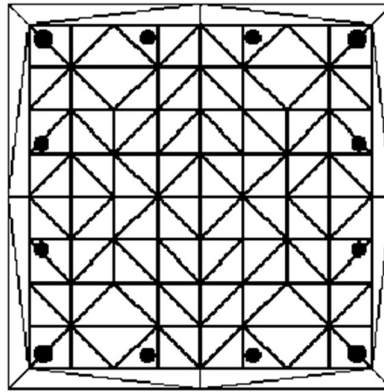


Figure 6.15 – Column section discretization in SeismoStruct

STEP 8: Similarly, beam element class is also selected as Inelastic force-based plastic hinge frame element type – `infrmFBPH`. Plastic hinge range is 16.67%. Rayleigh Damping is defined in column element class. For mode 1, period of 0.7 sec and damping ratio of 5% is considered. For mode 2, period of 0.3 sec and damping ratio of 5% is considered. The beam section discretization is done as shown below.

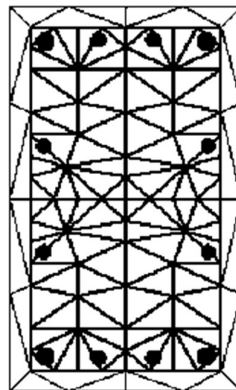


Figure 6.16 – Beam section discretization in SeismoStruct

STEP 9: All the beams and column members are assigned under Element Connectivity tab.

STEP 10: The floors are defined using Rigid Diaphragm Constraint type having restraint in X-Y plane.

STEP 11: Now we define the parameters for soil structure interaction with pile foundation, i.e., pile foundations macro-element – ssilink2, dashpot damping – dashpt and lumped mass – lmass All details of the above are discussed in Articles 6.2 to 6.4.

While defining lumped mass, mass-proportional damping is considered. For mode 1, period of 0.7 sec and damping ratio of 5% is considered. Mass parameter is calculated as 0.89759714. While defining link element, stiffness-proportional damping is considered. For mode 1, period of 0.7 sec and damping ratio of 5% is considered. Stiffness parameter is calculated as 0.01114086.

STEP 12: After this, the lumped mass element and link element are assigned to all the column base nodes at ground level under Element Connectivity tab. Before assigning the link element, we have to create duplicates of the structural nodes where the link element should be assigned. The nodes we will use to define the link element should have exactly the same coordinates in X, Y, Z directions as the original structural nodes. The duplicate node and original node will act as the link element end nodes. We will also have to define another two nodes as orientation nodes for a link element, ssilink2. The latter two nodes cannot be in the direction of any element axis. We are using default nodes in this case to define orientation of link element.

STEP 13: Next, all the translations and rotations of the column bases at ground level are restrained. It is important to note that restraints should be applied to the copies of the base nodes and not to the original base nodes.

STEP 14: Then we normalize our time history records of near field and far field earthquakes to a PGA of 1.0g and input the normalized motions in two directions in SeismoStruct. End of stage for Denali earthquake is given as 86 sec and number of Steps is given as 17200. This results in time step of 0.005 sec. End of stage for Loma Prieta earthquake is given as 40 sec and number of Steps is given as 2000. This results in time step of 0.02 sec.

STEP 14: After this, we applied the Dynamic Time History Load to all the column base nodes at ground level in X and Y directions. Loading type is set as acceleration and Curve Multiplier is set to 1.00. Seismostruct considers the self-weight of all assigned members automatically. It is important to note that loading should be applied to the copies of the base nodes and not to the original base nodes.

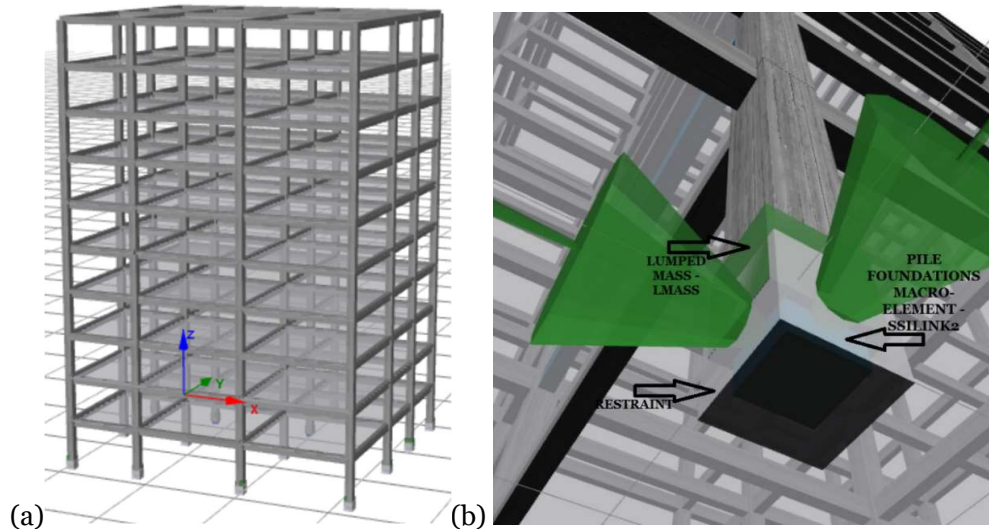


Figure 6.17 – (a) Isometric view of model in SeismoStruct (b) Link element, lumped mass and restraint at column base at ground level

6.6 - DISPLACEMENT TIME-HISTORIES OF ROOF AND BASE RESPONSES

The procedure to obtain displacement time history data for different floors from Seismostruct is as follows:

1. Run the program under Processor Tab.
2. After run is completed, go to post-Processor
3. Then go to Global Response Parameters → Structural displacements.
4. Select Displacement → X-axis or Y-axis.
5. Deselect Relative Displacement check box.
6. Select Views to Values.
7. Select the check boxes of the desired nodes.
8. Click on Refresh.
9. Copy the data to Microsoft Excel and plot the corresponding graphs.

After performing the entire analysis in SeismoStruct, displacement time-histories of the roof and the base have been plotted in case of every model. These plots are presented in Figure 6.18 to 6.33.

At first the output response data for X direction (as per model) is plotted. Similarly, response data for Y direction (as per model) is plotted for all the cases. Now we applied the 0.4 rule for combining the responses in the two directions for each case. This rule is explained in details in Equation 16. In that equation, we have considered γ as 0.4 or 40%.

We have presented only the combined response for bidirectional earthquake, keeping excess information flow in mind. It is important to note that all the responses presented below are corresponding to acceleration time history input normalized to PGA of 1.0g for both the near field and far field earthquakes.



Figure 6.18 – Resultant displacement time-history for base of a G+9 regular building with pile foundation on hard soil on plane ground under Loma Prieta earthquake

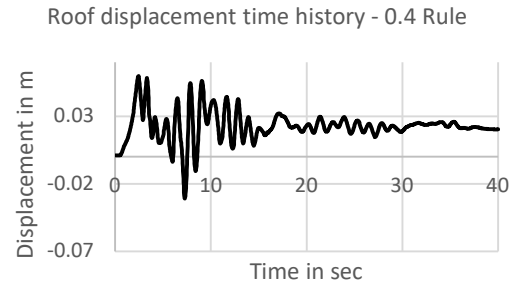


Figure 6.19 – Resultant displacement time-history for roof of a G+9 regular building with pile foundation on hard soil on plane ground under Loma Prieta earthquake

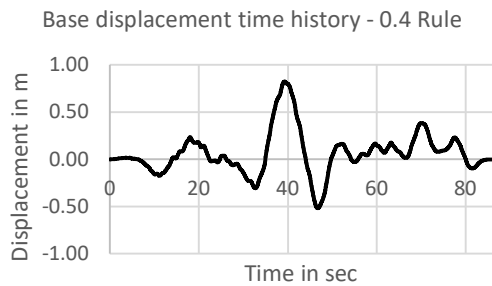


Figure 6.20 – Resultant displacement time-history for base of a G+9 regular building with pile foundation on hard soil on plane ground under Denali earthquake

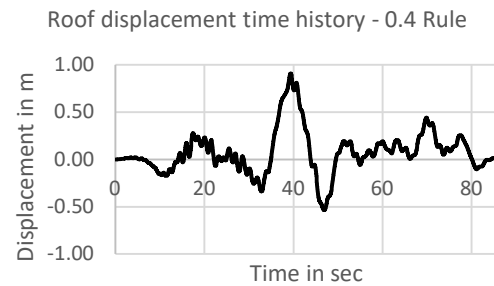


Figure 6.21 – Resultant displacement time-history for roof of a G+9 regular building with pile foundation on hard soil on plane ground under Denali earthquake

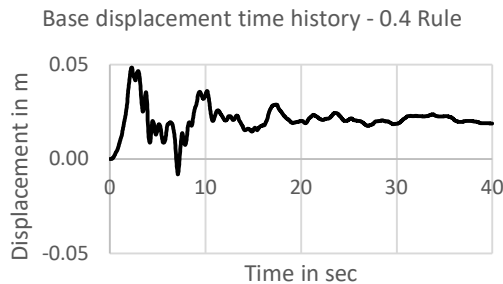


Figure 6.22 – Resultant displacement time-history for base of a G+9 regular building with pile foundation on medium soil on plane ground under Loma Prieta earthquake

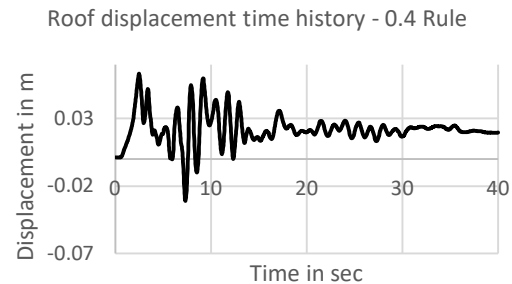


Figure 6.23 – Resultant displacement time-history for roof of a G+9 regular building with pile foundation on medium soil on plane ground under Loma Prieta earthquake

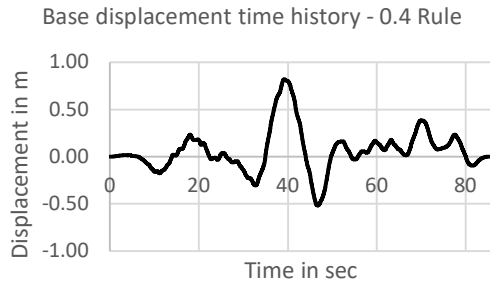


Figure 6.24 – Resultant displacement time-history for base of a G+9 regular building with pile foundation on medium soil on plane ground under Denali earthquake

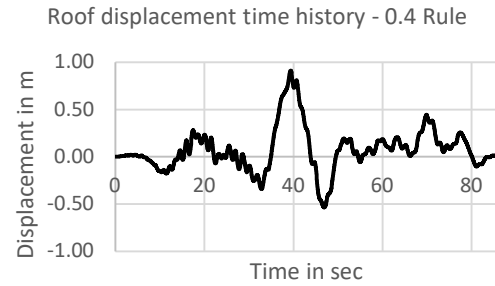


Figure 6.25 – Resultant displacement time-history for roof of a G+9 regular building with pile foundation on medium soil on plane ground under Denali earthquake

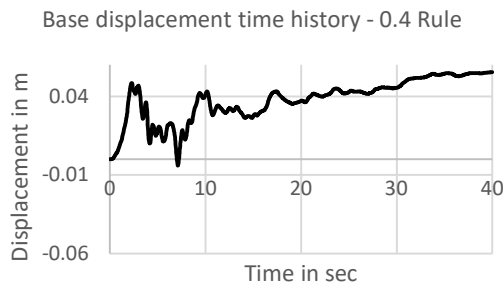


Figure 6.26 – Resultant displacement time-history for base of a G+9 regular building with pile foundation on soft soil on plane ground under Loma Prieta earthquake

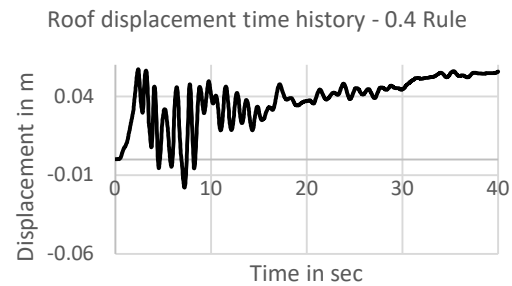


Figure 6.27 – Resultant displacement time-history for roof of a G+9 regular building with pile foundation on soft soil on plane ground under Loma Prieta earthquake

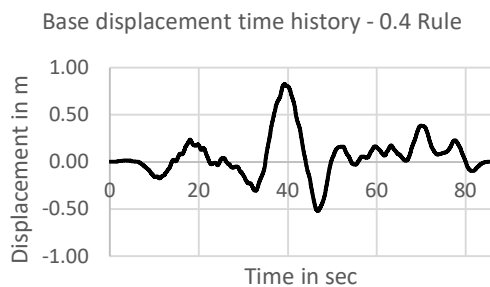


Figure 6.28 – Resultant displacement time-history for base of a G+9 regular building with pile foundation on soft soil on plane ground under Denali earthquake

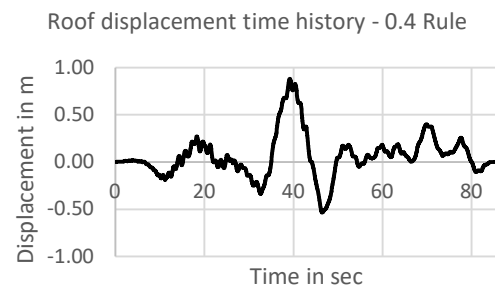


Figure 6.29 – Resultant displacement time-history for roof of a G+9 regular building with pile foundation on soft soil on plane ground under Denali earthquake

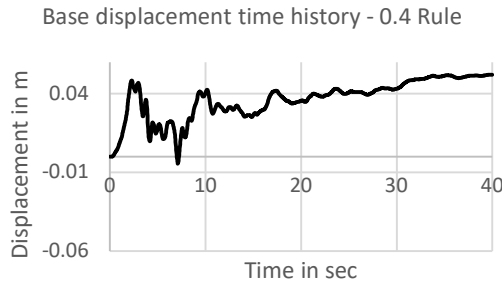


Figure 6.30 – Resultant displacement time-history for base of a G+9 regular building with pile foundation on soil 1 on plane ground under Loma Prieta earthquake

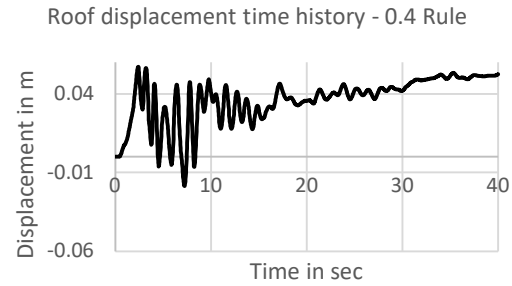


Figure 6.31 – Resultant displacement time-history for roof of a G+9 regular building with pile foundation on soil 1 on plane ground under Loma Prieta earthquake

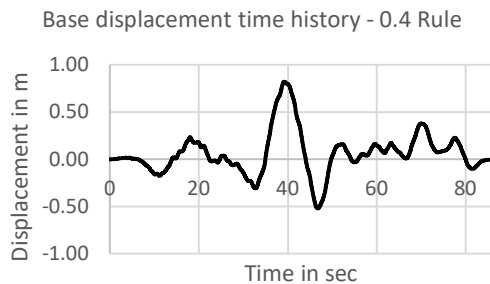


Figure 6.32 – Resultant displacement time-history for base of a G+9 regular building with pile foundation on soil 1 on plane ground under Denali earthquake

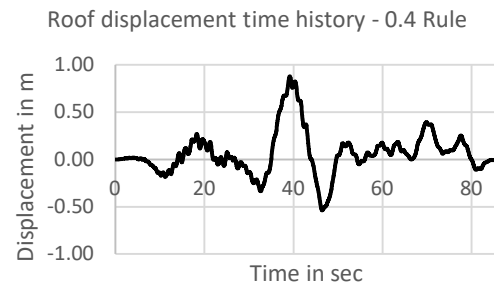


Figure 6.33 – Resultant displacement time-history for roof of a G+9 regular building with pile foundation on soil 1 on plane ground under Denali earthquake

The base response under the action of a particular earthquake differs mainly due to the variation in soil properties. It is to be mentioned that for most cases, when a particular building is subjected to a certain earthquake, roof drift is the highest when the building is located on hard soil. On the contrary, when the building rests on soft soil, roof displacement is the least. This may be due to higher flexibility effect of soft soil.

Further, the response of roof due to a far-field earthquake is more than the response of roof due to a near-field earthquake. This may be due to presence of low frequency wave in the far field ground motion. The displacement time history pattern varies considerably for near field and far field earthquake because of wide variation in the acceleration time history of the two earthquakes. For soil 1 and soft soil, the displacement time history has a gradually increasing profile after about 20 seconds for near field earthquake which is not the case for hard soil and medium soil.

6.7 - MAXIMUM DISPLACEMENT PROFILES

The maximum displacements of all the floors of each model are determined from the displacement time-history data of the respective floor. These values are plotted accordingly to obtain the maximum displacement profile of every building. These plots

are shown in Figure 6.34 to 6.35.

At first the maximum response data for X direction (as per model) is plotted. Similarly, maximum response data for Y direction (as per model) is plotted for all the cases. Now we applied the 0.4 rule for combining the time history responses in the two directions for each case and plot the corresponding maximum response data from the combined time history data thus obtained. In Equation 16, we have considered γ as 0.4 or 40%.

We have presented only the combined maximum response for bidirectional earthquake, keeping excess information flow in mind. It is important to note that all the responses presented below are corresponding to acceleration time history input normalized to PGA of 1.0g for both the near field and far field earthquakes.

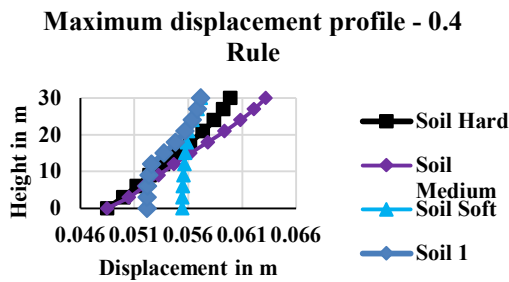


Figure 6.34 – Resultant maximum displacements of different floors of a G+9 regular building with pile foundation on plane ground under Loma Prieta earthquake

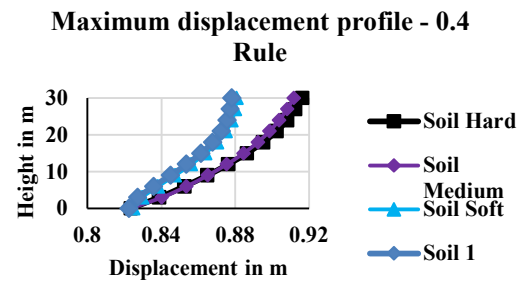


Figure 6.35 – Resultant maximum displacements of different floors of a G+9 regular building with pile foundation on plane ground under Denali earthquake

The figures clearly depict that, when a G+9 building is subjected to a far-field and near-field earthquake, its maximum displacement profile is concave upward. The shape of the maximum displacement profile strictly depends on the type of structure and soil. Building on medium soil tends to deflect more compared to buildings on other soil types for near field earthquake. On the contrary, for far field earthquake, building on hard soil tends to deflect more compared to buildings on other soil types. Finally, it is seen that the response of roof due to a far-field earthquake is more than the response of roof due to a near-field earthquake.

6.8 - MAXIMUM DRIFT PROFILES

Drift is a very important parameter in assessing the damage extent of a structure under earthquake. Definition and importance of drift are illustrated in Article 2.3.

At first the maximum response data for X direction (as per model) is plotted. Similarly, maximum response data for Y direction (as per model) is plotted for all the cases. Now we applied the 0.4 rule for combining the time history responses in the two directions for each case and thus obtained maximum drifts for all the floors in percentage.

We have presented only the combined maximum drift percentage for bidirectional

earthquake, keeping excess information flow in mind.

It is important to note that all the responses presented below are corresponding to acceleration time history input normalized to PGA of 1.0g for both the near field and far field earthquakes.

From equation 6, we get,

Drift in percentage of i th floor w.r.t. $(i-1)$ th floor = $(\text{displacement of } i\text{th floor} - \text{displacement of } (i-1)\text{th floor}) / \text{height between } i\text{th floor and } (i-1)\text{th floor} * 100$

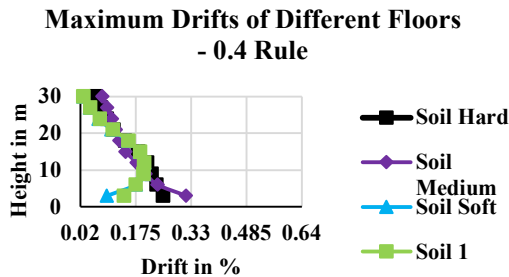


Figure 6.36 – Resultant maximum drifts of different floors of a G+9 regular building with pile foundation on hard soil on plane ground under Loma Prieta earthquake

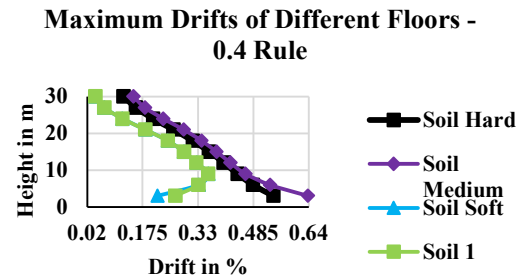


Figure 6.37 – Resultant maximum drifts of different floors of a G+9 regular building with pile foundation on hard soil on plane ground under Denali earthquake

After studying the maximum drift curves, the following points can be concluded. For soft soil and soil 1, maximum drift is obtained in 3rd and 4th floors for a G+9 building. For hard and soft soil, maximum drift is obtained in 1st floor. In all cases drift due to far field earthquake is more than due to near field earthquake. The variation in the pattern of the acceleration time histories quite well explains the phenomenon. Maximum drift is observed in medium soil for both near-field and far-field earthquakes.

6.9 - FRAGILITY CURVES

A detailed overview about the fragility curves along with different methods of plotting them has already been presented in Chapter 2 of this thesis. In this chapter at first PSDMs, for all the models, are developed from the percentage roof drifts. Thereafter, 2000 SAC/FEMA method [68] has been used for plotting the fragility curves considering IO, LS, CP and Indian Codal Limit. The PSDMs and fragility curves for all the models are shown in Figure 6.38 to 6.46.

After analyzing the PSDMs and fragility curves of frame buildings resting on uniform soil, several important remarks have been made. All the PSDMs are straight line in nature, which passes through the origin. The steep slope of the PSDM curve indicates the probability of exceeding the prescribed limit state (IO, LS, CP or Indian Codal Limit) under a specific earthquake intensity (in terms of PGA).

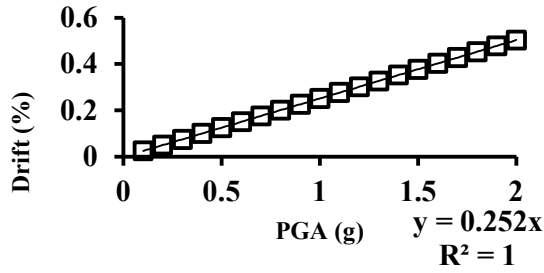


Figure 6.38 – PSDM for a G+9 regular building with pile foundation on hard soil on plane ground under Loma Prieta earthquake

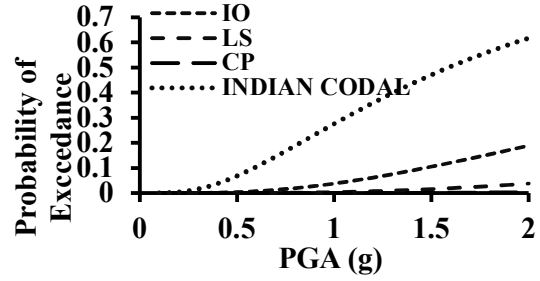


Figure 6.39 – Fragility curves for roof of a G+9 regular building with pile foundation on hard soil on plane ground under Loma Prieta earthquake

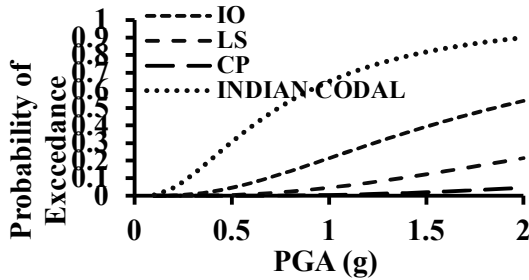


Figure 6.40 – Fragility curves for roof of a G+9 regular building with pile foundation on hard soil on plane ground under Denali earthquake

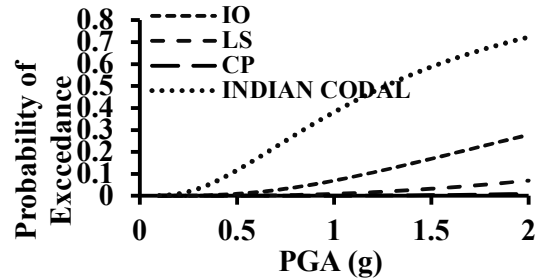


Figure 6.41 – Fragility curves for roof of a G+9 regular building with pile foundation on medium soil on plane ground under Loma Prieta earthquake

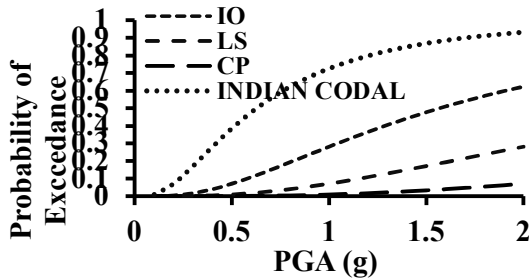


Figure 6.42 – Fragility curves for roof of a G+9 regular building with pile foundation on medium soil on plane ground under Denali earthquake

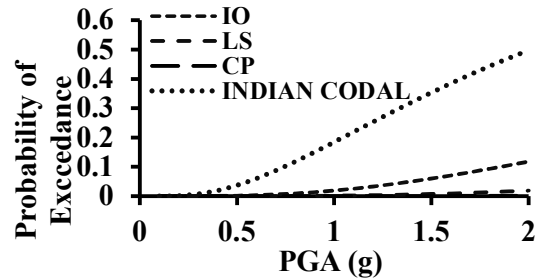


Figure 6.43 – Fragility curves for roof of a G+9 regular building with pile foundation on soft soil on plane ground under Loma Prieta earthquake

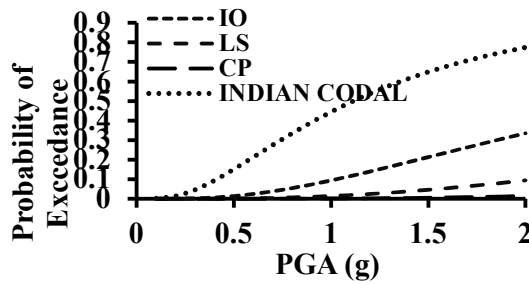


Figure 6.44 – Fragility curves for roof of a G+9 regular building with pile foundation on soft soil on plane ground under Denali earthquake

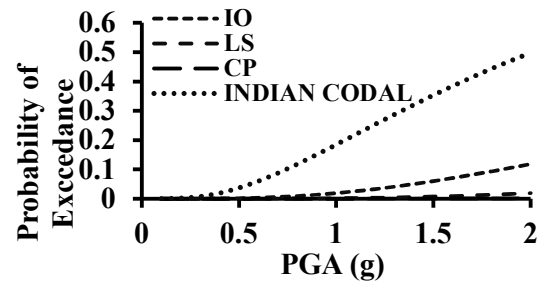


Figure 6.45 – Fragility curves for roof of a G+9 regular building with pile foundation on soil 1 on plane ground under Loma Prieta earthquake

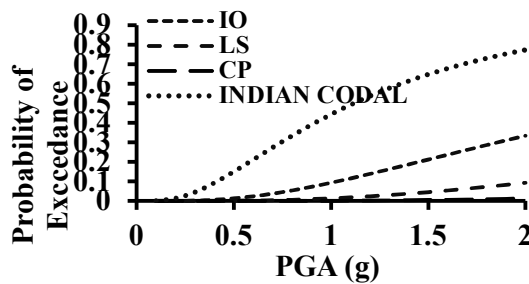


Figure 6.46 – Fragility curves for roof of a G+9 regular building with pile foundation on soil 1 on plane ground under Denali earthquake

After analyzing the PSDMs and fragility curves of frame buildings resting on uniform soil, several important remarks have been made. All the PSDMs are straight line in nature, which passes through the origin. The steep slope of the PSDM curve indicates the probability of exceeding the prescribed limit state (IO, LS, CP or Indian Codal Limit) under a specific earthquake intensity (in terms of PGA). Further, it is obvious that under a particular earthquake, the probability of exceeding Indian Codal Limit is the maximum and that of Collapse Prevention is the minimum. A G+9 building has the largest probability of exceeding a limit state when located on medium soil for both far and near field earthquake. However, it should also be noted that the probability of exceedance of a specific limit state for that soil-structure system is less when it is subjected to a near-field earthquake. Almost in all cases, the graph for CP is extremely flat almost touching the baseline.

6.10 - RELIABILITY CURVES

We have explained in details about reliability in Chapter 2 as well as Article 5.3. Here total 8 reliability curves have been generated for regular G+9 frame buildings located on three types of uniform soils (Hard, Medium and Soft) and one type of layered soils (Soil 1) in the Conterminous U.S. on plane ground with pile foundation which are subjected to a near-field (Loma Prieta) and a far-field (Denali) seismic excitation. These curves are displayed in Figure 6.47 to Figure 6.54.

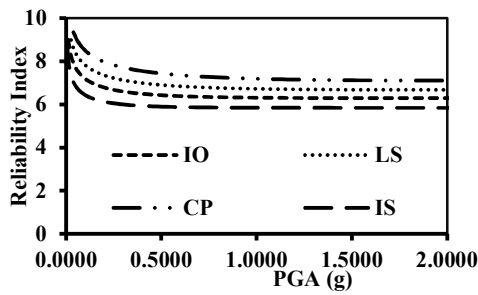


Figure 6.47 – Reliability Index for a G+9 regular building with pile foundation on hard soil on plane ground under Loma Prieta earthquake at Conterminous U.S.

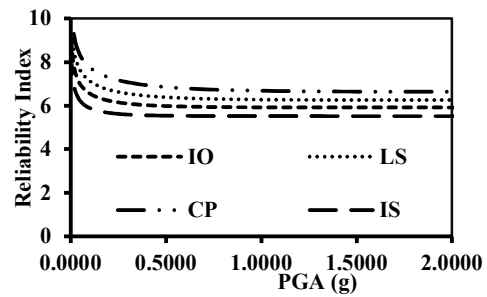


Figure 6.48 – Reliability Index for a G+9 regular building with pile foundation on hard soil on plane ground under Denali earthquake at Conterminous U.S.

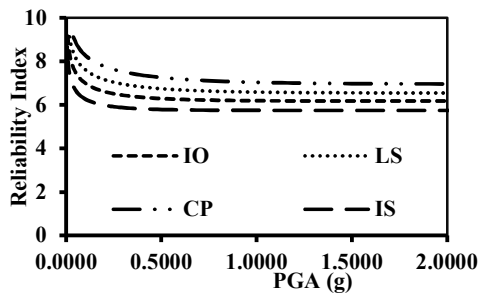


Figure 6.49 – Reliability Index for a G+9 regular building with pile foundation on medium soil on plane ground under Loma Prieta earthquake at Conterminous U.S.

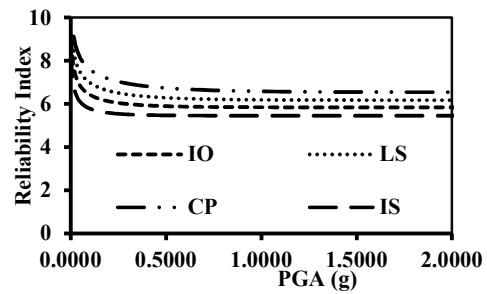


Figure 6.50 – Reliability Index for a G+9 regular building with pile foundation on medium soil on plane ground under Denali earthquake at Conterminous U.S.

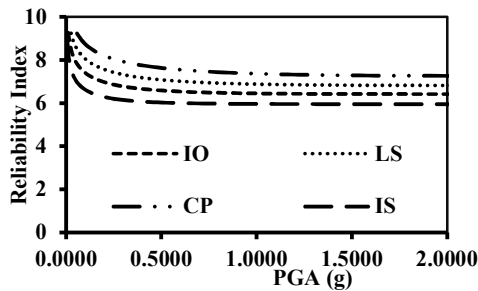


Figure 6.51 – Reliability Index for a G+9 regular building with pile foundation on soft soil on plane ground under Loma Prieta earthquake at Conterminous U.S.

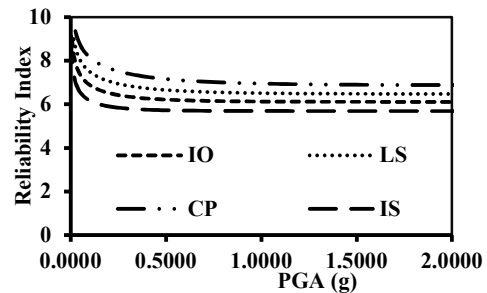


Figure 6.52 – Reliability Index for a G+9 regular building with pile foundation on soft soil on plane ground under Denali earthquake at Conterminous U.S.

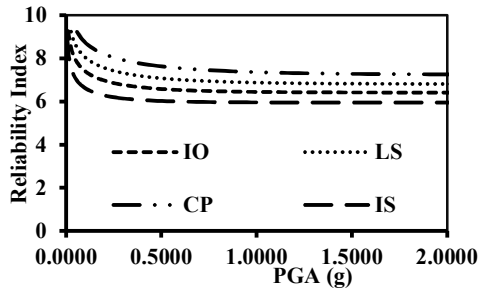


Figure 6.53 – Reliability Index for a G+9 regular building with pile foundation on soil 1 on plane ground under Loma Prieta earthquake at Conterminous U.S.

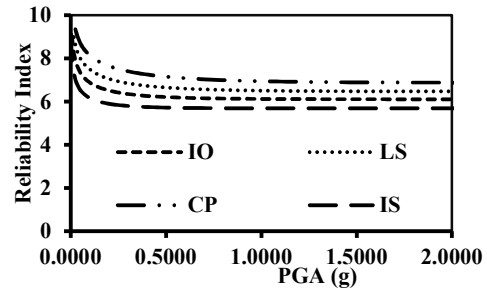


Figure 6.54 – Reliability Index for a G+9 regular building with pile foundation on soil 1 on plane ground under Denali earthquake at Conterminous U.S.

Discussion on reliability curves:

After analyzing reliability curves of frame buildings on pile foundation situated on uniform and layered soil, some important observations have been made. When a G+9 building with pile foundation is subjected to a particular earthquake, it has the least RI value when it is situated on medium soil. On the other hand, it has the maximum RI value when it is located on soft soil. It is also to be noted that in all cases of a G+9 building on pile foundation, RI of the soil-structure system is more when it is subjected to a near-field earthquake like Loma Prieta earthquake. The variation in the pattern of the acceleration time histories quite well explains the phenomenon.

CHAPTER 7: CONCLUDING REMARKS

7.1 - GENERAL

For a reliable assessment of seismic response of a structure, it is desirable that the structure be analyzed under bidirectional shaking covering all incidence angles. This is, however, computationally involved and time-consuming for routine design. Further, record-to-record variability inherent in seismic design results in potential variability in response.

To fully portray 'true' performance of structure, nonlinear response history analysis under bi-directional excitation compatible with the seismic activity of a region is essential. Current design often evaluates inelastic seismic demand under bi-directional shaking through combining responses under uni-directional excitation using simple rules.

It is a well-determined fact that dynamic soil structure- interaction (SSI) effect plays an important role on seismic response of structure. In the present study, an investigation has been carried out to understand the SSI effect on frame buildings constructed over both uniform and layered soils by nonlinear dynamic analysis using three-dimensional finite element modelling (FEM). For uniform soil, three types of soils (Hard, Medium and Soft) and while for layered soil seven types of layered soils (Soil 1 to Soil 7), each of which has six different layers, are taken for the present analysis. It is to be mentioned that for all the soil profiles fundamental frequency and amplification at fundamental frequency have been determined at frequency domain.

Various types of G+9 buildings on plane and sloping grounds are subjected to Loma Prieta (1989) earthquake motion as near-field and Denali (2002) earthquake as far-field seismic excitation under the above-mentioned soil condition. By the present analysis horizontal displacements and percentage drifts of all the storeys are computed and thus fragility curves for each storey are developed. Further on the basis of the fragility curve and seismic hazard curve of Conterminous U.S. reliability index have also been evaluated for different soil-structure combinations.

7.2 MAJOR FINDINGS

The major conclusions made from the study are:

1. When a building is subjected to an earthquake motion situated on hard soil, it has the least probability of exceeding a limit state. On the contrary, it has the largest probability of exceeding a limit state when located on soft soil.
2. In case of most G+9 building configurations, the probability of exceedance of a specific limit state for that soil-structure system is less when it is subjected to a near-field earthquake. Exceptionally, for vertically irregular building, the probability of exceedance value of the soil-structure system will be greater under the influence of near-field earthquake.
3. Irrespective of the type of soil and structure, when a G+9 building is subjected to a far-field or near-field earthquake, its maximum displacement profile is concave upward. The shape of the maximum displacement profile strictly depends on the type of structure and soil. This may be due to presence of seismic wave of all frequency content.

4. Generally, under the action of a near-field earthquake, the limit state exceedance probability is less compared to the far-field earthquake.
5. In most cases of a G+9 building, RI of the soil-structure system is more when it is subjected to a near-field earthquake like Loma Prieta earthquake. Exceptionally, in case of vertically irregular buildings, RI of the soil-structure system is more when it is subjected to a far-field earthquake like Denali earthquake.
6. Under the influence of a far-field earthquake RI of a soil-structure system is generally less than the RI of that system under the action of a near-field earthquake.
7. The base responses change only due to the variation in soil properties. In other words, change in building type does not alter the base response, if all other parameters are kept unchanged.
8. The roof and base responses under the action of a near-field earthquake are smaller than the far-field one. This may be due to the presence of low frequency seismic wave in far-field earthquake.
9. The displacement time history pattern varies considerably for near field and far field earthquake because of wide variation in the acceleration time history of the two earthquakes.
10. Maximum displacements of the floors always increase monotonically with their heights.
11. Vertical irregular building tends to deflect more compared to other building types for near field earthquake. On the contrary, for far field earthquake, vertical irregular building tends to deflect least compared to other building types.
12. In most cases drift due to far field earthquake is more than due to near field earthquake. The variation in the pattern of the acceleration time histories quite well explains the phenomenon. However, in cases of vertically irregular buildings, drift due to far field earthquake is less than due to near field earthquake.
13. Maximum drifts are observed in vertical irregular building as compared to other types of G+9 building structures in case of near field earthquake. In case of far field earthquake, maximum drifts are observed in regular building on sloping ground as compared to other types of G+9 building structures.
14. The generated PSDMs are actually straight lines passing through the origin. The steep slope of the PSDM curve indicates the probability of exceeding the prescribed limit state (IO, LS, CP or Indian Codal Limit) under a specific earthquake intensity (in terms of PGA). It is to be noted that under the action of a particular earthquake, the probability of exceedance of CP is the minimum and that of Indian Codal Limit is the maximum.
15. Highest probability of exceedance value of the soil-structure system is seen in case of building on sloping ground as compared to building on plane ground in case of far field earthquake. On the contrary for near field earthquake, lowest probability of exceedance value of the soil-structure system is seen in case of building on sloping ground as compared to building on plane ground.
16. For most cases, when a particular building is subjected to a certain earthquake, roof drift is the highest when the building is located on hard soil. On the contrary, when the building rests on soft soil, roof displacement is the least. This may be due to higher flexibility effect of soft soil.
17. For both far field and near field earthquake, deflection decreases from hard soil to soft soil.
18. Generally maximum drift is obtained in 2nd, 3rd and 4th floors in most of the cases of a G+9 building. As an exception maximum drift is obtained in 1st floor in cases of vertically irregular building on medium soil under far field earthquake, regular building on soft soil on sloping ground under near field earthquake and far field

- earthquake. Another huge exception is observed in case of vertically irregular building on soft soil under far field earthquake where maximum drift is obtained at roof.
19. A G+9 building has the largest probability of exceeding a limit state when located on soft soil.
 20. When a G+9 building is subjected to a particular earthquake, it has the most RI value when it is situated on soft soil. On the other hand, it has the least RI value when it is located on hard soil.
 21. Minimum RIs are observed in vertical irregular building as compared to other types of G+9 building structures in case of near field earthquake. In case of far field earthquake, generally, minimum RIs are observed in regular building as compared to other types of G+9 building structures.
 22. For layered soil, in case of far field earthquake, minimum RIs are observed in regular building on sloping ground as compared to other types of G+9 building structures.
 23. In case of G+9 building with pile foundation, for soil 1 and soft soil, the displacement time history has a gradually increasing profile after about 20 seconds for near field earthquake which is not the case for hard soil and medium soil.
 24. In case of G+9 building with pile foundation, building on medium soil tends to deflect more compared to buildings on other soil types for near field earthquake. On the contrary, for far field earthquake, building on hard soil tends to deflect more compared to buildings on other soil types.
 25. In case of G+9 building with pile foundation, for soft soil and soil 1, maximum drift is obtained in 3rd and 4th floors for a G+9 building. For hard and soft soil, maximum drift is obtained in 1st floor.
 26. In case of G+9 building with pile foundation, maximum drift is observed in medium soil for both near-field and far-field earthquakes.
 27. In case of G+9 building with pile foundation, a building has the largest probability of exceeding a limit state when located on medium soil for both far and near field earthquake.
 28. In case of G+9 building with pile foundation, when a G+9 building with pile foundation is subjected to a particular earthquake, it has the least RI value when it is situated on medium soil. On the other hand, it has the maximum RI value when it is located on soft soil.
 29. Representative results of spectral acceleration and characteristic length of Loma Prieta and Denali earthquake indicates that component characteristics appear to interchange over 90 and repeat over 180 as may also be expected from the transformation matrix.
 30. Representative results of spectral acceleration and characteristic length of Loma Prieta and Denali earthquake indicates that ground motion intensity is sensitive to orientations component-wise and relatively stable pair-wise.
 31. Representative results of spectral acceleration and characteristic length of Loma Prieta and Denali earthquake indicates that orientation corresponding to the peak intensity of one component is closely associated with the minimum of the other. Thus, NCI assumes a peak in this orientation.
 32. Representative results of spectral acceleration and characteristic length of Loma Prieta and Denali earthquake indicates that there exist certain orientations (intersection points) where intensities for two orthogonal components approach to be proximate. Thus, NCI may approach to minimum in this orientation.

7.3. LIMITATIONS OF PRESENT WORK

The limitations of present study are as follows:

1. Development of fragility curve by Monte Carlo method has not been carried out.
2. Input motion properties such as characteristics intensity and cumulative absolute velocity for different orientations was not studied.
3. Different irregular building configurations on pile foundation are not studied for all the different types of layered soils.
4. Buildings with different heights on pile foundation were not studied.
5. All the analyses were not performed for acceleration time history input normalized to different PGA values in terms of g (e.g., 0.1g, 0.2g, ..., 1.0g, 1.1g, ..., 2.0g). By doing so, we can obtain a more perfect PSDM curve.
6. Each model was not analyzed for different spectral acceleration of input accelerogram across orientations, $\psi = 0^\circ, 15^\circ, 30^\circ, \dots, 345^\circ, 360^\circ$ to obtain responses where building orientation is not parallel with orientation of input motion.

7.4. FUTURE SCOPES

1. Efficient seismic fragility analysis in the meta-model-based framework by efficient Monte Carlo Simulation can be performed.
2. Input motion properties such as characteristics intensity and cumulative absolute velocity for different orientations can be studied for Loma Prieta and Denali earthquake.
3. Reliability curves using various other seismic hazard curves, viz. Saltlake, Rajarhat, Sealdah, Howrah Station, Alaska etc. can be carried out in future.
4. Nonlinear time history analysis can be carried out by various other acceleration data from different stations for near and far field earthquake having different frequency ranges for better comparison study.
5. Different irregular building configurations on pile foundation can be studied for all the different types of layered soils.
6. Buildings with different heights on pile foundation can be studied.
7. All the analyses can be performed for acceleration time history input normalized to different PGA values in terms of g (e.g., 0.1g, 0.2g, ..., 1.0g, 1.1g, ..., 2.0g). By doing so, we can obtain a more perfect PSDM curve.
8. Each model can be analyzed for different spectral acceleration of input accelerogram across orientations, $\psi = 0^\circ, 15^\circ, 30^\circ, \dots, 345^\circ, 360^\circ$ to obtain responses where building orientation is not parallel with orientation of input motion.

In conclusion I wish to say that in working at the problem here dealt with I have had the loyal assistance of my guide Dr. A. Shiuly, and that I am indebted to him for several valuable suggestions.

REFERENCES

- [1] R. Roy, A. Roy, and G. Bhattacharya, "Estimating Seismic Response of RC Piers under Unidirectional and Bidirectional Shaking: A Mechanics-Based Approach," *J. Struct. Eng.*, vol. 146, no. 7, p. 04020113, 2020, doi: 10.1061/(asce)st.1943-541X.0002663.
- [2] A. Roy, A. Santra, and R. Roy, "Estimating seismic response under bi-directional shaking per uni-directional analysis: Identification of preferred angle of incidence," *Soil Dyn. Earthq. Eng.*, vol. 106, no. September 2017, pp. 163–181, 2018, doi: 10.1016/j.soildyn.2017.12.022.
- [3] S. Jeong and A. S. Elnashai, "Fragility analysis of buildings with plan irregularities," *4th Int. Conf. Earthq. Eng.*, no. 145, 2006.
- [4] D. Pramanik, A. K. Banerjee, and R. Roy, "Implications of bi-directional interaction on seismic fragilities of structures," *Coupled Syst. Mech.*, vol. 5, no. 2, pp. 101–126, 2016, doi: 10.12989/csm.2016.5.2.101.
- [5] A. Sengupta, L. Quadery, S. Sarkar, and R. Roy, "Influence of Bidirectional Near-Fault Excitations on RC Bridge Piers," *J. Bridg. Eng.*, vol. 21, no. 7, p. 04016034, 2016, doi: 10.1061/(asce)be.1943-5592.0000836.
- [6] A. Roy, G. Bhattacharya, and R. Roy, "Maximum credible damage of RC bridge pier under bi-directional seismic excitation for all incidence angles," *Eng. Struct.*, vol. 152, pp. 251–273, 2017, doi: 10.1016/j.engstruct.2017.09.008.
- [7] S. Chakroborty and R. Roy, "Seismic behavior of horizontally irregular structures: Current wisdom and challenges ahead," *Appl. Mech. Rev.*, vol. 68, no. 6, pp. 1–17, 2016, doi: 10.1115/1.4034725.
- [8] D. Kar and R. Roy, "Seismic Behavior of RC Bridge Piers under Bidirectional Excitations: Implications of Site Effects," *J. Earthq. Eng.*, vol. 22, no. 2, pp. 303–331, 2018, doi: 10.1080/13632469.2016.1233919.
- [9] K. Korkmaz, "Evaluation of Seismic Fragility Analyses," *14th World Conf. Earthq. Eng.*, p. 6, 2008.
- [10] A. Hadjian, "Earthquake reliability of structures," *13th World Conf. Earthq. Eng.*, no. 2295, p. Paper No. 2295, 2004, [Online]. Available: http://www.iitk.ac.in/nicee/wcee/article/13_2295.pdf.
- [11] L. Haj Najafi and M. Tehranizadeh, "Evaluation of seismic behavior for moment frames and eccentrically braced frames due to near-field ground motions," *Asian J. Civ. Eng.*, vol. 14, no. 6, pp. 809–830, 2013.
- [12] E. G. Abdelouafi, K. Benaissa, and K. Abdellatif, "Reliability Analysis in Performance-based Earthquake Engineering," *Procedia Eng.*, vol. 114, pp. 643–649, 2015, doi: 10.1016/j.proeng.2015.08.005.
- [13] M. Liu, "Reliability analysis of seismic shear-type structures," *Adv. Intell. Soft Comput.*, vol. 114, pp. 181–187, 2012, doi: 10.1007/978-3-642-03718-4_23.

- [14] A. Moustafa and S. Mahadevan, "Reliability analysis of uncertain structures using earthquake response spectra," *Earthq. Struct.*, vol. 2, no. 3, pp. 279–295, 2011, doi: 10.12989/eas.2011.2.3.279.
- [15] G. C. Foliente, P. Paevere, T. Saito, and N. Kawai, "Reliability assessment of timber shear walls under earthquake loads," *12th World Conf. Earthq. Eng. Auckland, New Zeal.*, no. January 2000, pp. 1–8, 2000.
- [16] P. Castaldo and T. Ferrentino, "Seismic reliability-based design approach for base-isolated systems in different sites," *Sustain.*, vol. 12, no. 6, 2020, doi: 10.3390/su12062400.
- [17] A. Mortezaei and S. M. Zahrai, "Seismic response of reinforced concrete building with viscoelastic damper under near field earthquake," *Asian J. Civ. Eng.*, vol. 10, no. 3, pp. 347–359, 2009.
- [18] I. Iervolino, G. Fabbrocino, and G. Manfredi, "Reliability methods for territorial seismic risk assessment," *13 th World Conf. Earthq. Eng.*, no. 550, p. 11, 2004.
- [19] Zabihullah, P. Singh, and M. Z. Aryan, "Effect of (Vertical & horizontal) geometric irregularities on the seismic response of RC structures," *Int. J. Emerg. Technol.*, vol. 11, no. 3, pp. 965–974, 2020.
- [20] D.-S. Moon, Y.-J. Lee, and S. Lee, "Fragility Analysis of Space Reinforced Concrete Frame Structures with Structural Irregularity in Plan," *J. Struct. Eng.*, vol. 144, no. 8, p. 04018096, 2018, doi: 10.1061/(asce)st.1943-541x.0002092.
- [21] J. Chambers and T. Kelly, "Nonlinear Dynamic Analysis - The Only Option for Irregular Structures," *13th World Conf. Earthq. Eng.*, no. 1389, p. 9, 2004.
- [22] D. P. Soni and B. B. Mistry, "Qualitative review of seismic response of vertically irregular building frames," *ISCT J. Earthq. Technol.*, vol. 43, no. 4, pp. 121–132, 2006.
- [23] B. M. Shah, R. Davis, and C. G. Nanda Kumar, "Seismic Fragility Analysis of Vertically Irregular Steel Framed Buildings," *IOP Conf. Ser. Mater. Sci. Eng.*, vol. 936, no. 1, 2020, doi: 10.1088/1757-899X/936/1/012043.
- [24] M. Hafezolghorani, F. Hejazi, R. Vaghei, M. S. Bin Jaafar, and K. Karimzade, "Simplified damage plasticity model for concrete," *Struct. Eng. Int.*, vol. 27, no. 1, pp. 68–78, 2017, doi: 10.2749/101686616X1081.
- [25] Y. Shakya and R. Suwal, "Seismic Deformation Analysis of Rockfill Dam," *J. Inst. Eng.*, vol. 10, no. 1, pp. 199–204, 2014, doi: 10.3126/jie.v10i1.10901.
- [26] K. Vijayendra, S. Prasad, and S. Nayak, "Computation of Fundamental Period of Soil Deposit : A Comparative Study," *Indian Geotech. Conf.*, no. 1, 2010, [Online]. Available: <http://gndec.ac.in/~igs/ldh/conf/2010/articles/045.pdf>.
- [27] A. G. N. Akhavan, Sh. Tavousi Tafreshi, "Fragility Assessment for Vertically Irregular Buildings with Soft Story," *Int. J. Civ. Environ. Eng.*, vol. 10, no. 10, pp. 1274–1282, 2016.

- [28] M. Priyadarshini, "Seismic Risk Assessment of RC Framed Vertically Irregular Buildings," *Natl. Inst. Technol. ROURKELA*, no. May, 2013, [Online]. Available: <http://ethesis.nitrkl.ac.in/5265/1/211CE2238.pdf>.
- [29] A. Ghanem and D. Moon, "Seismic Fragility Analysis of 3D Vertical Irregular Reinforced Concrete Structures," *Univ. Hawai'i Mānoa*, no. 1, pp. 1–16, 2021.
- [30] S. R. Patro, S. K. Sasmal, G. Suneel Kumar, P. Sarkar, and R. N. Behera, "Seismic Analysis of Vertical Geometric Irregular Building Considering Soil–Structure Interaction," *Lect. Notes Civ. Eng.*, vol. 138, pp. 545–556, 2021, doi: 10.1007/978-981-33-6564-3_46.
- [31] K. B. T. Latip Kumar Sharma, "Seismic Risk Assessment of Vertically Irregular Buildings," *IOE Grad. Conf.*, vol. 6, no. May, pp. 589–594, 2013, [Online]. Available: <http://ethesis.nitrkl.ac.in/5265/1/211CE2238.pdf>.
- [32] D. P. Robin, T. K. Padhy, D. Menon, and A. M. Prasad, "Seismic fragility of open ground story buildings in India," *9th US Natl. 10th Can. Conf. Earthq. Eng. 2010*, Incl. Pap. from 4th Int. Tsunami Symp., vol. 5, pp. 3446–3455, 2010.
- [33] R. Bhasker and A. Menon, "Characterization of ground motion intensity for the seismic fragility assessment of plan-irregular RC buildings," *Structures*, vol. 27, no. October, pp. 1763–1776, 2020, doi: 10.1016/j.istruc.2020.08.019.
- [34] P. Kumar and A. Samanta, "Seismic fragility assessment of existing reinforced concrete buildings in Patna, India," *Structures*, vol. 27, no. August 2019, pp. 54–69, 2020, doi: 10.1016/j.istruc.2020.05.036.
- [35] S. A. Aijaj and G. S. Deshmukh, "Seismic Analysis of Vertically Irregular Building," *SRTMU's Res. J. Sci.*, vol. 1, no. 2, pp. 67–86, 2012.
- [36] D. Cardone, M. Rossino, and G. Guesaldi, "Estimating fragility curves of pre-70 RC frame buildings considering different performance limit states," *Soil Dyn. Earthq. Eng.*, vol. 115, no. December 2014, pp. 868–881, 2018, doi: 10.1016/j.soildyn.2017.11.015.
- [37] M. Mouhine and E. Hilali, "Seismic vulnerability assessment of RC buildings with setback irregularity," *Ain Shams Eng. J.*, vol. 13, no. 1, 2021, doi: 10.1016/j.asej.2021.05.001.
- [38] S. H. Jeong and A. S. Elnashai, "Fragility relationships for torsionally-imbalanced buildings using three-dimensional damage characterization," *Eng. Struct.*, vol. 29, no. 9, pp. 2172–2182, 2007, doi: 10.1016/j.engstruct.2006.11.010.
- [39] A. Belejo, A. R. Barbosa, and R. Bento, "Influence of ground motion duration on damage index-based fragility assessment of a plan-asymmetric non-ductile reinforced concrete building," *Eng. Struct.*, vol. 151, pp. 682–703, 2017, doi: 10.1016/j.engstruct.2017.08.042.
- [40] M. S. Birzhandi and A. M. Halabian, "Fast fragility analysis of plan-asymmetric structures considering soil-structure interaction using flexible base 2 degrees of freedom Modal Pushover Analysis (F2MPA)," *Soil Dyn. Earthq. Eng.*, vol. 138, no.

August, 2020, doi: 10.1016/j.soildyn.2020.106270.

- [41] S. P. Stefanidou, A. G. Sextos, A. N. Kotsoglou, N. Lesgidis, and A. J. Kappos, "Soil-structure interaction effects in analysis of seismic fragility of bridges using an intensity-based ground motion selection procedure," *Eng. Struct.*, vol. 151, pp. 366–380, 2017, doi: 10.1016/j.engstruct.2017.08.033.
- [42] F. Cavalieri, A. A. Correia, H. Crowley, and R. Pinho, "Dynamic soil-structure interaction models for fragility characterisation of buildings with shallow foundations," *Soil Dyn. Earthq. Eng.*, vol. 132, no. November, 2020, doi: 10.1016/j.soildyn.2019.106004.
- [43] L. Su, H. P. Wan, Y. Dong, D. M. Frangopol, and X. Z. Ling, "Seismic fragility assessment of large-scale pile-supported wharf structures considering soil-pile interaction," *Eng. Struct.*, vol. 186, no. August 2018, pp. 270–281, 2019, doi: 10.1016/j.engstruct.2019.02.022.
- [44] A. Ajamy, B. Asgarian, C. E. Ventura, and M. R. Zolfaghari, "Seismic fragility analysis of jacket type offshore platforms considering soil-pile-structure interaction," *Eng. Struct.*, vol. 174, no. June, pp. 198–211, 2018, doi: 10.1016/j.engstruct.2018.07.066.
- [45] L. Su et al., "Seismic fragility analysis of pile-supported wharves with the influence of soil permeability," *Soil Dyn. Earthq. Eng.*, vol. 122, no. April, pp. 211–227, 2019, doi: 10.1016/j.soildyn.2019.04.003.
- [46] C. C. Mitropoulou, C. Kostopanagiotis, M. Kopanos, D. Ioakim, and N. D. Lagaros, "Influence of soil-structure interaction on fragility assessment of building structures," *Structures*, vol. 6, pp. 85–98, 2016, doi: 10.1016/j.istruc.2016.02.005.
- [47] S. M. Hoseyni, F. Yousefpour, A. Aghaei Araei, K. Karimi, and S. M. Hoseyni, "Effects of soil-structure interaction on fragility and seismic risk; a case study of power plant containment," *J. Loss Prev. Process Ind.*, vol. 32, pp. 276–285, 2014, doi: 10.1016/j.jlp.2014.09.009.
- [48] X. Wang, A. Ye, and B. Ji, "Fragility-based sensitivity analysis on the seismic performance of pile-group-supported bridges in liquefiable ground undergoing scour potentials," *Eng. Struct.*, vol. 198, no. March, p. 109427, 2019, doi: 10.1016/j.engstruct.2019.109427.
- [49] Seismostruct, "Pile Foundations macro-element - ssilink2," *Seism. Man.*, vol. 20, pp. 1–6, 2022.
- [50] C. H. Loh and M. J. Ma, "Reliability assessment of structure subjected to horizontal-vertical random earthquake excitations," *Struct. Saf.*, vol. 19, no. 1, pp. 153–168, 1997, doi: 10.1016/S0167-4730(96)00026-4.
- [51] J. R. Holliday, W. J. Gaggioli, and L. E. Knox, "Testing earthquake forecasts using reliability diagrams," *Geophys. J. Int.*, vol. 188, no. 1, pp. 336–342, 2012, doi: 10.1111/j.1365-246X.2011.05274.x.
- [52] R. Cairo, G. Dente, "Kinematic interaction analysis of piles in layered soils," *Univ.*

Calabr. Italy, vol. 14, no. 6, pp. 482–489, 2014.

- [53] C. Bolisetti, “Numerical and Physical Simulations of Soil- Structure Interaction,” Univ. Buffalo, State Univ. New York, no. November 2010, 2010.
- [54] B. Wang, J. Liu, Z. Cao, D. Zhang, and D. Jiang, “A multiple and multi-level substructure method for the dynamics of complex structures,” *Appl. Sci.*, vol. 11, no. 12, 2021, doi: 10.3390/app11125570.
- [55] J. J. Bommer and A. Marytínezpereira, “The effective duration of earthquake strong motion,” *J. Earthq. Eng.*, vol. 3, no. 2, pp. 127–172, 1999, doi: 10.1080/13632469909350343.
- [56] A. A. Correia, A. Pecker, S. L. Kramer, and R. Pinho, “Nonlinear Pile-Head Macro-Element Model: SSI effects on the Seismic Response of a Monoshaft-Supported,” 15th World Conf. Earthq. Eng., pp. 1–10, 2010.
- [57] S. Kramer, *Geotechnical Earthquake Engineering*. 1996.
- [58] T. K. Datta, *Seismic Analysis of Structures*. 2010.
- [59] R. W. Clough and J. Penzien, “Dynamics of structures,” *Earthq. Eng. Handb.*, pp. 3-1-3–40, 2002, doi: 10.1139/l90-078.
- [60] S. Escoffier and J. Chazelas, “Seismic soil structure interaction,” *ICPMG2014 – Phys. Model. Geotech. NPTEL*, pp. 1045–1051, 2014, doi: 10.1201/b16200-148.
- [61] J. P. Wolf, *Dynamic soil-structure interaction*. 1985.
- [62] J. A. Hunter et al., “Surface and downhole shear wave seismic methods for thick soil site investigations,” *Soil Dyn. Earthq. Eng.*, vol. 22, no. 9–12, pp. 931–941, 2002, doi: 10.1016/S0267-7261(02)00117-3.
- [63] R. Sarkar, D. K. Paul, and L. Stempniewski, “Influence of Reservoir and Foundation on the Nonlinear Dynamic Response of Concrete Gravity Dams,” *ISET J. Earthq. Technol. Pap. No. 490*, vol. 44, no. 2, pp. 377–389, 2007.
- [64] J. Lee and G. L. Fenves, “Plastic-Damage Model for Cyclic Loading of Concrete Structures,” *J. Eng. Mech.*, vol. 124, no. 8, pp. 892–900, 1998.
- [65] J. Lubliner, J. Oliver, S. Oller, and E. Onate, “A Plastic-Damage Model for Concrete,” *Int. J. Solids Struct.*, vol. 25, no. 3, pp. 299–326, 1989.
- [66] M. N. Fardis and T. B. Panagiotakos, “Seismic design and response of bare and masonry-infilled reinforced concrete buildings. Part II: Infilled structures,” *J. Earthq. Eng.*, vol. 1, no. 3, pp. 475–503, 1997, doi: 10.1080/13632469708962375.
- [67] I. Chowdhury and S. P. Dasgupta, “Computation of Rayleigh damping coefficients for large systems,” *Electron. J. Geotech. Eng.*, vol. 8 C, no. May, 2003.
- [68] FEMA 356, “Prestandard and Commentary for the Seismic Rehabilitation of Buildings,” no. November, p. 519, 2000.

- [69] J. P. Narayan, "Study of basin-edge effects on the ground motion characteristics using 2.5-D modelling," *Pure Appl. Geophys.*, vol. 162, no. 2, pp. 273–289, 2005, doi: 10.1007/s00024-004-2600-8.
- [70] J. P. Narayan and S. P. Singh, "Effects of Soil Layering on the Characteristics of Basin-Edge Induced Surface Waves and Differential Ground Motion," *J. Earthq. Eng.*, vol. 10, no. 4, pp. 74–80, 1991.
- [71] J. P. Narayan, "Effects of impedance contrast and soil thickness on basin-transduced rayleigh waves and associated differential ground motion," *Pure Appl. Geophys.*, vol. 167, no. 12, pp. 1485–1510, 2010, doi: 10.1007/s00024-010-0131-z.
- [72] J. P. Narayan, "Effects of P-wave and S-wave impedance contrast on the characteristics of basin transduced Rayleigh waves," *Pure Appl. Geophys.*, vol. 169, no. 4, pp. 693–709, 2012, doi: 10.1007/s00024-011-0338-7.
- [73] Bureau of Indian Standards New Delhi, "Criteria for Earthquake Resistant Design of Structures - General Provisions and Buildings Part-1," *Bur. Indian Stand. New Delhi*, vol. Part 1, pp. 1–39, 2002.
- [74] S. K. Nath, M. D. Adhikari, S. K. Maiti, N. Devaraj, N. Srivastava, and L. D. Mohapatra, "Earthquake scenario in West Bengal with emphasis on seismic hazard microzonation of the city of Kolkata, India," *Nat. Hazards Earth Syst. Sci.*, vol. 14, no. 9, pp. 2549–2575, 2014, doi: 10.5194/nhess-14-2549-2014.
- [75] J. Song and B. R. Ellingwood, "Seismic Reliability of Special Moment Steel Frames with Welded Connections: I," *J. Struct. Eng.*, vol. 125, no. 4, pp. 372–384, 1999, doi: 10.1061/(asce)0733-9445(1999)125:4(372).
- [76] J. Song and B. R. Ellingwood, "Seismic Reliability of Special Moment Steel Frames with Welded Connections: II," *J. Struct. Eng.*, pp. 372–384, 1999.
- [77] B. R. Ellingwood, "Earthquake Risk Assessment of Building Structures," *Reliab. Eng. Syst. Saf.*, vol. 74, no. 3, pp. 251–262, 2001.
- [78] A. M. Hasofer and N. C. Lind, "An exact and invariant first order reliability format," *J. Eng. Mech. Div.*, vol. 100, no. July, pp. 111–121, 1974.
- [79] A. Shiuly, R. B. Sahu, and S. Mandal, "Effect of soil on ground motion amplification of Kolkata City," *Int. J. Geotech. Earthq. Eng.*, vol. 5, no. 1, pp. 1–20, 2014, doi: 10.4018/ijgee.2014010101.
- [80] A. Shiuly, V. Kumar, and J. P. Narayan, "Computation of ground motion amplification in Kolkata megacity (India) using finite-difference method for seismic microzonation," *Acta Geophys.*, vol. 62, no. 3, pp. 425–450, 2014, doi: 10.2478/s11600-013-0169-2.
- [81] Z. Li, P. Kotronis, S. Escoffier, and C. Tamagnini, "A hypoplastic macroelement for single vertical piles in sand subject to three-dimensional loading conditions," *Acta Geotech.*, vol. 11, no. 2, pp. 373–390, 2016, doi: 10.1007/s11440-015-0415-7.
- [82] L. M. Zhang, "Behavior of Laterally Loaded Large-Section Barrettes," *J. Geotech.*

Geoenvironmental Eng., vol. 129, no. 7, pp. 639–648, 2003, doi: 10.1061/(asce)1090-0241(2003)129:7(639).

- [83] Z. Li, P. Kotronis, S. Escoffier, and C. Tamagnini, “Macroelement Modeling for Single Vertical Piles,” *Int. Soc. Soil Mech. Geotech. Eng.*, vol. 1, no. 2, pp. 161–162, 1984, doi: 10.1016/0266-1144(84)90012-8.
- [84] N. Graine, M. Hjiiaj, and K. Krabbenhoft, “Macro-Model for Rigid Pile Foundation in Cohesive-Frictional Soils: Determination of the Failure Surface,” 16th Eur. Conf. Earthq. Eng. Greece, Thessaloniki, June 18-21, 2018, no. November, 2018.
- [85] G. Gazetas, “Formulas and Charts for Impedances of Surface and Embedded Foundations,” *J. Geotech. Eng.*, vol. 117, no. 9, pp. 1363–1381, 1992.
- [86] F. Cavalieri and A. A. Correia, “Calibration and verification of a nonlinear macro-element for SSI analysis in the Groningen region,” *MOSAYK*, no. April, 2019.
- [87] SeismoStruct, “SeismoStruct User Manual,” SeismoStruct, p. 325, 2018, [Online]. Available: <https://seismosoft.com/>.
- [88] Seismosoft Ltd, “SeismoStruct Verification Report,” SeismoStruct, 2018, [Online]. Available: <http://www.seismosoft.com>.
- [89] SeismoStruct, “Technical Information Sheet - Nonlinear Analysis and Assessment of Structures,” SeismoStruct, pp. 1–40, 2018.
- [90] A. A. Correia and A. Pecker, *Nonlinear pile-head macro-element for the seismic analysis of structures on flexible piles*, vol. 19, no. 4. Springer Netherlands, 2021.

APPENDIX

Table A.1 – Pile foundations macro-element - SSILINK2 input parameters

Parameter	Symbol	Value	Unit
Pile diameter (D)	DIAM	0.4	m
Pile stiffness for vertical direction (Hard Soil)	K_VV	3341223	KN/m
Pile stiffness for vertical direction (Medium Soil)	K_VV	1167224	KN/m
Pile stiffness for vertical direction (Soft Soil)	K_VV	191816	KN/m
Pile stiffness for vertical direction (Soil 1)	K_VV	191816	KN/m
Pile stiffness for horizontal direction (Hard Soil)	K_HH	5109101	KN/m
Pile stiffness for horizontal direction (Medium Soil)	K_HH	2417201	KN/m
Pile stiffness for horizontal direction (Soft Soil)	K_HH	650058	KN/m
Pile stiffness for horizontal direction (Soil 1)	K_HH	580291	KN/m
Pile stiffness for rotational directions (Hard Soil)	K_MM	536391	KN/m
	K_HM	-1168854	KN/m
	K_TT	73824	KN/m
Pile stiffness for rotational directions (Medium Soil)	K_MM	411191	KN/m
	K_HM	-567583	KN/m
	K_TT	21921	KN/m
Pile stiffness for rotational directions (Soft Soil)	K_MM	295171	KN/m
	K_HM	-295190	KN/m
	K_TT	3020	KN/m
Pile stiffness for rotational directions (Soil 1)	K_MM	267733	KN/m
	K_HM	-282541	KN/m
	K_TT	3020	KN/m
Maximum horizontal pile head force with no eccentricity (Hard Soil)	QQ_H_MAX	1274	KN
Pile head yield moment (Hard Soil)	QQ_M_MAX	3954	KN-m
Maximum horizontal pile head force with no eccentricity (Medium Soil)	QQ_H_MAX	940	KN
Pile head yield moment (Medium Soil)	QQ_M_MAX	3228	KN-m
Maximum horizontal pile head force with no eccentricity (Soft Soil)	QQ_H_MAX	559	KN
Pile head yield moment (Soft Soil)	QQ_M_MAX	2283	KN-m
Maximum horizontal pile head force with no eccentricity (Soil 1)	QQ_H_MAX	647	KN
Pile head yield moment (Soil 1)	QQ_M_MAX	2518	KN-m
Superellipse BS parameters (Hard Soil)	Exp_nH	8.435	
	Exp_nM	2.000	
	GAMMA	-0.597	
Superellipse BS parameters (Medium Soil)	Exp_nH	7.738	
	Exp_nM	2.000	
	GAMMA	-0.632	
Superellipse BS parameters (Soft Soil)	Exp_nH	7.04	
	Exp_nM	2.000	
	GAMMA	-0.667	

Superellipse BS parameters (Soil 1)	Exp_nH	8.435	
	Exp_nM	2.000	
	GAMMA	-0.597	
Maximum Gap depth / soil wedge depth corresponding to the failure mechanism	ZW	3.73	m
Pile Flexural Stiffness = $E_p * I_p$	Eplp	31416	KN-m ²
Gap Evolution Parameter	BETA	1	
Minimum Gap Evolution Parameter	ETA	1	
Reference plastic modulus parameter	PL_H0	0.4	
Exponent for plastic modulus evolution	PL_nur	1	
Lower limit value for delta in unloading/reloading	Delta_LIM	0.1	
Young's modulus of the pile material	E _p	25000000000	N/m ²
soil modulus of deformation at a depth equal to the pile diameter (Hard Soil)	E _{SD}	1990000000	N/m ²
soil modulus of deformation at a depth equal to the pile diameter (Medium Soil)	E _{SD}	650000000	N/m ²
soil modulus of deformation at a depth equal to the pile diameter (Soft Soil)	E _{SD}	97000000	N/m ²
soil modulus of deformation at a depth equal to the pile diameter (Soil 1)	E _{SD}	97000000	N/m ²
Grade of Concrete	f _{ck}	25	Mpa
Moment of inertia of pile = $\pi D^4/64$	I _p or I _{bz}	0.0013	m ⁴
Poisson's Ratio (Hard Soil)	v	0.2	
Poisson's Ratio (Medium Soil)	v	0.32	
Poisson's Ratio (Soft Soil)	v	0.43	
Poisson's Ratio (Soil 1)	v	0.43	
soil shear modulus of deformation at a depth equal to the pile diameter (Hard Soil)	$G = E_{SD} / 2(1 + v)$	829166667	N/m ²
soil shear modulus of deformation at a depth equal to the pile diameter (Medium Soil)	$G = E_{SD} / 2(1 + v)$	246212121	N/m ²
soil shear modulus of deformation at a depth equal to the pile diameter (Soft Soil)	$G = E_{SD} / 2(1 + v)$	33916084	N/m ²
soil shear modulus of deformation at a depth equal to the pile diameter (Soil 1)	$G = E_{SD} / 2(1 + v)$	33916084	N/m ²
Half of width of circumscribed rectangle	B = D / 2	0.2	m
Half of length of circumscribed rectangle	L = D / 2	0.2	m
Area of pile	$A_b = \pi D^2 / 4$	0.125663706	m ²
	$\chi = A_b / 4L^2$	0.785398163	
Soil deposit depth	L _s	30	m
Shear wave velocity at a depth of one pile diameter (Hard Soil)	V _{SD}	600.423	m/sec
Shear wave velocity at a depth of one pile diameter (Medium Soil)	V _{SD}	350.865	m/sec
Shear wave velocity at a depth of one pile diameter (Soft Soil)	V _{SD}	150.369	m/sec

Shear wave velocity at a depth of one pile diameter (Soil 1)	V_{SD}	150.369	m/sec
Shear wave velocity at the bottom of the soil profile (Hard Soil)	V_{SL}	600.423	m/sec
Shear wave velocity at the bottom of the soil profile (Medium Soil)	V_{SL}	350.865	m/sec
Shear wave velocity at the bottom of the soil profile (Soft Soil)	V_{SL}	150.369	m/sec
Shear wave velocity at the bottom of the soil profile (Soil 1)	V_{SL}	600.423	m/sec
Soil deposit fundamental frequency (Hard Soil)	f_s	4.463	Hz
Soil deposit fundamental frequency (Medium Soil)	f_s	2.924	Hz
Soil deposit fundamental frequency (Soft Soil)	f_s	0.952	Hz
Soil deposit fundamental frequency (Soil 1)	f_s	4.463	Hz
Pile-head radiation damping coefficient (Hard Soil)	ξ_{HH}	0.004368696	
	ξ_{MM}	0.001340357	
	ξ_{HM}	0.002362088	
Pile-head radiation damping coefficient (Medium Soil)	ξ_{HH}	0.006819083	
	ξ_{MM}	0.002420762	
	ξ_{HM}	0.005465155	
Pile-head radiation damping coefficient (Soft Soil)	ξ_{HH}	0.004560000	
	ξ_{MM}	0.001013333	
	ξ_{HM}	0.002533333	
Pile-head radiation damping coefficient (Soil 1)	ξ_{HH}	0.021370559	
	ξ_{MM}	0.004749013	
	ξ_{HM}	0.011872533	
Soil deposit angular frequency (Hard Soil)	$\omega = 2\pi f_s$	28.043	rad/s
Soil deposit angular frequency (Medium Soil)	$\omega = 2\pi f_s$	18.371	rad/s
Soil deposit angular frequency (Soft Soil)	$\omega = 2\pi f_s$	5.984	rad/s
Soil deposit angular frequency (Soil 1)	$\omega = 2\pi f_s$	28.043	rad/s

Table A.2 – Dashpot damping element – dashpt input parameters

Parameter	Symbol	Value	Unit
Damping Coefficients for dashpot damping element (dashpt) (Hard Soil)	C1	0	tonne/sec
	C2 = C_{HH}	162.32	tonne/sec
	C3 = C_{HH}	162.32	tonne/sec
	C11	0	tonne-m ² /sec
	C22 = C_{MM}	5.23	tonne-m ² /sec
	C33 = C_{MM}	5.23	tonne-m ² /sec
	CH2M3 = C_{HM}	-20.08	tonne-m/sec
	CH3M2 = C_{HM}	-20.08	tonne-m/sec

Damping Coefficients for dashpot damping element (dashpt) (Medium Soil)	C1	0	tonne/sec
	C2 = C _{HH}	182.98	tonne/sec
	C3 = C _{HH}	182.98	tonne/sec
	C11	0	tonne-m ² /sec
	C22 = C _{MM}	11.05	tonne-m ² /sec
	C33 = C _{MM}	11.05	tonne-m ² /sec
	CH2M3 = C _{HM}	-34.44	tonne-m/sec
	CH3M2 = C _{HM}	-34.44	tonne-m/sec
Damping Coefficients for dashpot damping element (dashpt) (Soft Soil)	C1	0	tonne/sec
	C2 = C _{HH}	101.03	tonne/sec
	C3 = C _{HH}	101.03	tonne/sec
	C11	0	tonne-m ² /sec
	C22 = C _{MM}	10.19	tonne-m ² /sec
	C33 = C _{MM}	10.19	tonne-m ² /sec
	CH2M3 = C _{HM}	-25.49	tonne-m/sec
	CH3M2 = C _{HM}	-25.49	tonne-m/sec
Damping Coefficients for dashpot damping element (dashpt) (Soil 1)	C1	0	tonne/sec
	C2 = C _{HH}	90.19	tonne/sec
	C3 = C _{HH}	90.19	tonne/sec
	C11	0	tonne-m ² /sec
	C22 = C _{MM}	9.25	tonne-m ² /sec
	C33 = C _{MM}	9.25	tonne-m ² /sec
	CH2M3 = C _{HM}	-24.40	tonne-m/sec
	CH3M2 = C _{HM}	-24.40	tonne-m/sec